Author:
Hewson, Will J R

Title:
A New Aerodynamic Model for Unsteady Separated Flow on High Aspect Ratio Flexible Wings

A New Aerodynamic Model for Unsteady Separated Flow on High Aspect Ratio Flexible Wings

By

WILL JAMES RICHARD HEWSON

Department of Aerospace Engineering
UNIVERSITY OF BRISTOL

A dissertation submitted to the University of Bristol in accordance with the requirements of the degree of DOCTOR OF PHILOSOPHY in the Faculty of Engineering.

NOVEMBER 2019

Word count: 47,000

Abstract

Flow separation and dynamic stall have been an active research topic in the past decades. Traditionally, rotor blades have been at the forefront of research into dynamic stall. In recent years there has been an interest in high aspect ratio wings for commercial aircraft because of the potential for greater aerodynamic efficiency which has been necessitated by the requirement of greater fuel efficiency. However, future high aspect ratio wings will be more flexible to reduce mass, this in turn will lead to large deformations that can induce flow separation and stall.

Herein lies the motivation for this thesis, a tool is required that can rapidly give an engineering approximation to the response of a wing undergoing unsteady flow separation. The method developed in this thesis is capable of calculating the dynamic, aeroelastic response to an unswept, clean finite wing.

The proposed model is formulated through coupling the Beddoes-Leishman dynamic stall model with an unsteady lifting line theory for aerodynamic analysis of a finite wing undergoing unsteady motions. This is later extended to include a nonlinear beam model to produce an aeroelastic analysis tool. CFD (Computational Fluid dynamics) and experimental data is utilized to evaluate the model outputs for a finite wings undergoing pitching oscillations at high and low angles of attack. Overall the inclusion of a dynamic stall model offers significant improvement over uncorrected potential flow models.

ACKNOWLEDGEMENTS

I would firstly like to thank my supervisors Dr Dorian Jones and Dr Ann Gaitonde for their patience and support throughout this PhD. I would also like to thank all of the researchers involved on the Agile Wing Integration project, which this work forms a part of. This is also where the funding for this research orignates, through InnovateUK (grant no. UKRI-113041).

I would also like to thank Alexandre Payot and Matt Edwards for the innumerous hours we spent together, whether that be in the office, riding bicycles or finding a good pub.

Most importantly I would like to thank my parents for their unwavering support.

AUTHOR'S DECLARATION

I declare that the work in this dissertation was carried out in accordance with the requirements of the University's Regulations and Code of Practice for Research Degree Programmes and that it has not been submitted for any other academic award. Except where indicated by specific reference in the text, the work is the candidate's own work. Work done in collaboration with, or with the assistance of, others, is indicated as such. Any views expressed in the dissertation are those of the author.

SIGNED: ..... DATE: .....

TABLE OF CONTENTS

List of Tables

List of Figures

Figure **Page**

Roman Symbols

a, e, r	Empirical ONERA coefficients
b	Wing Semi-span (m)
c	Chord Length (m)
c_p	Pressure coefficient
$\mathbf{C}$	ULLT matrix
C_D	Drag force coefficient
C_{D_0}	Zero lift drag coefficient
C_{fx}, C_{fy}, C_{fxz}	Skin friction component in the x, y and z direction
C_{fxyz}	Magnitude of skin friction vector
c_l	2D aerofoil lift force coefficient
c_{l_α}	aerofoil lift curve slope (rad^{-1})
C_l	sectional lift force coefficient
C_{l_α}	sectional lift curve slope (rad^{-1})
C_L	3D integrated lift force coefficient
$C_{L\text{Max}}$	Maximum lift force coefficient
c_m	Aerofoil Moment coefficient
c_{m_α}	Aerofoil moment curve slope (rad^{-1})
C_m	Sectional moment coefficient
C_{m_α}	Sectional moment curve slope (rad^{-1})
C_{m0}	Zero lift moment coefficient

C_N	Normal force coefficient
C'_N	Normal force coefficient with first order lag
C_{n_s}	Static normal force coefficient
$C(k)$	Theodorsen function
d	Distance from surface nondimensionalised by chord
E	Total energy (J)
$\mathbf{E}$	ULLT matrix
f	Separation position nondimensionalised by the chord
f_0	Static separation position
f'	First order lagged separation position
f''	Second order lagged separation position
F	Coefficient for velocity influence in separated region
$\mathbf{F}$	ULLT matrix
F_1	Linear ONERA load
F_2	Non-linear ONERA load supplement
F_l	Linear extrapolation of static force curve
$\mathbf{G}$	ULLT matrix
h	Plunge displacement (m)
k_T	Turbulent kinetic energy
k	Reduced Frequency $\frac{\omega c}{2U_\infty}$
K	Kirchhoff relation $((1+\sqrt{f})/(2))^2$
M	Mach number
M_∞	Freestream Mach number
p	Pressure (Pa)
$\mathbf{P}$	ULLT matrix
Pr	Prandtl Number
$\mathbf{q}$	ULLT matrix
Re	Reynolds number
s	Beam coordinate system

S	Nondimensional distance travelled in semi-chords
S_1, S_2	Beddoes-Leishman separation point fit parameters
T	Temperature (°K)
T_P, T_V, T_F, T_{vl}	Beddoes-Leishman time constants
U_i	Velocity in tensor notation
U_∞	Freestream Velocity ($\mathrm{m\,s^{-1}}$)
v_T	Beam translational velocity ($\mathrm{m\,s^{-1}}$)
V_R	Beam rotational velocity ($\mathrm{m\,s^{-1}}$)
x	Chordwise direction (m)
y	Spanwise direction (m)
y^+	Sublayer scaled distance
$\mathbf{W}$	ULLT matrix

Greek Symbols

α	Angle of attack
α''	Lagged angle of attack w.r.t f''
α_0	Mean angle of attack
α_{0L}	Static zero lift angle of attack
α_1	Angle of attack amplitude
α_{corr}	Viscous corrective angle of attack, used in NULLT
α_{eff}^{3D}	Effective 3D angle of attack
α_{ss}	Critical (static stall) angle of attack
α_{ds}	Dynamic stall angle of attack
β	Prandtl-Glauert compressibility correction $(1 - M_\infty^2)$
γ	Beam strain
Γ	Circulation ($\mathrm{m^2\,s^{-1}}$)
Γ_T	Total circulation in attached and separated region

δ	Mach number dependent correction factor
δ_{ij}	Kronecker delta
$\Delta\alpha_c$	Experimental angle of attack correction
ΔF	Deviation from static force curve
θ_0	Geometrical twist
κ	Beam curvature
$\kappa_0(s)$	Beam pre-curvature
λ, s	Empirical ONERA coefficients
Λ	Sweep angle (°)
μ	Dynamic viscosity
ρ	Density ($\mathrm{kg\,m^{-3}}$)
σ	Empirical ONERA coefficient
σ_{ij}	Strain rate tensor
τ_1	Goman-Khrabrov relaxation time constant
τ_2	Goman-Khrabrov dynamic stall vortex lag
τ_{ij}^T	Favre stress
ϕ^B	Blending function
ω	Circular frequency (Hz)

Other Symbols

$\Re$	Real part of quantity
$\Im$	Imaginary part of quantity
$\uparrow$	$\dot{\alpha} > 0$
$\downarrow$	$\dot{\alpha} < 0$

CHAPTER 1

INTRODUCTION

1.1 Background

The current economic and environmental situation has initiated research into the design of more efficient commercial aircraft, for example one aspect of the Flightpath 2050 programme aims to reduce the CO_2 emissions produced by commercial aircraft by 75% before 2050 [1]. This supports other initiatives from ATAG (Air Transport Action Group) which drives for a 50% reduction in overall CO_2 emissions by 2050 (with respect to 2005 levels) [2]. In recent years there has been an increased interest in the viability of high aspect ratio wings (HARW) [3]. The primary reason for such interest lies in increased aerodynamic efficiency due the inverse relationship between the induced drag and wing aspect ratio. In the past 50 years, there has already been a trend for the aspect ratio of larger passenger jet aircraft to increase as demonstrated in Figure 1.1, which shows the relationship between aspect ratio and delivery year. There has also been considerable research into significantly increasing the aspect ratio further, an example of this is the development of the Sugar VOLT concept which is being considered by Boeing. The Sugar VOLT's truss-braced wing is sized to obtain an aspect ratio of 19.55 [4]. Further to this there has been interest in increasing wingspan by the inclusion of a freely hinged folding

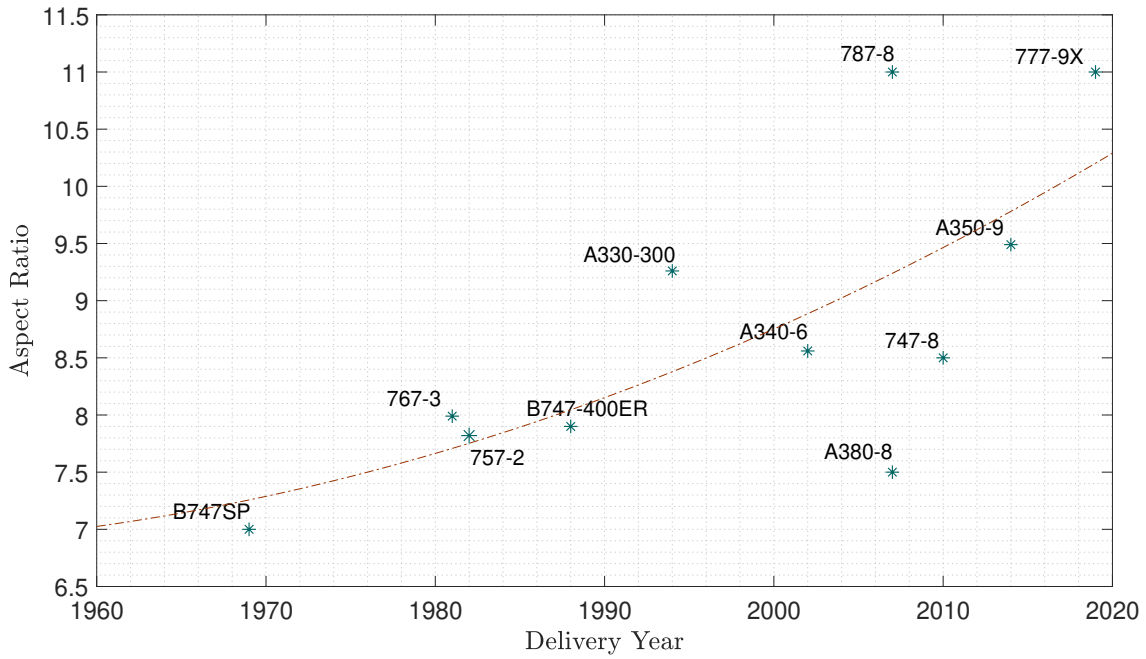

Figure 1.1: Main wing aspect ratio variation with year of delivery, dashed line represents quadratic least squares fit.

wingtip. The folding wingtip would allow the continued use of standard airport gates, with the benefits of a high aspect ratio wing and the potential of load alleviation [5]. The AlbatrossONE is an example of this approach, it is a small scale Airbus concept aircraft which has recently undergone flight testing. The AlbatrossONE features a wing with an aspect ratio of 18 and folding wingtips [5] [6]. It is clear that the benefits of high aspect ratio wings are being sought by aircraft manufacturers. The concept aircraft described above from Airbus and Boeing are shown in Figure 1.2.

However, whilst HARW offer potential efficiency gains through reduced induced drag, they introduce some detrimental behaviours too. HARW can experience larger deformations, especially when modern composite materials are utilized. Composite wings are able to replicate the load carrying abilities of aluminium wings with less structural stiffness [7]. For example, the composite wing on the Boeing 787 Dreamliner can experience a tip deflection of approximately 10% of the semi-span at cruise conditions. This is significantly more that an aluminum counterpart [8]. HARW also often have

(a) AlbatrossOne [6] (b) Boeing SugarVOLT (artist's impression) [4]

Figure 1.2: Concept aircraft from Airbus and Boeing

little sweep, this can reduce the bending-torsion coupling that is inherent in swept-back wings which can provide gust load alleviation since typically a swept-back wing will pitch nose-down when the wing bends up [3] [9] [10]. For this reason, they are typically reserved for high altitude, long endurance (HALE) aircraft. This work forms part of the Agile Wing Integration (AWI) project which was an Airbus UK led project involving Cranfield University, Loughborough University and the University of Bristol. The AWI project focused on the inclusion of lightweight, HARW which can help improve fuel efficiency of future commercial aircraft. This thesis focuses on the aerodynamic modelling of separated flow on finite wings, in order to be able to predict and understand the effect of aerodynamic nonlinearities on HARW, without resorting to high-fidelity CFD.

The combination of large deformations and lack of bending-torsion coupling for low sweep wings pushes the limits of current aeroelastic tools used in the early stage of design. It is commonplace for the aerospace industry to use potential flow methods for aerodynamic analysis. These can predict the steady and unsteady responses within the linear, attached flow regime [11]. These methods are relied upon so heavily because of the vast number of load cases that need to be simulated within each design cycle. However the ability to include the effects of the nonlinearities that can occur on flexible HARW will be vital in early design and therefore the effects of flow separation and even dynamic

stall should be included. Once flow separation occurs, assumptions of standard potential flow models are no longer valid. It is also worth noting that vorticity can be shed from not only the trailing edge and separation position, it can also be shed from the leading edge in the form of a dynamic stall vortex (DSV), which convects along the lifting surface. Dynamic stall is the focus of this thesis, in particular the development of methods that can model the effects of dynamic stall and are efficient enough to be used for early stage design. The method developed expands a 2D model of aerofoil stall, created using 2D data from CFD or experiment, into an efficient 3D model that can be used in the early stages of design for a flexible high aspect ratio wing. The testing of the model is based on a clean UAV wing design as this is the most likely first candidate for such flexible wing technology.

1.2 Static stall

Nonlinearities in the relationship between angle of attack and the aerodynamic forces & moments are introduced by flow separation. The simplest way in which to investigate flow separation is to limit the problem to be two-dimensional with the aerofoil and oncoming flow steady. It should be noted that a static flow problem may be unsteady. A static aerofoil at high angles of attack experiencing separated flow may well have a transient flow field and therefore the static aerofoil may have time-dependent aerodynamic forces and moments. Keeping an aerofoil fixed reduces the need to understand how the aerofoil motion affects the separation behaviour, furthermore it negates the need to model the shedding of a leading edge vortex which is a key feature of dynamic stall. It is for the aforementioned reasons that 2D static stall is discussed prior to the three-dimensional and dynamic counterpart.

1.2.1 Static Stall Mechanism

Static stall occurs on lifting surfaces when the critical angle of attack is exceeded. The critical angle of attack is the angle of attack at which the maximum lift coefficient is

achieved. The critical angle of attack does not represent the initiation of flow separation, by the point at which the critical angle of attack is reached it is common for substantial flow separation to be present. The angle at which the flow first begins to separate is the stall onset angle. The difference between the critical angle and stall onset angle is shown in Figure 1.3, highlighting how the stall onset and critical angle are manifested in a static lift coefficient response. Figure 1.3 displays experimental data for a NACA 0015 aerofoil [12] along with an extrapolated linear lift curve. Stall onset is near the point where the linear approximation deviates from the experimental results, with the critical angle set as the angle of attack where the maximum c_l is found.

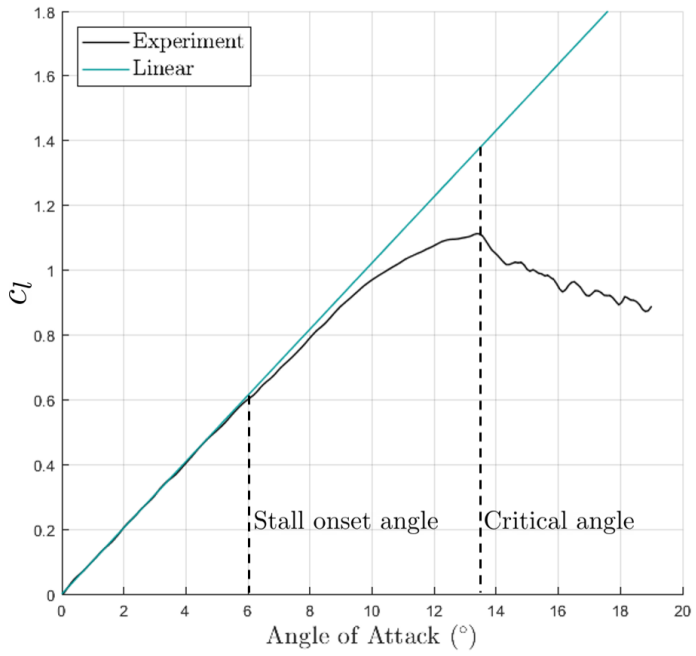

Figure 1.3: Definition of stall onset angle and critical angle of attack

Static stall experiments at low speeds were carried out by George B. McCullough and Donald E. Gault [13]. They presented three different stalling characteristics for symmetrical aerofoils at low speeds, these are as follows:

- Trailing edge stall, this classifies stall when the separation point occurs at the

trailing edge, moving towards the leading edge as the angle of attack increases.

- Leading edge stall, here the point of separation occurs at the leading edge, and usually no reattachment is seen downstream.
- Thin aerofoil stall, this is similar to leading edge stall, however reattachment may happen downstream. The point of reattachment generally will move towards the trailing edge as the angle of attack is increased.

Due to the fact that leading edge stall results in sudden flow separation across the aerofoil, it is associated with a more drastic response in the lift or normal forces.
Figure 1.4 describes how the lift, drag, normal and axial force act on a two-dimensional aerofoil. The lift (L) and drag (D) forces are defined as perpendicular and parallel to the freestream velocity vector respectively. Whilst the normal (N) and axial (A) force are defined as being normal and tangential to the aerofoil chord line. A moment (M) is also chosen to be calculated around a moment reference point, the sign convention for moment is for M to be positive nose up, as shown in Figure 1.4(b).

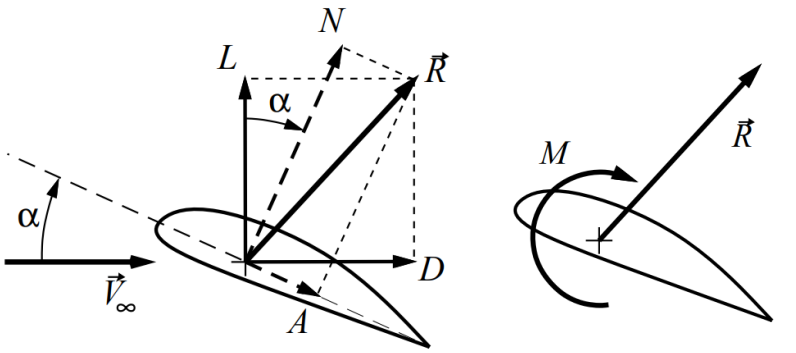

(a) Aerofoil forces

(b) Moment reference location

Figure 1.4: Definition of lift, normal, drag, chordwise forces and moment reference location. Taken from [14]

The angle made between the freestream velocity vector and the chord line is defined as the angle of attack, α. The lift, drag, normal and axial force can be related through the angle of attack:

$$L = N\cos\alpha - A\sin\alpha$$
$$D = N\sin\alpha + A\cos\alpha \tag{1.1}$$

Figure 1.5 illustrates the relationship between the angle of attack and lift force coefficient c_l, along with the non-dimensional separation position, f, for two theoretical aerofoils. The curves are obtained by using a special case of Kirchhoff flow which represents a model of trailing edge separation [15]. The Kirchhoff flow model is explained in more detail in Chapter 3, however the definition of the separation position is illustrated in Figure 1.6. For the leading edge stall case, the model is manipulated so that f rapidly moves from the TE to the LE of the aerofoil upon reaching the critical angle of attack. The Kirchhoff model is only valid for trailing edge stall mechanisms, however it gives some level of understanding of how the movement of the separation position controls the lift coefficient response of an aerofoil. Usually with leading edge stall a greater maximum lift coefficient c_l can be achieved, however the sudden severe flow separation has drastic consequences on the control of an aircraft. For this reason it is often preferred to utilise an aerofoil that has trailing edge stall characteristics.

1.3 Hysteresis

The static c_l vs incidence plots in Figure 1.3 and 1.5 are made with values obtained whilst increasing incidence. However the system becomes more complex if values are also obtained whilst decreasing incidence, when the phenomenon of hysteresis can be observed. The term hysteresis comes from the ancient Greek husterēsis meaning 'shortcoming, deficiency' or from husterein 'be behind' [16] and is used to describe the dependence of a physical system on its history.

Consider a harmonically pitching aerofoil at small amplitude, then a difference is observed between the flow fields at a particular incidence depending on whether the aerofoil

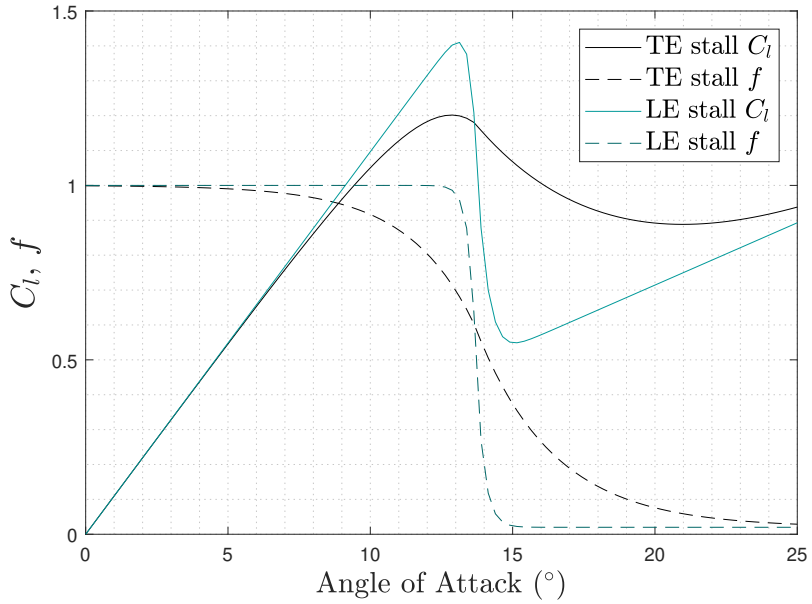

Figure 1.5: C_N againt angle of attack for leading edge and trailing edge stall mechanism. f represents the non-dimensional separation parameter.

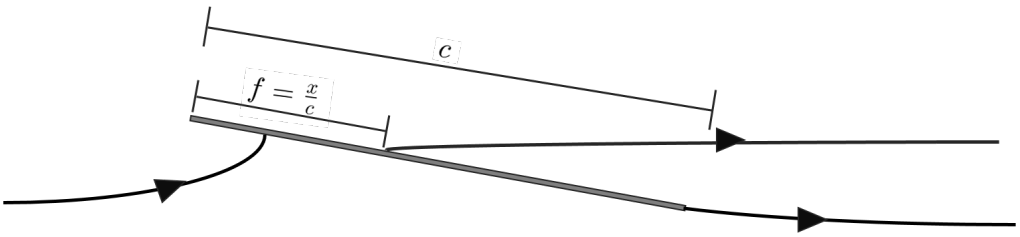

Figure 1.6: The Kirchhoff flow model representing trailing edge stall, illustrating nondimensional separation parameter, f.

has angle of attack increasing or decreasing angle of attack., because the speed and acceleration of the aerofoil surface will differ. This means the current state of the system depends on its previous time history and the solution can be sensitive to the sign of pitch rate, $\dot{\alpha}$ .Thus there is a phase lag, which leads to loops in, for example, the Cl vs angle of attack plots. An example of such loop can be seen in Figure 1.7. Note that for an aerofoil, the pitch angle is equal to the angle of attack (the angle between the chord line and freestream vector). For an aircraft the pitch angle is defined as the angle between the longitudinal axis of the aircraft and the horizon. The aircraft wing will likely have a different angle of attack that will vary with setting angle and washout.

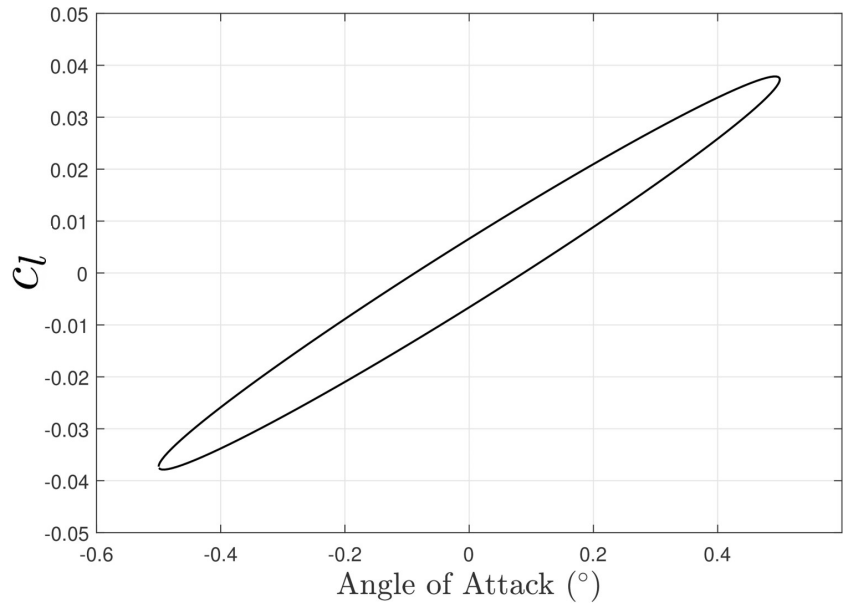

Figure 1.7: Dynamic c_l v α loop, attached flow

If the flow remains attached throughout the pitching oscillation then the dynamic lift coefficient loop disappears as the frequency tends to zero i.e. static conditions are approached. This type of phase lag behaviour is often referred to as rate-dependent hysteresis. Rate dependent hysteresis causes a lag between the input and output which depends on the frequency of the input, this can only occur in linear systems. As the rate of the input tends to zero, the phase lag between the input and output will inherentlyrem tend to zero [17].

If during the pitching motion the flow separates then the loops in the dynamic lift coefficient plot (see Figure 1.8) do not disappear as the motion frequency tends to zero i.e. non-unique solutions exist even under static conditions after changes in angle of attack [18]. This rate-independent hysteresis, means the nonlinear system of equations is inherently hysteretic. Only non-linear systems are hysteretic, in contrast to rate-dependent hysteresis that arises in both linear and nonlinear systems. The system has a persistent memory of the past states and inputs and as the input rate tends to zero [17] . For the flow cases where the angle of attack changes, the lift coefficient depends on the direction of

the change in the angle of attack even in the static measurement situation, see Figure 1.9.

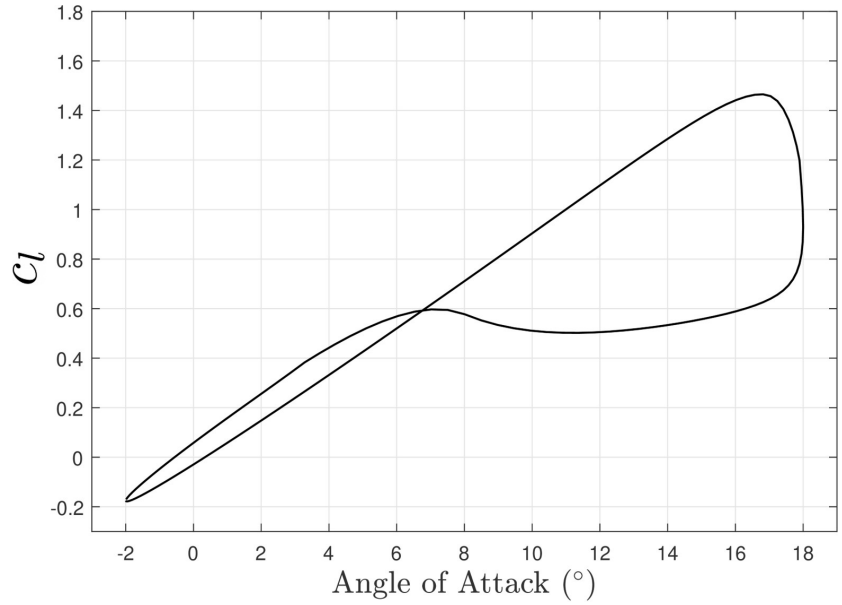

Figure 1.8: Dynamic c_l v α with flow separation

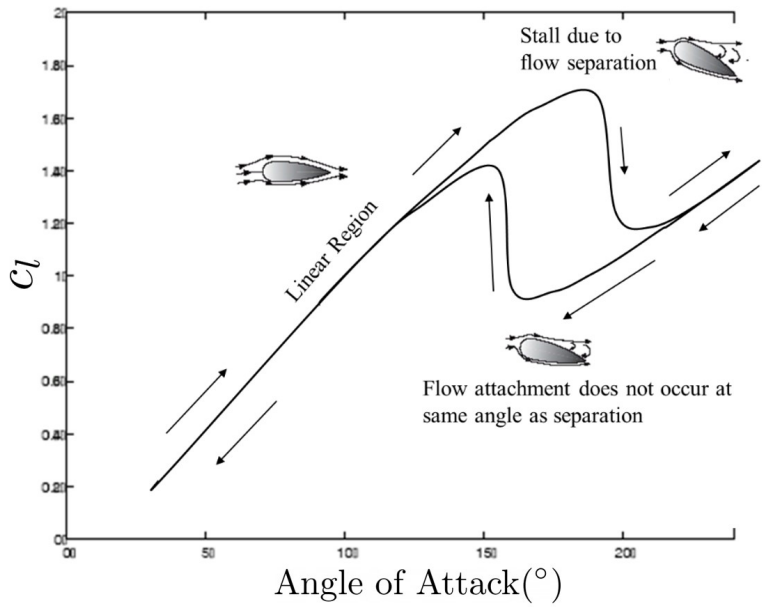

Figure 1.9: Illustration of static hysteresis and relationship with separation position, adapted from [19].

Thus the relationship between the aerodynamic forces and moments under static con-

ditions are not always unique. This is most prevalent when the separation position is sensitive to changes in angle of attack, i.e, $\frac{df}{d\alpha}$ is large and therefore larger gradients in the spanwise bound circulation can be experienced from sectional changes in the effective angle of attack. Therefore it is not unusual for static hysteresis to be present near the critical angle of attack. Figures 1.10(a) and 1.10(b) show static hysteresis in the lift and moment coefficients for a NACA 0015 aerofoil [12]. In this case greater flow separation was found when the angle of attack is reduced. This resulted in a static hysteresis loop in the region of the critical angle of attack. Away from this region the discrepancy between the upstroke and the downstroke diminishes. The multiple solution branches add extra complexity to the separated flow regime and care needs to be taken in detailing the way in which a static solution is derived.

It is also import to consider the hysteresis in the pitching moment coefficient. The direction of the moment hysteresis loop determines the aerodynamic damping effects. An example of a pitching moment hysteresis loop is given in Figure 1.11, which has arrows applied to show the direction. An anti-clockwise loop signifies that the structure is doing work on the aerodynamics, this gives positive aerodynamic damping. An anti-clockwise loop is present between an angle of attack of 7.0° and 12.9°. At 12.9° there is an intersection and the loop becomes clockwise at higher angles of attack. This causes the aerodynamics to do work on the structure, which is negative aerodynamic damping and can cause instabilities [20].

1.4 Unsteady attached aerodynamics

Lifting surfaces undergoing unsteady small amplitude motions are subject to linear, unsteady aerodynamic effects. These are often perceived through a magnitude and phase change in the aerodynamic force and moment responses. The phase lag can be due to an apparent angle of attack from the heaving velocity of the leading edge and the lag in the build up of circulation. These mechanisms lead to an effective angle of attack, α_E, which

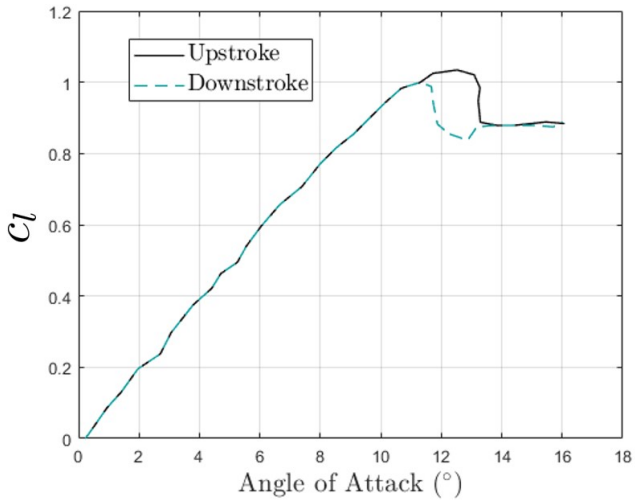

(a) Static Hysteresis in c_l

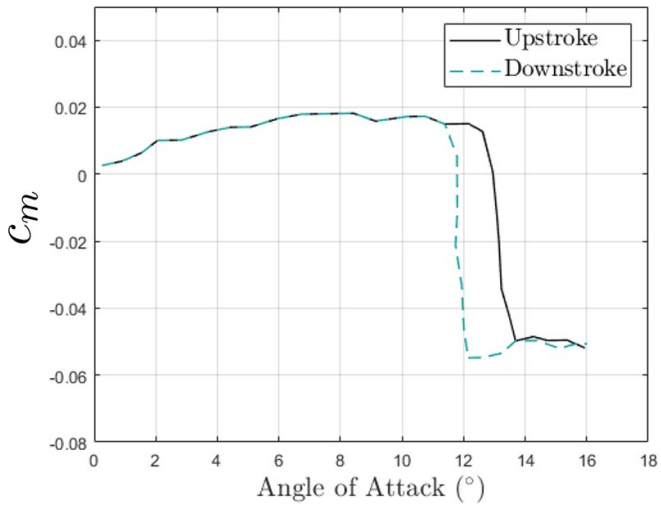

(b) Static Hysteresis in C_M

Figure 1.10: Static Hysteresis found in NACA 0015 aerofoil [12].

consists of additional pitch rate and plunging terms compared to the geometrical angle of attack, α. If an attached, quasi-steady flow is considered, for a flat plate undergoing a combination of pitching and plunging motions, the lift coefficient could be calculated as

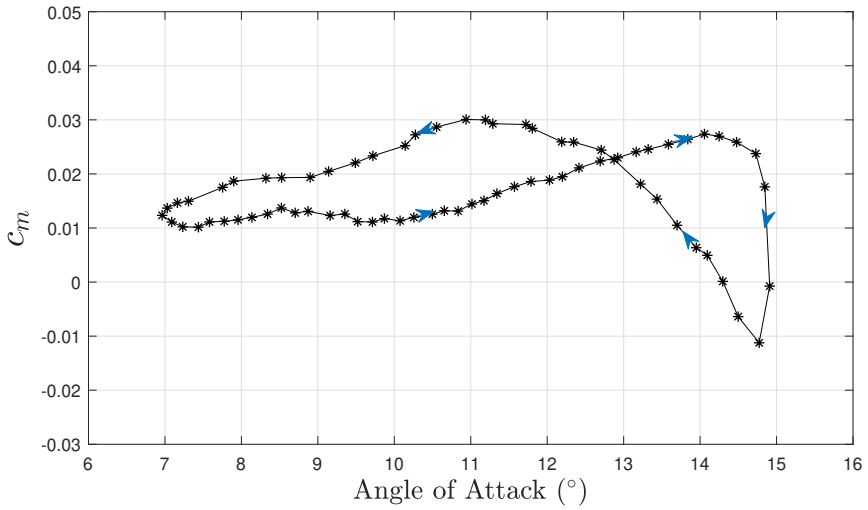

Figure 1.11: Pitching moment coefficient hysteresis for a NACA 0015 with pitching oscillation $\alpha = 11° \pm 4° \sin(0.15S)$, moment data from: [12].

follows from thin aerofoil theory [21] [22]:

$$C_L = 2\pi\left(\alpha + \dot{h} + \frac{1}{2}\dot{\alpha}\left(\frac{1}{2} - a\right)\right) \tag{1.2}$$

where the plunge rate, $\dot{h}$ and pitch rate, $\dot{\alpha}$ are translated into an effective angle of attack. The distance between the mid-chord and the pitch axis is represented by a. The terms within the bracket of Equation (1.2) form the effective angle of attack. Figure 1.12 shows an attached c_l response for a steady and quasi-steady pitching oscillation. This highlights the difference between the geometrical and effective angle of attack, $\Delta\alpha$. The unsteady response has a reduction in the slope of the aerodynamic coefficients (with respect to α) compared with a static response. Furthermore there is a phase change which creates the hysteresis loop. The magnitude and phase of the response is a result of how unsteady the problem is. In 1935 Theodorsen developed an unsteady model for the lift distribution for a pitching and plunging aerofoil. The model assumes inviscid, incompressible flow where the aerofoil is modelled as a flat plate with a planar wake [23]. The model was developed for sinusoidal movements in pitch and plunge and is therefore defined in the frequency domain. The Theodorsen model calculates the unsteady lift coefficient as

$$c_l = \underbrace{\frac{\pi}{2}\left[\ddot{h} + \dot{\alpha} - \frac{a}{2}\ddot{\alpha}\right]}_{\text{Apparent Mass}} + \underbrace{2\pi\left[\alpha + \dot{h} + \frac{1}{2}\dot{\alpha}\left(\frac{1}{2} - a\right)\right]}_{\text{Circulatory}} C(k) \tag{1.3}$$

The Theodorsen function, $C(k)$, is a transfer function that relates the reduced frequency, k, with the circulatory response. The reduced frequency defines the degree of unsteadiness of the problem, and is defined as follows:

$$k = \frac{\omega c}{2V_\infty} \tag{1.4}$$

Here ω is the circular frequency, c is the aerofoil chord length and V_∞ is the freestream velocity. The role of reduced frequency is detailed further in Section 1.6.3. The Theodorsen function is represented by Bessel functions of the first and second kind, however it is more conveniently approximated using the Jones approximation [24].

$$C(k) = 1 - \frac{0.165}{1 - \frac{0.0455}{k}i} - \frac{0.335}{1 - \frac{0.35}{k}i} \tag{1.5}$$

The magnitude and phase of $C(k)$ using the above approximation are shown in Figure 1.13. The unsteady response can then be calculated from Equation (1.3). Where $k = 0$, it can be seen in Figure 1.13 that the magnitude is 1, indicating no change from the static response, and the phase is 0, representing no change in phase. As k tends to infinity, the reduction in magnitude tends to an asymptote of 0.5. The phase (which manifests itself as the width of the hysteresis loop) reaches a maximum lag at $k = 1/3$, then reduces to 0 as k tends to infinity.

1.5 Dynamic stall process

When a lifting surface is undergoing a transient motion in which the angle of attack exceeds the stall onset angle, dynamic stall can occur. The events leading up to the occurrence of dynamic stall have been observed by many researchers [20] [25] [26] [27].

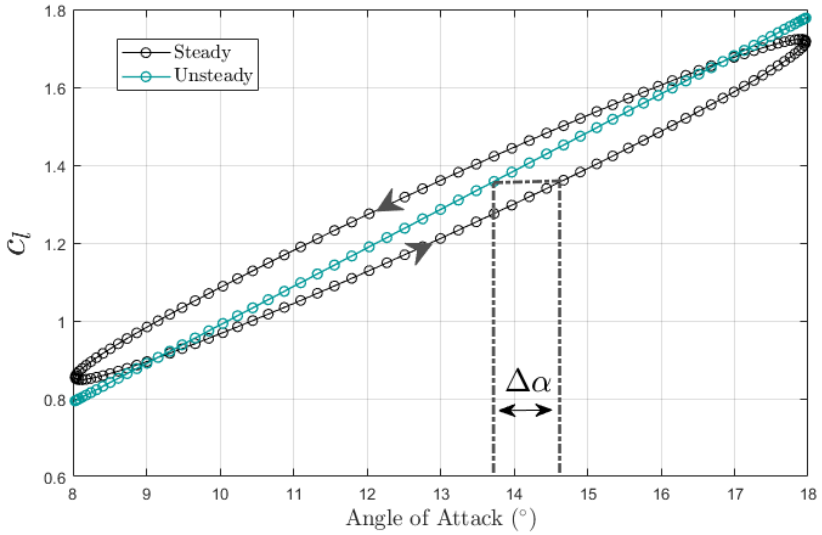

Figure 1.12: Illustration of effective angle of attack for a pitching motion

Figure 1.14 shows hysteresis loops for the lift, drag and pitching moment coefficients.

The defining events that occur during dynamic stall are summarised in Table 1.1 and the flow behaviour illustrated in Figure 1.15. Initially when the flow is nominally attached, the relationship between the angle of attack and aerodynamic coefficients is principally linear. At this stage the flow can be modelled using linear, unsteady aerofoil theory.

Increasing the angle of attack to the critical angle for the static case (point 1 in Figure 1.14), the lift and moment coefficients are still linear extrapolations of the attached flow, unlike what would be found in the static case. The delay in separation has been identified to be as a result of one of two mechanisms [21]. One of the mechanisms makes an inviscid assumption that the lag is caused by a reduced adverse pressure gradient when an aerofoil is pitching (compared to the static case), reducing the seen separation. On the other hand, whilst the aerofoil is pitching down the reverse is true and therefore the adverse pressure gradient is larger. This causes the boundary layer to be further from stall on the upstroke compared to the static case. The second mechanism is based on viscous theory and was termed the 'moving wall effect' by Ericsson and Reding [28].

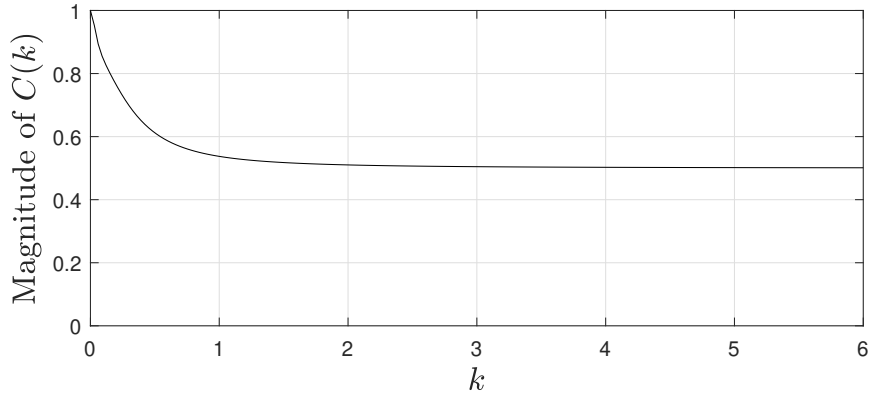

(a) Magnitude of $C(k)$

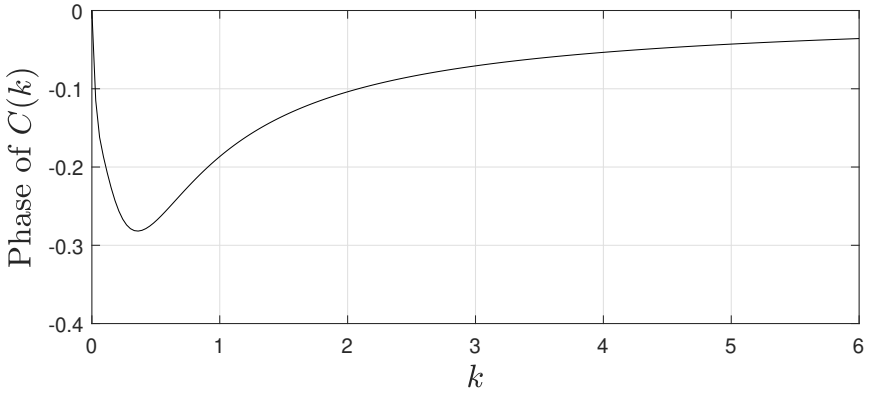

(b) Phase of $C(k)$

Figure 1.13: Magnitude and phase of Theodorsen function, $C(k)$.

This is based on the premise that as the leading edge of an aerofoil moves upwards, the boundary layer experiences an effect not dissimilar to that found on a rotating cylinder, hence the name moving wall effect. This gives a fuller boundary layer compared to the static case, which delays the separation. The opposite also stands for an aerofoil on the downstroke in which the moving wall effect promotes separation. Along with this a concentrated vortex can form at the leading edge, this is called a dynamic stall vortex (DSV). It should be noted that dynamic stall is often associated with a DSV being shed, [20] [29], however this is not necessary for dynamic stall to occur. Dynamic stall is classified as unsteady motion of a lifting surface with separation. For a complete description of the dynamic stall process, the event of a DSV forming and shedding is included below.

Upon reaching a critical pressure at the leading edge, a DSV convects along the upper surface of the aerofoil, this is referred to as dynamic stall onset [30] and is shown as point 4 in Figure 1.14 and Table 1.1. Whilst the DSV remains attached to the aerofoil, the normal force coefficient continues to increase. However, the convection of the DSV causes a significant change in the moment and drag coefficient. As the DSV moves towards the trailing edge the moment coefficient sharply becomes more negative (nose down), whilst the drag rapidly increases, this convection happens between points 3 and 4. When the DSV reaches the trailing edge at point 4, the normal force, drag and moment reach there largest values. This is followed by a DSV, which is shed from the trailing edge and the aerodynamic coefficients rapidly change. Figures 1.15(a) to 1.15(f) show contours of vorticity during the dynamic stall process, showing the formation and shedding of a DSV.

As the angle of attack is reduced the flow may start to reattach, however hysteresis will occur and the separation position can be different depending on $\dot{\alpha}$. This is highlighted by point 5 in Figure 1.14 where the separation remains more severe on the down-stoke in comparison with the up-stroke. Eventually the flow may reattach and the aerodynamic coefficients readjust to the linear regime.

It should be noted that the formation of a secondary vortex can also occur. After the dynamic stall vortex is shed and before the flow reattaches, McCroskey [20] reported a secondary vortex (and sometimes a tertiary vortex) travelling over the upper surface. Extra vortices were also noted by Spentzos [31], who postulates the secondary vortex is shed if the object undergoing stall remains above the critical angle after the DSV is shed. Leishman [32] believed there is evidence that there are weaker vortices shed near the maximum angle of attack.

An example flow field of a NACA 0009 undergoing dynamic stall, generated using 2D URANS, is shown in Figure 1.15. The NACA 0009 was used here for the reason that flows over thinner aerofoils tend to more readily separate from the leading edge and are hence

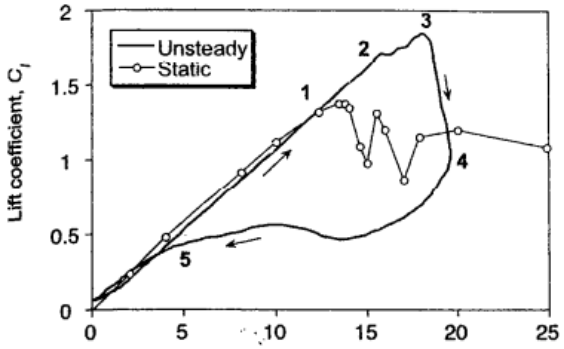

(a) c_l Hysteresis loop

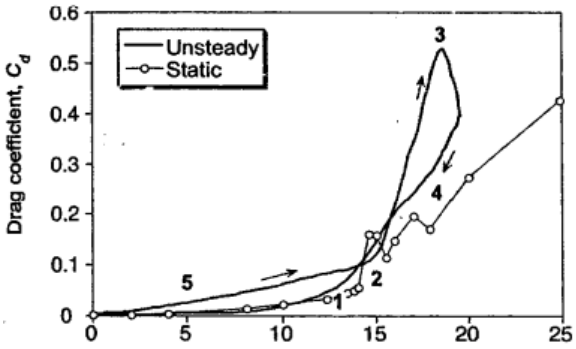

(b) c_d Hysteresis loop

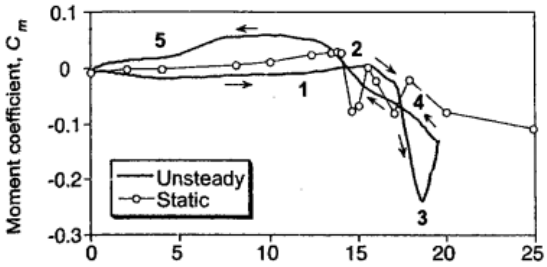

(c) c_m Hysteresis loop

Figure 1.14: How the aerodynamic forces and moments are affected by the dynamic stall process, taken from [32]

Number	Flow Description
1	Aerofoil exceeds the critical angle of attack, where static stall happen. Flow reversal takes place in the boundary layer.
2	The separation position reaches the leading edge, a formation of a leading edge vortex begins.
3	Vortex begins to convect across the upper surface of the aerofoil. There is a sharp drop in c_m and rise in c_d. c_l also continues to increase.
4	Maximum c_l, c_m and c_d, this is where the vortex reaches the trailing edge. After this point a rapid decay in aerodynamic coefficients will occur.
5	Flow attachment is delayed with respect to flow separation.

Table 1.1: Description of the dynamic stall process with reference to Figure 1.14

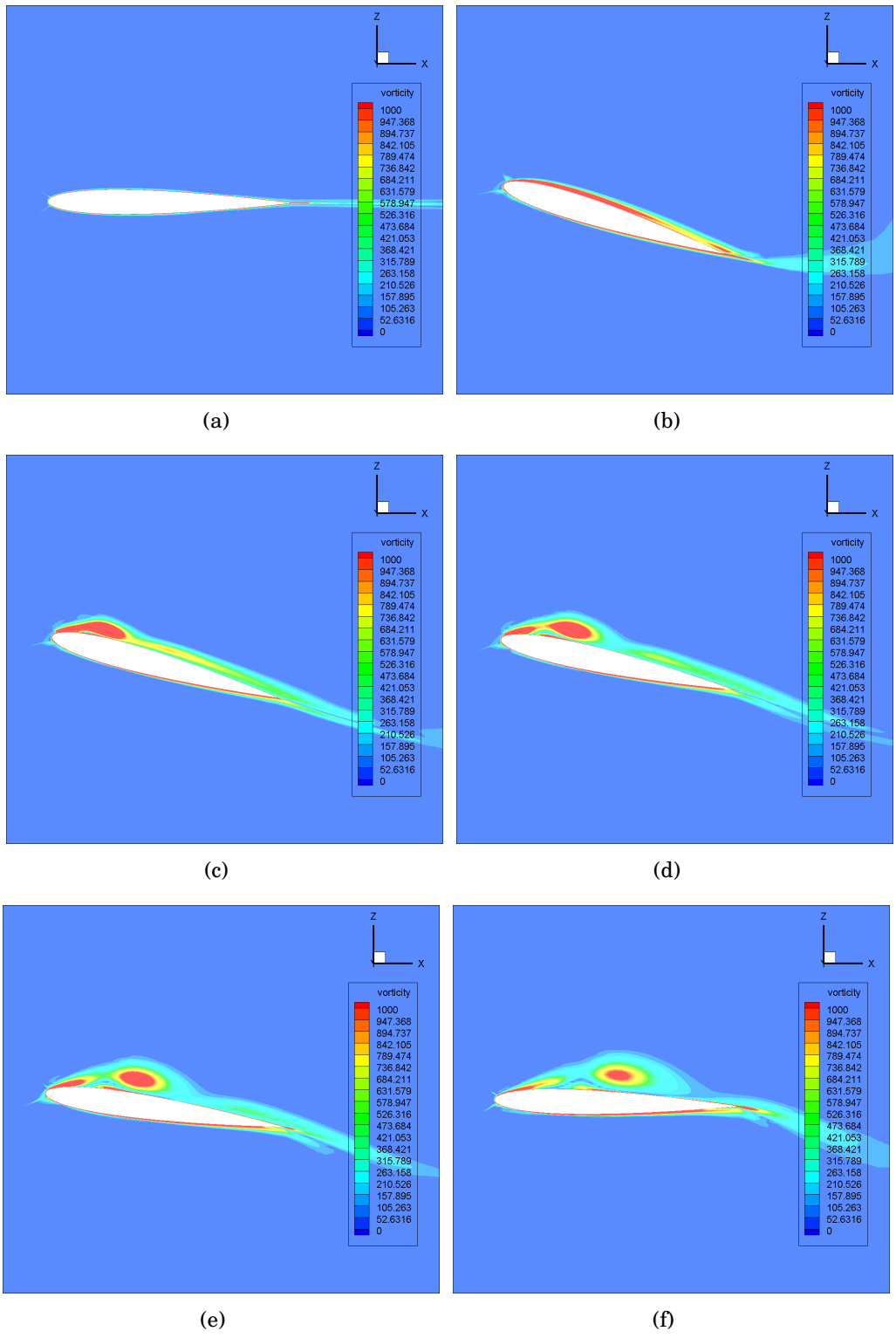

Figure 1.15: NACA 0009 Dynamic Stall Flow Fields: $\alpha = 0° + 26° \sin \omega t$, $Re = 2.1 \times 10^6$, $k = 0.55$. (a) $\alpha = 0.0° \uparrow$, (b) $\alpha = 25.3° \downarrow$, (c) $\alpha = 22.4° \downarrow$, (d) $\alpha = 18.3° \downarrow$, (e) $\alpha = 12.3° \downarrow$, (f) $\alpha = 2.3° \downarrow$

able to shed a dynamic stall vortex. The aerofoil is undergoing a pitching oscillation where $\alpha = 0° + 26° \sin \omega t$ and $k = 0.55$. Flowfield (a) shows the aerofoil at $\alpha = 0°$, where the flow is nominally attached. As the aerfoil is dynamically pitched up, the vorticity increases in the boundary layer, see flowfield (b). As the aerofoil continues to pitch up, a vortex forms at the leading edge, which eventually detaches and convects along the upper surface, flowfields (b), (c) and (d). As the vortex convects along the upper surface it has a noticeable effect on the moment, causing larges differences compared to the static data as the vortex travels further from the moment reference point (increasing the moment arm). Flowfields of the detached leading edge vortex convecting along the upper surface are shown in flowfields (e) and (f).

1.6 Parameters that influence Dynamic Stall

1.6.1 Compressibility

It is generally accepted that attached flow will remain approximately incompressible around an aerofoil if the free-stream Mach number, (M_∞), is below 0.3. However an experiment carried out by McCroskey, McAlister, Carr and Pucci [33] in 1981 shows high lift at Mach numbers greater than 0.2 can in fact produce local supersonic velocities. The study used a variety of aerofoils, mostly focused towards helicopter applications, however this phenomenon was also shown to occur for a NACA 0012 where significant density variations occurred when $M_\infty > 0.22$. The occurrence of higher local Mach numbers at the leading edge, for what would usually be a sub-critical Mach number, can at least be partly attributed to the delay of the separation that dynamic stall brings. In 1977 Dadone [34] investigated how the Mach number impacted the distribution of the dynamic pressure on pitching aerofoils. It was found that as the Mach number increased, the stall separation changed from being initiated by an adverse pressure gradient, to being shock induced. Whilst M_∞ is increasing and provides flow without compressibility effects, the maximum lift coefficient, $C_{L\max}$, experienced during dynamic stall increases. However once compressibility effects occur, $C_{L\max}$ becomes inversely proportional to M_∞.

Interestingly, reduced frequency has a large impact on the separation of the boundary layer in subsonic flows (increasing the reduced frequency delays separation). However for supercritical flows the relationship between the reduced frequency and separation alters. Carr *et al.*[35] analysed results from McCroskey's work [33] and showed that the maximum attainable C_p, for $M_\infty = 0.3$, has virtually no relationship with reduced frequency. This can be attributed to shock-induced separation. At higher Mach numbers, a shock can form close to the leading edge, generating a strong adverse pressure gradient. The adverse pressure gradient forces the separation position, which can lead to premature separation [21].

In 1995 Carr and Chandrasekhara [36], assessed the impact of compressibility on dynamic stall. They used previous results obtained by Carr *et al.* in 1982 [35], in which eight aerofoils underwent a pitch ramp. Note that this experiment was conducted with a positive pitch ramp ($\dot{\alpha} > 0$). Pitch ramps were a popular motion, partly due to the fact a constant pitch rate could be used to avoid the formation of hysteresis loops. When the flow could be considered incompressible, 7 of the 8 aerofoils featured a trailing edge stall, which was identified in the experiment as flow reversal beginning at the trailing edge, this can be seen in Figure 1.16 [35]. The graphs show the chord-wise separation point at three Mach numbers, as the angle of attack is increased. After the initial trailing edge flow reversal, the aerofoils can continue to pitch approximately a further 5° before full dynamic stall occurs, shown by flow reversal at the leading edge. There is only a single aerofoil that experiences a leading edge stall, the NLR-1, for which the dynamic stall vortex forms simultaneously with the leading edge flow reversal. However, if M_∞ is increased to 0.3, where flow will become moderately compressible over all the aerofoils, leading edge stall becomes dominant for the majority of the aerofoils.

This is important because a leading edge stall which can suddenly cause the aerofoil to shed a dynamic stall vortex, leads to the occurrence of dynamic stall at much lower angles of attack. Carr and Chandrasekhara postulate that the dramatic conversion of

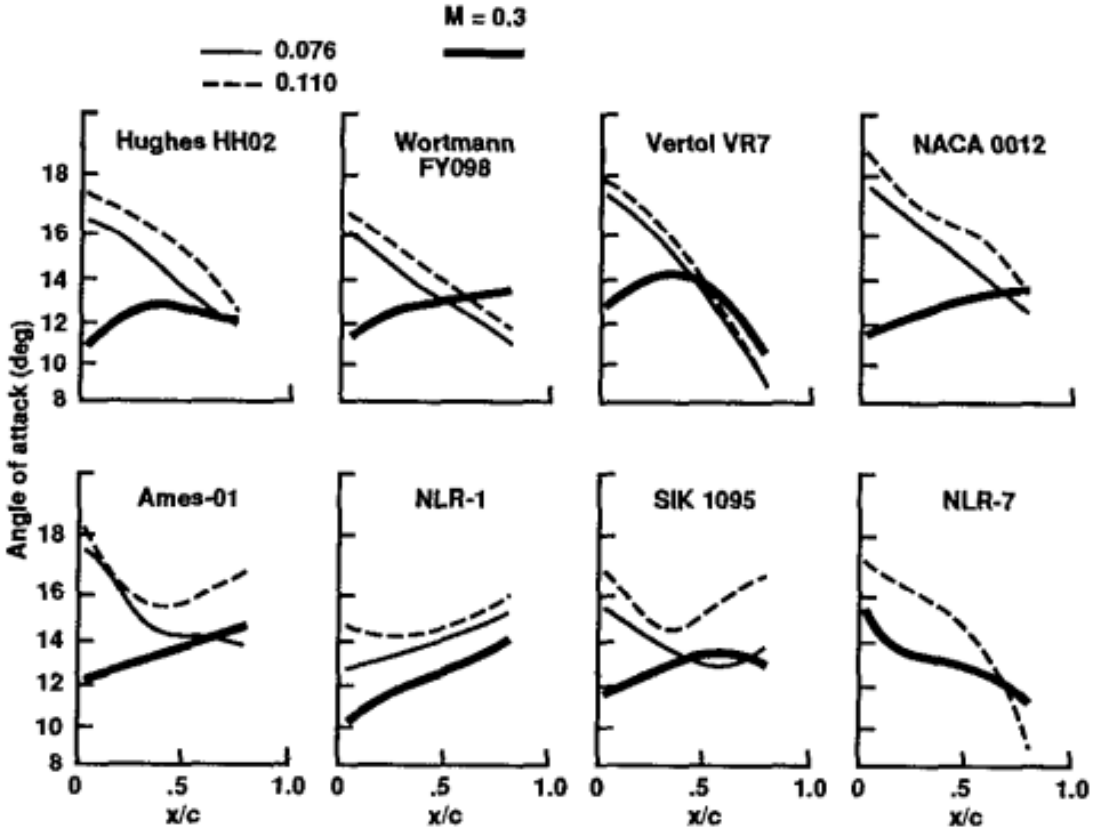

Figure 1.16: Flow Separation Characteristics for Aerofoils Undergoing Dynamic Stall. $Re = 4.0 \times 10^6, M_\infty = 0.3$. Lines represent the separation point position with angle of attack - taken from reference [35]

.

trailing edge to leading edge stall is likely due to a higher local Mach number (M_{local}). Figure 1.17 [37] shows the maximum local Mach number as a function of the free-stream Mach Number. This demonstrates that during dynamic stall, free-stream Mach numbers as low as 0.2 can create areas of sonic flow, and if M_∞ is increased to 0.3, the flow is found to contain local supersonic flow regions.

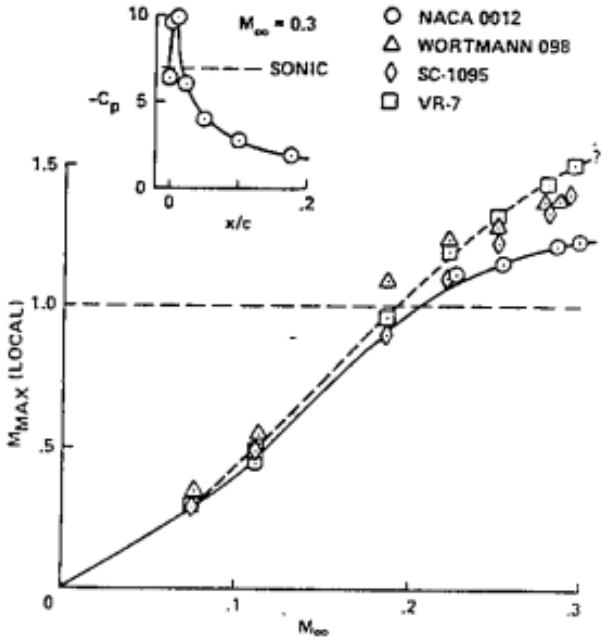

Figure 1.17: Maximum Local Mach Number at the Leading Edge of an Aerofoil Experiencing Dynamic Stall as a Function of Free-stream Mach Number- taken from[37]

.

1.6.2 Type of Motion

In flight, motions are rarely purely pitching or plunging , more often they are a mixture of rotations and translations. In 1977 Fukushima and Dadone [38] compared the dynamic stall process between a pitching and vertically translating aerofoil experimentally. The only aerodynamic data acquired from the experiments were chord-wise pressure differences. This is noted to be a shortcoming by the authors. Obtaining the difference in chord-wise pressure for the upper and lower surface does not allow the events on the upper and lower surfaces to be separated from one another. This could be an issue for the breakdown of the leading edge suction when the stagnation point is moving on the lower surface. The dynamic stall tests were performed for two aerofoils, the Boeing-Vertol V0012 and V23010-1.58 [38], which are both rotorcraft sections. Notwithstanding these limitations, their results indicate that at low free-stream velocities, the lower surface should remain fairly unaffected by dynamic stall, with the majority of events occurring

on the upper surface.

The aerofoil motions were expressed as follows:

$$\alpha(t) = \alpha_0 + \alpha_1 \sin \omega t \quad \text{(pitching)} \tag{1.6}$$

$$h(t) = -h_1 \sin \omega t \quad \text{(heaving/plunging)} \tag{1.7}$$

where α_0 represents the mean angle of attack and α_1 represents the amplitude. It should be noted that the effective instantaneous angle of attack was not matched between the pitching and heaving motions. It may well have been advantageous to match the mean angle of attack and then adjust the vertical translation speed for the heave motion so that the effective angle of attack would have been equal to that of the pitching aerofoil. The authors made a comparison between the leading edge pressures during pitching and translation for the two aerofoils. For the V23010-1.58 aerofoil, the loss of leading edge suction was much more noticeable for the pitching motions compared to the translation. The authors also found differences between the pitching and plunging motion in flow separation. Rival and Tropea, [39] conducted a similar experiment on the dynamic stall process on pitching and plunging aerofoils, using a Selig-Donovan SD7003 profile. However this study reached a different conclusion, finding that pitching and plunging cases are nearly identical. Any differences in lift and moment were concluded to be due to the position of the shed vortex relative to the aerofoil, which can impact lift and moment production.

1.6.3 Reduced Frequency

The reduced frequency, k, plays an important role in the severity of dynamic stall. Carr *et al.* [40] investigated the effect of reduced frequency on a NACA 0012 in a pure pitch oscillation. The reduced frequency was varied between k = 0.02 and 0.25. The most noticeable trend is that increasing reduced frequency delays the flow separation along with the shedding of the dynamic stall vortex. When the reduced frequency was less

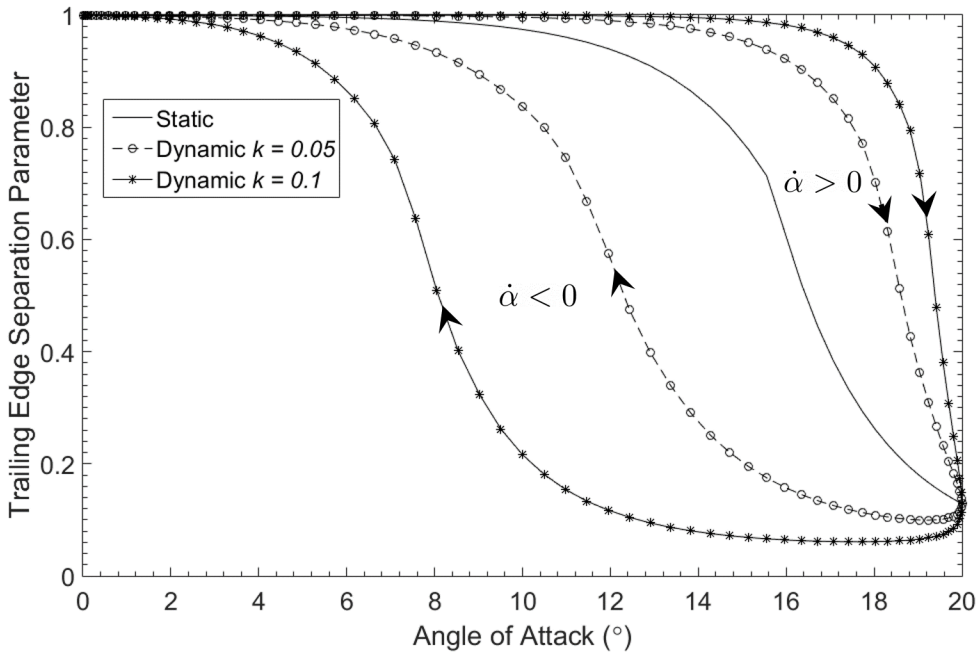

Figure 1.18: Effect of Reduced Frequency, k, on the Trailing Edge Separation Point.

than 0.05, the dynamic stall vortex shed into the wake before the maximum incidence was reached, if it formed at all. However in cases where $k > 0.2$, the dynamic stall was delayed long enough that the vortex was still shedding on the down-stroke with the lift continuing to increase, even though the angle of attack was decreasing. Figure 1.18 shows a semi-empirically calculated trailing edge separation point for a NACA 0012, which was calculated using techniques detailed in Section 3.2. The aerofoil undergoes a pitching oscillation defined by $\alpha = 10^\circ + 10^\circ \sin \omega t$. The figure presents the static trailing edge separation point and the separation point when undergoing the aforementioned motion at $k = 0.05$ and 0.10. It can be seen that increasing the reduced frequency allows the flow to remain attached at higher angles of attack whilst pitching up and thus reaching a greater lift coefficient. However there is a delay in the reattachment on the down-stroke which often results in a more severe stall. The separation point is a good indication of the lift coefficient since separation brings a reduction in circulation.

Much work has been undertaken to consider the effect of non-dimensional pitch rate on

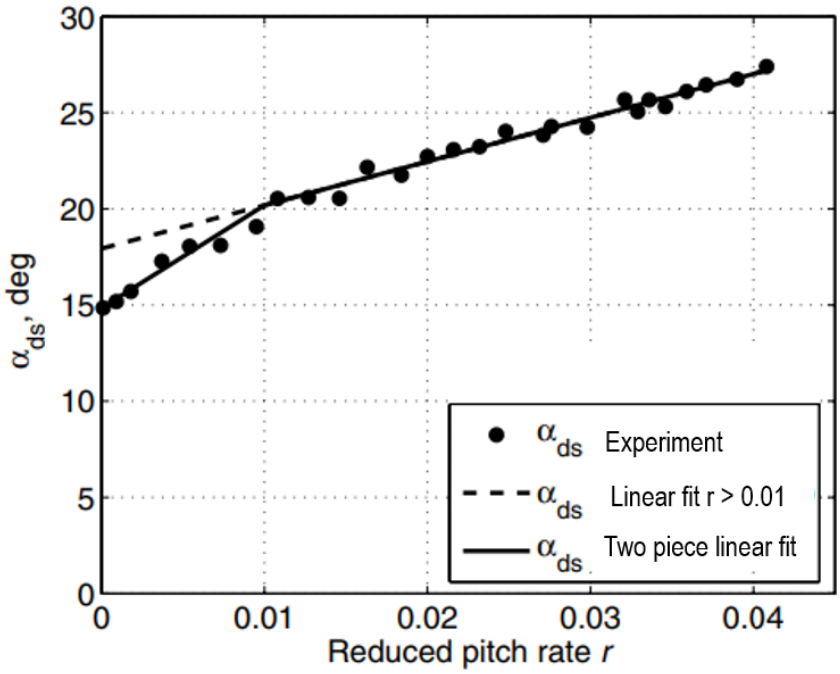

Figure 1.19: Effect of non-dimensional pitch rate, r, on the dynamic stall onset angle of attack. Adapted from [41].

dynamic stall. In principle, the non-dimensional pitch rate represents a similar quantity to the reduced frequency. The non-dimensional pitch rate takes the form, $r = \frac{\dot{\alpha} b}{V}$, where $\dot{\alpha}$ is the pitch rate, b is the semi-chord length and V is the freestream velocity. Sheng, Gallbraith and Coton showed that the delay between the static critical angle and the dynamic stall onset angle of attack can be correlated to the non-dimensional pitch rate [41]. It should be noted that this is only valid when $r > 0.01$, which according to [42] delimits the boundary of quasi-steady aerodynamics and dynamic stall. Figure 1.19 shows the relationship between the reduced pitch rate and the dynamic stall onset angle of attack, α_{ds}. It shows a linear relationship between r and α_{ds}. There is discontinuity in the relationship, as previously mentioned, when $r < 0.01$. However a two piece linear fit is able to capture this relationship well.

1.6.4 Angle of Attack Variation

The reduced frequency of pitching motions, see Equation (1.4), is often used to compare dynamic data. The reduced frequency does provide an insight into the unsteady aerodynamic effects, however the variation of the mean angle and oscillation amplitude variation are also parameters that must be considered. In 1977 Carr, McAlister and McCroskey [40], carried out experiments where the mean amplitude of oscillation was held constant however the amplitude of the pitching motion was varied. The cases run were $\alpha = 15^\circ + 6^\circ \sin \omega t$, $\alpha = 15^\circ + 10^\circ \sin \omega t$ and $\alpha = 15^\circ + 14^\circ \sin \omega t$, all with the same reduced frequency of $k = 0.15$. The hysteresis of the lift and moment coefficient are drastically different for the three oscillation amplitudes. Carr *et al.* [40] conclude this occurs due to a difference in the strength and timing of the dynamic stall vortex. At the smallest amplitude the vortex is shed at the maximum angle of attack, which is significantly earlier than if the amplitude was increased. However for the oscillation with the highest amplitude, $\alpha = 15^\circ + 14^\circ \sin \omega t$, Carr *et al.* found there were no reduced frequencies in which the vortex would not shed before the maximum angle of attack was reached.

The effect of mean angle of oscillation, with a constant amplitude was investigated early on by Carta [43]. Carr *et al.* [40] revisited this in their parametric study. Three pitching oscillation experiments were carried out, with the amplitude remaining constant throughout. In these cases, $\alpha = 6^\circ + 6^\circ \sin \omega t$, $\alpha = 11^\circ + 6^\circ \sin \omega t$ and $\alpha = 15^\circ + 6^\circ \sin \omega t$ were used with $k = 0.15$ and $Re = 2.5 \times 10^6$. For the first case where the mean angle was given by $\alpha_0 = 6^\circ$, the aerofoil did not stall, and the results in the dynamic case varied very little from the static. For the case where $\alpha_0 = 11^\circ$, the maximum angle of attack only exceeded the static stall angle by a small margin. At low reduced frequencies, the aerofoil would stall. However the authors found that when a reduced frequency, $k = 0.24$ was used, the aerofoil would not stall at any point in the cycle, with the aerodynamic hysteresis loop remaining elliptical in shape. This is likely due to the aforementioned correlation between reduced frequency and lag in separation position movement. When

the mean angle of attack was increased close to the critical angle, $\alpha_0 = 15°$, it was found that a premature stall occurred. This is due to the fact that the starting incidence is close to that of static stall.

1.6.5 Reynolds Number

In 1957 Donald E. Gault [44] investigated the static stalling characteristics of aerofoils over a range of Reynolds numbers. He correlated leading edge curvature with the stalling mechanism. Leading edge curvature was measured by the position of the upper-surface at 0.0125% percent of the chord. The original chart can be seen in Figure 1.20. If the NACA 0012 is taken as an example, the upper-surface ordinate at $0.0125x/c$ is approximately 1.88%. Figure 1.20 would suggest that for a NACA 0012 with a flow of Reynolds number $> 2.0 \times 10^6$, a trailing edge stall would occur. However if the Reynolds number is reduced to the order of 10^5, it becomes more likely to exhibit thin aerofoil stall or even leading edge stall.

Investigating the effect of Reynolds number on dynamic stall can be challenging since it is difficult to significantly vary the Reynolds number without introducing compressibility effects; which can dominate the dynamic stall process. There are not many authors who have documented this. However in 1977 Carr *et al.* [40] studied the effects of Reynolds number, along with reduced frequency and amplitude of oscillations over a selection of aerofoils. The Reynolds number was found to have the smallest significance to dynamic stall in the parametric study. At lower Reynolds the flow reversal was more gradual from the trailing edge to the leading edge. At the higher Reynolds numbers tested ($Re \geqslant 2.0 \times 10^6$) the flow breakdown between the quarter chord and the leading edge were in effect concurrent, however the dynamic stall process on the forward section of the aerofoil was not drastically altered. Therefore the effect of Reynolds number is mostly manifested in the static response, and the aerofoil geometry dictates how sensitive the response is to different Reynolds numbers.

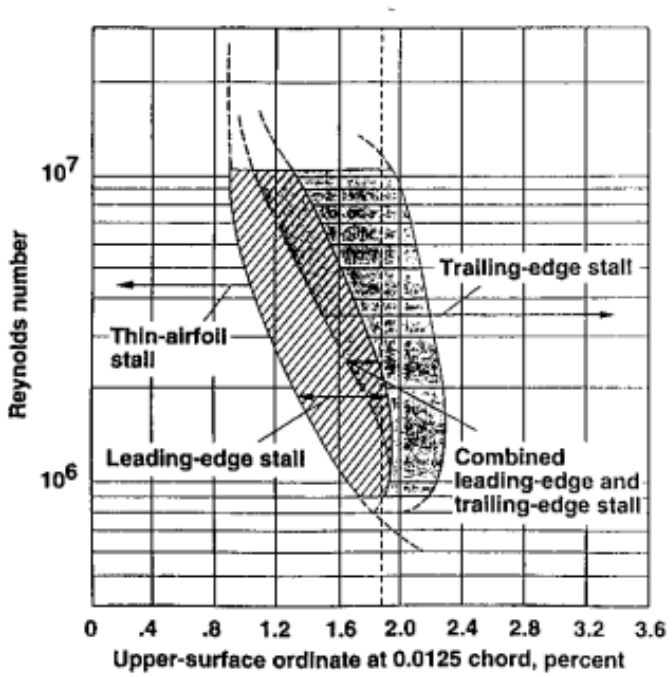

Figure 1.20: Stalling Characteristics for Leading Edge Curvature Correlated to Reynolds Number, taken from reference [44]

.

1.6.6 Sweep

In 1979 Hilaire, Carta, Fink and Jepson [45] investigated the effect of sweep on dynamic stall. The aerofoil used was a NACA 0012 in swept and unswept configurations, with the swept wing having a backward sweep angle of $\Lambda = 30°$. Hilaire *et al.* found that generally the swept back wing gave favourable properties during dynamic stall, delaying separation to a higher angle of attack. Also due to sweep the negative pitching moment (that increases as the DSV is shed), is reduced in magnitude and the lift hysteresis loops also appear narrower. Leishman [46] produced a figure showing the separation point with respect to the angle of attack for both an unswept NACA 0012 and a NACA 0012 with a sweep angle $\Lambda = 30°$. It is clear from the results that the swept NACA 0012 has a separation point closer to the trailing edge when undergoing the same pitch oscillation. Consequently there will be a reduced loss in circulation from the trailing edge stall and

thus the variation in the lift coefficient over the cycle will be smaller. A recommendation made by Hilaire *et al.* was to modify simple sweep theory to model the effect of sweep when an aerofoil is undergoing dynamic stall. This was first addressed in 1989 by Leishman who introduced a swept-flow component to the Beddoes-Leishman model [46]. This component has a primary effect on the trailing edge stall, reducing the extent of separation at the trailing edge. Leishman used the UTRC data constructed by Hilaire *et al.* [45] to verify his implementation. A good level of similarity was found between the experimental and model results. This also provided another source of independent data for the Beddoes-Leishman model to be validated against.

1.6.7 Two-Dimensional versus Three-Dimensional Flow

Early work on dynamic stall was dominated by investigation on two-dimensional aerofoils. In the early 90's Horner *et al.* [47], investigated a three-dimensional wing, looking at the effect that tip vortices have on dynamic stall. The experiment consisted of a flat plate undergoing pitching oscillations at reduced frequencies of k = 1.0 and 2.0. Two mean angles of attack were investigated, 0° and 10°. Two different tip conditions were investigated. The first was formed by leaving a gap of 2" between the tip and the walls of the tunnel. The second configuration was created by attaching an acrylic splitter plate to the wing tip in order to hinder the formation of the tip vortex. Visualisation of the flow was achieved by using horizontal and vertical smoke planes. The development of the dynamic stall vortex was strongly affected by the tip vortices. In the three-dimensional case where the tip vortices were present, the leading edge vortex moved upwards as it was shed over the upper surface away from the wing tips. However the tip vortex suppressed this behaviour near the wing tips forming what was named an Ω shaped vortex by Horner *et al.* due to the close resemblance to the symbol. However in the run with the splitter at the wing tip, the leading edge vortex remained attached to the upper surface, creating a Π shaped vortex. This is summarised in a series of drawings created by Horner *et al.* [47] which are displayed in Figure 1.21.

CFD simulations were carried out by Spentzos [48] to investigate the three-dimensional

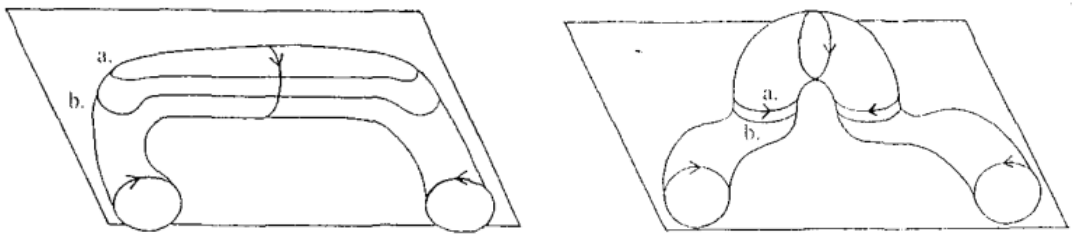

(a) 2D DSV Formation, Π shape (b) 3D DSV Formation, Ω shape

Figure 1.21: Sketches of dyanmic stall vortex formation taken from [47]

vortex interaction further. It was found that the interaction between the tip and dynamic stall vortices lead to a more gradual stall than the two dimensional case. However the tip vortex at high angles of attack formed a second suction peak near the tip. This was seen to strongly affect the moment and drag coefficients highlighting the shortcomings of scaling two dimensional results to a three dimensional case. The qualitative difference between two and three dimensional dynamic stall has also been investigated by Kaufmann, Gardner and Costes [49] using CFD. Differences and similarities between static and dynamic stall on a two and three dimensional OA209 aerofoil and wing respectively were analysed. They found, for static changes in angle of attack that there was a reduction in effective angle of attack of around 5° and a more gradual lift curve slope due to three-dimensional effects. When undergoing dynamic pitching, a spanwise variation in the DSV was found to exist. As with the experiments conducted by Honer *et al.*[47], the tip vortex retains the dynamic stall vortex near the tip, however the vortex at the root rises from the aerofoil surface.

1.7 Numerical Methods

Separated flow of a Newtonian fluid is governed by the Navier-Stokes (N-S) equations, which are equations for conservation of mass, momentum and energy together with equations of state which come from fundamental fluid properties. Solution of these equations analytically is impossible for anything but simple geometries & conditions and certainly

not for aerospace flows. Solutions are therefore found using numerical methods. High Fidelity Computational Fluid Dynamics (CFD) methods to solve the N-S equations are now fairly widely used for steady flow, however for unsteady flows in the aerospace field their use is much more limited due to the high computational cost. In particular there have only been a limited number of studies of three-dimensional CFD simulations capturing dynamic stall, with the vast majority of CFD cases having been two-dimensional to date. Three-dimensional dynamic stall has extra complexities, a finite wing has unsteady flow aspects not present in a two-dimensional case. On a finite wing undergoing dynamic stall, vortex interaction between the dynamic stall vortex and the tip vortices will occur, along with wall effects and spanwise flows. These interactions are important in the accurate modelling of three-dimensional dynamic stall. The first published account of dynamic stall simulated in three-dimensional flow, using CFD, was by Newsome and Seiler in 1994 [50]. The CFD simulation was set-up to replicate experiments carried out by Schreck and Helin [51]. A straight wing of aspect ratio 2, constructed from NACA 0015 aerofoil sections was used. The wing was pitched at a reduced frequency of $k = 0.1$ and 0.2, from an angle of attack of 0° to 60°. The Reynolds number used in the simulation was $Re = 5.6 \times 10^4$ and the Mach number used in the simulations was $M_\infty = 0.2$. For an early attempt of modelling dynamic stall in three-dimensions, the results obtained by Newsome *et al.* showed a good likeness to the experimental data. However it should be taken into consideration that the Reynolds number was low enough for the flow to remain in the laminar regime. Again, due to the computing resources available at the time, the mesh resolution at the wing tips were not adequate to fully resolve the tip vortices, which are crucial in three-dimensional modelling of dynamic stall. The results at the higher non-dimensional pitch rate of 0.2 proved to be closer to the experimental results than the lower pitch rate of 0.1. This is likely due to the less severe separation that the higher frequency would experience. However whilst the simulation captured the main flow features of dynamic stall, stall arose prematurely compared to the experiment.

Spentzos *et al.* in 2005 [31] recreated the CFD work of Newsome [50]. The CFD solver

used was a Parallel MultiBlock Solver (PMB), a code developed by the University of Glasgow, capable of solving the three dimensional Reynolds Averaged Navier-Stokes (RANS) equations. This was claimed by the author to be the first detailed computational study on dynamic stall. The aim of the work was to compare the difference between two-dimensional and three-dimensional dynamic stall flow-fields. Two simulations were conducted, both setup to follow experimental configurations. The first was a two-dimensional simulation that replicated an experiment carried out by Wernert *et al.* [52]. The second simulation used a three dimensional wing and was set up to follow the experiments of Schreck and Helin [51]. However it should be noted that the Mach number in the three-dimensional simulation did not match the experiment undertaken by Schreck *et al.*. The CFD simulation used a Mach number of $M_\infty = 0.2$ which was chosen to match the aforementioned simulations of Newsome and Seiler in [50]. The actual Mach number in the experiments was $M_\infty = 0.03$. The reason for the difference is that the CFD codes used experienced poor convergence at very low Mach numbers due to ill conditioning caused by the large discrepancy between acoustic and convective wave speeds [53]. Thus, a slightly higher M_∞ is often used to improve convergence with the solution still getting close to the lower M_∞ result. The Reynolds number however is kept the same between the experiment and CFD, meaning that the model used by Spenzos is scaled. Ericsson and Reding [25] indicate that when dynamic scaled models are increased to the full model geometry, the scaling for Reynolds number and reduced frequency are not equivalent and therefore the results can be deceptive. However the results were concluded to compare favorably to the experiments and showed promise for future simulations.

Two years later in 2007, Spentzos *et al.* [54] conducted further three-dimensional RANS simulations, however this time the planform was altered to add sweep and increase the aspect ratio. Spentzos *et al.* ran their simulations to match experimental data. The first validation case was based upon experimental work done by Moir and Coton [55] which was conducted in a smoke tunnel at the University of Glasgow. A wing with an aspect

ratio of 3.0 made up of NACA 0012 sections underwent ramping and oscillatory motions. A relatively low Reynolds number of $Re = 1.3 \times 10^4$ with a Mach number of $M_\infty = 0.1$ was used. The second validation test case was carried out by Berton *et al.*, where a low aspect ratio tapered wing underwent ramping and oscillatory motions at a Reynolds number of 1×10^6. CFD was found to be in good agreement with the experiments by Berton *et al.*

Work has been carried out by Kaufmann *et al.* [56] which compared three-dimensional dynamic stall simulations using the RANS equations with the ONERA structured code elsA with and the unstructured DLR-TAU code. The URANS elsA simulations used the Spalart-Allmaras and the $k-\omega$ Kok + SST turbulence models, whilst the DLR-TAU runs used the Spalart-Allmaras and Menter SST turbulence models,. The finite wing composed of OA209 sections was used with an aspect ratio of 3.0, at a Mach number of 0.16 and a Reynolds number of 1×10^6. Although a similar grid resolution was used in both codes, large discrepancies between the results were found in both the static and dynamic cases. The computational set-up replicated the experiments by Le Pape, Palilhas, David and Deluc [57]. When both the elsA and DLR-TAU were compared with the experimental data, qualitative agreement was found. However in the static case, the critical angle was delayed by 2.2° in the elsA results compared with that found using DLR-TAU. The DLR-TAU code calculated a critical angle 1° larger than experimental data, thus elsA produced a value 3.2° higher. This highlights the difficulties present when modelling three-dimensional separation and stall.

More recently, computational work has been carried out by Kaufmann, Mrez and Gardner [58] which assessed the ability of the compressible URANS CFD solver DLR-TAU [59] to simulate dynamic stall on a finite pitching wing. The finite wing made up from the DSA-9A section, with an aspect ratio of 6.2, which according to the authors was the highest aspect ratio wing studied in CFD dynamic stall investigations. The dynamic stall case where $k = 0.049$ showed very good agreement with experimental data. It should be noted that the experimental showed large cycle-to-cycle variations, and the data was

averaged before comparing. This work also compared the data to 2D simulations, using the DSA-9A aerofoil. Overall the 2D simulations showed strong similarities to the 3D data, especially in terms of maximum sectional loads. It is quite possible that the use of an increased aspect ratio wing over previous computational dynamic stall simulations by the same author, [56] [49], aided the ability to accurately model dynamic stall on a finite wing.

The studies above show that computational fluid dynamics (CFD) is capable of modelling the viscous flow physics associated with flow separation and dynamic stall. However CFD simulation costs are too demanding for the early design phase [60] and thus is a technique better reserved for later stages when less simulations are required. Furthermore, whilst nonlinear coupled CFD-FEM simulations can be used to evaluate the nonlinear aeroelastic responses of a finite wing, the expense of these simulations are far too great for the sheer volume needed in the early design stage.

More computationally inexpensive methods to calculate the aerodynamic coefficients for a finite wing are available. These however are compromised by either being restricted to the assumption of attached flow or do not account for three-dimensional effects such as tip-loss or spanwise flow. A common method used is 2D strip theory, often based on indicial aerofoil responses, which is used in design for the computational advantages [61], [62]. Here a finite wing is assumed to be constituted of a discrete number of aerofoils in which the aerodynamics of each section is treated individually and thus as two-dimensional. In order to account for tip loss and spanwise flow, a three-dimensional potential flow method can be implemented. Commonly, when considering time domain methods, these come in the form of either lifting line theory (LLT) or vortex lattice method (VLM), which can also be extended to solve unsteady flow problems. These methods are governed by Laplace's equation for the velocity potential and are formulated by distributing singularity elements on a surface where the flow potential is to be determined [63]. The LLT method just considers a vortex line coincident with the local

quarter chord allowing a spanwise variation of induced velocity to be obtained. Whereas the VLM uses both a chordwise and spanwise distribution of vortex rings which in turn can give both chordwise and spanwise velocity variations. However these methods are based on the assumption of inviscid flow and therefore cannot model the effects of flow separation and dynamic stall. Modifications are therefore needed in order to account for separated flow. Further information on potential flow methods is given in subsequent chapters.

Methods have been developed which offer a more compact way to model the effects of dynamic stall on aerofoils than using CFD. Dynamic stall models are able to predict the unsteady aerodynamics under separated conditions. Initially the models were developed for rotorcraft applications, where the lack of symmetry in the lift between advancing and retreating blades necessitated blades to dynamically pitch. At high angles of attack this can initiate dynamic stall and in turn impact the flight envelope [64]. A multitude of dynamic stall models are available for two dimensional flow, for example, the Beddoes-Leishman [65], ONERA [66], Goman-Khrabrov [67] and Boeing-Vertol [68] (these models will be discussed in more detail in subsequent chapters where they are utilised). Typically dynamic stall models, such as the Leishman-Beddoes model, are based on physical reasoning. However other models take a more mathematical approach to stall modelling, such as the Goman-Khrabrov model. What is common between the vast majority of dynamic stall models is the reliance on aerofoil data obtained from experiments or CFD. The models generally require semi-empirical coefficients that are calculated by the fitting of static and dynamic responses. More detail on such procedures is given in later chapters.

It is also reasonably common to incorporate a dynamic stall model into the strip theory formulation described previously, allowing for a level of separation modelling [61]. However strip theory neglects any three-dimensional effects which have been shown to be important, even when the aspect ratio is large [69]. Tang and Dowell [27] ran experiments on a wing made up of NACA 0012 sections with an aspect ratio of 1.5

undergoing pitch oscillations. Readings were taken at three spanwise sections (50%, 75% and 90% of the span). This work was aimed at extending the two dimensional ONERA model [66] into three dimensions. The conclusions of the paper were that the results were qualitatively similar to the two dimensional case. No results were given for the section at 90% of the span at high angles of attack, which is unfortunate as these may have been able to highlight the three-dimensionality of the flow.

Due to the nonlinear impact that unsteady flow separation and dynamic stall may have on the aeroelastic response of a HARW aircraft, the nonlinearities should be considered in the preliminary design stages. Uncovering these phenomena using higher order methods late in the design process could cause avoidable and very costly design iterations. Thus there is a need for a computationally inexpensive method, capable of predicting the aeroelastic response to a finite wing undergoing unsteady separation. This requirement for a new aeroelastic model is addressed in this research. The new aerodynamic model developed in this work is based on coupling a 2D dynamic stall model with unsteady lifting line theory (ULLT). The 3D nonlinear ULLT model is intended for use in the early design phase where current low-fidelity techniques are unsuitable to model the flow physics that may occur on finite wings. This approach could also be applied to medium-to-low aspect ratio rigid wings: the lifting line theory used in the approach is valid for wings with an aspect ratio greater than four [70]. This thesis shall however focus on flexible, high aspect ratio wings which can experience more separation and therefore greater three-dimensional flow where strip theory is inadequate. This is coupled to a nonlinear intrinsic beam formulation that can capture the geometric nonlinearities that large deformations can introduce. This approach also has the advantage of avoiding any three dimensional mesh generation, which is currently a bottleneck in the CFD process [60]. This is especially useful for preliminary design where a large parameter space is to be explored, allowing for multiple configurations to be rapidly analyzed.

1.8 Outline of Thesis

Chapter 2 introduces the CFD code which has been used to provide data to construct some models and model evaluation. Both two-dimensional and three-dimensional static and dynamic simulations are described and used to generate the required results. The challenges of using CFD for modelling separated flows have had to be addressed. These are mainly associated with mesh generation and turbulence modelling.

The third chapter looks at lower-order models that are capable of simulating the response of a two-dimensional aerofoil under dynamic stall conditions. Some of the key dynamic stall models are introduced and the Beddoes-Leishman model is implemented and compared to experimental data for a NACA 0015 profile and CFD data for a NACA LRN 1015 aerofoil section.

The fourth chapter introduces some of the more popular aerodynamic models that are used in the early design phase of civil aircraft. The models are based on the potential flow equations with both steady and unsteady models considered. The performance of the models are then validated using experimental data at both low and high angles of attack.

Chapter 5 takes the work from chapters three and four to produce a model that is capable of capturing unsteady separated flow and dynamic stall on clean finite wings. This represents the major contribution of this thesis and outlines the technology needed in the early design stages of highly flexible HARW configurations. To demonstrate the methods suitability to such configurations, the model is validated against experimental and computational studies. Further to this the model is coupled to a nonlinear intrinsic beam model. This allows for inexpensive aeroelastic calculations to be conducted in the early design stages. CFD is used to compare the output from the new aeroelastic model, through the use of defined motion that matches the aeroelastic deformation from the new aeroelastic model. The chapter finishes by comparing the model to XFoil/XLFR5 to

asses its static performance against a widely used package.

The work is then concluded in Chapter 6, summarising the main findings within this thesis. This is followed by suggestions for future advancements on the work presented here and its limitations.

CHAPTER 2

COMPUTATIONAL FLUID DYNAMICS

The focus of this thesis is on the development of a computationally efficient model for 3D dynamic stall for use in early stage design. However, high fidelity CFD has an important role in this work. Two-dimensional CFD will be used as an alternative to build a more efficient three-dimensional model. Three-dimensional CFD will be used to compare and evaluate the model outputs. This chapter focuses on modelling flow separation using Computational Fluid Dynamics. Static and dynamic simulations are evaluated for a NACA LRN 1015 profile, both as a two-dimensional aerofoil and as a finite wing. The behaviour of the finite wing and its aerofoil counterpart is evaluated. Methods for grid refinement are presented, and the difficulties of creating a grid that can be applied to a wide variety of cases with varying amounts of flow separation are discussed. The chapter finishes by looking at stall cell patterns on a finite wing.

2.1 Governing Equations

2.1.1 Navier-Stokes

In order to model fluid motion the Navier-Stokes (N-S) equations are utilised. The N-S consist of three momentum equations and the continuity equation is added in order to solve them. The continuity, momentum and energy equations are presented in tensor notation Equations 2.1 to 2.3 respectively [71].

$$\frac{\partial \rho}{\partial t} + \frac{\partial \rho U_i}{\partial x_i} = 0 \tag{2.1}$$

$$\frac{\partial \rho U_i}{\partial t} + \frac{\partial \rho U_j U_i}{\partial x_j} = -\frac{\partial p}{\partial x_j} + \frac{\partial \tau_{ji}}{\partial x_j} \tag{2.2}$$

$$\frac{\partial \rho E}{\partial t} + \frac{\partial U_j(\rho E + p)}{\partial x_j} = \frac{\partial U_i \tau_{ij}}{\partial x_j} - \frac{\partial q_j}{\partial x_j} \tag{2.3}$$

In the above equations, ρ represents the density, p is the pressure, $\mathbf{x}$ is a position vector of the Cartesian coordinates with $(x_1, x_2, x_3) = (x, y, z)$, $\mathbf{U}$ is a velocity vector with the components $(u_1, u_2, u_3) = (u, v, w)$ and E is the total energy. The total energy is constituted from the specific internal energy, e, and the square of the velocity magnitude, $E = e + U_i U_i$. The heat flux is calculated using:

$$q_j = -c_p \frac{\mu}{\mathrm{Pr}} \frac{\partial T}{\partial x_j} \tag{2.4}$$

where T is temperature, Pr is the Prandtl number (the ratio of momentum diffusivity to thermal diffusivity), μ is the dynamic viscosity and c_p is the specific heat coefficient. The relationship between the stress and strain rate for the fluid is represented by τ_{ij} and is given as [71]

$$\tau_{ij} = 2\mu\sigma_{ij} - \frac{2}{3}\mu \frac{\partial U_k}{\partial x_k} \delta_{ij} \tag{2.5}$$

In Equation 2.5, δ_{ij} is the Kronecker delta , which is defined as

$$\delta_{ij} = \begin{cases} 1 & \text{if} \quad \mathrm{i = j} \\ 0 & \text{otherwise} \end{cases} \tag{2.6}$$

and σ_{ij} is the instantaneous strain rate tensor.

2.1.2 Reynolds-averaged Navier-Stokes

CFD has the potential to model external separated flows through solving Equations (2.1) to (2.3), however this still remains a challenge for both two and three dimensional flows. This is mainly due to the fact that the separation position is sensitive to the calculated skin friction. If the computational resources were available to run Direct Numerical Simulation (DNS), this would resolve all length and time scales and give a reliable prediction. In order to solve all length and time scales, a grid resolution finer than the smallest turbulent length scales coupled with a time step shorter than the shortest turbulent time scale would need to be implemented. This is currently not viable, except for low Reynolds number flows, which are not representative of normal aerospace conditions.

Another option is Large Eddy Simulation (LES). This solves the larger turbulence scales and models to average out the smaller scales that have a universal behaviour and a predictable impact on the solution. The smaller length scales are typically those smaller than the grid resolution [72] and the grid resolution will be significantly coarser than used in DNS. This however still comes at a high computational cost for high Reynolds number flow and thus is still not widely adopted in industry and never in the early design phase. The approach therefore used extensively in aerospace applications, and thus in this study, is called Reynolds Averaging. Flow quantities are averaged to obtain equations for the mean flow quantities. Variables are split into the sum of mean and fluctuating components,

$$A(x_i,t) = \bar{A}(x_i,t) + A'(x_i,t) \tag{2.7}$$

with the mean part found as an ensemble average or by averaging over a time interval, T, longer than the turbulent time scales, but shorter than other unsteady phenomena

timescales. The mean part of the quantity is then,

$$\bar{A}(x_i,t) = \frac{1}{T}\int_{-T/2}^{T/2} A(x_i,t+\tau)\,d\tau \tag{2.8}$$

For incompressible flow this leads directly to a set of unsteady RANS equations for the mean flow variables with the influence of turbulence acting through Reynolds stresses that arise in the equations. These terms are modelled using turbulence models. However, for compressible flows there are fluctuations in density, velocity and pressure and so additional terms arise in the equations which also need to be modelled. To overcome this issue, density weighting (or Favre averaging) of certain variables is introduced as follows:

$$A = \tilde{A} + A'' \tag{2.9}$$

The mean part in Equation (2.9) is the density weighted average [73] which is given by

$$\tilde{A} = \frac{\overline{\rho A}}{\overline{\rho}} \tag{2.10}$$

Here the overbar means averaging as in Equation (2.8). The flow variables can then be decomposed into the mean and fluctuating components [71]

$$\begin{aligned} U_i &= \tilde{U}_i + U_i'' \\ \rho &= \overline{\rho} + \rho' \\ p &= \overline{p} + p' \\ T &= \tilde{T} + T'' \\ E &= \tilde{E} + E'' \\ q_j &= \overline{q}_j + q_j' \end{aligned} \tag{2.11}$$

The N-S equations then become:

$$\frac{\partial \overline{\rho}}{\partial t} + \frac{\partial \overline{\rho}\tilde{U}_i}{\partial x_i} = 0 \tag{2.12}$$

$$\frac{\partial \overline{\rho}\tilde{U}_i}{\partial t} + \frac{\partial \overline{\rho}\tilde{U}_j}{\partial x_j} = -\frac{\partial \overline{p}}{\partial x_i} + \frac{\partial}{\partial x_j}\left(\overline{\tau}_{ji} - \overline{\rho U_i'' U_j''}\right) \tag{2.13}$$

(2.14)

$$\frac{\partial \overline{\rho}\tilde{E}}{\partial t} + \frac{\partial \tilde{U}_j(\overline{\rho}\tilde{E} + \overline{p})}{\partial x_j} = \frac{\partial\left(\tilde{U}_i\tilde{\tau}_{ji} + \tilde{U}_i - \overline{\rho U_i'' U_j''}\right)}{\partial x_j} - \frac{\partial\left(\overline{q}_j + q_j^T\right)}{\partial x_j} + \frac{\partial \overline{\tau_{ji}U_i''} - \overline{\rho U_j'' \frac{1}{2} U_i'' U_i''}}{\partial x_j}$$

In Equations (2.13) and (2.14) the term $-\overline{\rho U_i'' U_j''}$ represents the Favre-averaged Reynolds stress tensor [71]. The Favre stress tensor, τ_{ji}^T, is given by a turbulence model because it does not have an analytical relationship with the mean flow quantities. This is commonly achieved by using a Boussinesq eddy-viscosity model to relate the Favre stress to the mean flow quantities:

$$\tau_{ij}^T = 2\mu_t\tilde{\sigma}_{ij} - \mu_t\frac{2}{3}\frac{\partial \tilde{U}_k}{\partial x_k}\delta_{ij} - \frac{2}{3}\overline{\rho}k_T\delta_{ij} \tag{2.15}$$

where k_T is the turbulent kinetic energy. It should be noted that for flows where $\overline{\rho}k_T\delta_{ij} << p$, (most flows below hypersonic conditions), the molecular diffusion term, $\overline{\tau_{ji}U_i''}$ and the turbulent transport term, $\overline{\rho U_j'' \frac{1}{2} U_i'' U_i''}$, found in Equation (2.14) can be approximated as zero [71]. Further to this the kinetic energy component, $\frac{2}{3}\overline{\rho}k_T\delta_{ij}$ can also be set to zero [73]. These expressions are substituted into Equations (2.12) to (2.14) to obtain

$$\frac{\partial \overline{\rho}}{\partial t} + \frac{\partial \overline{\rho}\tilde{U}_i}{\partial x_i} = 0 \tag{2.16}$$

$$\frac{\partial \overline{\rho}\tilde{U}_i}{\partial t} + \frac{\partial \overline{\rho}\tilde{U}_j}{\partial x_j} = -\frac{\partial \overline{p}}{\partial x_i} + \frac{\partial}{\partial x_j}\left(\overline{\tau}_{ji} + \tau_{ji}^T\right) \tag{2.17}$$

$$\frac{\partial \overline{\rho}\tilde{E}}{\partial t} + \frac{\partial \tilde{U}_j(\overline{\rho}\tilde{E} + \overline{p})}{\partial x_j} = \frac{\partial\left(\tilde{U}_i\tilde{\tau}_{ji} + \tilde{U}_i\tau_{ji}^T\right)}{\partial x_j} - \frac{\partial\left(\overline{q}_j + q_j^T\right)}{\partial x_j} \tag{2.18}$$

where the Favre stress tensor can now be defined as:

$$\tau_{ij}^{T} = 2\mu_t \tilde{\sigma}_{ij} - \mu_t \frac{2}{3} \frac{\partial \tilde{U}_k}{\partial x_k} \delta_{ij} \tag{2.19}$$

Note that Favre Reynolds Averaged N-S equations used for compressible flow are generally just referred to as the RANS equations in literature and these form the basis for the DLR-TAU solver [59] used to carry out the CFD simulations in this thesis.

2.1.3 DLR-TAU

The CFD approach used in this work is the Reynolds Averaged Navier-Stokes (RANS) equations. The RANS equations simulate the mean flow and utilize turbulence models for the turbulent flow quantities. The DLR-TAU code is developed by the German Aerospace Center (DLR) and is an unstructured, finite volume, compressible RANS solver. It is used widely within industry, with a key example user being Airbus. The DLR-TAU software package contains modules for grid adaption and deformation, preprocessing, and a number of grid partitioning methods. The solver uses an edge based dual cell approach, for the calculation of the inviscid fluxes. Either a central first or second order upwind scheme can be used. DLR-TAU uses a dual-grid approach, the supplied mesh is referred to as the primary grid and a secondary grid is produced by placing new vertices at the centroid of the primary grid cells, [74]. A second order dual time stepping scheme is used for time integration where a Runge-Kutta scheme is used in pseudo-time, [75], with convergence acceleration aided by a multi-grid algorithm. The multi-grid algorithm makes use of varying levels of grid fineness, which helps to aid solution convergence. Alongside this a Lower-Upper Symmetric Gauss-seidel (LU-SGS) scheme is available, which has been shown to be more stable for some applications [74].

In the following two-dimensional and three-dimensional CFD simulations, a central inviscid flux discretization has been used along with a Runge-Kutta scheme and multi-grid algorithm. The turbulence model used for all simulations is the Spalart-Allmaras negative turbulence model [76]. The Spalart-Allmaras turbulence model is a form of

Linear Eddy Viscosity Model (LEVM) and is a one equation model. This often proves to be less computationally expensive than more complex Non Linear Eddy Viscosity Models (NLEVM), or Reynolds Stress Transport Models (RSTM), yet has been shown to perform well in comparison, even for modelling separated flows [77].

2.1.4 The use of CFD in this work

Unsteady three-dimensional CFD is computationally demanding. However, it is often necessary for modelling wings at high angles of attack. Unsteady two-dimensional CFD can be used at a fraction of the 3D cost. It is therefore worth investigating how much information can be acquired about the 3D problem using 2D simulations. This work considers an aerofoil along with a straight, untapered wing comprised of the same section, with 3° of washout. Two-dimensional CFD will be used to form a viscous database of results that can be used to correct inviscid, three-dimensional models. Three-dimensional CFD is also carried out in order to provide a baseline that can be used for model validation and serves no purpose in the correction process.

The assumption made in this work is that the principles of the developed methodology can be proven by requiring that the 2D and 3D simulations used are comparable, i.e. the same turbulence model and comparable meshes as a result of same chordwise distribution of nodes (and same time resolution used in transient cases) are used between the simulations. It is accepted that a different 2D simulation may give a "better" solution, but it is assured that when this is placed within the 3D model the result will be comparable to a "better" 3D solution. For this reason a more detailed investigation with the accuracy of turbulence modelling for separated flow has not been carried out.

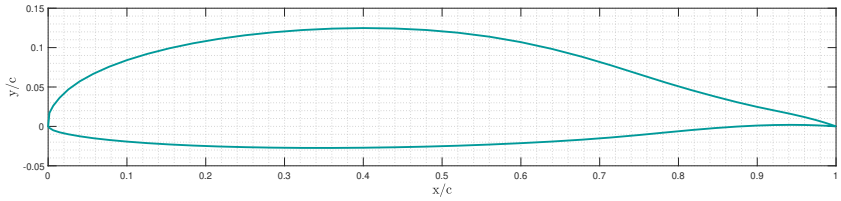

Figure 2.1: NACA LRN 1015 Aerofoil Profile

2.2 Two Dimensional CFD

2.2.1 NACA LRN1015 Geometry

The primary aerofoil section used for the two-dimensional CFD in this thesis and for the generation of a straight finite wing is the NACA LRN 1015. The reason behind this choice was a concurrent project within the research group, entitled AEROGUST [78], which also utilised this profile within aerodynamic research. The only requirement for an aerofoil in this research was for it to exhibit trailing edge separation. It will be shown that the section meets this criteria and hence was also selected for the possibility of some cross-over work. The LRN represents a "Low Reynolds Number" aerofoil [79] and the section has a maximum thickness to chord ratio t/c of 15.2%. At this t/c, the aerofoil should exhibit trailing edge stall properties [44], which will allow the Kirchhoff flow model to be used for this aerofoil [15]. The geometry of the NACA LRN 1015 is shown in Figure 2.1. Experimental data is also available [79] to validate the static two-dimensional C_p distribution.

The aerofoil will be subject to both static and a range of dynamic motions to form a database of results. A database is necessary in order to build the model developed in this thesis that is capable of evaluating the aerofoil load response at both low and high angles of attack. The small sample of results presented in this Chapter show the most prominent features found in the c_l and c_m responses.

2.2.2 Aerofoil Meshing

Before running CFD, the domain must be discretized into a grid. There are three main types of meshing strategy that can be used, these are structured, unstructured and hybrid grids. The quality of the mesh used within the CFD simulation will have an impact on the quality of the results obtained and computational expense. Therefore the meshing stage is an important step in the CFD process and should be carefully considered.

Structured grids have regular connectivity, where the elements are quadrilaterals in two-dimensional meshes and hexahedrons for three-dimensional grids. Structured grids have the connectivity of the mesh defined in the storage arrangement which is space efficient. The use of structured grids is commonly reserved for simpler geometries, however the domain to be discretized can be split up into multiple blocks (multiblock) to aid the structured meshing of more complex geometries. A good quality structured grid, that has elements well aligned with flow, can reduce errors that arise from numerical diffusion [80] .

Unlike structured grids, the mesh connectivity is not explicit for unstructured meshes and needs to be supplied alongside the grid points. This can be computationally less efficient however allows for a more diverse element geometry, which is useful when meshing complex configurations. However the benefit of unstructured grid generation is the ability to have any number of nodes within a control volume, given that the solver can handle them. An unstructured grid can also be refined locally by the addition of extra elements, this cannot be done in a structured grid. Unstructured meshes are easier to generate using automated meshing tools because they require less human experience and can therefore expedite the mesh generation routine [60]. However since cells adjacent to the surface may not be aligned to the flow, resolution of the flow in the boundary layer may require a finer mesh in this region.

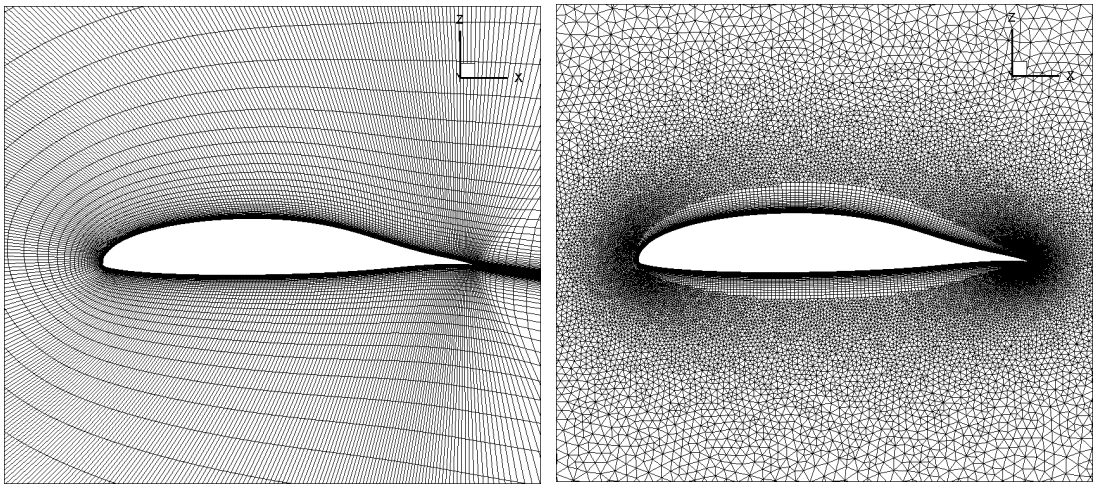

(a) Structured mesh for NACA LRN 1015 (b) Hybrid mesh for NACA LRN 1015

Figure 2.2: Structured and hybrid meshing technique for NACA LRN1015

Hybrid techniques are often used because they contain advantages of both structured and unstructured grids. The hybrid technique allows a structured grid to be placed near surfaces. This allows for a grid that is better aligned with the flow which more accurately resolves the boundary layer [81]. Also to properly resolve the boundary layer, the grid spacing normal to the wall has to be much finer than the rest of the mesh and a structured mesh routine can create a higher quality prism layer. An example of a structured and hybrid grid, for a NACA LRN 1015 section is shown in Figures 2.2(a) and 2.2(b) respectively. For the hybrid mesh, the structured prismatic layer is first generated, after which an unstructured discretization is used to fill the remaining volume.

The NACA LRN 1015 aerofoil mesh in this study uses a hybrid technique. The wall induces large gradients in the solution variables and adequate wall spacing is needed to capture this. This zone is referred to as the inner layer, and is made of the the following zones:

- Viscous sublayer ($y^+ \leq 5$)
- Buffer layer ($5 < y^+ \leq 30$)
- Log-law region ($y^+ > 30$)

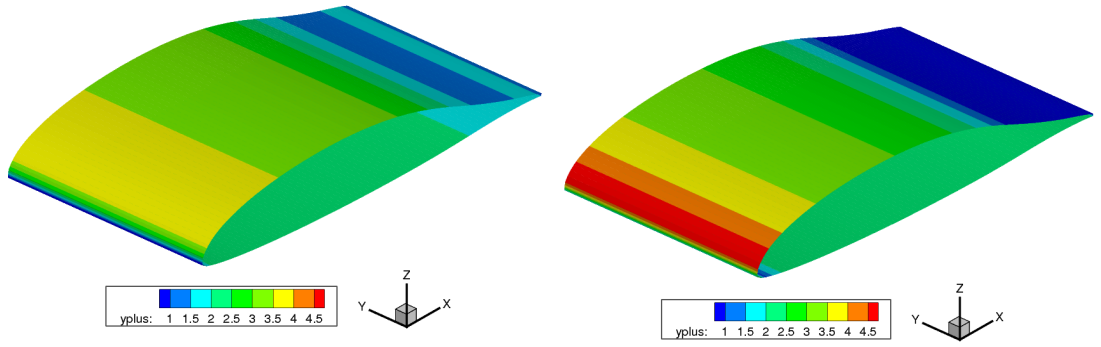

(a) Low angle of attack, $\alpha = 2°$ (b) High angle of attack, $\alpha = 16°$

Figure 2.3: Two-dimensional NACA LRN 1015 y^+ values at low and high angle of attacks.

The $y+$, which is the sublayer scaled distance is given by

$$y^+ = \frac{y\sqrt{\rho_w \tau_w}}{\mu_w} \tag{2.20}$$

where ρ_w, μ_w and τ_w are the density, viscosity and shear stress calculated at the wall. Therefore in order to model the viscous sublayer at the near wall, the y^+ should be less than 5. The y^+ found in the present simulations is between 1 and 4.5, contours of y^+ are shown at both a low and high angle of attack in Figure 2.3. Results matching experiments have been achieved when modelling separated flow with a y^+ of 4, [82]. A larger y^+ lowers the computational expense, and taking into consideration that three-dimensional simulations are ultimately to be carried out, intentionally with a similar y^+, a maximum y^+ of 4.5 is deemed appropriate.

For the rest of the domain an unstructured mesh is used; the boundary conditions of both end planes are set to symmetry planes. The mesh used for the aerofoil is displayed in Figure 2.4. This highlights the meshing technique around the leading and trailing edge, as well as a view from further out to help visualise the mesh density. Key information for the NACA LRN 1015 mesh can be found in Table 2.1, note that the mesh is quasi-three dimensional, with one cell in the spanwise direction.

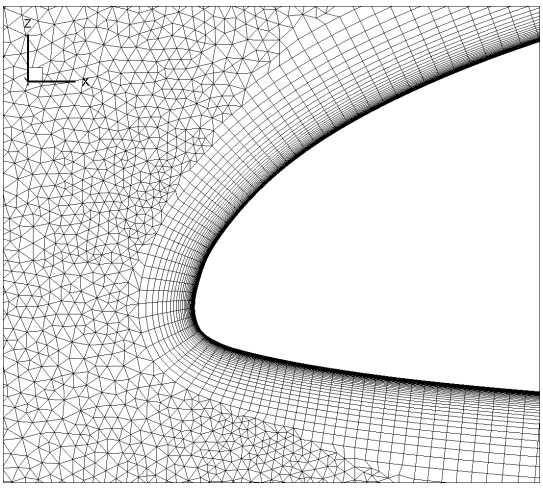

(a) Close up of mesh around the leading edge

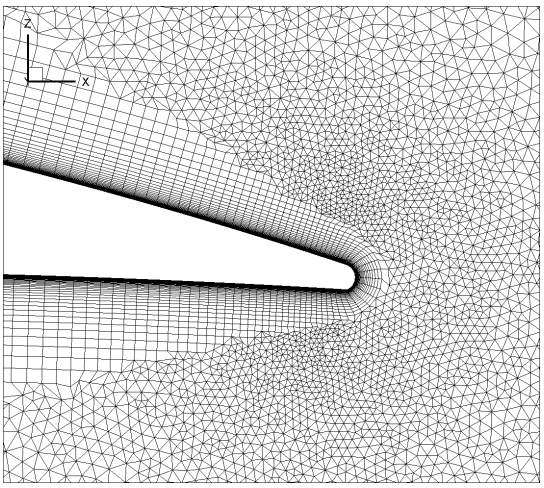

(b) Close up of mesh around the trailing edge

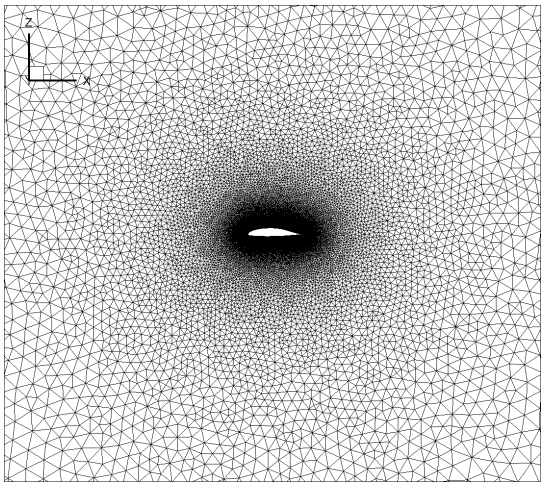

(c) Indication of the mesh density/cell growth

Figure 2.4: NACA LRN 1015 aerofoil mesh

Finite Wing Mesh Information	
Number of Points	127374
Number of Hexahedra	27238
Number of Prisms	72369
Number of Surface Triangles	144738
Number of Surface Quadrilaterals	55005

Table 2.1: Aerofoil mesh information

2.2.3 2D CFD Pressure Distribution Validation

Experiments were carried on a two-dimensional NACA LRN 1015 by Hicks and Cliff [79]. The experiments took place in the AMES transonic wind tunnel which has a $2' \times 2'$ working section. A sweep of Reynolds numbers was performed and will be used to validate the chordwise C_p distribution produced by the 2D static CFD. In this work, the effects of compressibility are not considered, therefore the experimental data at the lowest two Reynolds numbers of 5×10^5 and 1×10^6 which corresponds to Mach numbers of 0.2 and 0.5 respectively are used. Originally an angle of attack correction was applied to the experimental data using $\Delta\alpha_c = \delta(c/h)c_L$, where c/h represents the aerofoil chord to tunnel height ratio, δ is a Mach number dependent correction factor and c_L is the lift coefficient. An overriding conclusion of the experiment is that the angle of attack correction, $\Delta\alpha_c$, was larger than expected and found to be over 3° in some circumstances. In the same report a 2D CFD code was run and compared to the experimental data. In order to do so, the lift coefficient, Reynolds number and Mach number were matched. For the comparison between the experiment and the CFD used in this work, the angle of attack of the 2D CFD in [79] was used instead of matching lift coefficient. The angle of attack used in the 2D CFD from [79] includes the correction derived from the experimental data, $\Delta\alpha_c$, and therefore allows direct comparison with the experimental data, without having to consider a further correction.

Figures 2.5 and 2.6 show the CFD pressure coefficient along with the experimental values. The first C_p distribution in Figure 2.5(a) is for $\alpha = -2.496°$. This is the lowest angle of attack presented, however due to the relatively large α_{0L} the aerofoil still produces lift. In this case there is an intersection in the pressure coefficient on the upper and lower surface at approximately $x/c = 0.1$. This is well captured by the CFD as is the remainder of the pressure distribution. The largest discrepancy seen is at $x/c = 0.7$ and is observed on the upper surface. The CFD predicts a more gradual increase in C_p over the rear of the aerofoil compared to the more abrupt change in the experimental data. Similar outcomes are shown in Figures 2.5(b) and 2.5(c), which show the static

C_p distribution for angles of attack 3.084° and 4.698° respectively. The peak C_p is well captured, as is the stagnation point on the lower surface. In the case $\alpha = 3.084°$ the C_p is once again computed to increase more gradually than the experiment on the upper surface towards the rear of the aerofoil. However, for $\alpha = 4.698°$ this appears to match more closely. The maximum angle of attack presented is 5.998° shown in Figure 2.5(d). It would have been advantageous for greater angles of attack to have been utilized given the major separation that is considered in this work, however the validation is limited by the available experimental data. At $\alpha = 5.998°$ the CFD is able to reproduce the experimental pressures well, however the leading edge suction is overestimated whilst the lower surface pressures are underestimated. It should be noted that similar results were found using the CFD methods presented by Hicks and Cliff [79] and it is concluded that a qualitatively good agreement was found.

Two further cases are presented for a higher Reynolds number of 1×10^6 in Figures 2.6(a) and 2.6(b). The figures display the chordwise C_p for angles of attack $\alpha = 1.171°$ and $\alpha = 2.810°$ respectively. As with the previous cases at the lower Reynolds number, the pressure coefficient is suitably modelled on both the upper and lower surfaces.

2.2.4 Static Separation and Stall Simulations

Up to this point the two-dimensional CFD mesh has been scaled down to match the conditions of the discussed experiment [79]. However the aerofoil section used in the following CFD will have a chord length of 2 m. The freestream velocity will also be held constant at $102.06\,\mathrm{m\,s^{-1}}$ giving a Reynolds number of 2×10^7 and a freestream Mach number, $M_\infty = 0.3$, to avoid localised supersonic flow. The simulations are assumed to be at sea-level with the reference pressure set to 101 325 Pa and reference temperature 288.15 K.

Due to the high gradients that can be found in separated flow fields, the mesh adaption module within the DLR-TAU code [59] was utilized. The adaption module requires a

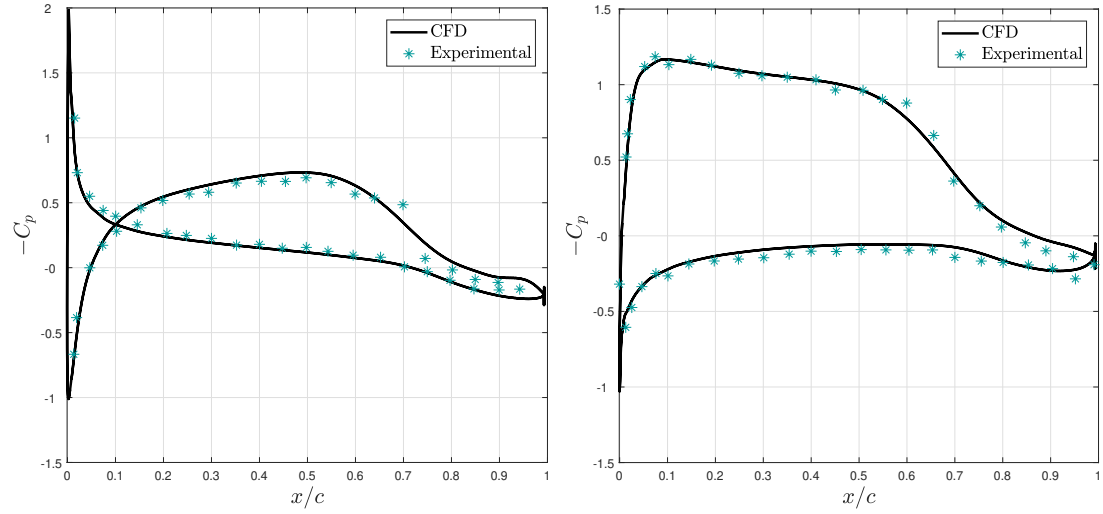

(a) $\alpha = -2.496°$

(b) $\alpha = 3.084°$

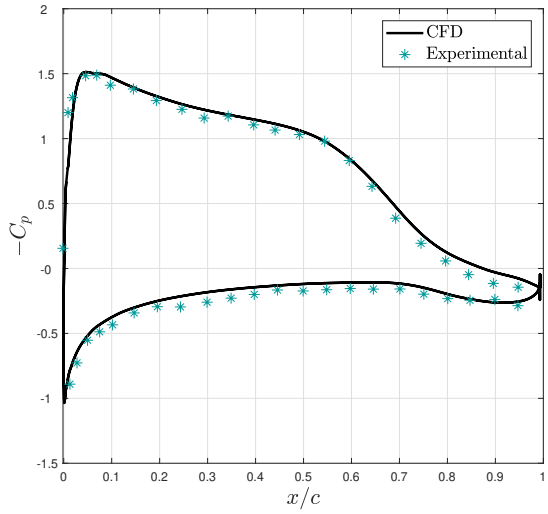

(c) $\alpha = 4.698°$

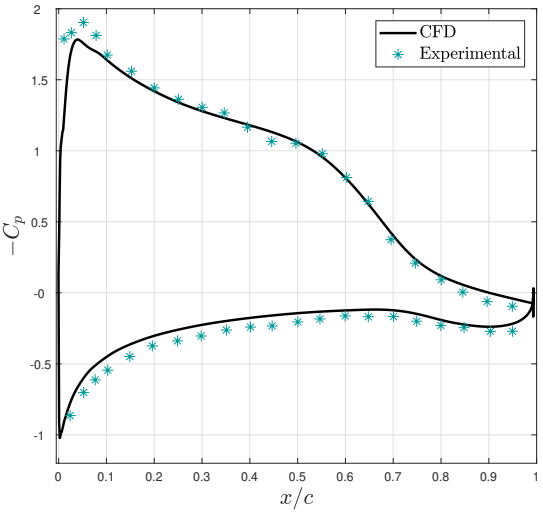

(d) $\alpha = 5.998°$

Figure 2.5: Two-dimensional C_p distribution for the NACA LRN 1015 Profile, $\mathrm{Re} = 5 \times 10^5$.

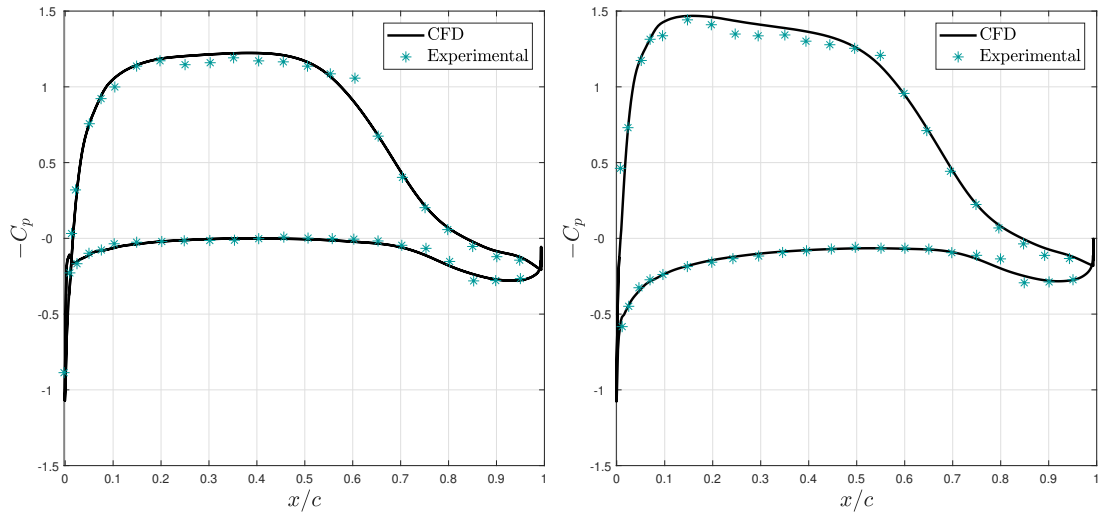

(a) $\alpha = 1.171°$ (b) $\alpha = 2.810°$

Figure 2.6: Two-dimensional C_p distribution for the NACA LRN 1015 Profile, Re = 1×10^6.

primary grid and a corresponding solution file in order to adapt the mesh. For the adaption process, initially the routine was used for the baseline mesh with a flow solution for the static case at $\alpha = 12°$, this was chosen because it is close to the critical angle of attack for the two-dimensional section. The adaption routine was able to add up to 50% extra grid points based on the velocity gradients calculated within the inputted flow solution. Once the grid was adapted, a new flow solution was calculated allowing the adapted grid to undergo a further adaption routine. Once this was complete for the static case $\alpha = 12°$, an identical procedure was carried out for $\alpha = 15°$ followed by $\alpha = 17°$.

A static sweep in angle of attack was conducted, with α ranging between $-7°$ and $20°$. The solutions were all run independently, i.e. the solution was not started from any previous run. The lift and moment coefficient response for the static sweep are displayed in Figures 2.7(a) and 2.7(b) respectively. Note that the moment is taken around the quarter-chord position. As previously mentioned, Figures 2.7(a) and 2.7(b) confirm that the NACA LRN 1015 has a relatively low zero lift angle of attack at approximately $-5°$. The critical angle of attack is approximately 12°, with a corresponding maximum c_L of 1.7. There is a trailing edge stall mechanism which gives a rather gradual reduction

in lift after the stall angle is exceeded. However at $\alpha = 17°$ both the lift and moment coefficient show a change in behaviour, this is manifested more clearly through the c_m curve. This seems to be linked to the separation position moving fore of the mid-chord where the more cambered trailing section ends. Figure 2.8 shows the chordwise skin friction,C_{fx}, contours for a selection of angles of attack, ranging from $-7°$ to $21°$. For two-dimensional flow, the change of sign of C_{fx} from positive to negative indicates flow separation. It is clear from the figure that the NACA LRN 1015 aerofoil exhibits trailing edge separation under the simulated conditions, with the separation position initiating at the trailing edge and gradually moving towards the leading edge as the angle of attack is increased.

2.2.5 Dynamic Separation and Stall Simulations

2.2.5.1 Mesh Deformation

For the static cases the freestream velocity can be rotated in order to achieve the desired angle of attack. However for the dynamic simulations, mesh deformation is utilized in order to achieve temporal changes to the angle of attack. When deforming the surface mesh, the surrounding volume mesh must also be deformed. In order to do so, radial basis functions (RBFs) are used for the interpolations of the displacement of the surface points. Interpolation using RBFs is a popular technique for mesh deformation, this is due to the robustness and ability to preserve mesh quality [83]. However the cost of the deformation process scales with the number of surface points, n_s, as $O(n_s^3)$. In order to reduce the computational expense of the deformation, a structured coarsening is applied to reduce the number of surface points considered in the RBF interpolation [84].

When the surface displaces, the surrounding volume mesh must also be adapted. The RBF interpolation is used for the interpolation of deflections in space. The RBF deformation in DLR-TAU uses a blending function, $\phi^B(d)$, that reduces the displacement of the volume

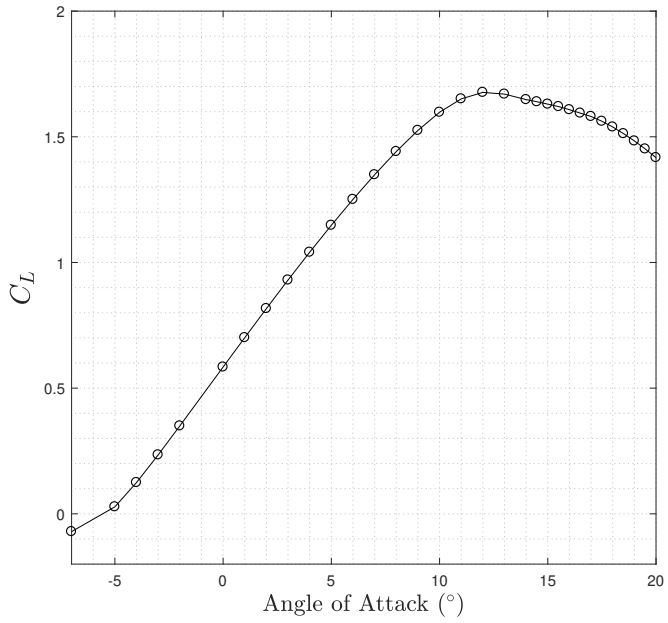

(a) NACA LRN 1015 static c_L

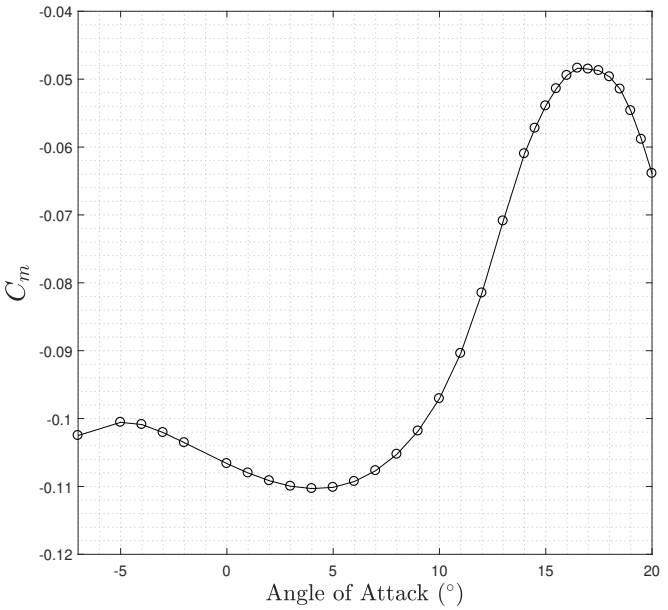

(b) NACA LRN 1015 static c_m

Figure 2.7: Two-dimensional lift and moment coefficient for static sweep in angle of attack. Moment is taken around the quarter-chord.

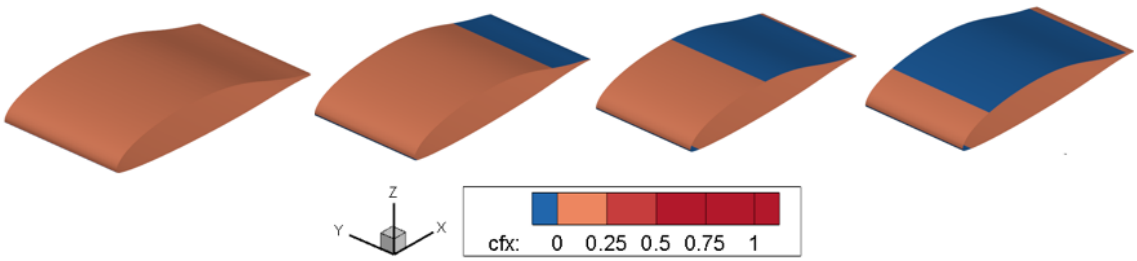

Figure 2.8: Two dimensional separation position movement from CFD. From left to right, $\alpha = -7°$, $\alpha = 6°$, $\alpha = 17°$, $\alpha = 21°$

grid away from the deformed surface, [85].

$$\phi^B(d) = \begin{cases} f(d) & 0 \leqslant d \leqslant 1 \\ 0 & d > 1 \end{cases} \tag{2.21}$$

where $f(d)$ is the blending function and d is the distance from the surface normalised by the support radius where cells within the support radius are able to deform to help preserve the mesh cell quality. An example of this is shown in Figure 2.9 for a rotation of an aerofoil mesh of 20° about the quarter-chord. For the initial 1.5 chord lengths of the surface, the full displacement is applied to the grid ($\phi^B(d) = f(1)$), this is shown in Figure 2.9(a). At 3.5 chord lengths away from the surface points, there is a zero weighting to the blending function, ($\phi^B(d) = 0$), therefore the grid points remain fixed during the deformation. This is shown in Figure 2.9(b), where the undeformed and deformed grids overlap exactly at a distance greater than $3.5c$ from the aerofoil surface. In the zone between the full and zero weighting, a smooth function, $f(d)$, is used to specify the deformation.

2.2.5.2 Two-Dimensional Dynamic Results

The dynamic results presented here are just a small sample of a much wider database of results, more of which can be produced using the formulation in Appendix B. The dynamic data comes in the form of pure pitching oscillations, in which the angle of attack is defined by:

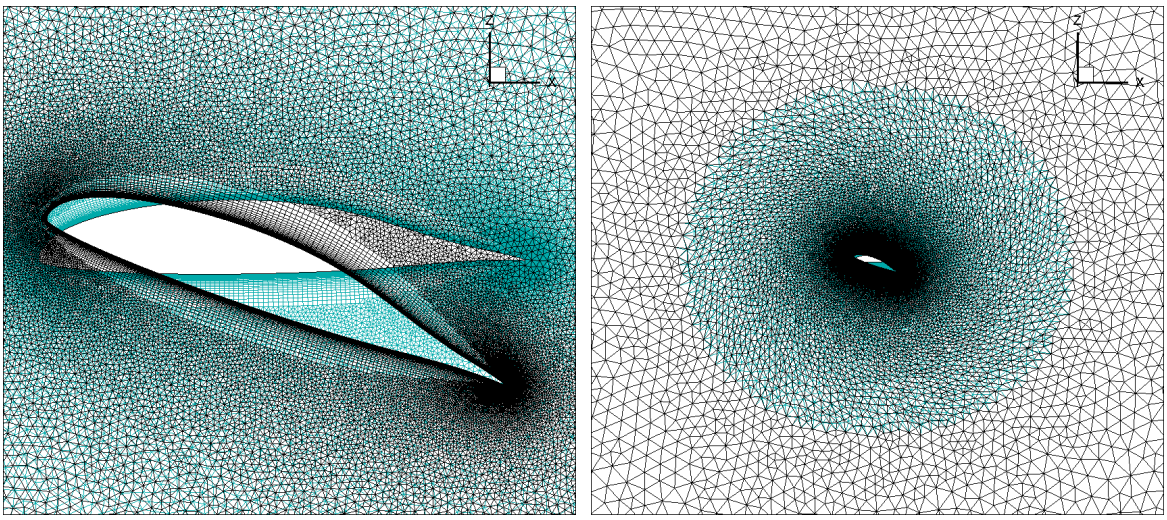

(a) RBF deformation - close to surface (b) RBF deformation - far from surface

Figure 2.9: Example of RBF deformation, superposed initial and deformed grid.

$$\alpha(t) = \alpha_0 + \alpha_1 \sin(\omega t) \tag{2.22}$$

which is perhaps more conveniently represented in terms of the reduced frequency, k, and the non-dimensional semi-chord transit time, S, where S is equal to $2V_\infty t/c$.

$$\alpha(S) = \alpha_0 + \alpha_1 \sin(kS) \tag{2.23}$$

For the time discretization used in each case, 128 timesteps were used in each pitching cycle, a very similar resolution to that used in the work carried out by Spentzos *et al.* [31].

The results are divided into two groups, firstly results are presented where little separation is apparent. The second group focuses on the post-stall regime, where separation dominates the flow. The result of changing the reduced frequency, mean amplitude and amplitude of pitching oscillation is also investigated and related back to the theory discussed in Section 1.6.

Initially presented is the c_L response for the case with the smallest mean angle of attack, $\alpha = 3°$, coupled with the lowest amplitude of $2°$, see Figure 2.10(a). This case features

nominally attached flow and for this reason the hysteresis loop takes a very similar form to what would be expected from an inviscid solver, which is an anti-clockwise hysteresis loop that is symmetrical about the major axis. Note that the reduced frequency in this case is 0.1, however due to the fact there is little separation this will have a predominately linear effect on the response and therefore only frequency influences the width of the hysteresis loop, i.e the minor axis of the lift hysteresis loop. Also plotted within the figure is the static lift curve, the hysteresis loop is centred around the static values.

Increasing the amplitude of the pitching motion to 4° and lowering the reduced frequency to 0.05, which in turn reduces the lag in the separation position movement, causes more separation to be present. The C_L response for these values is shown in Figure 2.10(b). At the lower angles of attack the flow is nominally attached. However at the top of the pitching cycle, separation begins to impact the response, this results in a slight collapse in the lift coefficient. The direction of the hysteresis loop remains anti-clockwise.

Increasing the mean amplitude of attack to 7°, with an amplitude of 2°, initiates further separation. The collapse of the c_L at the top of the stroke becomes much more apparent as shown in Figure 2.11(c).

If the amplitude of the pitching motion is increased to 6°, as in Figure 2.11(d), a different topology arises where the hysteresis loop intersects itself forming a figure of eight shape. This is the first occurrence of a clockwise hysteresis loop, which is present in this case when $\alpha > 9.5°$, at lower angles it still remains anti-clockwise. This can be seen as an intermediate stage between attached flows and those that are dominated by separation which exhibit a solely clockwise hysteresis loop. The moment coefficient hysteresis loops for the same cases are displayed in Figure 2.11. For all of the cases the dynamic C_M response remains centered about the static c_m curve. This is a useful observation for the development of a moment model for the NACA LRN 1015 aerofoil.

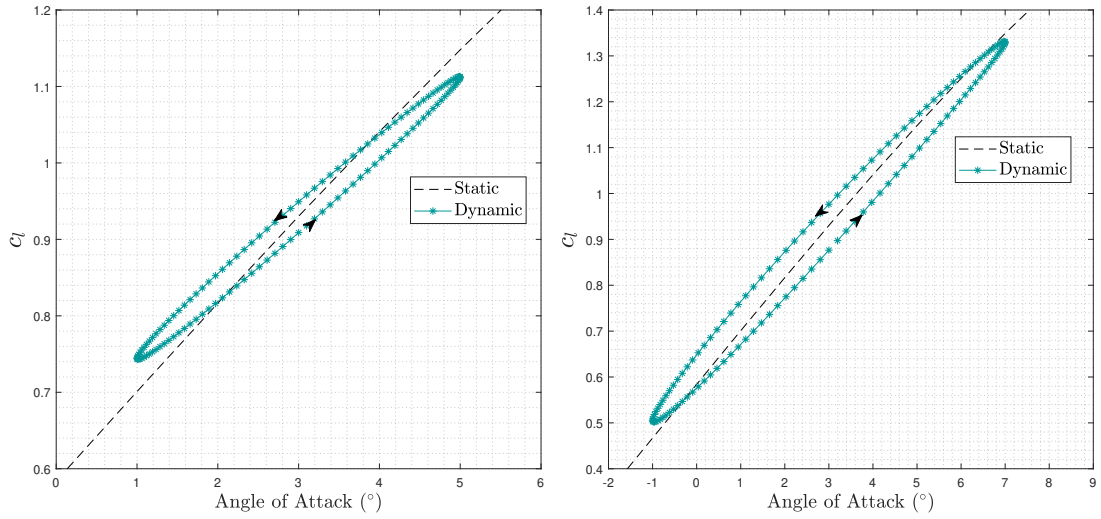

(a) $\alpha = 3° \pm 2° \sin(0.10S)$

(b) $\alpha = 3° \pm 4° \sin(0.05S)$

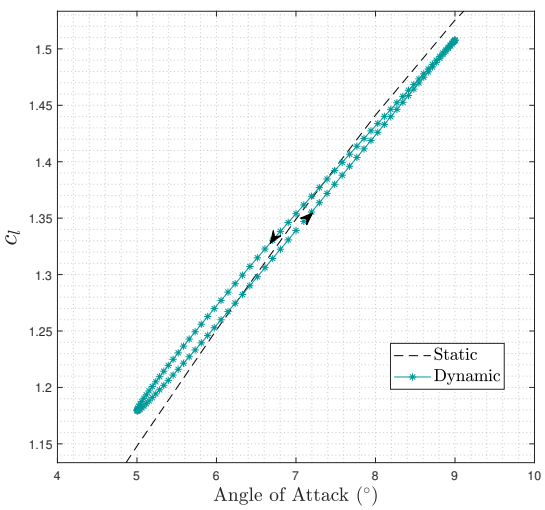

(c) $\alpha = 7° \pm 2° \sin(0.10S)$

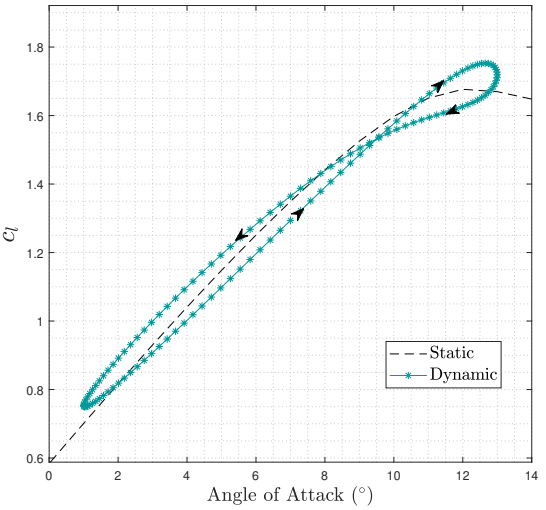

(d) $\alpha = 7° \pm 6° \sin(0.05S)$

Figure 2.10: Two-dimensional dynamic c_L results for the NACA LRN1015 aerofoil - mild separation.

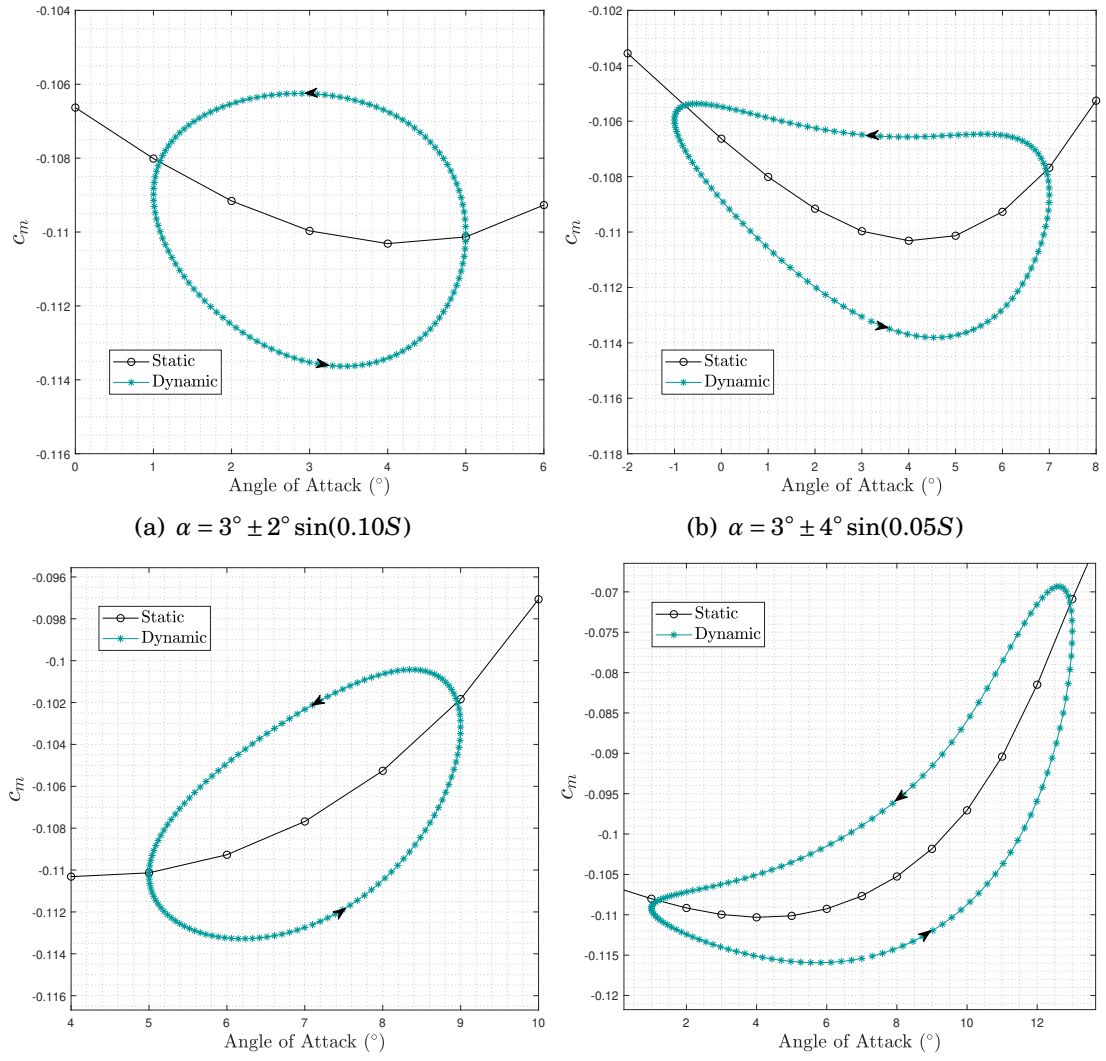

(a) $\alpha = 3° \pm 2° \sin(0.10S)$

(b) $\alpha = 3° \pm 4° \sin(0.05S)$

(c) $\alpha = 7° \pm 2° \sin(0.10S)$

(d) $\alpha = 7° \pm 6° \sin(0.05S)$

Figure 2.11: Two-dimensional dynamic c_M results for the NACA LRN1015 aerofoil - mild separation.

The remaining cases will feature flows that are dominated by separation, where the geometrical angle of attack surpasses the critical angle. The first case is displayed in Figure 2.12(a). Here the maximum angle of attack of 13° is slightly higher than the static stall angle, however this is sufficient to result in a clockwise lift hysteresis loop. The mean angle is increased to 14° and the amplitude to 4° in Figure 2.12(b), here it can be seen that the dynamic case is able to result in significantly higher lift coefficients than the static response, achieving a $c_{L\max}$ of 1.85, compared to the static $c_{L\max}$ of 1.7. If a case is run where the angle of attack is kept above the critical angle throughout the motion, the response for the NACA LRN1015 becomes more elliptical, as shown in Figure 2.12(c). Finally in Figure 2.12(d) a large amplitude case is displayed. The angle of attack range in this case is between 8° and 20°. The dynamic response still remains centered on the static data, highlighting the usefulness of the static data. The corresponding moment coefficients, are displayed in Figure 2.13. These show that the severity of the separation has a less discernible effect on the moment hysteresis loops, the dynamic response stays centered on the static moment data and the hysteresis loop remains in an anti-clockwise direction.

Figures 2.14(a) and 2.14(b) show the c_l and c_m response for altering the mean angle of attack. The amplitude of oscillation is fixed at ±4°, along with the reduced frequency at $k = 0.10$. This once again shows how the aerodynamic coefficients remain a perturbation of the static data. Changing the reduced frequency and keeping the other parameters the same also gives similar results. Figure 2.15(a) show the c_l response to the $\alpha = 14 \circ \pm 4° \sin(kS)$, where k is varied between 0.10 and 0.15. Increasing k gives a higher maximum c_l due to the greater lag in the separation position. However this also delays reattachment and therefore results in less lift during the downstroke. This is the result that was found in the literature in Section 1.6. The moment coefficient also reacts to the delayed separation position, forming a larger hysteresis loop, as shown in Figure 2.15(b).

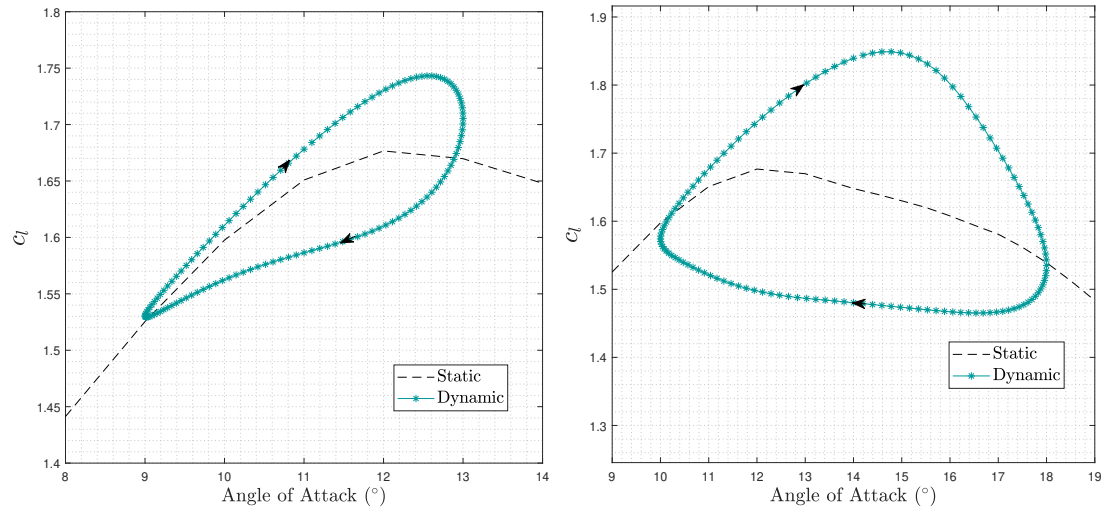

(a) $\alpha = 11° \pm 2° \sin(0.10S)$

(b) $\alpha = 14° \pm 4° \sin(0.10S)$

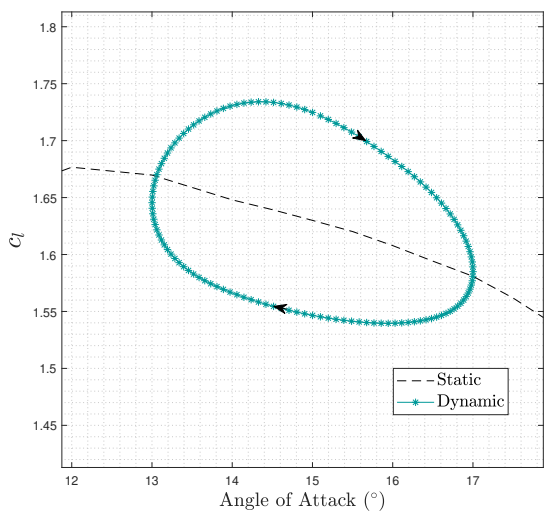

(c) $\alpha = 15° \pm 2° \sin(0.10S)$

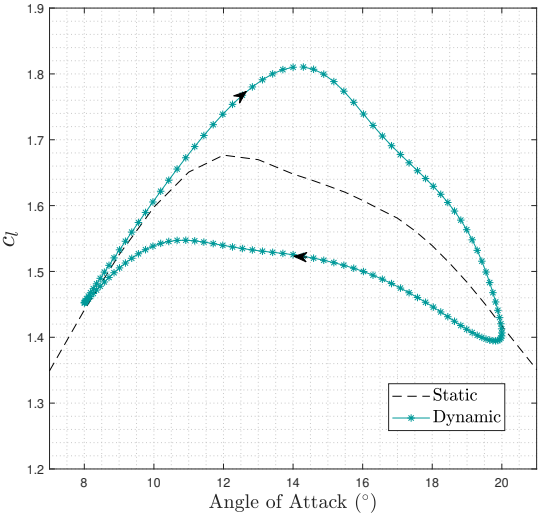

(d) $\alpha = 14° \pm 6° \sin(0.05S)$

Figure 2.12: Two-dimensional dynamic c_l results for the NACA LRN1015 aerofoil - severe separation.

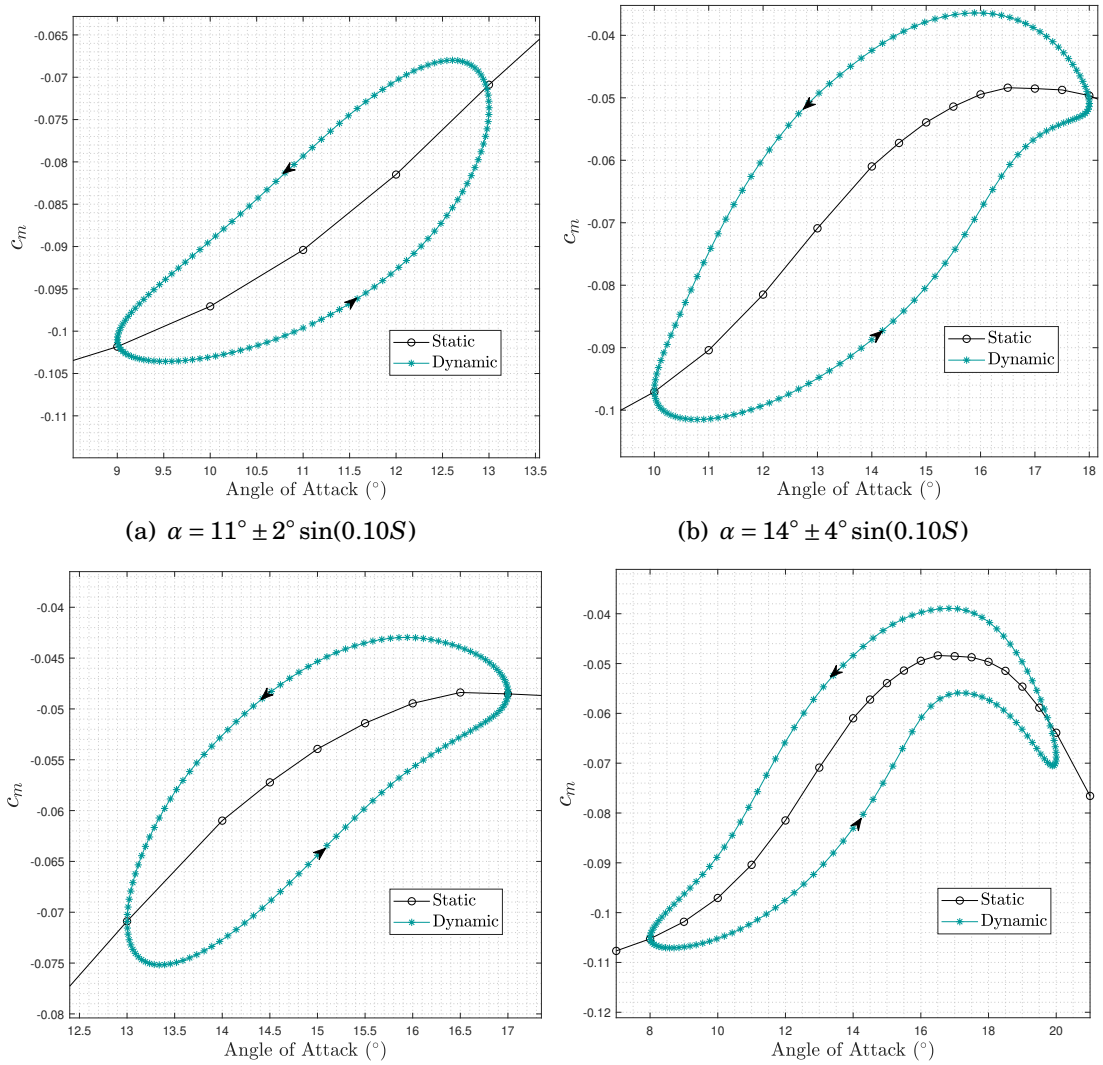

(a) $\alpha = 11° \pm 2° \sin(0.10S)$

(b) $\alpha = 14° \pm 4° \sin(0.10S)$

(c) $\alpha = 15° \pm 2° \sin(0.10S)$

(d) $\alpha = 14° \pm 6° \sin(0.05S)$

Figure 2.13: Two-dimensional dynamic c_m results for the NACA LRN1015 aerofoil - severe separation.

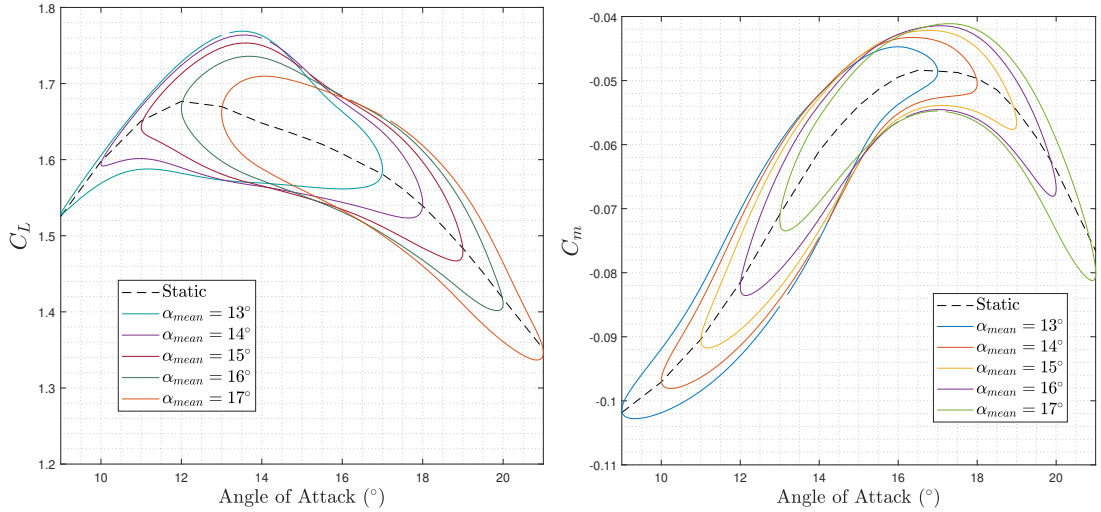

(a) Mean angle effect on c_l (b) Mean angle effect on c_m

Figure 2.14: Two-dimensional lift and moment coefficient for static sweep in mean angle of attack.

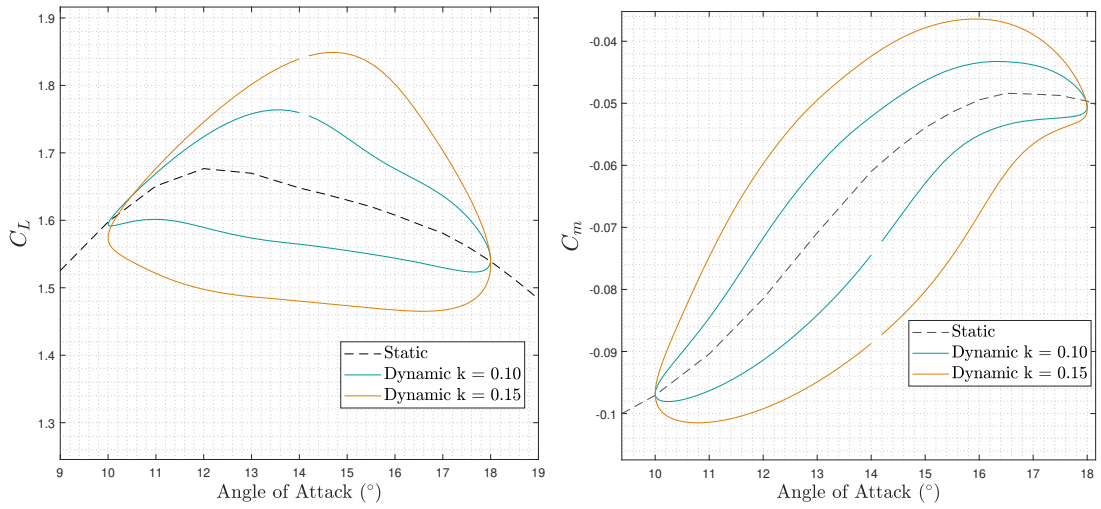

(a) Reduced frequency effect on c_l (b) Reduced frequency effect on c_m

Figure 2.15: Two-dimensional lift and moment coefficient at two reduced frequencies.

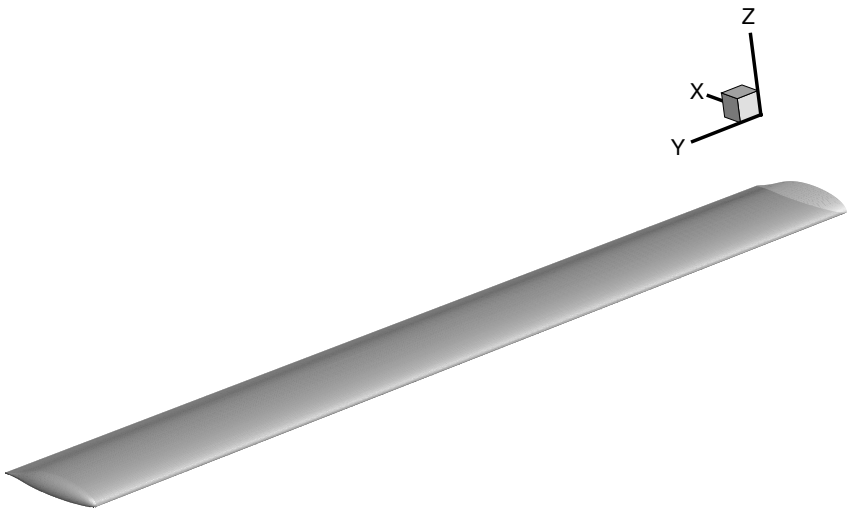

Figure 2.16: Clean UAV wing model, Aspect ratio = 12.5, NACA LRN 1015 profile throughout.

2.3 Three Dimensional Simulations

2.3.1 UAV Aerofoil and Wing Model

For the CFD wing model, a clean half-wing of aspect ratio 12.5 is used. The wing consists of a NACA LRN 1015 profile throughout, this is shown in Figure 2.16 This wing is identical to that used in the aforementioned AEROGUST project, where is was termed 'UAV wing' [86]: this name will also be used here. The wing has washout defined by a +3° twist at the root and this linearly decreases to 0° at the tip. Note that the wing angle of attack is defined relative to the tip. Therefore at $\alpha = 0°$, the wing root has a local angle attack of 3°. There is a tip cap on the wing, this is created by drawing a semi-circle of diameter equal to the local thickness and centered on the chord line. The wing is modelled as a viscous wall and the plane intersecting the root has a symmetry plane boundary condition, as consistent with previous CFD URANS simulations in the literature [31] [54] [56] [58] [87]. A symmetry plane is useful in reducing the computational expense of the simulation, and is valid when there is no net flow normal to the symmetry plane [59] . The rest of the mesh extremities are modelled as a farfield boundary condition.

2.3.2 Meshing

A hybrid grid is used for the finite wing calculations presented here, a structured part forms a prism layer near the wing surface and an unstructured mesh fills the rest of the domain. The mesh used for the three-dimensional CFD runs is presented in Figure 2.17. This unstructured mesh simplifies the discretization between the wing tip and the neighboring domain, an issue Spentzos [54] notes when using structured meshing strategies. However it still allows for a structured zone near the surface of the wing to capture the boundary layer, the y^+ values are shown at a low and high angle of attack in Figure 2.18. The y^+ values are intentionally similar to the 2D aerofoil mesh to create a comparable mesh.

2.3.2.1 Grid adaption

In a similar manner to the two-dimensional cases, mesh adaption was used to refine areas of the mesh which experienced high gradients. For the adaption process, initially the routine was used for the baseline mesh with a flow solution for the static case at $\alpha = 12°$, this was chosen because it is close to the critical angle of attack for the two-dimensional section. The adaption routine was able to add up to 50% extra grid points based on the velocity gradients calculated within the inputted flow solution. Once the grid was adapted, a new flow solution was calculated allowing the adapted grid to undergo a further adaption routine. Once this was complete for the static case $\alpha = 12°$, an identical procedure was carried out for $\alpha = 15°$ followed by $\alpha = 17°$. The resulting mesh was used for all static and dynamic cases presented, regardless of the severity of the flow separation. The mesh information is displayed in Table 2.2.

2.3.3 Static Separation and Stall Modelling

In a similar manner to the two-dimensional data, a static sweep of the angle of attack was conducted for the finite wing. Again, as with the 2D aerofoil, the freestream flow vector angle was modified removing the need for mesh deformation when statically

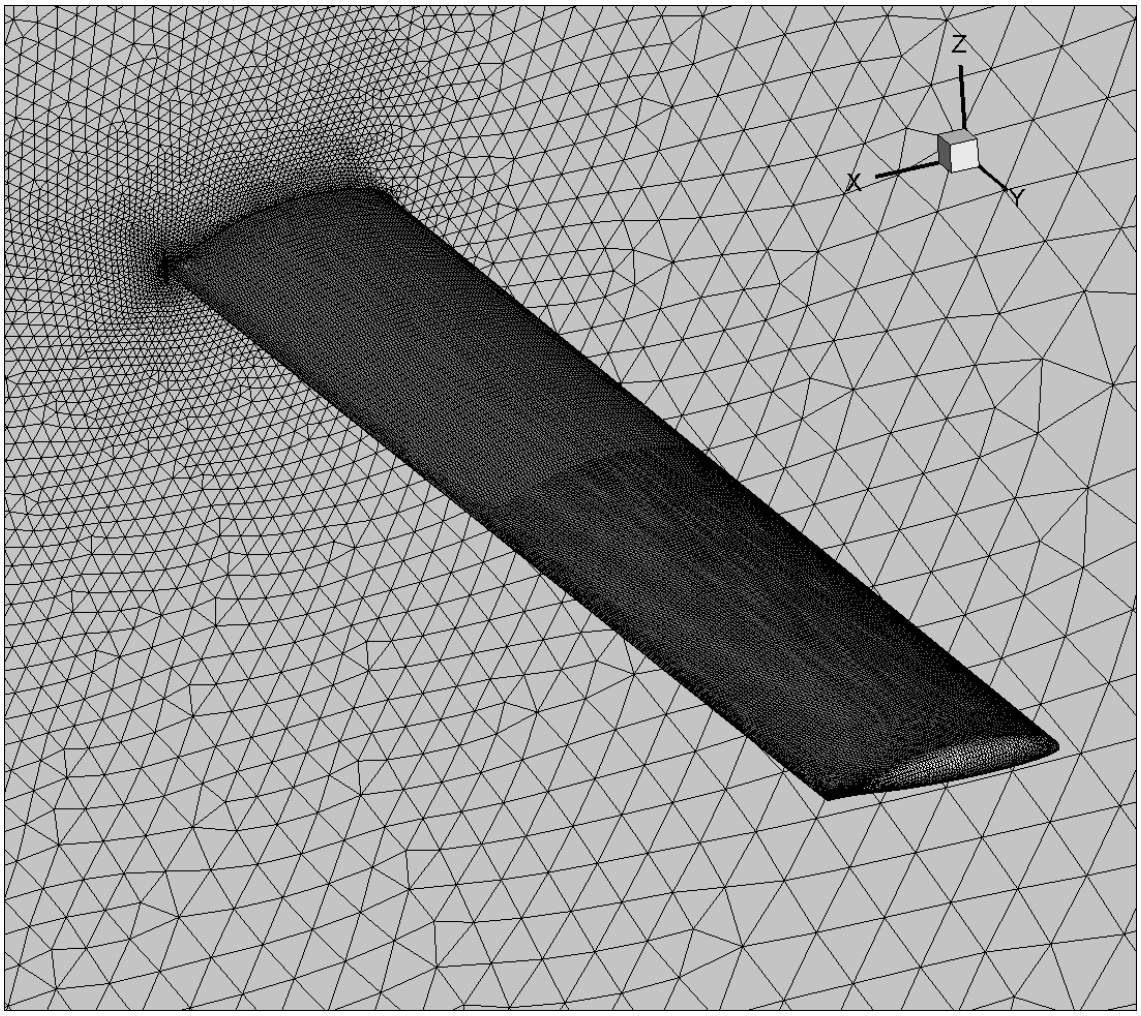

Figure 2.17: 3D surface mesh and symmetry plane

Finite Wing Mesh Information	
Number of Points	1176316
Number of Tetrahedra	1752309
Number of Prisms	1708140
Number of Surface Triangles	82638
Number of Surface Quadrilaterals	5400

Table 2.2: Finite wing mesh information

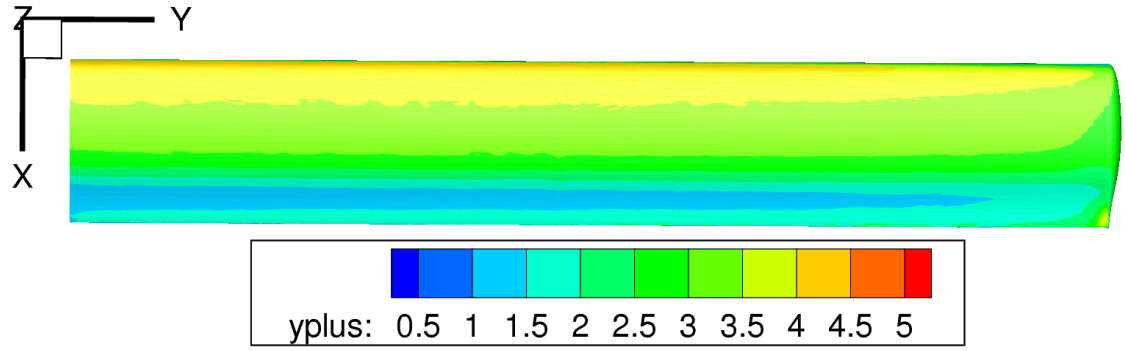

(a) y^+, $\alpha = 0°$

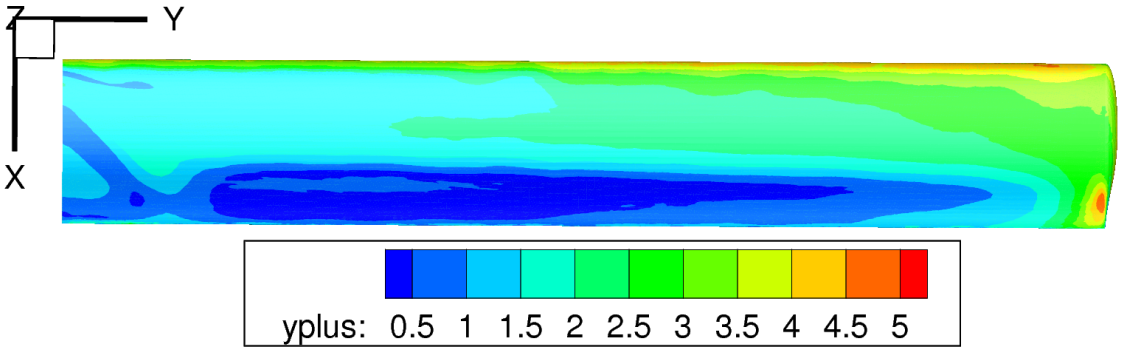

(b) y^+, $\alpha = 17°$

Figure 2.18: y^+ values for the finite wing at low ($\alpha = 0°$) and high ($\alpha = 17°$) angles of attack.

changing the angle of attack. Figures 2.19(a) and 2.19(b) show the C_l and C_l/C_l for the three-dimensional wing, at different spanwise locations. Also included in the figures are the 2D counterparts. Note that the angle of attack in Figures 2.19(a) and 2.19(b) are offset by the spanwise twist present in the wing, this is to make the comparison with the two-dimensional data clearer. The maximum C_l that is achieved in the static data is similar for the 2D and 3D data, with $C_l^{\max} \approx 1.7$. The lift curve slope, as expected, reduces closer to the tip as a result of the downwash imposed by the tip vortex. Overall the behaviour of the 3D C_l response is similar to that of the 2D data, with a stretching transformation due to the aforementioned reduction in the lift curve slope. Note that the relation C_m/C_l is shown in Figure 2.19(b). This effectively gives the distance from the quarter chord to the aerodynamic centre of the aerofoil. This is presented because this

is what is used later in Chapter 3 for fitting the CFD data. A similar pattern of results was obtained in the work of Piziali [12], where the three-dimensional data had similar characteristics to the sectional data, with the inclusion of a lag in the angle of attack. This indicates that obtaining two dimensional sectional data gives an insight into the three-dimensional problem. This observation proves useful and allows for a 2D database of results, through modifications, to ultimately correct a 3D problem.
The most significant difference between the 2D and 3D results is attributed to the strip located closest to the symmetry plane at $y/b = 0.04$. Here, the separation is more severe after the critical angle of attack is exceeded and appears to behave differently to the 2D data. This is believed to be a result of three-dimensional flow separation forming a stall cell close to the centerline of the wing. The strip located closest to the wing tip, $y/b = 0.99$, shows a different behaviour, this is simply due to the fact it is located on the tip cap.

2.3.4 Dynamic Separation and Stall Modelling

The finite wing underwent rigid, unsteady, changes to the angle of attack which was achieved through the use of the mesh deformation routine detailed previously.

In order to present the three-dimensional lift and moment results, it is chosen to represent them with a surface. This is useful since the spanwise distribution of lift and moment is desired, not just the overall integrated values. The utilization of meshed surfaces will be commonplace in the rest of this thesis. The surface is a hysteresis loop that is extended into a third dimension which represents the spanwise position. The results presented in Figures 2.20(a) to 2.23(b) are just a sample from a much larger database of unsteady RANS results. The cases selected demonstrate the general stall behaviour of the rigid wing. These results also have not been validated against any other CFD or experiments, this is simply because there are not any documented static or dynamic cases for the UAV wing within the literature. The primary purpose of the unsteady cases are for validating the model developed in this thesis, with the cases of principal interest containing flow separation. Also note that Figure 2.20(a) contains the

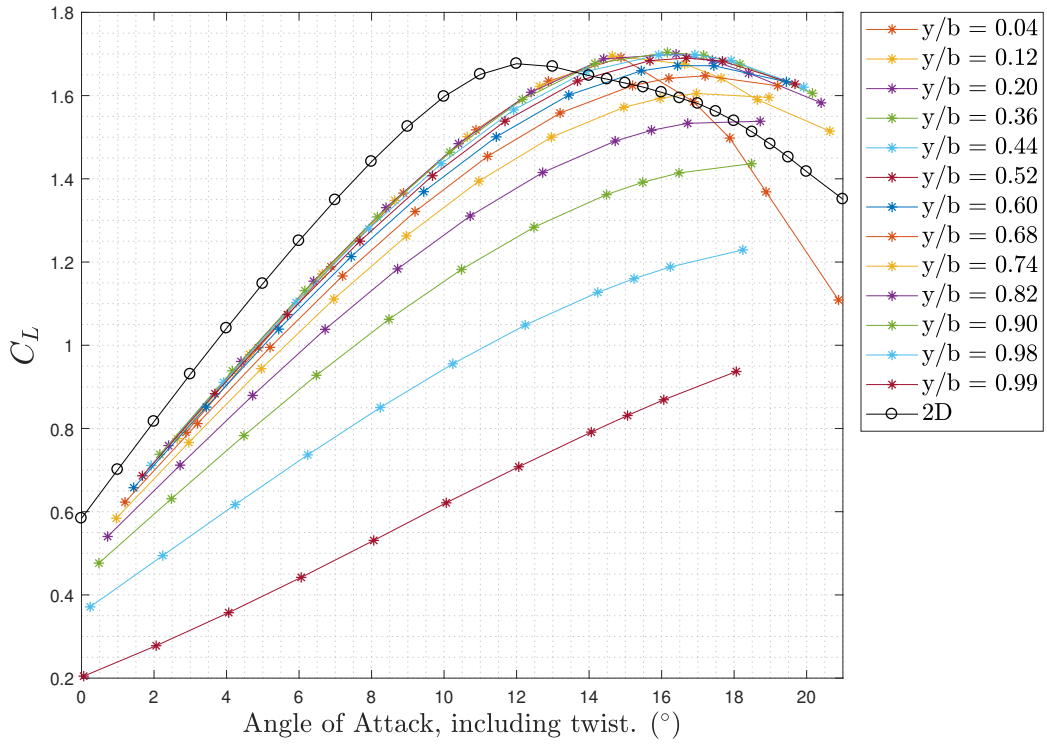

(a) NACA LRN 1015 wing static C_l

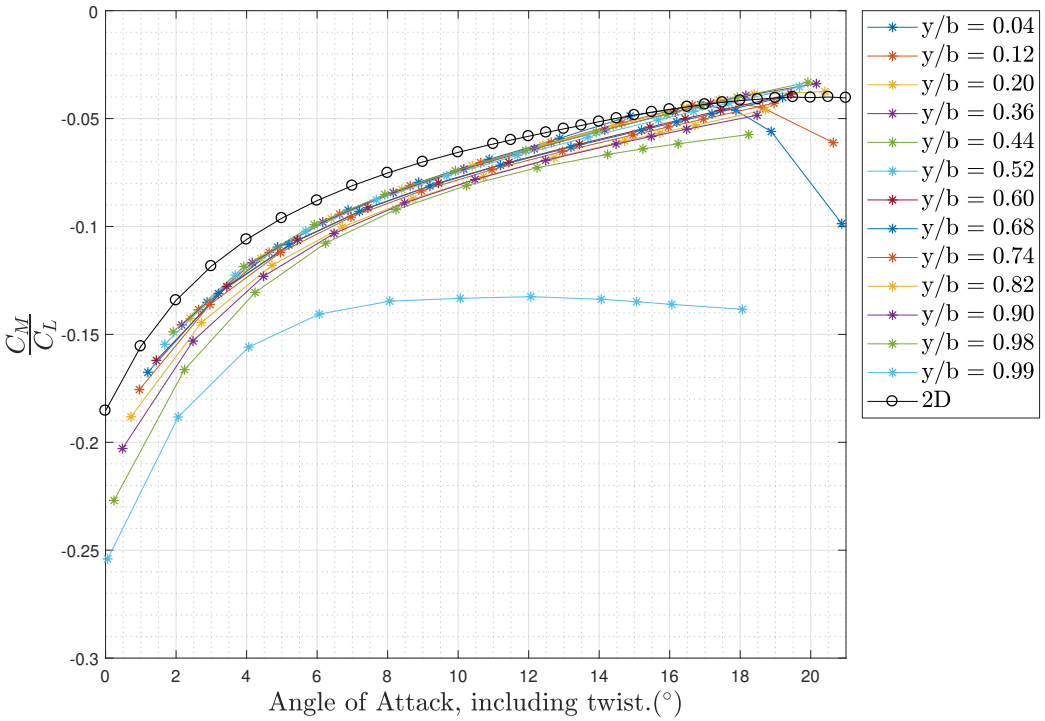

(b) NACA LRN 1015 wing static C_m

Figure 2.19: Two-dimensional lift and moment coefficient for static sweep in angle of attack, moment taken around the quarter-chord.

spanwise distribution of C_l all the way to the end of the tip cap, whereas the following figures do not. As previously detailed, the tip has a cap, which will not be modelled in future chapters and therefore is excluded from the figures. The lift distribution on the tip cap will be highly three-dimensional and dominated by the tip vortex and modelling this is not desired in the present work.

Firstly looking at the C_l data, in Figures 2.20(a) to 2.21(b), the spanwise behaviour of the C_l is identified for pitching at an increasing mean angle of attack. In Figure 2.20(a) the lowest mean angle is presented with $\alpha_0 = 11^\circ$. Here the surface gradually tapers towards the tip, showing a gentle transition in the spanwise C_l hysteresis and correlating to a gradual change in the separation position along the span of the wing. Another case of light stall is shown in Figure 2.20(b), this case is similar is setup to the previous, however the mean angle of attack is increased to 12°. With the 3° of twist at the root, it will be experiencing considerable separation. As with the static data, the C_l at the root begins to rapidly decrease, giving a much wider hysteresis loop. The result of increasing the amplitude of the pitching oscillation and reduced frequency, whilst keeping the mean angle at 12° is shown in Figure 2.21(a). The combination of the increased reduced frequency and amplitude furthers the loss of lift at the root, which continues to be the defining feature. The final C_l case is displayed in Figure 2.21(b) which is the output for the motion $\alpha = 14^\circ \pm 4^\circ \sin(0.10S)$. With the root twist, the geometrical angle of attack is 21° which allows deep stall to occur. The flow at the tip remains nominally attached as a result of the tip vortex.

The moment coefficients are displayed in a similar manner, using a surface formed by C_m, α and the spanwise position, these are presented in Figures 2.22(a) to 2.23(b). As with the spanwise lift distribution, the sectional moment coefficient on the tip cap is not sought after. Figure 2.22(a) gives the spanwise moment distribution up to including the tip cap, whereas the rest of the figures do not. The pitching moment coefficient experiences oscillations which are not as evident in the lift coefficient plots. The exact

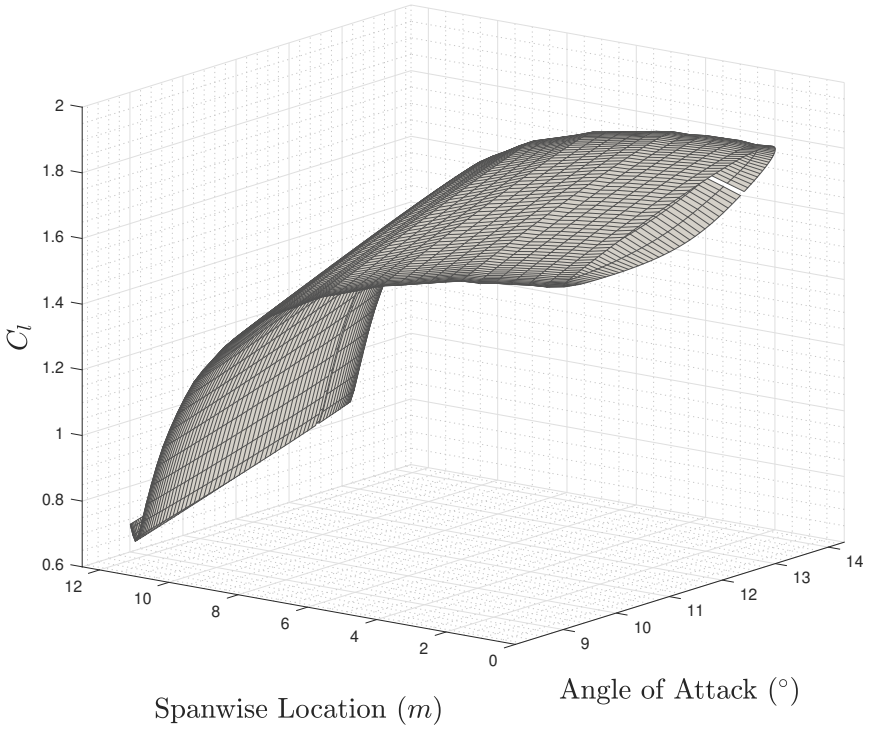

(a) $\alpha = 11° \pm 2° \sin(0.15S)$

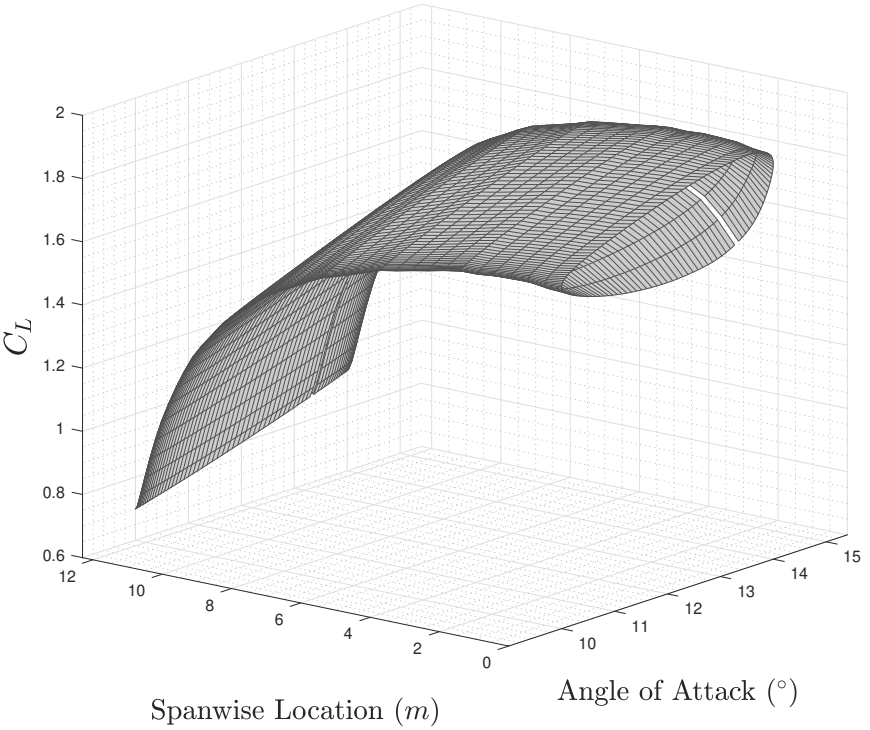

(b) $\alpha = 12° \pm 2° \sin(0.15S)$

Figure 2.20: UAV wing URANS C_l surface

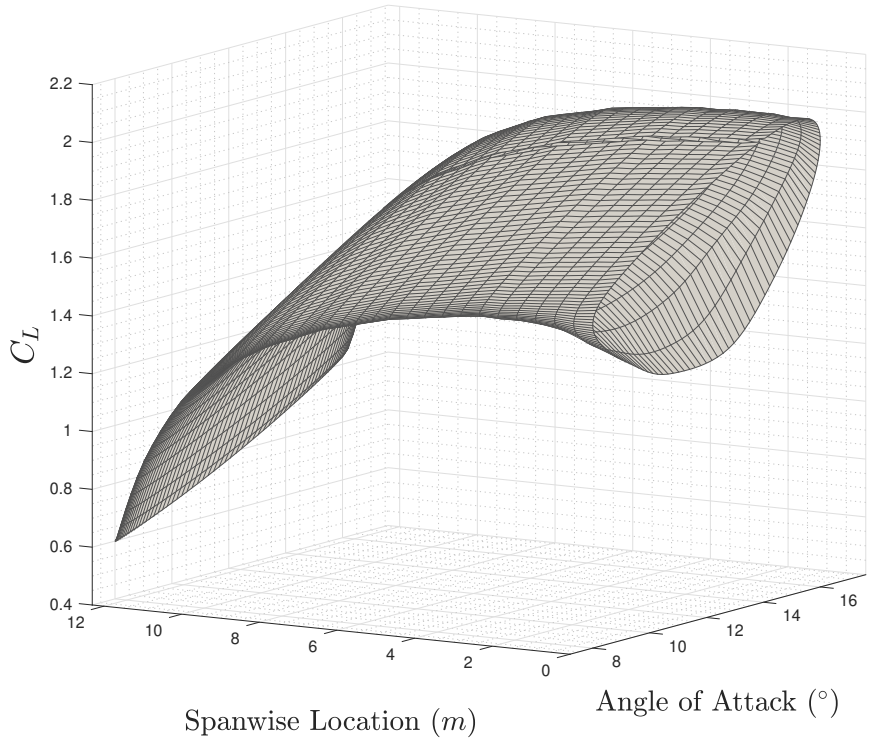

(a) $\alpha = 12° \pm 4° \sin(0.20S)$

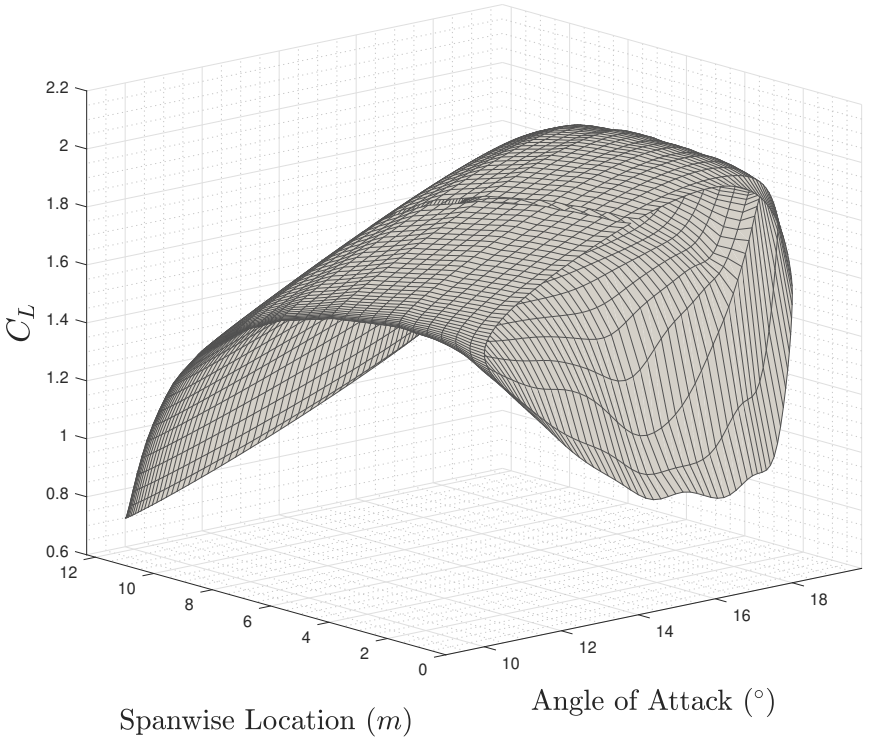

(b) $\alpha = 14° \pm 4° \sin(0.10S)$

Figure 2.21: UAV wing URANS C_l surface

reason for this is not entirely understood, however it is thought to be due to the pitching moment being more sensitive to transients in the flow from the pitching oscillations. It can also be observed that the relationship between α and C_m in the experimental data produced by Piziali [12] also shows a nosier relationship compared to that of α and C_l.. Two main features are noticed in the sectional moment coefficient. Firstly in all cases there is an increase in the C_m close to the tip, whereas the sections close to the root stay centered at values that were found for the two-dimensional aerofoil, see Figure 2.7(b). This infers that the sections close to the root are behaving in a similar manner to the constituting aerofoil section. As the angle of attack increases, the aforementioned severe separation close to the root has a large impact on the local C_m. It can be seen that peak root moment coefficient builds, reaching a value of -0.039 in Figure 2.23(a). It then collapses when undergoing the pitching motion $\alpha = 14^\circ \pm 4^\circ \sin(0.20S)$, shown in Figure 2.23(b). The C_m for the outboard sections remain more predictable, as deviations from the static values.

2.3.5 Stall Cells

Stall cells are three-dimensional cellular structures that can form on the suction side of a wing that experiences flow separation [88]. Stall cells can manifest themselves as three-dimensional separation patterns. Unlike a truly two-dimensional case, where flow is restricted to separate or attach at a single chordwise point. Three-dimensional separation and attachment has more complex mechanisms, these can be visualized by the skin friction vectors.

Whilst skin friction patterns are useful in describing the three-dimensional separation mechanism, it does not determine the whole separation mechanism. In order to do that one would need to look at the flow away from the surface as well. However for the model to be developed, the only requirement is to be able to identify the occurrence of three-dimensional flow separation and not a complete understanding of the flow structure.

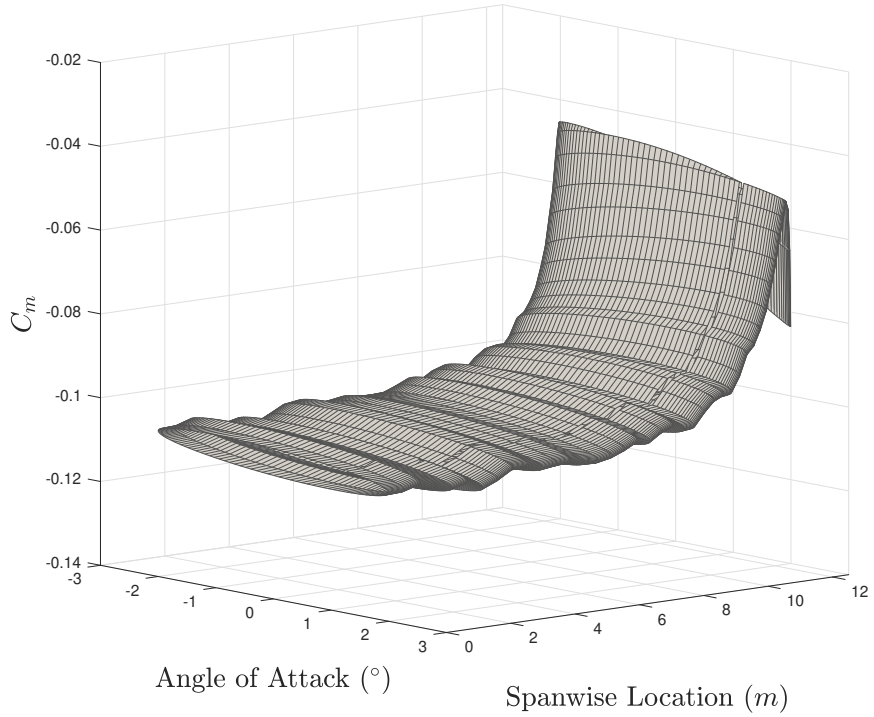

(a) $\alpha = 0° \pm 2° \sin(0.10S)$

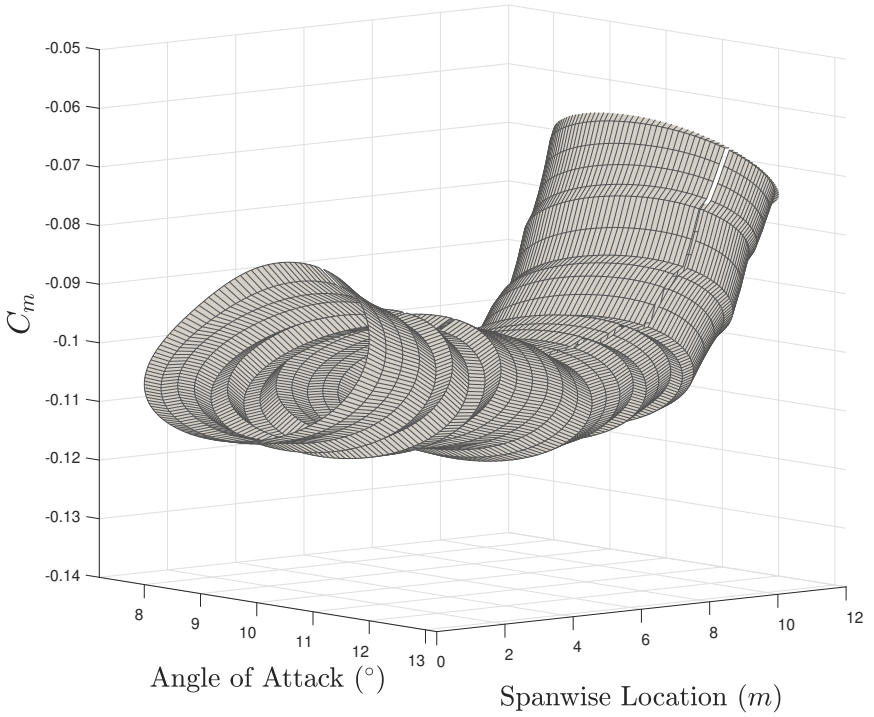

(b) $\alpha = 10° \pm 2° \sin(0.20S)$

Figure 2.22: UAV wing URANS C_m surface

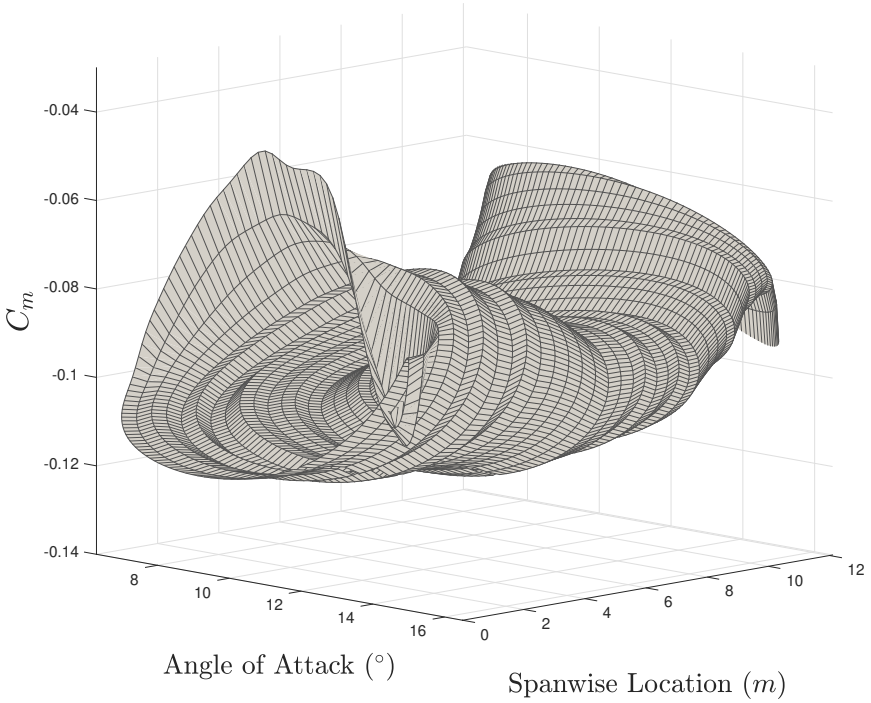

(a) $\alpha = 11° \pm 4° \sin(0.15S)$

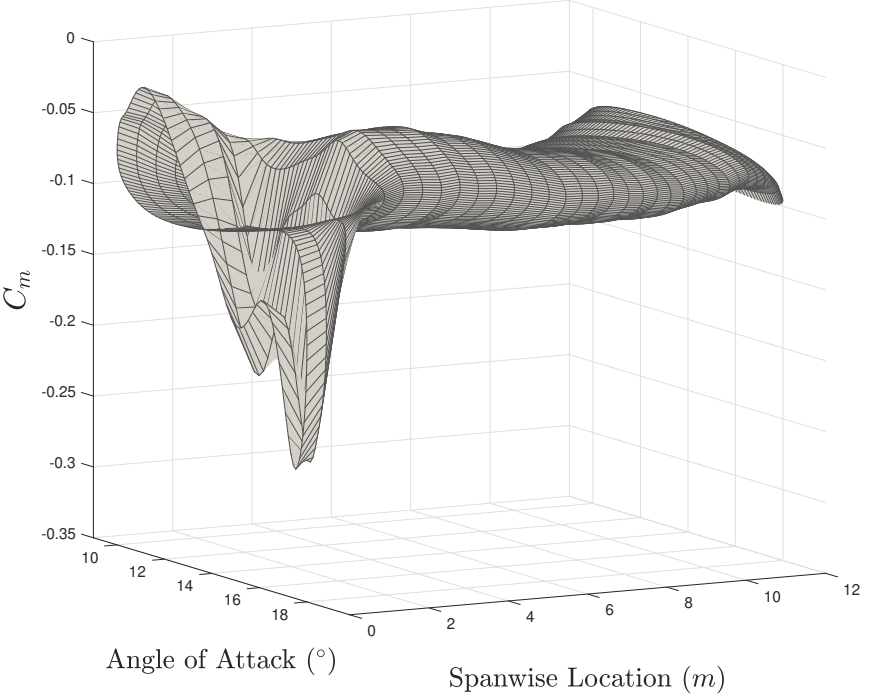

(b) $\alpha = 14° \pm 4° \sin(0.20S)$

Figure 2.23: UAV wing URANS C_m surface

A stall cell forms on a wing composed of NACA LRN 1015 sections at a static geometrical angle of attack, $\alpha = 17°$. This is shown in Figure 2.24(a) using skin friction streamlines, where the skin friction streamlines are calculated using, C_{fx}, C_{fy} and C_{fz}, which are the x, y and z components of the skin friction coefficient. The surface of the wing is also contoured with the magnitude of the skin friction coefficients, C_{fxyz}. The body shown in Figure 2.24(a) is a half wing model, with the centreline on the left hand side. It is clear from the surface streamlines that the flow is behaving in a more complex, three-dimensional way in the region of the centerline. Further towards the tip there is a distinct flow separation line, where the flow is behaving in a more orderly, two-dimensional manner. This is similar to the observations made by Winkleman and Barlow [89]. It was observed that flow separation was more severe close to the centerline and as a result, the flow was highly three-dimensional. It was also noticed that flow near the centerline suffered leading edge separation which rapidly moved closer to the trailing edge when traversing towards the tip. Close to the centerline, the leading edge separation caused a large loss of lift, this is similar to the CFD result shown in Figure 2.24(b). There is an abrupt reduction in the C_l near the symmetry plane that recovers after the flow separation becomes less severe. The separation line is plotted below the C_l plot on the half wing model which has been processed to better distinguish the separated regions. It can be seen that a separation line, where the skin friction streamlines are parallel to the chord, forms at a spanwise location of approximately 2.5 m, and with this a more typical C_l distribution is found.

Multiple stall cells may form along the span, generally increasing with the aspect ratio, Weihs and Katz [88] giving number of stall cells, $n_{sc} = AR/2.28$ based on the work of Winkleman and Barlow [89]. Note that for non-integer values of n_{sc} the value is simply rounded to the nearest integer. Therefore for the half wing UAV case shown in Figure 2.24, 2.5 stall cells would be expected. However the UAV has a 3° washout and the aforementioned relationship is for an untwisted wing, which could be the reason behind a single central cell where the total angle of attack is greatest.

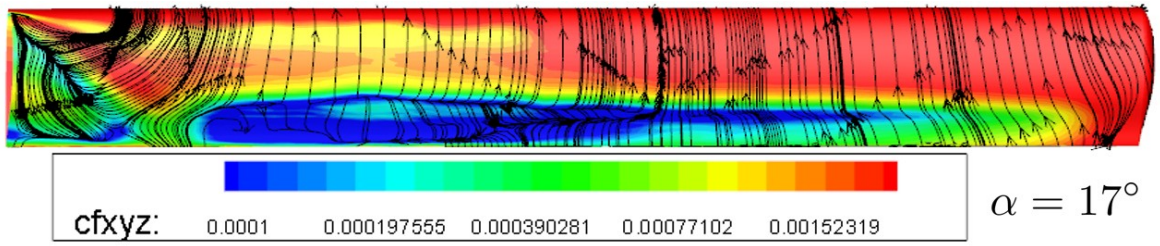

(a) Skin friction, C_{fxyz} contours and streamlines

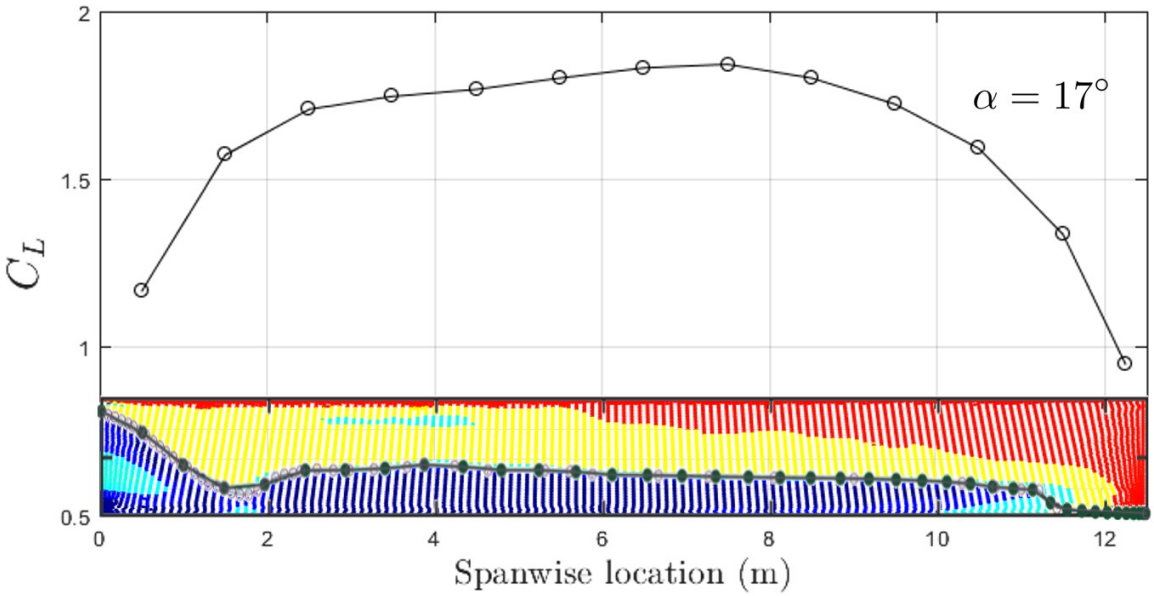

(b) Stall cell C_l distribution with spanwise separation line

Figure 2.24: UAV wing stall cell formation

CHAPTER 3

TWO-DIMENSIONAL SEPARATED FLOW MODELS

The new model developed in this research combines a two-dimensional dynamic stall model with a three-dimensional potential flow model. This chapter introduces some of the popular two-dimensional dynamic stall models. Dynamic stall models are able to describe the unsteady forces and moments when an aerofoil is undergoing some arbitrary motion. The Beddoes-Leishman model is then further explored and explained. An example of building the Beddoes-Leishman model using CFD data for a NACA LRN 1015 aerofoil section is given, the Beddoes-Leishman model is then evaluated against 2D CFD. The process is repeated using a NACA 0015 which uses experimental data [12]. The 3D model will be coupled in Chapter 5 with the potential flow models described in Chapter 4. The 3D model is then validated against experimental data for a straight wing constructed from the NACA 0015 section and CFD data for a NACA LRN 1015 sections. Understanding the accuracy of the 2D model is vital in understanding the performance achieved by the 3D model.

3.1 Overview of Dynamic Stall Models

The following section will give a brief overview of some of the popular 2D dynamic stall models. This is followed by an in-depth implementation of the Beddoes-Leishman model which has been used in the development of a new 3D dynamic stall model in this research.

3.1.1 Goman–Khrabrov Model

The Goman and Khrabrov model [67] (G-K) is a state-space model that uses an internal dynamic variable, f, the trailing edge separation position. A key advantage of the G-K model is that few semi-empirical coefficients are needed to model unsteady aerodynamic forces. The G-K model requires just two coefficients, τ_1 and τ_2. The coefficient τ_2 is a time lag that physically represents the time taken for a dynamic stall vortex to form and convect, whereas τ_1 is a relaxation time constant. In order to evaluate an unsteady response, the trailing edge separation parameter for static conditions, f_0, must be known. It should be noted that physically f_0 may well not represent the actual separation location since it is a function that is derived from the lift curve slope obtained using CFD. The dynamic trailing edge separation point is evaluated by solving the first order differential equation

$$\tau_1 \frac{df}{dt} + f = f_0(\alpha - \tau_2 \dot{\alpha}) \tag{3.1}$$

There has also been some success fitting the Goman-Khrabrov model using integrated C_L data from a full CFD aircraft model [90]. Once f has been found, it can then be used in the Kirchhoff flow model [15] which relates the separation position to lift or normal force coefficient. This is described in more detail for the Beddoes-Leishman model in Section 3.2.2.

3.1.2 Boeing-Vertol Model

The Boeing-Vertol, or Gamma function method, was introduced by Gross and Harris [91] in 1969 and modified by Gormont [68] in 1973. This is a pragmatic method, where 2D

dynamic stall is delayed with respect to the 2D static stall by an empirically derived angle of attack, $\Delta\alpha_D$. This allows the critical angle of attack for dynamic stall, α_{DS}, to be calculated by applying the delay angle, $\Delta\alpha_D$, to the static critical angle α_{SS} as follows: $\alpha_{DS} = \alpha_{SS} + \Delta\alpha_D$. The term "gamma-function", γ, is then essentially a semi-empirical term which is dependent on the aerofoil profile, along with the Reynolds and Mach numbers. The delay term is then calculated as a function of $\dot{\alpha}$ due to the fact that increasing the $\dot{\alpha}$ is known to delay flow separation, as previously discussed in Chapter 1. The delay term is then $\alpha_D = \gamma\sqrt{\dot{\alpha}c/\,U_\infty}$. The linear unsteady flow effects, which manifest themselves through hysteresis loops, must also be added to the delay. The final delayed angle can then be used to interpolate the aerofoil static data curves.

3.1.3 ONERA Model

The ONERA model describes 2D dynamic stall by representing the moment and lift coefficients of an aerofoil using non-linear differential equations. The model was introduced by Tran and Petot in 1981 [66] and was updated by Peters [92] and later by Petot [93]. The original version of the model is considered here. The model requires semi-empirical coefficients that delineate the motion of the aerofoil. Classically, in order to obtain the coefficients, an experiment is required in which the aerofoil under consideration is pitched at a range of frequencies around a number of mean angles [94]. The amplitude of the oscillation is generally very small, this idea comes from the fact that a nonlinear system will predominately behave linearly for small variation in the input parameters. This behaviour is not always the case, however for stall configurations the lift and moment will remain linear for changes in the angle of attack close to 0.5° [93]. Harmonic variations in α can be written as

$$\alpha = \alpha_m + \Re\left(\alpha_v e^{ikt}\right) \tag{3.2}$$

In general the resulting force response will be a summation of harmonic terms, however if the amplitude of the oscillation is small then the force response can frequently be

approximated using just a first order linear approximation as

$$F = \bar{F} + \Re\left(\tilde{F} e^{ikt}\right) \tag{3.3}$$

For this approximation to be accurate, the higher order terms must be small so that they may be neglected. This approximation holds especially well at lower angles of attack, but often less so at higher angles of attack.

At higher angles of attack, where nonlinearity becomes significant, the aerodynamic loads can be expressed using two components: a linear component which describes attached flow and a non-linear component which models the separated flow. The total aerodynamic load, F, can then be calculated as the sum of linear unsteady loads where stall is absent, F_1, and non-linear unsteady loads, F_2 [93].

$$F = F_1 + F_2 \tag{3.4}$$

$$\dot{F}_1 + \lambda F_1 = \lambda F_l + (\lambda s + \sigma)\dot{\alpha} + s\ddot{\alpha} \tag{3.5}$$

$$\ddot{F}_2 + a\dot{F}_2 + rF_2 = -(r\Delta F + e\dot{\alpha}) \tag{3.6}$$

where F_l is the linear extrapolation of the static curves and ΔF is the difference between the static aerodynamic coefficient which is extrapolated into the stall region and the measured coefficient at the angle of attack being examined. A representation of how ΔF is obtained in shown in Figure 3.1. The six coefficients for the mathematical model, λ, s, σ, a, r and e are functions of the angle of attack and the velocity of the free-stream flow [94].

3.2 Theory and Implementation of the Beddoes-Leishman Model

Initially the Goman-Khrabrov, ONERA and Beddoes-Leishman dynamic stall models were implemented and tested by the author [95]. It was found that the Beddoes-Leishman model performed best for the NACA 0012 testcase used. The Beddoes-Leishman (B-L) is

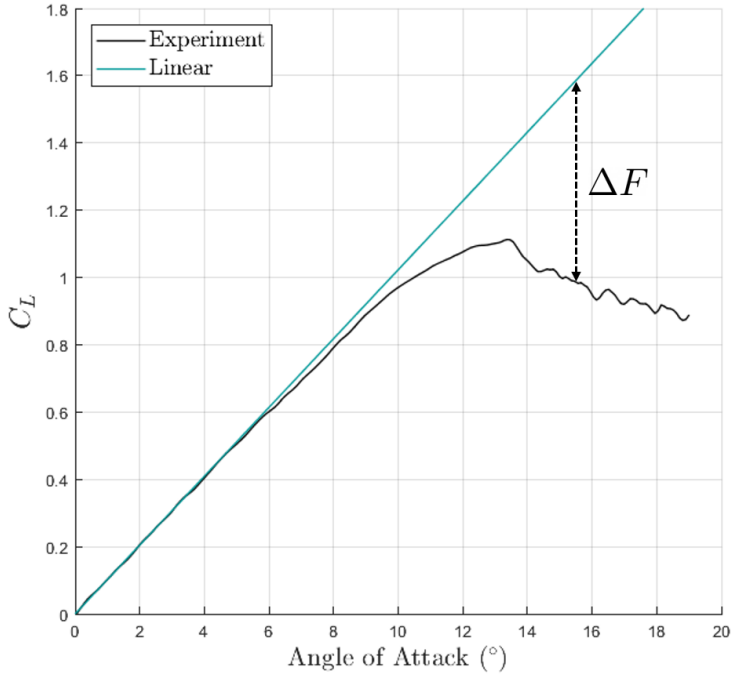

Figure 3.1: Representation of ΔF

also more frequently found in the literature. For this reason it was chosen to be used in the 3D development. It is important that the 2D dynamic stall model is able to reliably represent the CFD or experimental data because errors will be carried forward into the 3D model developed in this research. As the B-L model was selected for use in the 3D model developed in this thesis, more details will be given on the theory and implementation of the model and the method by which the semi-empirical coefficients are determined.

The breakdown of the B-L model into its key components is illustrated in the flow chart of Leishman [96] in Figure 3.2. It should be noted that in the present study the model is to be used as part of a 3D model for dynamic stall in cases which exhibit trailing edge stall, therefore leading edge stall will be avoided. The leading edge stall module of the Beddoes-Leishman is still included in the implementation. However it is modified so that it can be activated only on occasions when the trailing edge separation position reaches the leading edge. Researchers such as Hansen *et al*. [97] removed the leading edge stall

module altogether and therefore only wind turbine applications with thicker aerofoils were investigated.

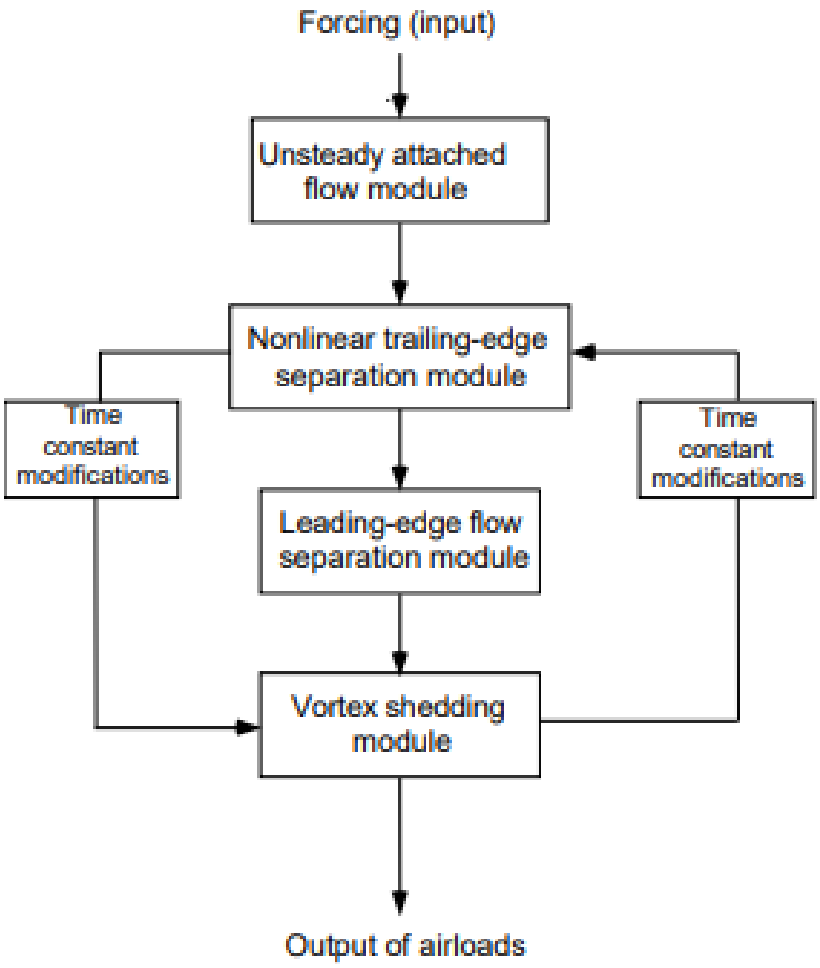

Figure 3.2: Beddoes-Leishman model structure [96]

3.2.1 Unsteady Attached Flow

An accurate model of the attached flow is created using indicial response functions. An indicial function gives the response to an impulse that is instantaneously applied and held constant thereafter, i.e. a step function. The B-L model splits the attached flow response into circulatory and non-circulatory, or impulsive, components. The impulsive component

is instantly present in response to the instantaneous aerofoil change in apparent angle of attack and then decays with time, whereas the circulatory component increases with time, eventually reaching the steady-state levels. The total attached flow response is calculated using indicial functions which are the responses to an instantaneous motion at time zero which remains thereafter. A series of these responses is summed together to represent an arbitrary motion. In this work this is achieved using a finite-difference solution to Duhamel's integral [98]. Importantly this enables an arbitrary angle of attack time history to be modelled. Within the B-L model, this is formulated using deficiency functions, the impulsive and circulatory functions.

3.2.1.1 Circulatory normal force

The circulatory normal force, $C_{N_n}^C$ can be given by [65]:

$$C_{N_n}^C = C_{N_\alpha}[\alpha_n + X_n + Y_n - \alpha_{0L}] = C_{N_\alpha}(\alpha_E - \alpha_{0L}) \tag{3.7}$$

where α_n and α_E are the instantaneous geometric and effective unsteady angles of attack respectively. The subscript n represents the current instance and C_{N_α} is the normal force curve slope. The unsteady wake effects are implemented through the deficiency functions X_n and Y_n. When the change in angle of attack is very small, the unsteady wake effects become negligible and the steady-state solution is reached. The deficiency functions are given as:

$$X_n = X_{n-1}\exp\left(-b_1\beta^2\Delta S\right) + A_1\Delta\alpha_n\exp\left(-b_1\beta^2\Delta S/2\right) \tag{3.8}$$

$$Y_n = Y_{n-1}\exp\left(-b_2\beta^2\Delta S\right) + A_2\Delta\alpha_n\exp\left(-b_2\beta^2\Delta S/2\right) \tag{3.9}$$

where ΔS is the change in non-dimensional time in semi-chords, $\delta\alpha_n$ is the change in angle of attack, β is the Prandtl-Glauert compressibility factor, $A_1 = 0.3$, $A_2 = 0.7$, $b_1 = 0.14$ and $b_2 = 0.53$ which are exponents of the indicial response function. These parameters were obtained in earlier work by Beddoes on the computation of unsteady

aerofoil lift [99]. The parameters were found by fitting the inidical model to unsteady experimental aeorfoil data.

3.2.1.2 Impulsive normal force

The impulsive normal force coefficient, $C^I_{N_n}$, is given by [65]:

$$C^I_{N_n} = \frac{4K_\alpha T_I}{M}\left(\frac{\Delta\alpha_n}{\Delta t} - D_n\right) \tag{3.10}$$

where the deficiency function, D_n, for the impulsive response is given as:

$$D_n = D_{n-1}\exp\left(\frac{-\Delta t}{K_\alpha T_I}\right) + \left(\frac{\Delta\alpha_n - \Delta\alpha_{n-1}}{\Delta t}\right)\exp\left(\frac{-\Delta t}{2K_\alpha T_I}\right) \tag{3.11}$$

Here, T_I is an impulsive time constant that governs the decay of the forces as a result of propagating pressure disturbances. It is given by $T_I = c/a$. K_α is often taken to be a constant of value 0.75 [100] [101]. However more accurately it can be represented as a function of the Mach number [65] where as $M \to 0$, $K_\alpha \to 0.75$.

$$K_\alpha = \frac{0.75}{(1-M) + \pi\beta^2 M^2(A_1 b_1 + A_2 b_2)} \tag{3.12}$$

Once the circulatory and impulsive force coefficients have been obtained, the total normal force coefficient for attached flow, $C^P_{N_n}$, can be calculated by summing the two components.

$$C^p_{N_n} = C^C_{N_n} + C^I_{N_n} \tag{3.13}$$

Only the normal or lift force coefficient is calculated for the attached flow conditions.

3.2.1.3 Moment

The B-L model does not need to model the attached moment as it does not have a role in the calculation of the lagged separation position as this is derived from the either the lift or normal force. The nonlinear moment is calculated after the lagged separation position is known. The attached flow component of the attached moment coefficient can be inferred from the effective angle of attack, α_E, shown in Equation (3.7).

3.2.2 Trailing Edge separation

The nonlinear responses of trailing edge separation are included through the implementation of Kirchhoff flow [15],

$$C_{N_s} = C_{N_\alpha}\left(\frac{1+\sqrt{f}}{2}\right)^2(\alpha - \alpha_{0L}) \tag{3.14}$$

where C_{N_s} is the static normal coefficient response and α_{0L} is the zero lift angle of attack. The overarching idea of the trailing edge separation subsystem is to place two lags on the separation location in order to represent the unsteady pressure and boundary layer effects. Equation (3.14) is generally represented by a two piece exponential curve fit [65] [102] with a breakpoint at $f = 0.7$ [46][102]. This is commonly chosen due to the fact $f \approx 0.7$ corresponds to the critical angle of attack for many aerofoils [65]. However it's not unusual for the separation position at the stall angle to be moved close to the leading edge [103]. The two piece fit used here is given by

$$f = \begin{cases} 1 - 0.3\exp((\alpha - \alpha_1)/S_1), & \text{if } \alpha \leq \alpha_1, \\ 0.04 + 0.66\exp((\alpha_1 - \alpha)/S_2), & \text{if } \alpha > \alpha_1. \end{cases} \tag{3.15}$$

where α_1 in this equation is the angle of attack at which $f = 0.7$. S_1 and S_2 are parameters from the fit which define the static stall behaviour. The pressure lag associated with the unsteady attached normal coefficient $C^p_{N_n}$ is calculated by once again employing a deficiency function.

$$C'_{N_n} = C^P_{N_n} - D_{P_n} \tag{3.16}$$

where C'_{N_n} is the pressure lagged normal force coefficient and the deficiency function, D_{P_n}, is given as follows:

$$D_{p_n} = D_{p_{n-1}} \exp\left(\frac{\Delta S}{T_p}\right) + \left(C^p_{N_n} - C^p_{N_{n-1}}\right) \exp\left(\frac{\Delta S}{2T_p}\right) \tag{3.17}$$

This allows for a delay in the critical angle being reached compared to the static aerofoil response, given a positive pitch rate. Equation (3.17) introduces the first unsteady semi-empirical coefficient, T_p which is Mach number dependent but is also largely profile independent [65]. In order to transfer this into a lag on the separation position, a delayed angle of attack can be calculated as follows:

$$\alpha_{f'_n} = \frac{C'_{N_n}}{C_{N_\alpha}} \tag{3.18}$$

Equation (3.15) can be employed with the lagged angle of attack $\alpha_{f'_n}$ to achieve the lagged separation position f'_n. After this, an additional first order lag is placed on f' culminating in a final unsteady trailing edge separation parameter f''. The second lag is to account for effects arising from the unsteady boundary layer.

$$f''_n = f'_n - D_{f_n} \tag{3.19}$$

where the deficiency function D_{f_n} is calculated in a similar manner to D_{p_n}

$$D_{f_n} = D_{f_{n-1}} \exp\left(\frac{\Delta S}{T_f}\right) + \left(f'_n - f'_{n-1}\right) \exp\left(\frac{\Delta S}{2T_f}\right) \tag{3.20}$$

The time constant T_f, as T_p, is Mach number dependent. However it is much more sensitive to changes in aerofoil profile. The unsteady normal force accounting for the delay in the separation position can be evaluated using Kirchhoff flow with the addition of the impulsive component of the attached flow, see section 3.2.1.2.

$$C_{N_n}^f = C_{N_\alpha}\left(\frac{1+\sqrt{f_n''}}{2}\right)^2(\alpha_{E_n}-\alpha_{0L}) + C_{N_n}^I \tag{3.21}$$

Which can also be expressed as:

$$C_{N_n}^f = \left(\frac{1+\sqrt{f_n''}}{2}\right)^2 C_{N_n}^C + C_{N_n}^I \tag{3.22}$$

The moment calculations within the Beddoes-Leishman model rely on static moment data to be curve fitted, note that there is no specific attached flow model. In the original Beddoes-Leishman formulation, it is suggested the fit could take the form [65] :

$$\frac{C_M - C_{M_0}}{C_{N_s}} = K_0 + K_1(1-f) + K_2\sin(\pi f^m) \tag{3.23}$$

In Equation (3.23), K_0 represents the offset of the aerodynamic centre from the quarter chord, $K_0 = 0.25 - x_{ac}$. K_1 represents the effect of the separated flow region on the centre of pressure. K_2 determines the moment stall behaviour. Finally, m is there to give more flexibility to the fitting process. Once K_0 has been evaluated from the static data, K_1 and K_2 can be found by solving the linear system of equations found in Equation (3.23).

The lagged separation position, f'', can be substituted in Equation (3.23) to find the circulatory contribution to the unsteady moment based on the separation position. Including the non-circulatory contribution, the final equation for the moment coefficient is:

$$C_M = C_{N_s}(K_0 + K_1(1-f'') + K_2\sin(\pi f''^m)) + C_{M_0} - \frac{\pi c\dot{\alpha}}{4U_\infty} \tag{3.24}$$

3.2.3 Leading Edge Separation and Vortex shedding module

The final time constants to be determined are those relevant to the build up and shedding of a dynamic stall vortex. The vortex lift coefficient, C_N^v, represents some excess circulation that builds up, and is only shed into the wake once the lagged normal coefficient,

C'_{N_n} exceeds an empirically derived value. This is typically most prominent for aerofoils that have a leading edge stall mechanism. The aerofoils considered in this research experience a trailing edge stall mechanism, however the vortex lift is still implemented. Typically C_{N1} is chosen to be close to the C_N obtained at the critical angle however for thicker aerofoils this is not valid. If the trailing edge stall position reaches the leading edge in this implementation, the vortex lift module will be activated.

Once this is exceeded the excess circulation is shed across the suction side of the aerofoil and is defined to convect at just under half the freestream velocity, here it is taken as $0.45U_\infty$ [104] [105]. The vortex lift, C_{v_n} can be calculated by finding the difference between the attached circulatory lift and the Kirchoff lift using the delayed separation position, i.e, substituting f'' into Equation (3.22). Therefore C_{v_n} can be evaluated as follows:

$$C^v_{N_n} = \begin{cases} C^v_{N_{n-1}} \exp\left(\frac{-\Delta S}{T_v}\right) + \left(C_{v_n} - C_{v_{n-1}}\right) \exp\left(\frac{-\Delta S}{2T_v}\right) & \text{if } 0 < \tau_{v_n} < T_{vl} \\ C^v_{N_{n-1}} \exp\left(\frac{-\Delta S}{T_v}\right) & \text{else} \end{cases} \tag{3.25}$$

where τ_{v_n} keeps track of the vortex location so vortex lift is only apparent when the DSV is over the aerofoil. Note that $\tau_{v_n} = 0$ represents the time of the vortex being released at the leading edge and $\tau_{v_n} = T_{vl}$ the time when the DSV reaches the trailing edge.
It is at this point that the total lift can be calculated by summing the lift coefficient (with the inclusion of separation) and the vortex lift.

$$C_N(t) = C^f_N(t) + C^v_N(t) \tag{3.26}$$

3.2.4 Beddoes-Leishman model adaptions

Over the years the Beddoes-Leishman model has undergone some adaptions. An example of which is the inclusion of a state space unsteady attached flow module [106]. This also features the inclusion of further impulsive terms that are not present in the original Beddoes-Leishman model paper [65]. Further to this modifications to the stall onset

criterion have been suggested by Sheng et al. [103] which aim to improve the prediction of stall-onset, particularly for cases at low Mach numbers. The Beddoes-Leishman model has also seen improvements to the reattachment phase of dynamic stall. This has been achieved through the modification of the dynamic stall lag parameters. Dimitriadis [21] summarised the modifications to the parameter T_f as follows:

$$T_f = \begin{cases} T_{f_0} & \text{if} \quad 0 \leq t - t_{v_0} \leq T_{v_1} \quad \text{and} \quad \bar{\alpha}\dot{\bar{\alpha}} \geq 0 \\ \frac{1}{3}T_{f_0} & \text{if} \quad T_{v_1} < t - t_{v_0} \leq 2T_{v_1} \quad \text{and} \quad \bar{\alpha}\dot{\bar{\alpha}} \geq 0 \\ \frac{1}{2}T_{f_0} & \text{if} \quad 0 \leq t - t_{v_0} \leq 2T_{v_1} \quad \text{and} \quad \bar{\alpha}\dot{\bar{\alpha}} < 0 \\ 4T_{f_0} & \text{if} \quad t - t_{v_0} > 2T_{v_p} \end{cases} \tag{3.27}$$

where T_{f_0} is the original value of T_f. These modifications to the original model are not included in the current work, and future work should be carried out to understand the impact of this.

3.3 Using CFD to Build and Evaluate the Beddoes-Leishman Model

3.3.1 Fitting CFD Static Parameters

Here the Beddoes-Leishman model is built using the two-dimensional CFD results for the NACA LRN 1015 described in Chapter 2. The first step in building the Beddoes-Leishman model was fitting the Kirchhoff flow model to the static data. The static data for the NACA LRN 1015 profile was first displayed in Figure 2.7 and will be the data source used for this initial fit. The Kirchhoff flow model determines a relationship between the trailing edge separation position, f, and the angle of attack in order to reproduce either the normal force coefficient, C_N, or lift force coefficient, C_L, through Equation (3.14) (as long as the chosen force coefficient is used to build the model). For the following fit c_l will be used which is a common approach [97]. The fit was determined by three semi-empirical constants (S_1, S_2 and α_1), along with lift-curve slope, $c_{l\alpha}$, and zero lift angle of attack, c_{l0}, which can be obtained from the static data. For the c_l the

semi-empirical constants are determined using a two-piece exponential fit, defined by parameters S_1 and S_2 and a break point which occurs at α_1. It was found that the most convenient way of fitting the aforementioned semi-empirical constants was to use an optimization routine. This allowed some flexibility in α_1 where traditionally this value has to be supplied based on some threshold [97]. A nonlinear least squares fit was used to determine the static semi-empirical parameters. The absolute difference between the Kirchhoff fit and the supplied static data was minimized, this gave an excellent fit, as shown in Figure 3.3(a). The static parameters needed for the Kirchhoff fit (S_1, S_2, α_1, c_{l0}, and $c_{l\alpha}$), are presented in Table 3.1.

The static moment coefficient was also fitted using the relationship defined in Equation (3.23) and the resulting fit is shown in Figure 3.3(b). Solving the linear set of equations needed to fit the data, with $m = 0.5$, this was done through trial and error. This could have been achieved using an optimisation, similar to what was carried out for the semi-empirical coefficients for the lift coefficient. However, for the single parameter, trial and error was deemed sufficient. The semi-empirical constants for the moment, K_0, K_1 and K_2 are found to be -0.0150, -0.0100 and 0.0542 respectively.

$c_{l_\alpha}(rad^{-1})$	$\alpha_{0L}(^\circ)$	$\alpha_1(^\circ)$	$S_1(rad)$	$S_2(rad)$
6.7089	−5.0482	13.086	0.0687	0.1043

Table 3.1: Static parameters for the Beddoes-Leishman model, fitted from the 2D NACA LRN 1015 data.

3.3.2 Fitting CFD Dynamic Parameters

In order to fit the dynamic, unsteady Beddoes-Leishman parameters (T_p, T_f, T_V, T_{vl} and C_{L1}), an optimisation routine is employed using a genetic algorithm. An example output of this is shown in Figures 3.4(a) to 3.4(d). The optimisation is given a set of training cases and minimizes the combined total difference for all the model runs and the training data. The genetic algorithm within the MATLAB global optimisation toolbox is used. Other MATLAB optimisation techniques were also tested, such as lsqnonlin and

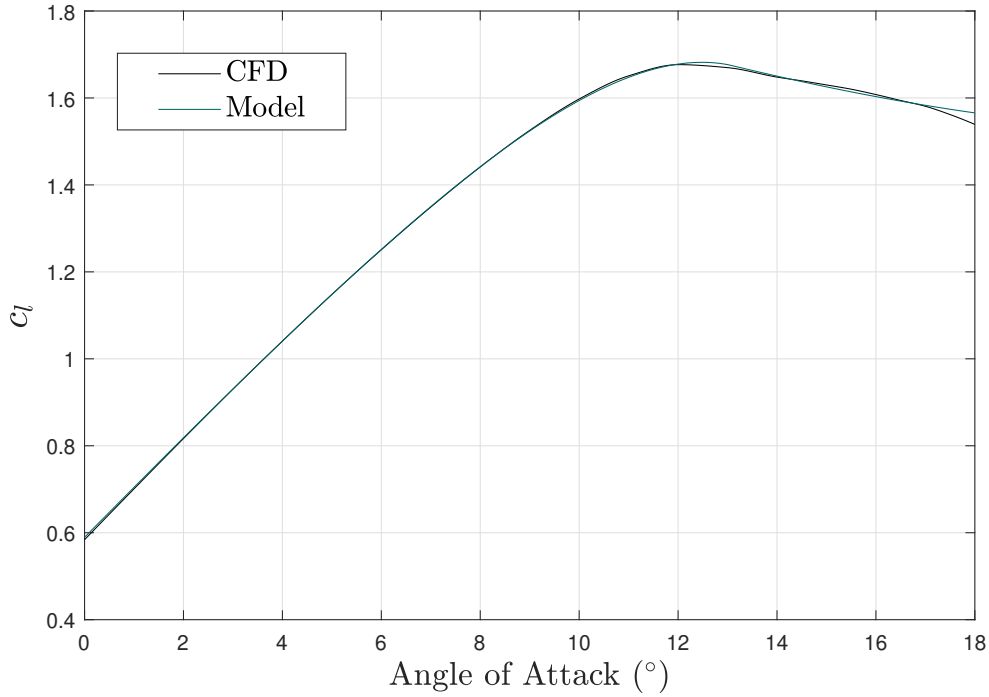

(a) Static c_l, Kirchhoff Model representation of the CFD for the NACA LRN 1015

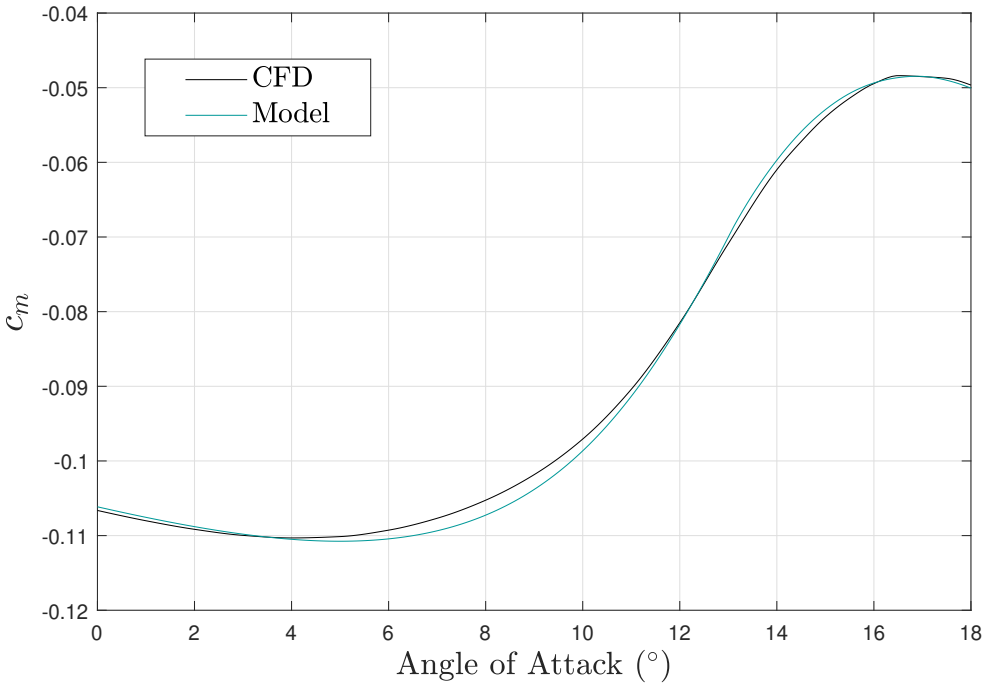

(b) Static c_m, Fitted Model representation of the CFD for the NACA LRN 1015

Figure 3.3: Kirchhoff 2D static fit for the NACA LRN 1015

fmincon. All aforementioned optmisation methods were able to give satisfactory fits. In order to obtain the time constants, T_p, T_f, T_V, T_{vl}, an initial guess of 0 was used which was also the lower bound for the time constants since it is not physical to have a negative lag. An upper bound also needs to be set, in this case all time constants have an upper bound of 30. This is likely high and could be lowered in future uses. The lower and upper bounds of C_{L1} were set to 0.5 and 2.5 respectively, with an initial guess of 1.5 used. The semi-empirical coefficients can then be found which best represent the cases supplied. For a qualitative example of the optimisation, Figure 3.4 shows this procedure applied to just a single case which demonstrates the excellent fit the routine can find. Obviously the optimisation routine needs to consider a large number of cases, Figure 3.4 simply gives a visual indication of the fit that can be achieved using this procedure.

The training cases should contain a range of mean angles of attack, variation of angles and reduced frequencies due to the fact these have been shown to be important for characterizing dynamic stall, which was discussed in Chapter 1.6; the full set of polynomial fits for the training data can be found in Appendix A. It appears useful to include a greater number of cases around the static stall angle of attack, this is because the model parameters are most sensitive to changes in the data in this region. When there is little separation it is obvious the defining Beddoes-Leishman parameters will have little effect on the output, with the inviscid 2D potential flow model corrected for $c_{l\alpha}$ and α_{0L} being prominent in the result. Also where there is severe separation, $f < 0.3$ for much of the cycle, the geometry of the nonlinear c_l hysteresis remains circular and relatively insensitive to the parameters, an example of this is in Figure 3.13(b). The key cases to determine the Beddoes-Leishman semi-empirical constants are cases which pass through the static stall angle and therefore should be abundant in the optimisation process. This also aids the ability to predict the angle of attack at which dynamic stall happens, this can be as important as calculating the magnitude of the forces and moments. There is a potential for future work to generate an algorithm that automates the selection of cases used for building the B-L model. The optimised semi-empirical coefficients for the

dynamic data is shown in Table 3.2.

T_p	T_f	T_V	T_{vl}	C_{L1}
1.8272	1.5423	4.5793	8.248	1.7742

Table 3.2: Dynamic parameters for the Beddoes-Leishman model, fitted from the 2D UAV data.

As previously noted, C_{L1} is not taken in the conventional manner for aerofoils with leading edge stall mechanisms. Instead it is used as a way to trigger the vortex lift module at a critical c_l when the trailing edge separation position reaches the leading edge. It was found that the vortex lift contribution was much smaller than the circulatory and impulsive contributions for the aerofoils and cases presented here.

3.3.3 Dynamic Results for NACA LRN 1015 using CFD data

3.3.3.1 Lift Coefficient

Here a sample of Beddoes-Leishman outputs are validated against two-dimensional URANS. The results are chosen to demonstrate the general effect the unsteady flow separation has on the c_l hysteresis loops. The first case looks at nominally attached flow, where the Beddoes-Leishman model relies strongly on the corrected attached flow module. The result is displayed in Figure 3.5(a), which shows a pitching motion defined by $\alpha = 3^\circ \pm 4^\circ \sin(0.10S)$ and can be seen to remain elliptical. The minimum value of the lagged separation position f'' is 0.94, confirming this case considers mostly attached flow.

The second case presented is for $\alpha = 7^\circ \pm 6^\circ \sin(0.15S)$ and the c_l hysteresis loop is shown in Figure 3.5(b). At the lower angles of attack in the cycle, the flow remains mostly attached. When the angle surpasses 8°, the lift hysteresis loop self intersects, which is caused by the increase in flow separation. The Beddoes-Leishman model is able to capture this phenomenon. However the loop intersection angle is slightly increased, but

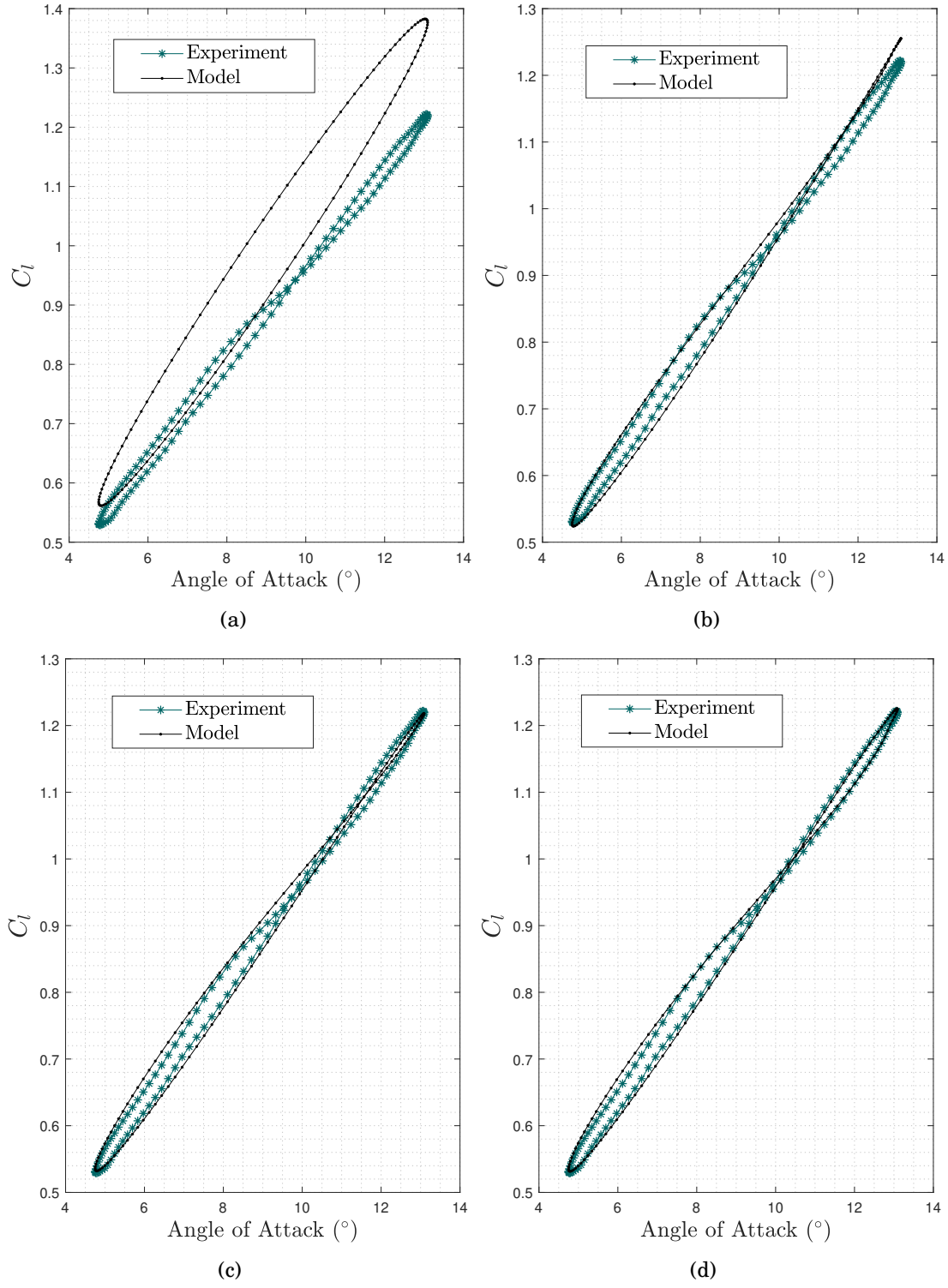

Figure 3.4: Developing stages of the optimisation for the unsteady B-L parameters

the peak c_l well matched.

Next is a pitching motion defined by $\alpha = 11^\circ \pm 6^\circ \sin(0.10S)$ in Figure 3.5(c). This was found to be difficult due to the fact it is a large amplitude case, centred close to the critical angle. Dynamic stall is delayed to approximately 14° and this is captured by the model. However the peak c_l is underestimated by the model but only by 2.2%. This also raises some potential changes that could be made to the optimisation routine. If desired a weighting could be placed on the upstroke where the flow separates since modelling reattachment with CFD is perhaps more challenging [107]. The case in Figure 3.5(c) shows the highest angles of attack ($\alpha > 15^\circ$) matching very well. This could perhaps skew a minimum in the cost function, where a solution matching the peak c_l may be preferred.

The last case presented shows the c_l hysteresis for $\alpha = 14^\circ \pm 4^\circ \sin(0.05S)$ where the post stall regime dominates, presented in 3.5(d). The model is able to reproduce the CFD well: the error in the maximum c_l is 1.3% and at the top of the stroke (maximum angle of attack), the error is 1.3%.

3.3.3.2 Moment Coefficient

The unsteady moment model within the Beddoes-Leishman formulation is less sophisticated than the lift modelling. The unsteady moment response is restricted to be a perturbation of the static moment data. Figure 3.6 displays the model moment prediction with CFD data. All cases exhibited similar behaviour where the model underestimated the maximum and overestimated the minimum c_m. The general trend of the c_m loops however were correct. Figures 3.6(a) and 3.6(b) show this behaviour, with the peak c_m underestimated by 7.35% and 28.3% respectively.

Figures 3.6(c) and 3.6(d) show that the model predicts an intersection in the moment response which was not apparent in the CFD, yet both capture the general shape of the response because the CFD is centered on the static data. The simpler moment model

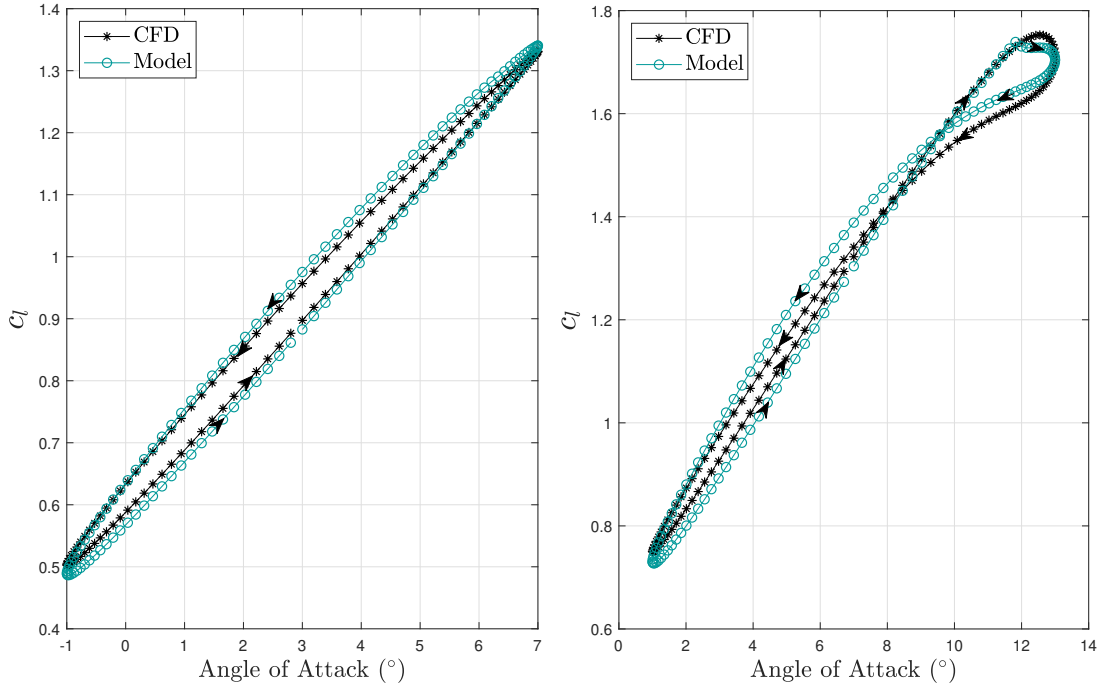

(a) $\alpha = 3° \pm 4° \sin(0.10S)$

(b) $\alpha = 7° \pm 6° \sin(0.15S)$

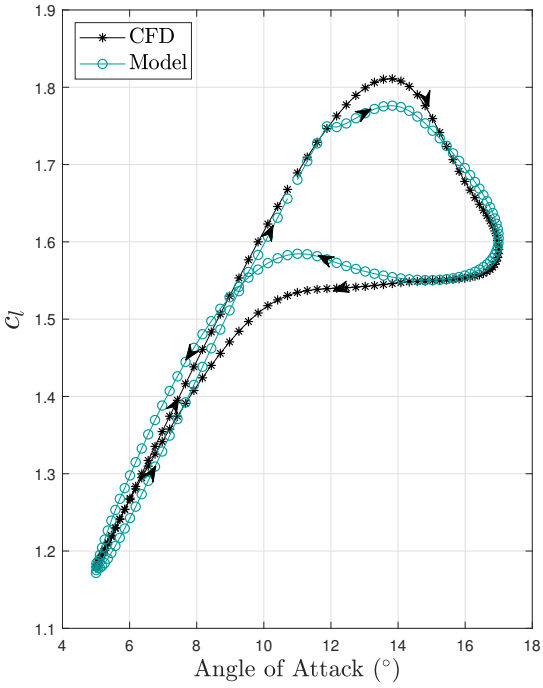

(c) $\alpha = 11° \pm 6° \sin(0.10S)$

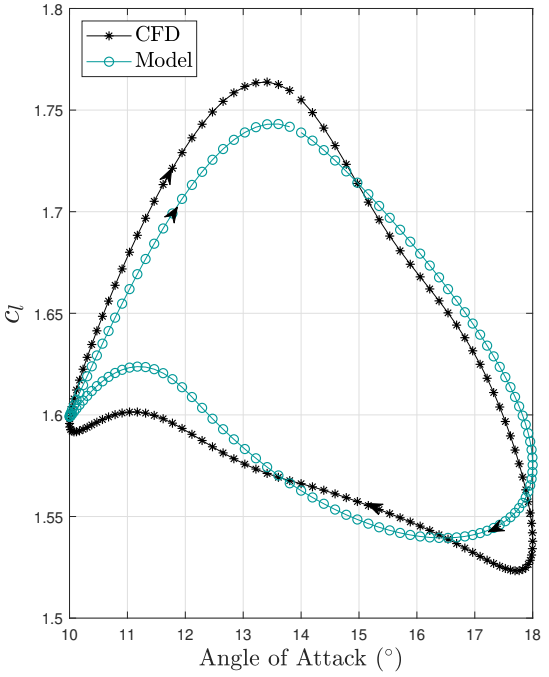

(d) $\alpha = 14° \pm 4° \sin(0.05S)$

Figure 3.5: Beddoes-Leishman and 2D dynamic CFD c_l results

is extended for the three-dimensional test cases, therefore the shortcomings in the 2D implementation will be carried forward.

3.4 Using Experimental Data to Build and Validate the Beddoes-Leishman Model

As introduced in Chapter 2, Piziali [12] conducted an experimental investigation of a NACA 0015 aerofoil section as well as a finite wing composed of the same section. The finite wing was unswept, untwisted and untapered, with an aspect ratio of 10. The primary operating condition for the test used a nominal Reynolds number of 2.0×10^6. This yeilded a Mach number of 0.278 and freestream velocity of 313 fps ($95.4\,\mathrm{m\,s^{-1}}$). The intention of the work was to build a comprehensive database of results where unsteady flow separation and dynamic stall are present. The two-dimensional experimental data has also been utilised in this study in order to build a Beddoes-Leishman dynamic stall model and assess the performance. The experimental data originates from four spanwise sections on the finite wing at locations y/b = 0.250, 0.475, 0.800, 0.900. The wing features a splitter plate with the intention of keeping the flow two-dimensional. In later chapters the three-dimensional counterpart (with the splitter removed) is used. This ensures that the 2D and 3D are obtained at the same flow conditions and therefore the data used are consistent with one another. Firstly the quasi-steady data is considered. The quasi-steady data was acquired by a pitch oscillation where the frequency is very low, at around one cycle per minute.

It should be noted that the experiments were performed with and without a boundary layer trip. The data set chosen for use in this work was without the boundary layer trip activated. The tripped data would have been preferred, however inconsistencies were found between the dynamic cases which appear to be caused by experimental errors.

Importantly, both differential and absolute pressure transducers were used on the wing

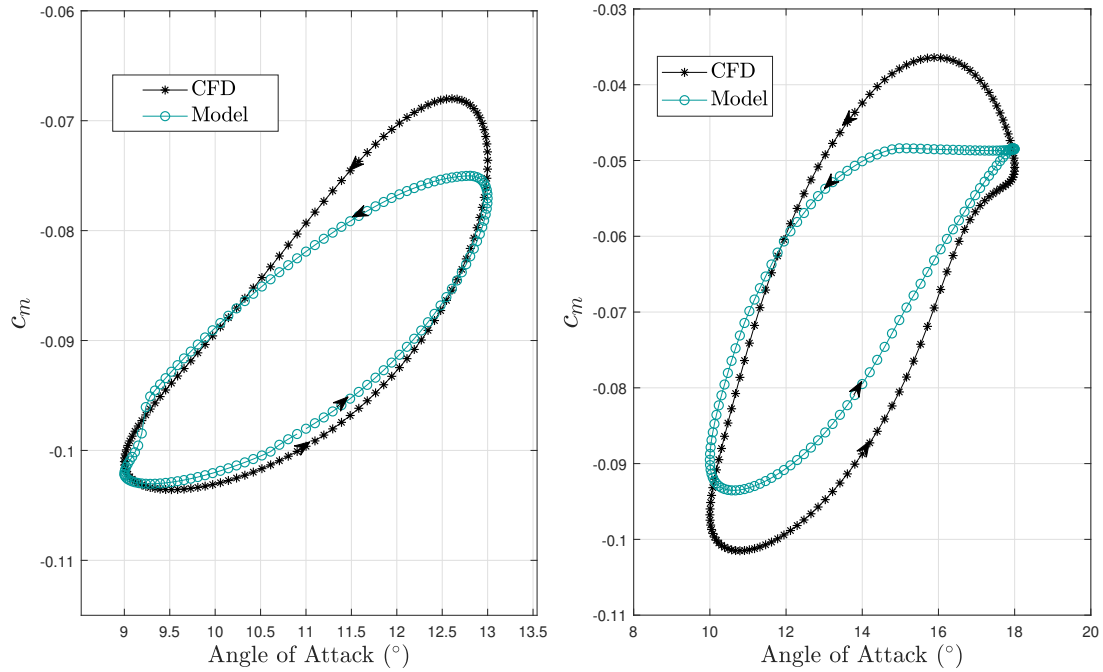

(a) $\alpha = 11° \pm 2° \sin(0.1S)$ (b) $\alpha = 14° \pm 4° \sin(0.15S)$

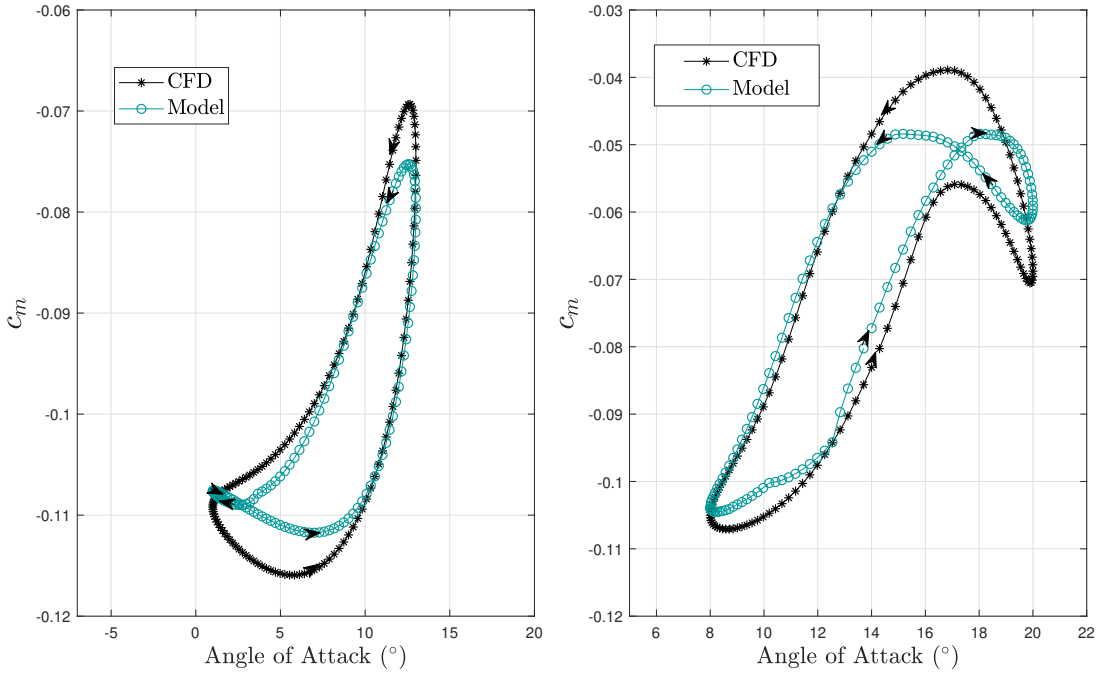

(c) $\alpha = 7° \pm 6° \sin(0.05S)$ (d) $\alpha = 11° \pm 6° \sin(0.05S)$

Figure 3.6: Beddoes-Leishman and 2D dynamic CFD c_m results

model and the use of differential pressure transducerswere identified to cause errors in both the lift and moment coefficients [12]. In the results presented, four spanwise locations are used, these are located at y/b = 0.250, 0.475, 0.800 and 0.900. It should be noted that only the transducers at y/b = 0.5 are absolute. The remaining three differential pressures neglect the chordwise pressure component and thus must be corrected. Piziali [12] used the quasi-steady c_l and c_m data from the absolute pressure transducer to derive a correction factor for the differential pressure transducers. This was achieved using the two-dimensional setup with the splitter plate. Piziali used a second order least squares fit for 5 measured errors [12] and this is reproduced in Figure 3.7. However with only one of the five measured points above the stall angle of attack, it is difficult to quantify the error when a significant amount of flow separation is present. It appears that the second order least squares fit suggested by Piziali [12] is not valid past the critical angle and thus is unsuitable to correct the c_l in this region. This is apparent from the one measured error at $\alpha = 16^\circ$ which is almost 2% less than the fit. In the present research a piecewise cubic hermite interpolating polynomial has been used for interpolation and an extrapolating of the differential pressure transducer errors.

The use of differential pressure transducers also caused errors with the moment coefficient. This had a rather large effect on the moment slope, $\frac{dC_m}{d\alpha}$, when including the chordwise pressure the moment slope reduced by approximately 40%, this is shown in Figure 3.8. Only very limited data is presented in the report published by Piziali [12] which can be used to correct the differential transducers for the c_m. For this reason it is not possible to obtain a smooth correction. Instead a curve is fitted through the raw data points before being applied to the moment data acquired from the differential pressure transducers.

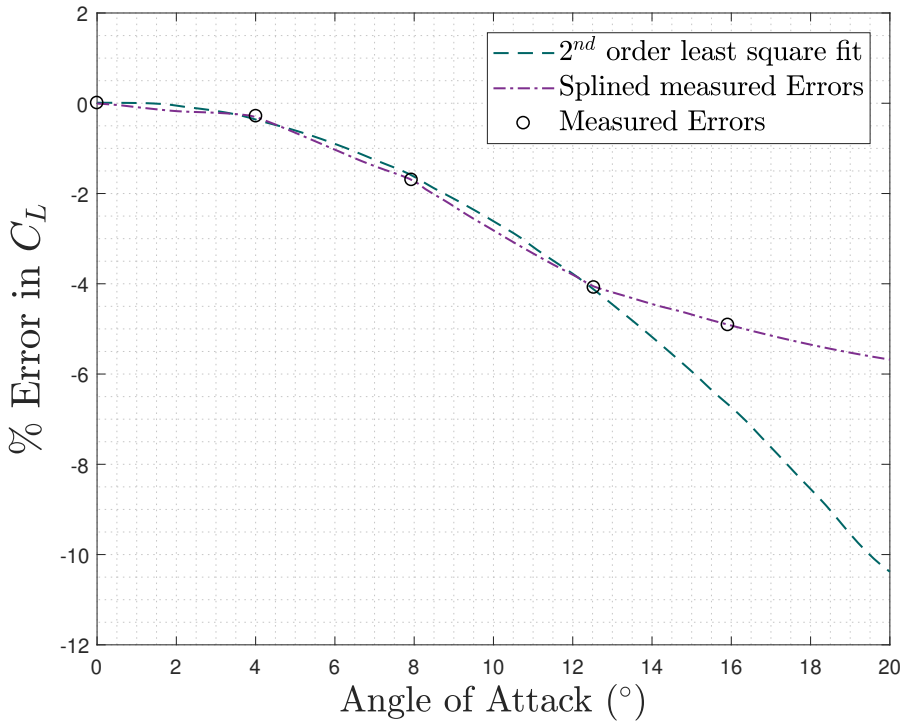

Figure 3.7: Error in differential pressure transducers for the lift coefficient [12]

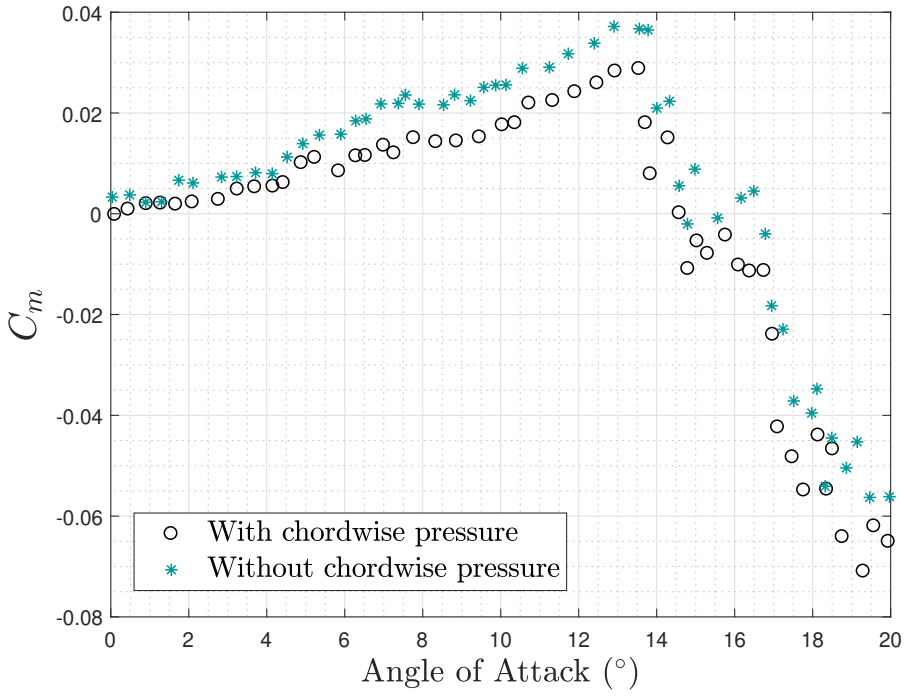

Figure 3.8: Error in differential pressure transducers for the moment coefficient (taken about the quarter-chord) [12]. Without chordwise pressure represents the differential pressure transducer. With chordwise pressure is the absolute transducer.

3.4.1 Static Experimental Results

In a similar manner to Section 3.3, the static data was first fitted by identifying the defining Kirchhoff parameters through the use of an optimisation routine. This achieves the Kirchhoff flow model for the averaged experimental data for the NACA 0015 and is presented in Figure 3.9(a), along with the parameters defining the fit in Table 3.3. As was the case with the CFD data, the Kirchhoff flow model is able to closely reproduce the averaged experimental data. The relationship between α and f, obtained from the fit, is also shown in Figure 3.10. This highlights the breakpoint in the two piece exponential fit, this occurs approximately where $\alpha = 13°$.

When fitting the moment, the polynomial fit described in Equation (3.23) was utilised. After solving the linear set of equations with $m = 0.8$, the semi-empirical constants for the moment, K_0, K_1 and K_2 are found to be 0.0200, -0.1276 and 0.0728 respectively. The result of the moment fit is displayed in Figure 3.9(b).

C_{l_α}	α_{0L}	α_{ss}	S_1	S_2
6.2735	$-0.3173°$	13.48°	0.1350	0.0311

Table 3.3: Static parameters for the Beddoes-Leishman model, fitted from the experimental static data [12].

3.4.2 Dynamic Experimental Results

In order to find the remaining parameters from the dynamic data, a genetic algorithm is once again used, where the cost function is the error between the experimental data and the model reconstruction, in which the remaining parameters T_p, T_f, T_V, T_{vl} and C_{L_1} are the design variables. The dynamic semi-empirical constants are displayed in Table 3.4. A sample output from a multiple case optimization is shown in Figure 3.11.

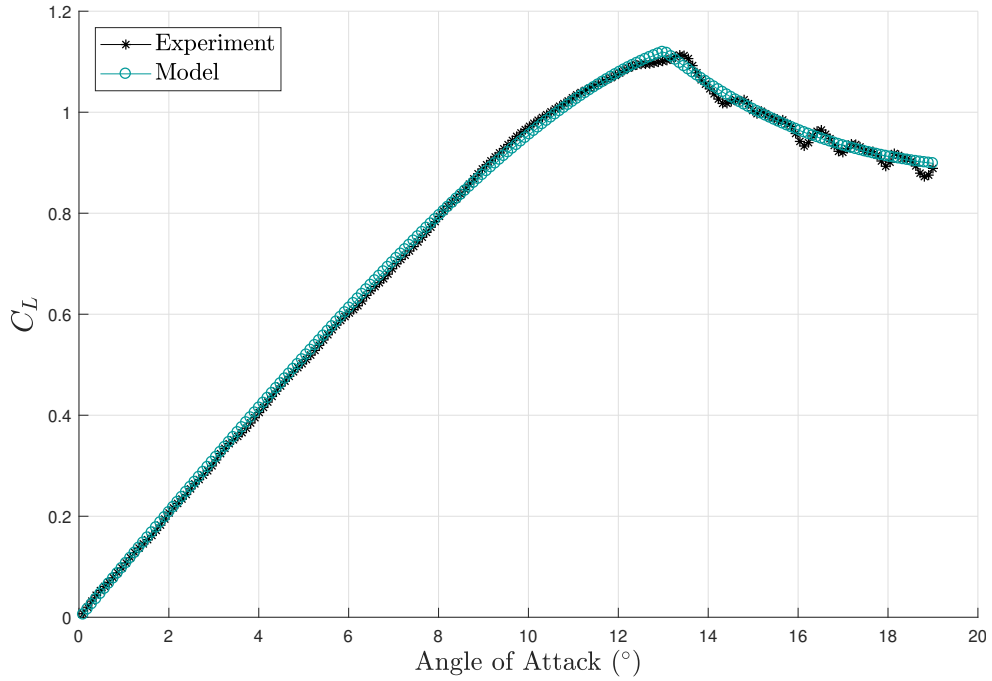

(a) Static Kirchhoff fit for the averaged experimental static c_l

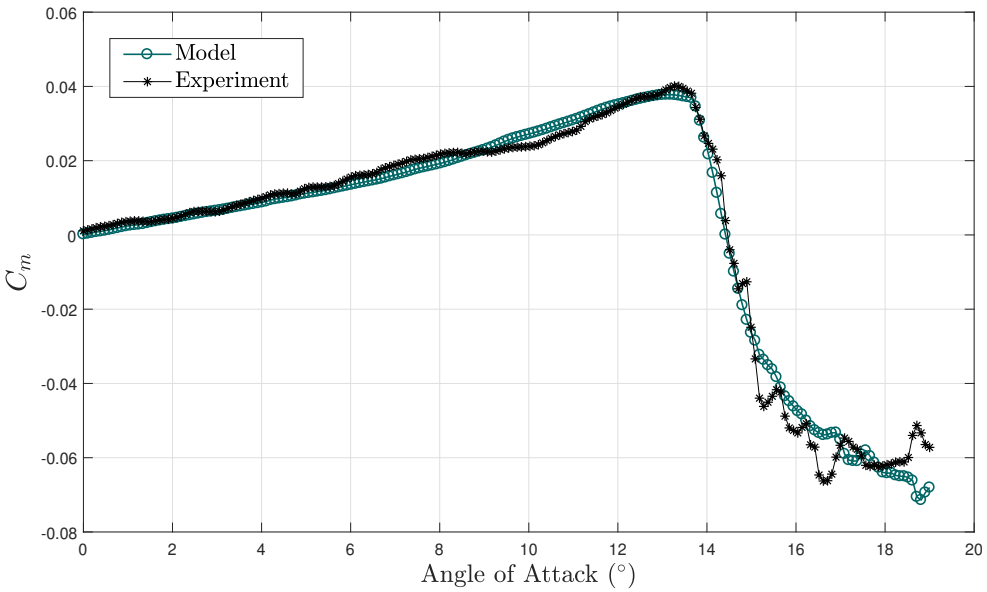

(b) Static Kirchhoff fit for the averaged experimental static c_m

Figure 3.9: Beddoes-Leishman and 2D Static Experimental Data

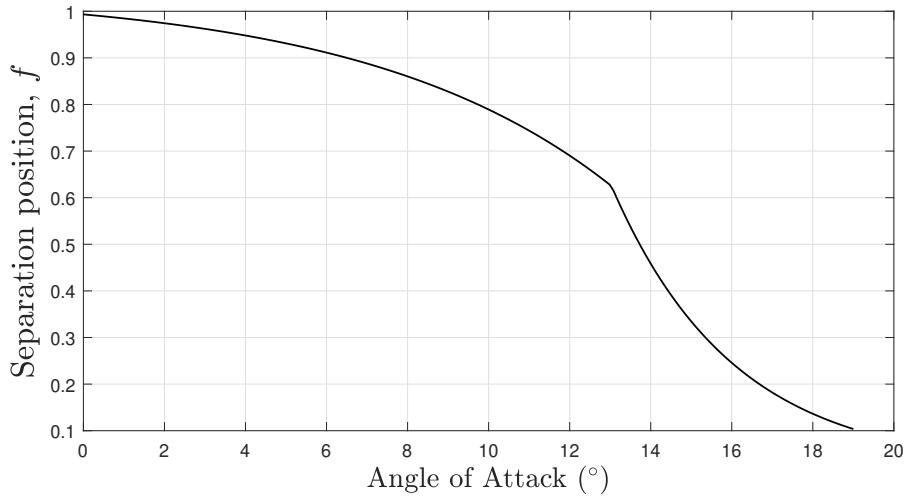

Figure 3.10: The static separation behaviour, experimental data from Piziali [12]

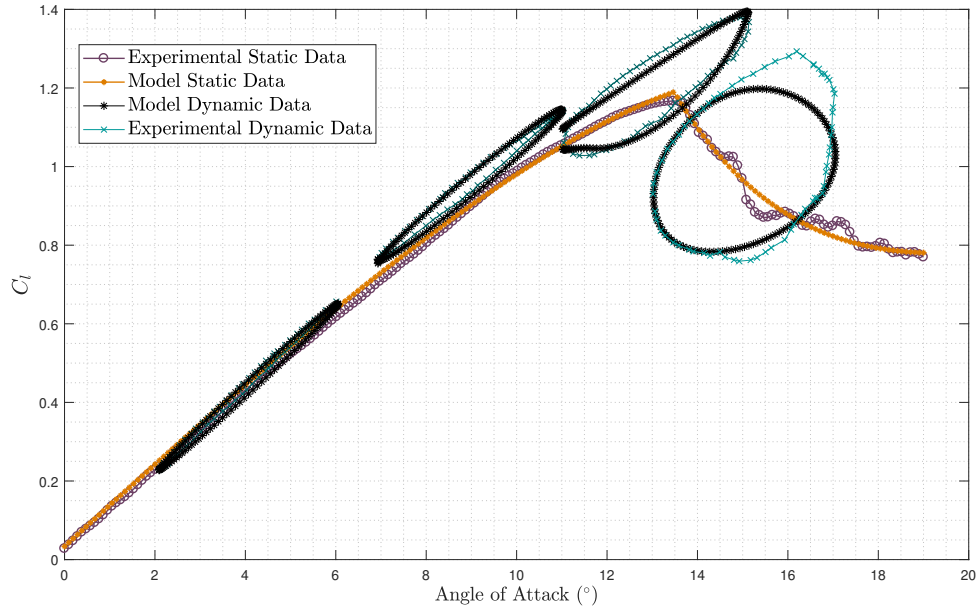

Figure 3.11: Multiple case response for the Beddoes-Leishman model fitted to experimental data

T_p	T_f	T_V	T_{vl}	C_{L1}
1.5024	9.7953	9.8952	13.4819	1.2964

Table 3.4: Dynamic parameters for the Beddoes-Leishman model, fitted from the experimental static data [12].

3.4.2.1 Lift Coefficient

A selection of results from the Beddoes-Leishman model are presented with the corresponding dynamic, two-dimensional NACA 0015 data from experiments conducted by Piziali [12]. As with the static data, the dynamic data was averaged across the spanwise sections. Once again, the cases presented will start with nominally attached flow. Figure 3.12(a) shows the c_l hysteresis loop for the pitching motion defined by $\alpha = 4.03^\circ \pm 4.04^\circ \sin(0.038S)$. A good match is obtained here, with peak error $< 1\%$. Due to the fact the attached model will be relatively unmodified by the separation module, this shows the lift curve slope and zero lift correction is performing as expected.

The next case presented in Figure 3.12(b) shows the signs of light stall, with the experimental results portraying the early stages of the aforementioned intersection of hysteresis loop, giving a figure-of-eight appearance. The model predicts the intersection, however it is found to happen at approximately $\alpha = 9^\circ$, whereas the experimental data finds it to occur at $\alpha = 10^\circ$. The peak c_l is also slightly underestimated at 1.06, compared to the experiment at 1.07. However the overall physics of the case are deemed to be well captured.

Figure 3.12(c) is for the pitching oscillation $\alpha = 8.92^\circ \pm 4.17^\circ \sin(0.095S)$, therefore the maximum angle of attack is approximately equal to the critical angle. This is also the case that was presented to show the evolution of the optimisation routine to fit the dynamic parameters in Figure 3.4. Unlike the Figure 3.4, multiple other cases are considered within the optimisation routine. Comparing this with the final model optimised with multiple training cases gives an idea of the compromise that optimising multiple cases has, i.e. the fit in Figure 3.12(c) is visably worse than in Figure 3.4. The final model still performs very well, capturing the hysteresis loop intersection with reasonable accuracy.

In the next case presented the static stall angle is exceeded. This case is for a pitching motion $\alpha = 10.95^\circ \pm 4.04^\circ \sin(0.038S)$ and is shown in Figure 3.12(d). In this case the

model is able to accurately predict the lift coefficient during the upstroke, however reattachment on the downstroke is found to happen sooner than in the experiment. This is nevertheless still a satisfactory result from the optimised Beddoes-Leishman model, with a peak error of less than 5%.

Increasing the mean angle, resulting in a pitching motion $\alpha = 10.94^\circ \pm 4.18^\circ \sin(0.095S)$, induces much more flow separation. This is displayed in Figure 3.13(a). Again, the upstroke is matched very well, with the peak c_l fractionally underestimated. As for the flow reattachment, the same applies as in the previous case with the model predicting earlier flow reattachment than the experimental data. The reattachment could perhaps be improved by modifying the Beddoes-Leishman time delay parameters as mentioned in Subsection 3.2.4.

The case $\alpha = 13.01^\circ \pm 1.99^\circ \sin(0.038S)$, proves to be one of the most difficult cases to model. This is likely due to the mean angle being very close to the critical angle, with only a relatively small deviation in angle of attack. The results shown in 3.13(b) are determined from the same model optimised over multiple cases, however little improvement was achieved if the optimisation routine was tasked to generate semi-empirical parameters for this case alone. The model still is capable of predicting the peak lift very well, however on this occasion it is the upstroke where the model performs most poorly. The largest error is at the bottom of the stroke, with an error of 4.2%.

The final case presented represents the deep stall regime, with the pitching motion $\alpha = 15.05^\circ \pm 2.03^\circ \sin(0.095S)$. The model is unable to reproduce the peak lift in this case, underpreditcing it by 6.8%. It is worth noting that if the two-dimensional potential flow model is run in isolation, i.e. the flow is assumed fully attached, the peak c_l is 1.89 in this case, which is a 43% overestimation. This puts into context somewhat performance of the B-L model and the impact modelling the unsteady flow separation has on the results.

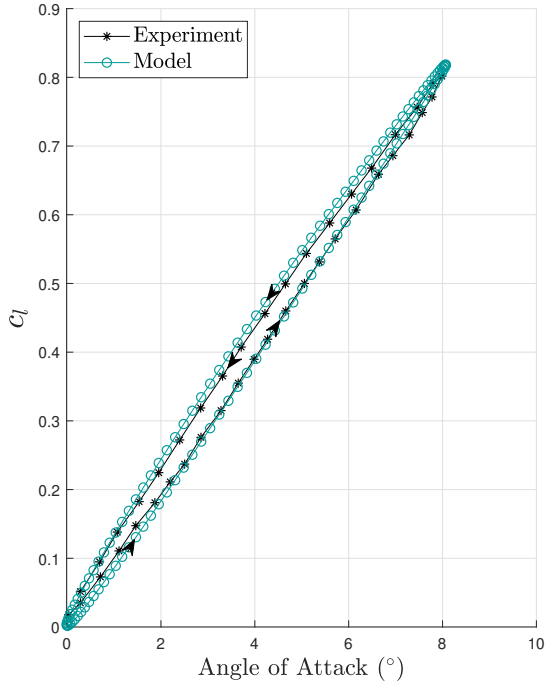

(a) $\alpha = 4.03° \pm 4.04° \sin(0.038S)$

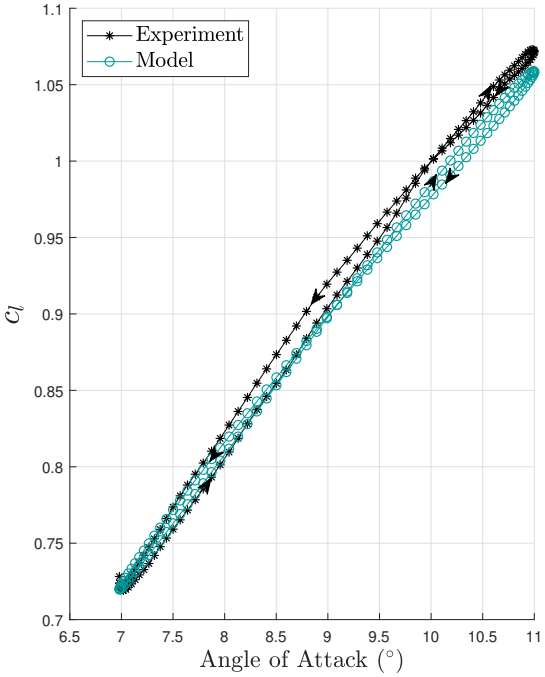

(b) $\alpha = 8.99° \pm 2.01° \sin(0.038S)$

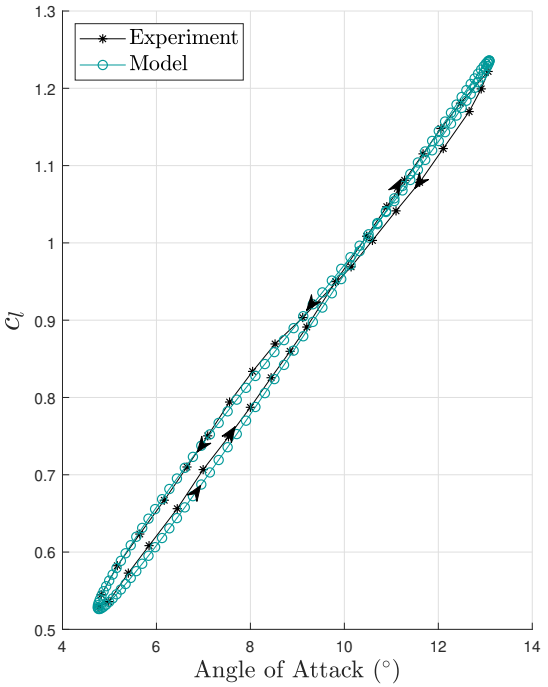

(c) $\alpha = 8.92° \pm 4.17° \sin(0.095S)$

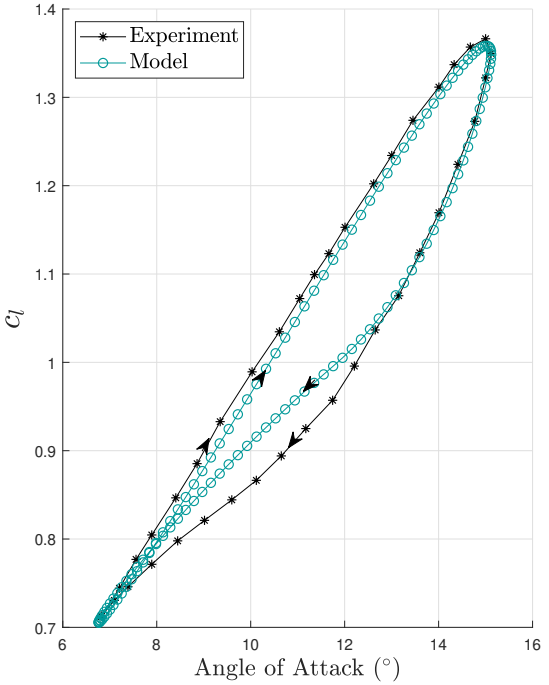

(d) $\alpha = 10.95° \pm 4.04° \sin(0.038S)$

Figure 3.12: Beddoes-Leishman and 2D experimental results

3.4.2.2 Moment Coefficient

The moment model is compared to the experimental c_m data in Figures 3.14(a) to 3.14(d). It was found that the model gave better predictions for the experimental NACA 0015 data compared to the CFD data for the NACA LRN 1015 in terms of capturing intersections (presented previously in Figures 3.6(a) to 3.6(d). The response to the pitching motion $\alpha = 7^\circ \pm 6^\circ \sin(0.05S)$ is shown Figure 3.14(a). The overall behaviour, including the maximum and minimum c_m is well modelled. At higher angles of attack, the moment hysteresis loop forms an intersection. This is particularly well predicted for the motion $\alpha = 11^\circ \pm 6^\circ \sin(0.05S)$ shown in Figure 3.14(c). However close to the top of the stoke the experimental data shows a sharp decrease in moment that the model cannot predict. A similar event happens for the motion $\alpha = 14^\circ \pm 4^\circ \sin(0.15S)$. The moment in this case is very well modelled when the aerofoil is pitching up, the largest errors were found on the down stroke. This large drop in pitching moment is likely due to a dynamic stall vortex being present on the aft section of the aerofoil. Improved modelling of the vortex would likely give a better prediction of the moment in this region.

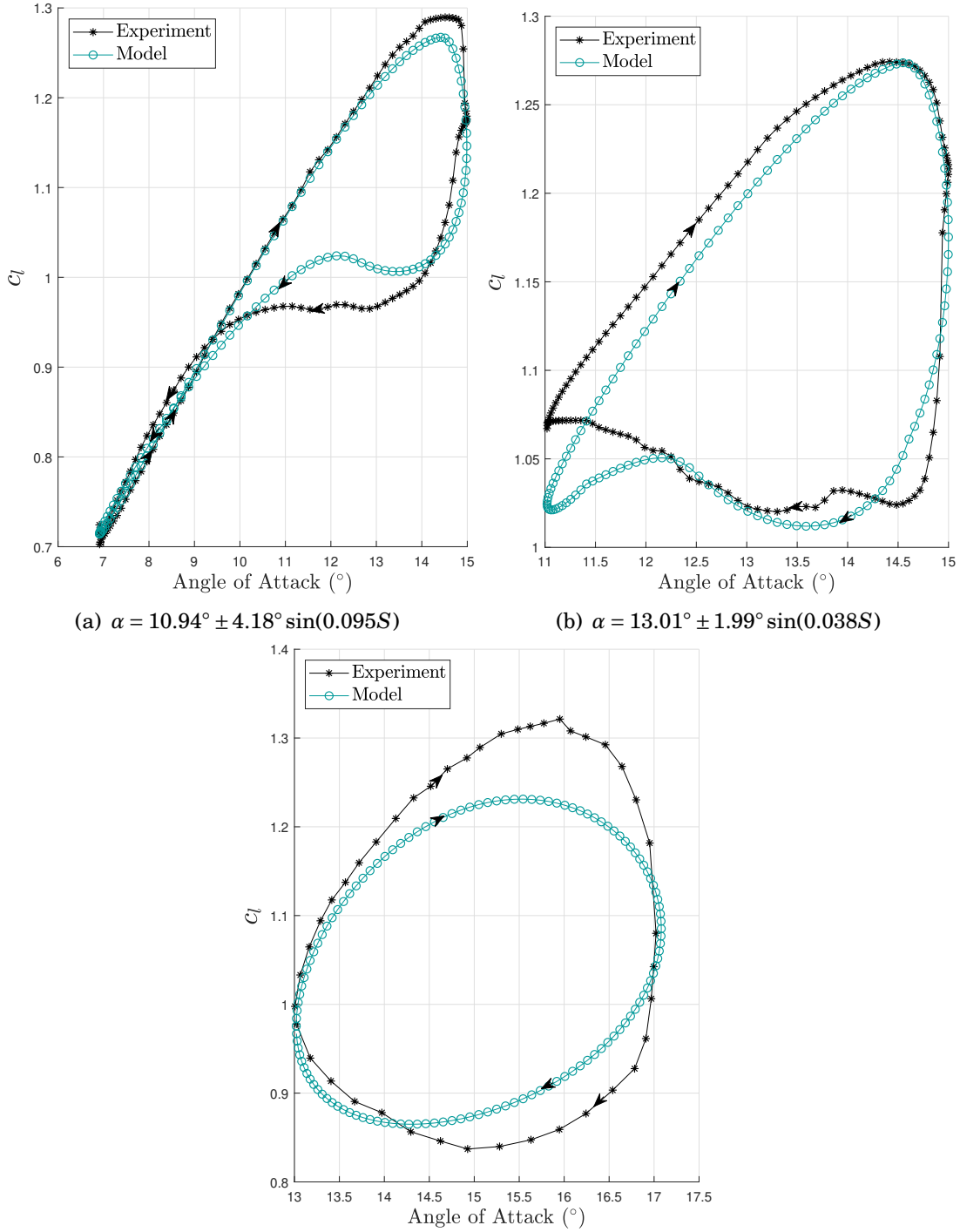

(a) $\alpha = 10.94° \pm 4.18° \sin(0.095S)$

(b) $\alpha = 13.01° \pm 1.99° \sin(0.038S)$

(c) $\alpha = 15.05° \pm 2.03° \sin(0.095S)$

Figure 3.13: Beddoes-Leishman and 2D experimental results

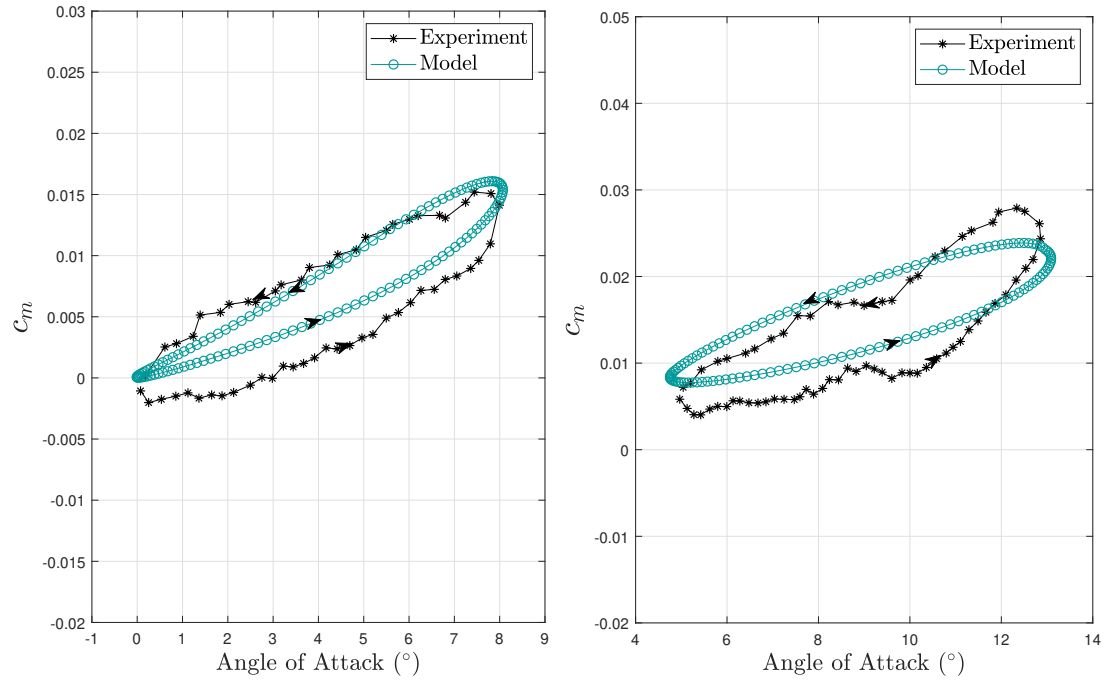

(a) $\alpha = 7° \pm 6° \sin(0.05S)$

(b) $\alpha = 11° \pm 2° \sin(0.1S)$

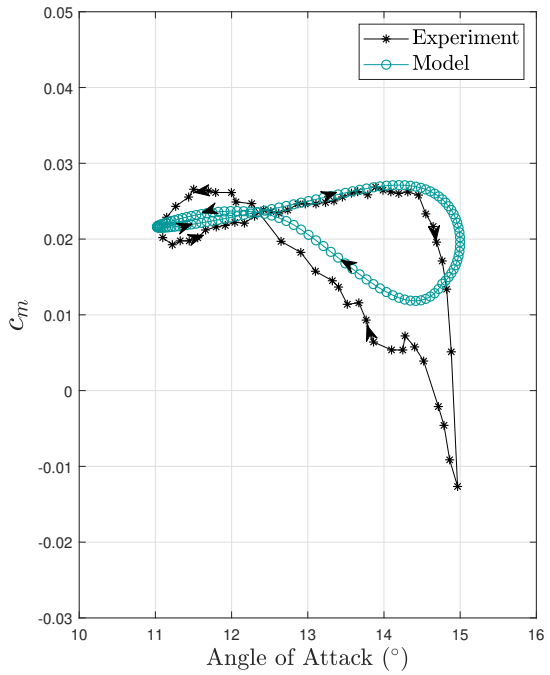

(c) $\alpha = 13° \pm 2° \sin(0.05S)$

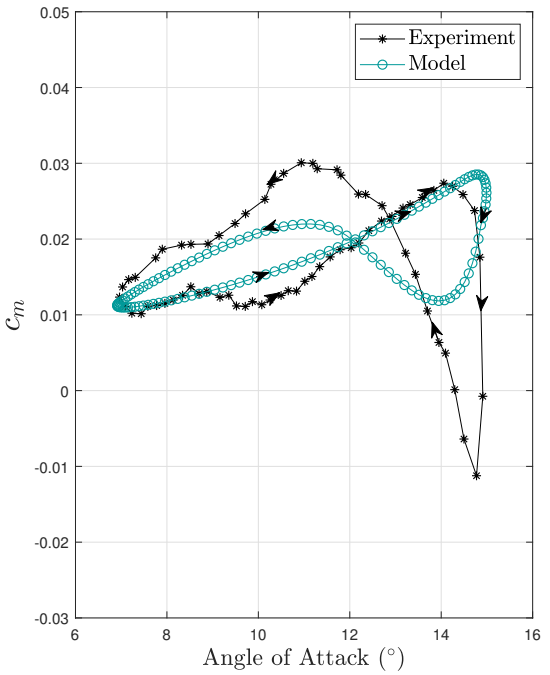

(d) $\alpha = 11° \pm 4° \sin(0.15S)$

Figure 3.14: Beddoes-Leishman and 2D dynamic experimental c_m results

CHAPTER 4

THREE-DIMENSIONAL ATTACHED FLOW MODELS

This research aims to develop a new efficient method to model unsteady flow separation on finite wings that is suitable to be applied in the early design phase. The model relies on a two-dimensional stall model to update a 3D unsteady potential flow model. This chapter introduces some of the most widely used three-dimensional potential flow methods for solving both steady and unsteady inviscid flows. One of the key parts of this chapter is the implementation of the unsteady lifting line theory which is used in the new model as discussed in Chapter 5. The unsteady lifting line theory is also compared with unsteady vortex lattice methods. Further to this it is compared to experimental data. The limitations of these models will also be outlined. The selection of the unsteady lifting line for use in the new coupled model is hence justified.

4.1 Steady 3D Potential Flow Models

4.1.1 Lifting Line Theory

4.1.1.1 Classical Prandtl Lifting Line Theory

In 1914 Ludwig Prandtl and Max Munk introduced a model for predicting the lift and induced drag on a straight, finite wing in incompressible flow, [108]. The underlying theory is based on a bound lifting vortex line placed at the quarter chord, in which the strength is allowed to vary along the span, $\Gamma(y)$. This bound vortex is fixed to the wing in contrast to free vortices and is called the lifting line. Trailing edge vortices are then assumed to be shed continuously along the span of the wing with equal strength to the spanwise change in circulation on the lifting line $d\Gamma(y)$. The shed vortices are aligned with the chordline and produce a force free wake sheet. Prandtl hypothesised that each chordwise section of the wing had equal lift to that of an identical two-dimensional aerofoil with the equivalent circulation. The sectional circulation in this case is modified by three-dimensional effects compared to the equivalent aerofoil circulation at the same geometric angle of attack. Now once the spanwise circulation distribution is known, the model calculates the sectional lift via the 2D Kutta-Joukowski law

$$L'(y) = \rho_\infty V_\infty \Gamma(y) \tag{4.1}$$

where $L'(y)$ is the lift per unit span, ρ_∞ and $\mathbf{V}_\infty$ represent the freestream density and velocity vector respectively. The sectional lift coefficient is then

$$C_l(y) = \frac{\rho_\infty V_\infty \Gamma(y)}{0.5\rho_\infty V_\infty^2 \mathrm{c}(y)} = \frac{2\Gamma(y)}{V_\infty \mathrm{c}(y)} \tag{4.2}$$

The problem is that the appropriate circulation distribution for the wing depends on the downwash shed across the wing, which itself depends on the circulation. Hence further information is needed to close the problem as described in the brief outline of the model below. The first step in Prandtl's method is to consider the vertical velocity, $w(y)$, induced

by the trailing vorticity on the bound vortex. This varies along the span and the value of $w(y)$ is generally negative i.e. a downwash. From the Biot-Savart law, the downwash velocity induced at a point $(0, y0)$ on the lifting line by an element of the vortex filament shed at point y with strength $d\Gamma$ is given by:

$$dw_{y_0 y} = -\frac{d\Gamma}{4\pi}\frac{\cos(\beta)\,dx}{r^2} \tag{4.3}$$

where dx is the length of the small vortex element and the terms β and r are defined in the schematic shown in Figure 4.1

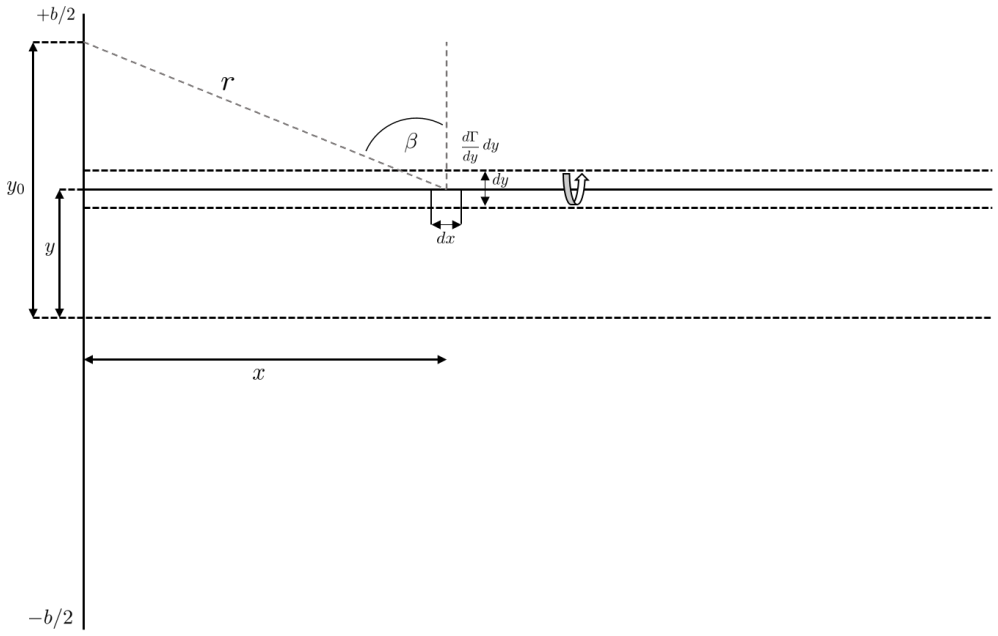

FIGURE 4.1. Calculating downwash from a trailing edge vortex schematic, adapted from [109]

Then integrating in x, the influence of the semi-infinite trailing vortex filament at y is given by

$$w_{y_0 y} = -\frac{d\Gamma}{4\pi}\int_0^\infty \frac{\cos(\beta)dx}{r^2} = -\frac{d\Gamma}{4\pi}\frac{1}{y_0 - y} \tag{4.4}$$

In order to find the total downwash induced on the lifting line at $y = y_0$ by all the continuous distribution of shed vortices, this must be integrated across the span to give

$$w_{y0} = -\frac{1}{4\pi}\int_{-b/2}^{b/2}\frac{1}{y_0 - y}d\Gamma = -\frac{1}{4\pi}\int_{-b/2}^{b/2}\frac{d\Gamma/dy}{y_0 - y}dy \tag{4.5}$$

The induced angle of attack due to the shed vorticity is then given by

$$\alpha_{ind}^{LLT} = \tan^{-1}\left(\frac{w_{y0}}{V_\infty^x}\right) \tag{4.6}$$

And assuming small angles

$$\alpha_{ind}^{LLT} = \left(\frac{w_{y0}}{V_\infty^x}\right) = -\frac{1}{4\pi V_\infty^x}\int_{-b/2}^{b/2}\frac{d\Gamma/\mathrm{d}y}{y_0 - y}dy \tag{4.7}$$

Combining this with the geometric angle of attack, α_∞

$$\alpha_\infty(y) = \tan^{-1}\left(\frac{V_\infty^z}{V_\infty^x}\right) + \theta_0(y) \tag{4.8}$$

where $\theta_0(y)$ represents any geometrical twist at the spanwise position. This gives an effective angle of attack

$$\alpha_{eff}^{\mathrm{LLT}} = \alpha_\infty + \alpha_{ind}^{\mathrm{LLT}} \tag{4.9}$$

now the 2D analogy of Prandtl assumes that the sectional wing lift at $y0$ is given by

$$c_l(y_0) = a_0(y_0)\left(\alpha_{eff}^{LLT}(y_0) - \alpha_{0_L}(y_0)\right) \tag{4.10}$$

where $a_0(y)$ is the lift curve slope of the aerofoil section at y. Then equating Equations 4.2 & 4.10 and substituting for the induced incidence yields the Fundamental Lifting Line Equation.

$$\alpha_\infty(y_0) = \frac{2\Gamma(y_0)}{a_0(y_0)V_\infty c(y_0)} + \alpha_{l=0}(y_0) + \frac{1}{4\pi V_\infty}\int_{-s}^{+s}\frac{(d\Gamma/dy)dy}{(y_0 - y)} \tag{4.11}$$

where the only unknown is the circulation. Once this has been determined the lift can be found from Equation (4.2). The solution is in the form of an infinite Fourier series, however this is often in practice truncated to include only a finite number of terms which are determined by satisfying Equation (4.11) at a finite number of locations [110]. Versions based on direct numerical solutions of Equation (4.11) have also been developed [110].

It should be noted that the classical approach only yields reasonable approximations for single unswept wings, with a high aspect ratio and no dihedral. More general versions of the LLT method have subsequently been developed to address these restrictions.

4.1.1.2 Numerical Lifting Line Theory

The classic lifting line theory introduced by Prandtl has been extended by a number of authors to simulate flows where the classical method is unsuitable. These methods use a three-dimensional vortex lift law so that the sectional lift is given by $\rho \boldsymbol{V_x} \times \boldsymbol{\Gamma}$ [110], [70], in contrast to the 2D Kutta-Joukowski law used in the classical method. Whereas the classical method only includes the impact of the velocities induced by the free vortices on the bound vortex, these methods also include velocities induced by other bound vortex segments as appropriate. So for the example of a swept wing the bound vorticity on one half of the wing produces downwash on the other half. Including the additional terms impacts both the lift and the induced drag of the wing. The key benefit of using this approach is the ability to model the aerodynamics of swept wings, dihedral and multiple lifting surfaces.

The method implemented in this work is referred to as the numerical lifting line theory method and is based on the methods described by Phillips & Snyder [110] and Katz & Plotkin [70]. The methods [110], assume that the wing is divided into a finite number of spanwise sections. Each finite section has a horseshoe vortex so that a finite number of vortices is shed across the wing, see for example Figure 4.2. For each horseshoe vortex

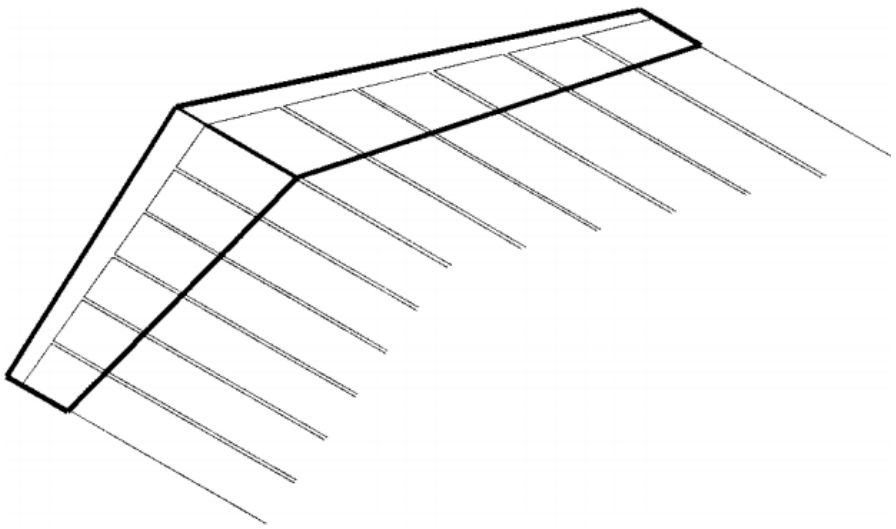

Figure 4.2: Distribution of horseshoe vorticies for numerical lifting line theory [110]

the bound part aligns with the quarter chord of the wing, thus it follows any sweep and dihedral. The trailing parts begin at the quarter chord line and extend downstream to infinity. They align with the chordwise direction so that for adjacent horseshoe vortices the right hand trailing vortex of one overlaps the left hand trailing vortex of its neighbour. The strengths of the horseshoe vortices are found by imposing a no normal flow boundary condition at the three quarter chord points, which are located at a spanwise position midway between the trailing vortices. This is called the collocation point.

A sample output of the numerical lifting line theory method for a wing with sweep, $\Lambda = 30°$, is shown in Figure 4.3. Also included is the output of an Unsteady Vortex Lattice Method (UVLM), see Section 4.1.2, which is run until convergence to a steady output. It should be noted that numerical lifting line theory methods [110] [70] are in fact a special case of the more general vortex lattice method with a single horseshoe vortex in the chordwise direction [111].

To apply the boundary conditions at the collocation points it is necessary to find the velocity induced by a finite straight vortex filament at an arbitrary point in 3D space

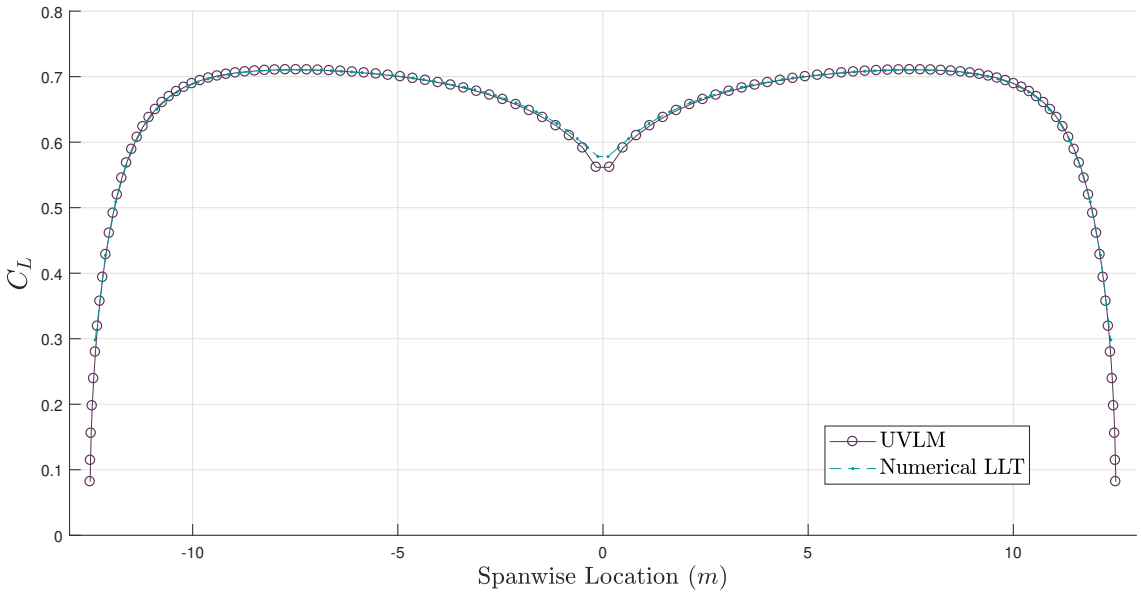

Figure 4.3: Comparing the C_l output from UVLM and a numerical lifting line theory on an untapered swept wing, $\Lambda = 30$, with aspect ratio, $AR = 12$ and $0°$ dihedral angle.

using the Biot-Savart law. Using the notation from Figure 4.4 [70] it can be shown that

$$\boldsymbol{V} = \frac{\Gamma}{4\pi} \frac{\boldsymbol{r}_1 \times \boldsymbol{r}_2}{|\boldsymbol{r}_1 \times \boldsymbol{r}_2|^2} \boldsymbol{r}_0 \cdot \left(\frac{\boldsymbol{r}_1}{r_2} - \frac{\boldsymbol{r}_2}{r_2} \right) \tag{4.12}$$

where $\boldsymbol{r_0} = \boldsymbol{r_1} - \boldsymbol{r_2}$.

A potential issue with Equation in 4.12 is that there is a zero division error if $\boldsymbol{r_1}$ and $\boldsymbol{r_2}$ are collinear. As described by Phillips and Synder [110] it can therefore be more convenient to adapt this form of the Biot-savart law. As shown by Katz and Plotkin [70], the equation for the induced velocity can be rewritten as

$$\boldsymbol{V} = \frac{\Gamma}{4\pi} \frac{(r_1 + r_2)(\boldsymbol{r}_1 \times \boldsymbol{r}_2)}{r_1 r_2 (r_1 r_2 + \boldsymbol{r}_1 \cdot \boldsymbol{r}_2)} \tag{4.13}$$

then when the bound vortex along with two trailing vortex legs are considered, the induced velocity due to the complete horseshoe vortex can be calculated with:

$$\boldsymbol{V} = \frac{\Gamma}{4\pi} \left[\frac{\hat{\boldsymbol{u}}_\infty \times \boldsymbol{r}_2}{r_2 (r_2 - \boldsymbol{v} \cdot \boldsymbol{r}_2)} + \frac{(r_1 + r_2)(\boldsymbol{r}_1 \times \boldsymbol{r}_2)}{r_1 r_2 (r_1 r_2 + \boldsymbol{r}_1 \cdot \boldsymbol{r}_2)} - \frac{\hat{\boldsymbol{u}}_\infty \times \boldsymbol{r}_1}{r_1 (r_1 - \hat{\boldsymbol{u}}_\infty \cdot \boldsymbol{r}_1)} \right] \tag{4.14}$$

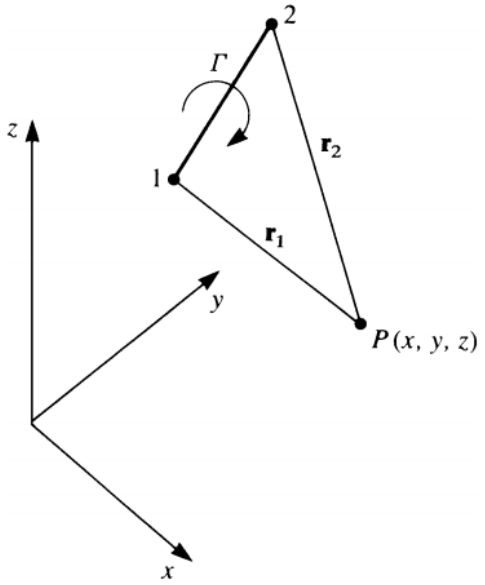

Figure 4.4: Notation for Biot-Savart law from [70]

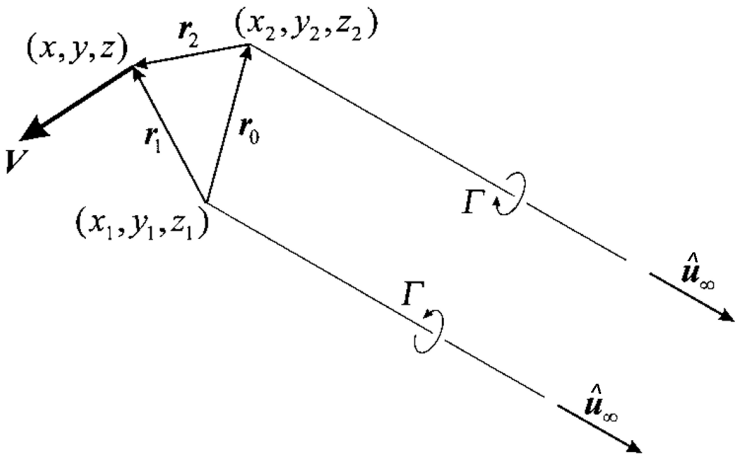

Figure 4.5: Definition of vectors used for complete horseshoe vortex, adapted from [110]

where $\hat{u}_\infty$ is the unit vector in the direction of the freestream. Using Equation (4.14), an aerodynamic influence matrix, A, can be formed. This should be calculated with respect to the unit normal of the wing chord line $\hat{\boldsymbol{n}}_i$. The definitions of the vectors in 4.14 are given in Figure 4.5.

After the induced velocity contributions from all horseshoe vortices at each collocation

point is available, the resulting set of linear equations can be solved for the horseshoe vortex strengths. Subsequently force coefficients may be evaluated.

4.1.2 Vortex Lattice Method

The Vortex Lattice Method (VLM) is very similar in principle to the numerical lifting line method. In this case the surface is divided in the chordwise direction as well as the spanwise direction yielding a surface panelling, see for example Figure 4.6. The advantage of the VLM is thus the ability to obtain a chordwise force distribution, as well as a spanwise loading. The ability to discretize in the chordwise direction allows the effects of camber to be modelled directly, which the numerical lifting line inherently cannot.

A horseshoe vortex is placed on each of the surface panels with the bound vortex at the panel quarter chord. Due to superposition of the trailing line vortices this situation is exactly equivalent to having a series of vortex rings on each panel, with semi-infinite trailing vortices only emanating from the panels adjacent to the trailing edge of the wing. It should be noted that utilising this vortex ring representation allows the VLM method to also be used to model the effects of camber, by placing the vortex rings along the camber line. Furthermore the wake itself can be modelled with vortex rings so that wake roll up can be modelled.

Now the velocities induced by all vortex rings at all collocation points are calculated. Boundary conditions are applied at collocation points at the three-quarter chord, spanwise centred position within each panel. The strength of the vortex rings are then found by solving the linear system yielded by the boundary conditions.

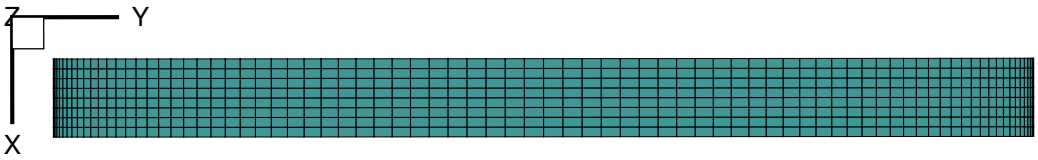

Figure 4.6: Vortex Lattice Mesh, with cosine spacing for a wing of AR 12.5. Eight chordwise panels and 80 spanwise panels are used.

4.2 Unsteady 3D Potential Flow Models

4.2.1 Strip Theory

Strip theory is sometimes used to estimate the wing loads but it is not a true three-dimensional model [61]. Strip theory divides the wing into a given number of strips, where each is modelled independently, therefore each spanwise segment is simply a two-dimensional model. This approach in effect ignores the induced velocities from the trailing vortices and usually provides an overestimation of the strip loads. For this reason strip theory should only be used when the wing aspect ratio is large. Even then the inclusion of a three-dimensional wake has been shown to be important [69]. Techniques have been implemented, for example the work by Cook [62] where a lift distribution obtained from a VLM has been applied to the strip loads based on the spanwise location. This has been shown to be a beneficial addition to strip theory, however under stall conditions, it is still necessary to capture the influence of high gradients in spanwise bound vortex strength, $d\Gamma/dy$. Modified strip theory is also a popular technique for modelling unsteady aerodynamic forces on high aspect ratio wings. In modified strip theory, parameters such as the lift curve slope may be approximated for finite-span effects, however not directly calculated. As previously mentioned, Patil and Hodges have incorporated a dynamic stall model into the modified strip theory formulation, allowing for a level of separation modelling [61].

4.2.2 Unsteady Lifting Line Theory

In order to model the unsteady attached flow on a finite wing, Boutet and Dimitriadis [112] proposed an unsteady lifting line theory (ULLT) method. The unsteady lifting line theory method is based on the classical Prandtl lifting line theory to model the three-dimensional induced downwash and the Wagner function for the unsteady circulation build up. The resulting model is a closed form, time-domain unsteady model capable of simulating the attached flow around a finite wing. The unsteady lifting line places a bound vortex coincident with the quarter chord of the wing and the trailing portion of each horseshoe vortex is positioned to be in the direction of the freestream. Although the model is based on classical lifting line theory, it is a useful technique to obtain the influence of spanwise strips upon one another, which is a key feature ignored by techniques such as strip theory, where 2D loads are integrated over the span.

The unsteady lifting line model is completed by coupling Prandtl's lifting line theory with Wagner's function using the unsteady Kutta-Joukowsky theorem, as formulated by Boutet and Dimitriadis [112]. For a detailed description of the model, the reader is referred to the aforementioned paper. The Wagner function is capable of modelling the unsteady lift on a two-dimensional aerofoil for arbitrary pitching motions partly due to the fact that it is formulated in the time domain. The unsteady response is evaluated by the convolution of step changes in angle of attack. The step response is approximated using Jones' sum of exponentials. For example Wagner's time-domain indicial response function can be approximated by [113]:

$$\Phi(t) = 1 + A_{\Phi 1} e^{b_{\Phi 1} t} + A_{\Phi 2} e^{b_{\Phi 2} t} \tag{4.15}$$

where $A_{\Phi 1} = -0.165$, $A_{\Phi 2} = -0.335$ $b_{\Phi 1} = -0.045$ and $b_{\Phi 2} = -0.300$.

As with a steady lifting line, it is necessary to compute Fourier coefficients, A_n, at the j spanwise positions on the wing. However since the unsteady response is required, the rate of change of circulation with respect to time, $\dot{\Gamma}$, needs to be considered. For this,

the unsteady Kutta-Joukowski theorem is used, the usages are described by Boutet & Dimitriadis [114] and further explained by Katz & Plotkin [70]. The unsteady cirulatory lift, using the unsteady Kutta-Joukowski theorem is given as [112]:

$$C_l(t,y) = \frac{2\Gamma}{u_\infty c(y)} + \frac{2\dot{\Gamma}}{u_\infty^2} \tag{4.16}$$

As in the steady lifting line, the circulation strength of the bound vortex, Γ, can be represented using a Fourier series. Since the unsteady Kutta-Joukowski contains a $\dot{\Gamma}$ term, the time derivative of the Fourier coefficients, $\dot{A}_n$, will also need to be computed. Boutet & Dimitriadis [114] give the Fourier series representation as follows:

$$C_l(t,y) = C_{L\alpha} \sum_{n=1}^{j} \left(\frac{c_0}{c} A_n + \frac{c_0}{u_\infty} \dot{A}_n \right) \tag{4.17}$$

The Wagner function can now be utilised to modify the sectional circulatory lift coefficient undergoing a step change in downwash, $w(y)$. At each spanwise position, six states are used to represent the aerodynamic behaviour of a given strip . There are $6j$ states when considering the entire wing, where j is the number of spanwise strips. The states are defined as follows [112]:

$$\begin{aligned}
\dot{z}_1(t,y) &= h - \tfrac{b_{\Phi 1} u_\infty}{b_c} z_1(t,y) & \dot{z}_4(t,y) &= \alpha - \tfrac{b_{\Phi 2} u_\infty}{b_c} z_4(t,y) \\
\dot{z}_2(t,y) &= h - \tfrac{b_{\Phi 2} u_\infty}{b_c} z_2(t,y) & \dot{z}_5(t,y) &= \tfrac{w_y}{u_\infty} - \tfrac{b_{\Phi 1} u_\infty}{b_c} z_5(t,y) \\
\dot{z}_3(t,y) &= \alpha - \tfrac{b_{\Phi 1} U}{b_c} z_3(t,y) & \dot{z}_6(t,y) &= \tfrac{w_y}{u_\infty} - \tfrac{b_{\Phi 2} u_\infty}{b_c} z_6(t,y)
\end{aligned} \tag{4.18}$$

where b_c is the semi-chord in metres. This combined with the j Fourier coefficients gives rise to a system of $7j$ ordinary linear differential equations (ODEs). Boutet & Dimitriadis show that the ODE for the Fourier coefficients and the aerodynamic states can be written as follows in equations 4.19 and 4.20 respectively.

$$m_0 \sum_{n=1}^{j} \left(\left(\frac{c_0}{c_i} + \Phi(0) \frac{n c_0}{4s \sin(\theta_i)} \right) A_n + \frac{c_0}{U_\infty} \dot{A_n} \right) \sin(n\theta_i) = \mathbf{C_i}\dot{\mathbf{q}} + \mathbf{D_i}\mathbf{q} + \mathbf{E_i}\mathbf{z_i} \tag{4.19}$$

$$\dot{\mathbf{z_i}} = \mathbf{W_i z_i} + \mathbf{F q} - \mathbf{G}\frac{m_0 c_0}{4s}\sum_{n=1}^{j} n A_n(t)\frac{\sin(n\theta_i)}{\sin\theta} \tag{4.20}$$

where

(4.21)

$$\mathbf{q} = [h(t,y) \quad \alpha(t,y)]^T$$

$$\mathbf{z} = [z_1(t,y) \quad z_2(t,y) \quad z_3(t,y) \quad z_4(t,y) \quad z_5(t,y) \quad z_6(t,y)]^T$$

$$\mathbf{D} = \frac{a_0(y)}{U}[\Phi(0) \quad U\Phi(0) + d\Phi(0)]$$

$$\mathbf{E} = \frac{c_{l_\alpha}(y)U}{b_c}\left[-\frac{A_{\Phi1}c_1^2}{b_c} - \frac{A_{\Phi2}c_2^2}{b_c} \quad A_{\Phi1}b_{\Phi1}\left(1 - b_{\Phi1}\frac{d}{b}\right) \quad A_{\Phi2}b_{\Phi2}\left(1 - b_{\Phi2}\frac{d}{b}\right) \quad A_{\Phi1}b_{\Phi1} \quad A_{\Phi2}b_{\Phi2}\right]$$

$$\mathbf{G} = [0 \quad 0 \quad 0 \quad 0 \quad 1 \quad 1]^T$$

$$\mathbf{C} = \frac{c_{l_\alpha}(y)}{U}\Phi(0)[1 \quad d]$$

$$r = -\frac{c_{l_\alpha}(y)}{U}(h(0,y) + dx(0,y))$$

$$\mathbf{W} = -\frac{U}{b}\,\mathrm{diag}(b_{\Phi1}, b_{\Phi2}, b_{\Phi1}, b_{\Phi2}, b_{\Phi1}, b_{\Phi2})$$

$$\mathbf{F} = \begin{bmatrix} 1 & 1 & 0 & 0 & 0 & 0 \\ 0 & 0 & 1 & 1 & 0 & 0 \end{bmatrix}^T$$

where d is the non-dimensional distance by semi-chord, between the mid-chord and the pitch axis. Assembling Equations 4.19 and 4.20 into a matrix form allows the system of ODEs to be solved and the Fourier coefficients A_n to be evaluated. The Fourier coefficients can then be used to calculate the sectional lift coefficient through the use of Equation 4.17.

$$\begin{bmatrix} \mathbf{M_A} & \mathbf{0} \\ \mathbf{0} & \mathbf{I} \end{bmatrix}\begin{bmatrix} \dot{\mathbf{A}}_\mathbf{n} \\ \dot{\mathbf{z}} \end{bmatrix} = \begin{bmatrix} -\mathbf{F} & \mathbf{E} \\ \mathbf{G} & \mathbf{W} \end{bmatrix}\begin{bmatrix} \mathbf{A_n} \\ \mathbf{z} \end{bmatrix} + \begin{bmatrix} \mathbf{C}[\dot{\mathbf{q}}] + \mathbf{D}[\mathbf{q}] \\ \mathbf{F}[\mathbf{q}] \end{bmatrix} \tag{4.22}$$

The unsteady lifting line theory method has been coded in order to be used as part of a model developed in this thesis.

4.2.2.1 Unsteady Numerical Lifting Line Theory

It is also worth noting that the numerical lifting line theory can be extended to unsteady flows as recently demonstrated by Izraelevitz, Zhu and Triantafyllou [113]. An unsteady

numerical lifting line theory (UNLLT) has the advantage of being able to model effects such as sweep with less computational expense than a UVLM. This is achieved by the implementation of a wake model instead of representing the wake as individual vortex rings. For this reason, the numerical lifting line theory has achieved a similar fidelity to the UVLM, albeit with a more compact wake representation that cannot capture either wake roll-up or intersection. This work only considers unswept cases where the ULLT is sufficient, however an UNLLT would be a useful extension to allow more diverse planforms to be modelled.

4.2.3 Unsteady Vortex Lattice Method

The unsteady vortex lattice method (UVLM) is formulated in a similar manner to the VLM, however at each time step, vorticity is shed into the wake from the trailing edge vortex elements. The vorticity shed into the wake is of the same strength as the trailing edge panel allowing for the Kutta condition to be enforced. The code used here was formulated and implemented by Wales *et al.* [115]. The UVLM is able to record the full wake history capturing the true wake position and roll up, this is shown in Figure 4.7.

This is unlike the ULLT which relies on a wake model that is often assumed to be a straight line in the direction of the freestream vector combined with the instantaneous motion vector, whether this be at the $\frac{1}{4}$ or $\frac{3}{4}$ chord. Despite the true unsteady wake geometry not being captured, the assumption is found to work well even for large curvature in the wake [113]. Another advantage of the UVLM is the ability to handle the intersection of the wake with either the wing or other wake elements, this however requires special attention in order to avoid the Biot-Savart calculation producing singularities.

In the implementation used, the wake panels shed have the ability to be transformed into vortex particles, as shown in Figure 4.7. As the wake particles travel further from the wing, their influence becomes smaller, reducing proportionally with the square of the distance. Therefore to accelerate the code the particles are agglomerated together, the

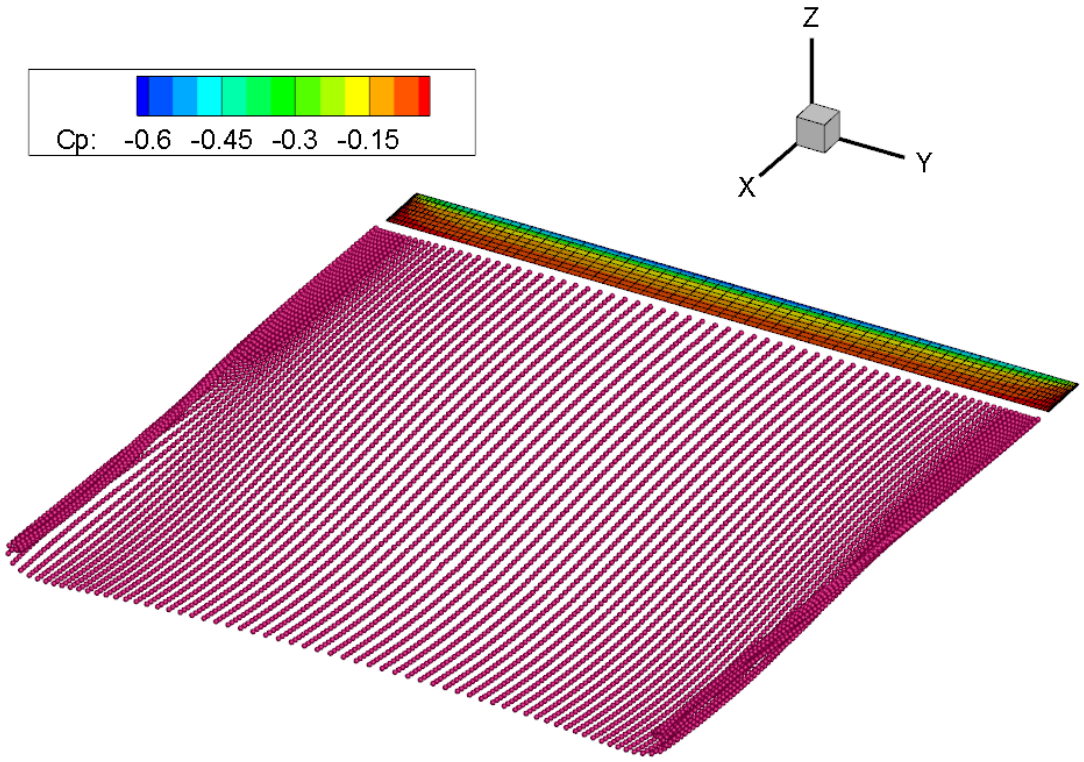

Figure 4.7: Example of UVLM wake particles and wake roll-up

octree structure used to do this is displayed in Figure 4.8.

4.3 Validation of ULLT

4.3.1 Using UVLM

A logical choice of aerodynamic model to validate the unsteady lifting line is the unsteady vortex lattice method since both models are based on the potential flow equations. In order to look at the unsteady response, a straight, finite wing of aspect ratio 12.5 is subject to static and dynamic pitching motions.

In the test cases presented here, both the UVLM and ULLT have the same number of spanwise elements. The UVLM also had a chordwise discretization, with eight vortex rings as seen in Figure 4.6. Simpson, Palacios and Murua demonstrated up to 50 chord-

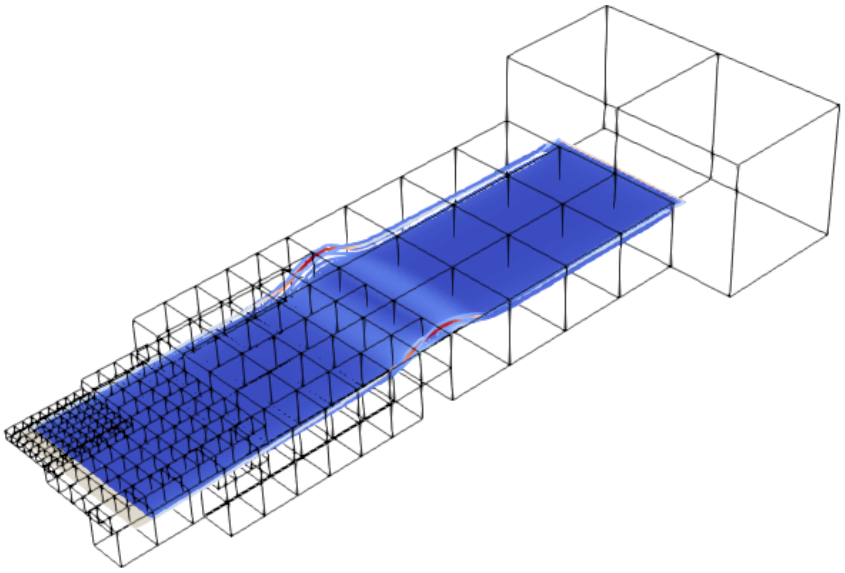

Figure 4.8: Example of UVLM octree structure, [115]

wise vortex rings are needed for convergence in C_d [116]. A more extensive study was conducted by Boutet and Dimitiradis in which the use of up to 100 chordwise vortex rings were investigated. To achieve full convergence in the moment coefficient, 75 vortex rings were used. Fritz and Long [117] show UVLM results comparing the convergence of the lift coefficient with number of panels for pitching and plunging cases. It was concluded that increasing the number of chordwise panels from five to ten only gave "a slight improvement in the accuracy of the results". Other work has demonstrated success with six chordwise vortex rings [118]. It is noted that a refinement study on the number of chordwise panels would give more confidence in the comparison between UVLM and ULLT. The lift coefficients have been integrated in the chordwise direction to allow the two potential flow models to be directly compared.

4.3.1.1 Static Response

The static case is achieved by allowing the ULLT and UVLM to reach a steady-state C_l for a fixed angle of attack. The steady-state response of the ULLT shows good agreement with the UVLM. Figures 4.9 and 4.10 show the static response from both the ULLT and UVLM for an angle of attack of 5° and 10° respectively. Close to the root, the error is very small, < 1%, however near the tip, the curvature of the lift distribution increases and it is here the largest errors are found. For the static cases investigated, the ULLT consistently replicates the UVLM to a good order of accuracy.

4.3.1.2 Dynamic response

The unsteady response of the wing is investigated in Figures 4.12 and 4.13, both test cases are presented for a pure pitching oscillations. Firstly Figure 4.12 shows the C_l response to the sinusoidal pitching motion $\alpha = 0° + 4° \sin(0.1S)$. A good match between the potential flow models is found, a normalized root mean squared deviation (NRMSD) of 4.64%. The case in Figure 4.13 shows the C_l response to a sinusoidal pitching motion at a higher mean angle and frequency, $\alpha = 4° + 3° \sin(0.2S)$. A slightly lower NRMSD error of 3.28% is found here. Overall a good agreement is found between the ULLT and the UVLM. As suggested by Hoerner [119], there are some discrepancies between lifting line and lifting surface approaches, however these are small, especially for high aspect ratio wings, and thus not considered further. As with the static case, the peak errors appear near the tip where there is a lot of curvature in the lift distribution.

4.3.2 Using experimental data

The ULLT model has also been compared to low angle of attack (max angle of attack 5°) quasi-steady experimental data produced by Piziali [12]. Once again, the model is supplied with the correct $C_{L\alpha}$ and α_{0L} from corresponding two-dimensional data contained within the same set of results. The comparison was capped at $\alpha = 5°$ to avoid comparison where separation is dominant. Figure 4.14 shows the lift coefficient surface for a

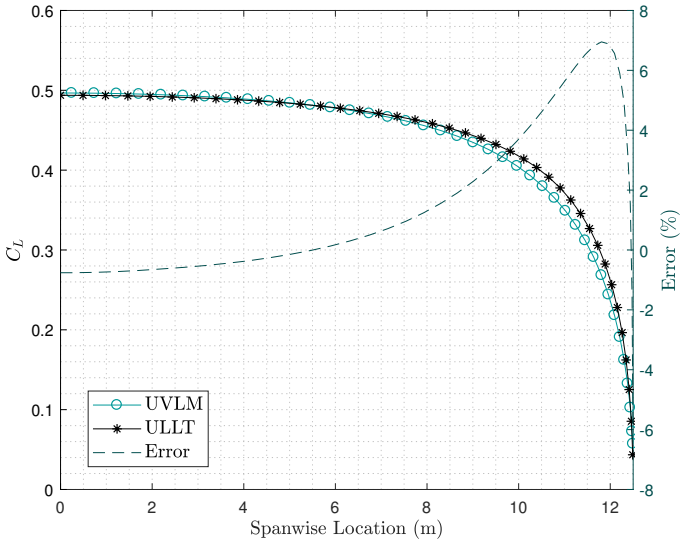

Figure 4.9: Steady test case, $\alpha = 5°$

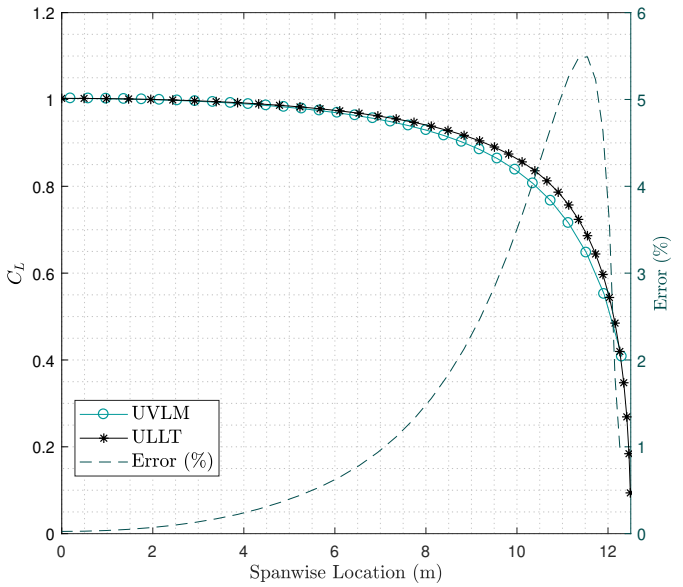

Figure 4.10: Steady test case, $\alpha = 10°$

Figure 4.11: Static results for the ULLT and UVLM converged on steady solutions

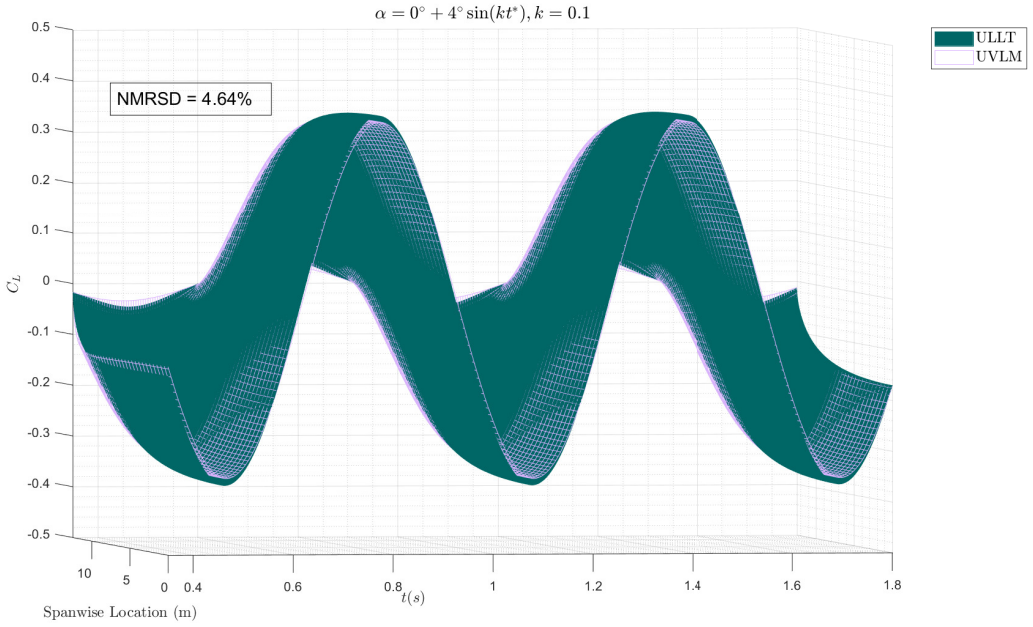

Figure 4.12: ULLT validation using UVLM case 1

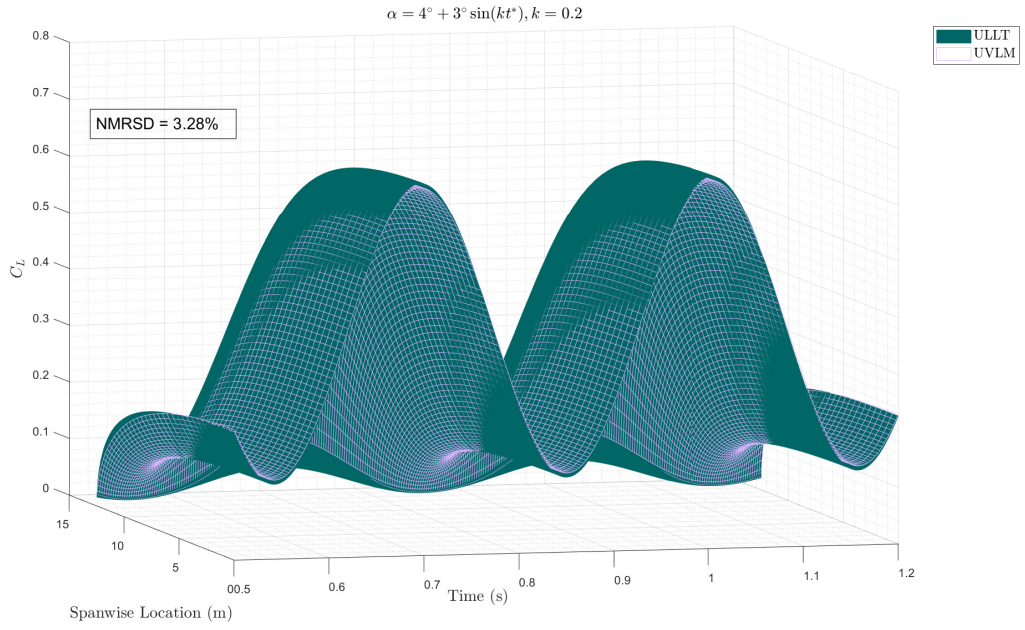

Figure 4.13: ULLT validation using UVLM case 2

quasi-steady input to the ULLT ($k = 0.0001$). At the aforementioned reduced frequency, no discernible hysteresis is present in the model output. Presented with the C_l surface are three repeats of the equivalent experimental case. When the angle of attack is low the model gives very reasonable results, which is the key element for the new coupled model developed in this research and presented in the next chapter. In the low angle of attack run, the experimental data contains oscillations in the C_l, even when taking these into account the maximum error is seen to be 15%. This is acceptable considering the resulting mean error is $\approx 5\%$.

The issue is that potential flow methods fall short when flow separation become prominent. Figure 4.15 shows the quasi-steady response for the aforementioned case however this time at a higher angle of attack range of 12° to 20°. The NACA 0015 section is subject to substantial flow separation and therefore the fundamental linear assumptions of the unsteady lifting line leads to considerable overestimation of the lift coefficient. At the largest angle of attack shown the ULLT over predicts the lift in excess of 100%. Even close to the tip where a tip vortex induces the most downwash, the separated flow still reduces the lift produced leading to the ULLT giving an unrealistic result. This directly shows that for separated flows the ULLT is inadequate and justifies the aim of this research to develop a new efficient coupled method for this flow regime.

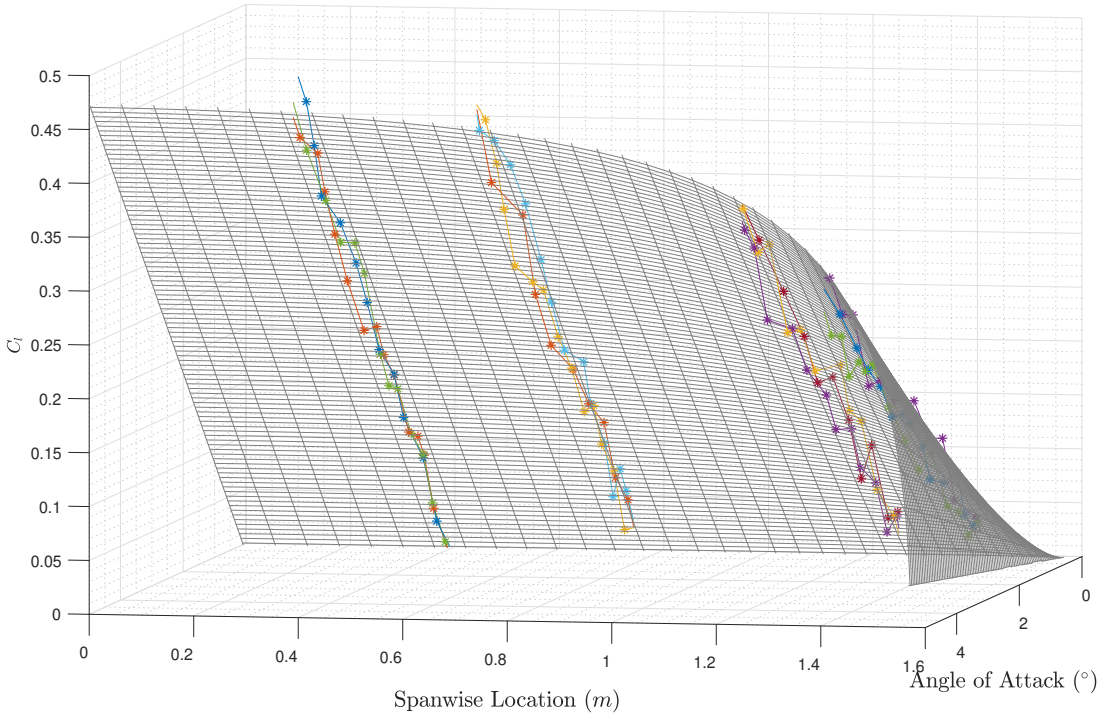

Figure 4.14: Low angle of attack experimental data [12] and ULLT

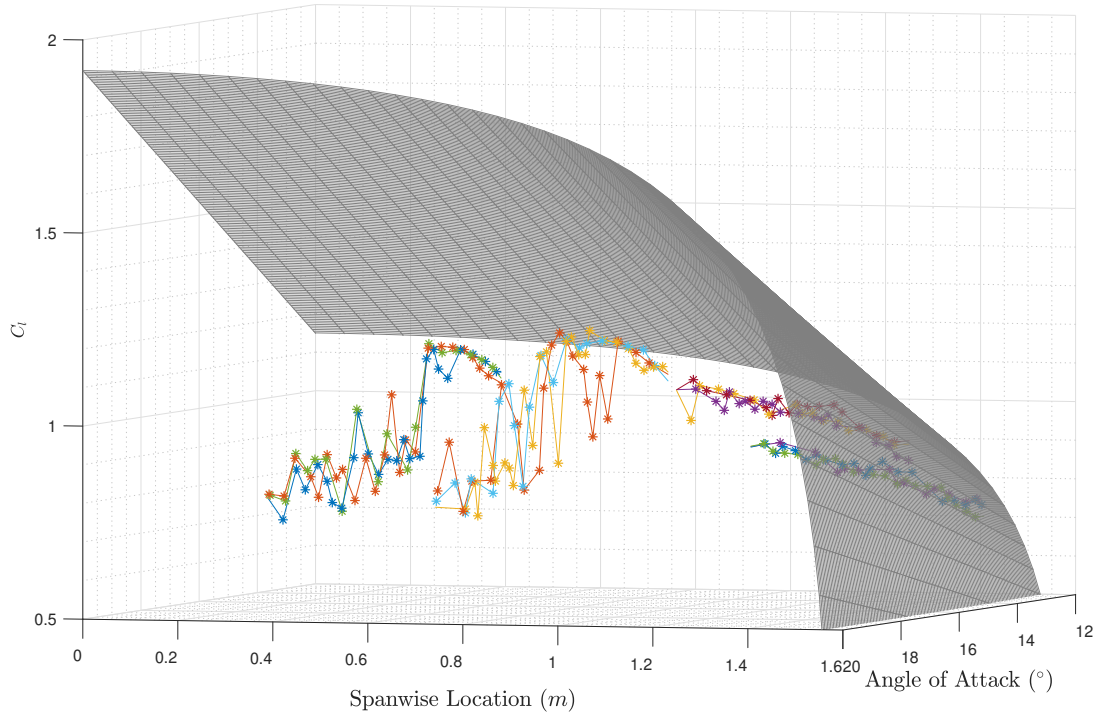

Figure 4.15: High angle of attack experimental data [12] and ULLT

CHAPTER 5

NONLINEAR UNSTEADY 3D MODEL FOR SEPARATED FLOW AND DYNAMIC STALL

In this chapter the new efficient model for 3D dynamic stall developed in this research is presented. The building blocks from earlier chapters, the B-L stall model and the 3D unsteady lifting line theory are coupled together to meet the aim set at the start of the research. The result is an efficient nonlinear lifting line method that is suitable for early stage design. The coupled model has been compared against experimental data for rigid pitching motions. The new nonlinear unsteady lifting line is then coupled to a nonlinear intrinsic beam formulation in order to carry out aeroelastic calculations. CFD is used to evaluate the aeroelastic cases by rigidly deforming the CFD mesh with the displacements returned from the model. Lastly the coupled model is also compared to a static nonlinear lifting line theory which is available as part of the XFLR5 package.

5.1 Nonlinear Unsteady Lifting Line Theory Formulation

The principle behind the nonlinear unsteady lifting line model is the introduction of a corrective angle of attack which contains alterations to the incidence due to the effects of flow separation and dynamic stall. In traditional potential flow methods, such as ULLT, vorticity can only be shed from the trailing edge of a wing. However in reality upon flow separation vorticity is shed from various chordwise separation positions across the span of the wing. Vorticity can also be shed in the form of a dynamic stall vortex which convects past the wing.

5.1.1 Coupling 2D Unsteady Database with 3D Unsteady Lifting Line Theory

Taking account of the effects of flow separation through the use of a corrective angle of attack approach has been explored by other researchers. Van Dam [120] implemented a method which introduced a similar corrective angle that used static, two-dimensional, viscous sectional data to update each spanwise station. The aforementioned work focused on static cases. However, in 2017 after this research was commenced a similar approach using unsteady 2D viscous data was implemented by Parenteau, Plante, Laurendeau and Costes [121]. This used a similar algorithm for updating the angle correction to [120], however unsteady periodic data was introduced.

To simulate a pure pitching motion for a finite wing with just a single amplitude and reduced frequency, the method of Parenteau requires the generation of a database of two-dimensional data of the same frequency and pitching amplitude. This effectively involves a sweep of mean amplitude motions as shown in Figure 5.1(a). Here the lift coefficient response for a dynamically pitching aerofoil is presented, at a single amplitude of 6° and reduced frequency of 0.1 for a variety of mean angle of attacks. The method relies on the interpolation of the data shown in Figure 5.1(a) after an unsteady corrective

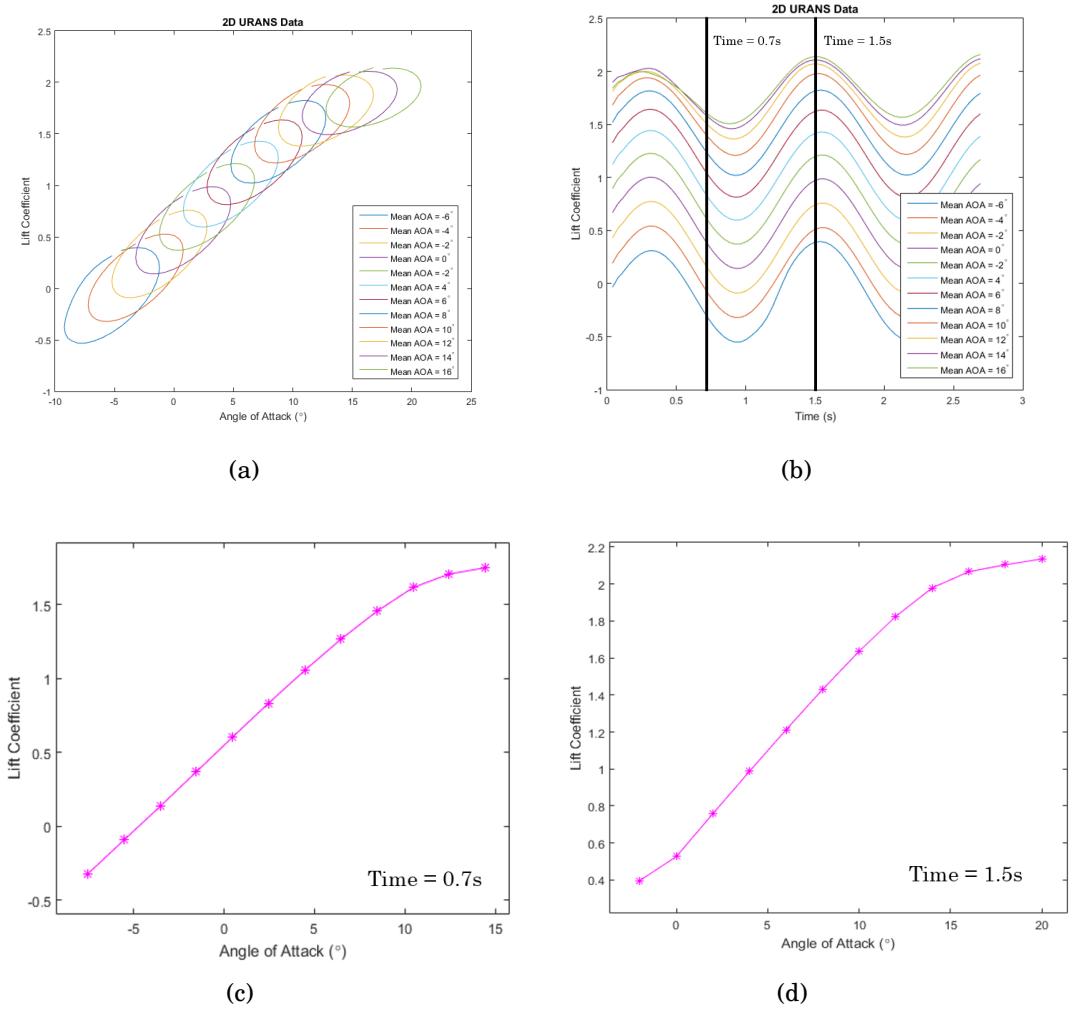

Figure 5.1: Example database with decomposition for directly using 2D URANS

angle is calculated and used. However, since the relationship between c_l and α is not distinct, the data is plotted against time because c_l and t have a one to one relationship (unlike c_l and α). The decomposed data is presented in Figure 5.1(b). From this the data can be interpolated at the desired time. This effectively gives a nonlinear lift curve slope at each instance where each entry to the database can transferred back to the instantaneous angle of attack. This is shown at $t = 0.7$ and 1.5 seconds in Figures 5.1(c) and 5.1(d) respectively.

A major drawback to this method is the motion of each strip must be similar to the 2D

viscous database. For example if a database had been obtained for sinusoidal pitching oscillations defined by the parameters mean incidence, amplitude and frequency; this would limit the cases the model could evaluate to be sinusoidal pitching oscillations within the range of 2D oscillations. Whilst this still has definite benefits over three dimensional CFD in computational time and negates the necessity of three-dimensional mesh generation, it falls short when the motion is no longer forced, making it not applicable within aeroelastic calculations. It is also worth mentioning that even if a wing is pitched with a single frequency sine wave, it will not necessarily experience the same single harmonic sine wave. Figure 5.2(a) shows the mid-semispan geometrical angle of attack given for a sinusoidal pitching oscillation defined by $\alpha = 17.12^\circ \pm 4.04^\circ \sin(0.038S)$, for the first three pitching cycles. Also displayed is $\Delta\alpha_{3D}$ which represents the change in angle due to downwash caused by the influence of the other spanwise stations. As shown in Figure 5.2(a), the effective angle of attack which is calculated by summing the geometric angle of attack and the induced angle is not truly the same sinusoid. As the wing aspect ratio $\rightarrow \infty$, $\Delta\alpha_{3D} \rightarrow 0$. For the inviscid case where the separation position is forced to be at the trailing edge, the induced angle is a sinusoid of the same, single frequency, therefore the effective angle of attack is still purely a sinusoidal oscillation as shown in Figure 5.2(b).

For the reasons explained in this subsection, using a two-dimensional database of unsteady aerofoil data is not a suitable method to supply a viscous correction. However the dynamic stall models implemented in Chapter 3 are a viable replacement for the two-dimensional URANS data. Firstly a dynamic stall model needs a less comprehensive database, since once the dynamic stall model is built there is a functional representation of the behaviour of the aerofoil. Furthermore, unlike using a database of periodic URANS data, a dynamic stall model is applicable to non-periodic motions. This is the most significant advantage because this opens up the opportunity to include the coupled model in aeroelastic calculations where the motion of a wing is not predetermined. The use of a dynamic stall model does bring disadvantages compared to using higher order data, as

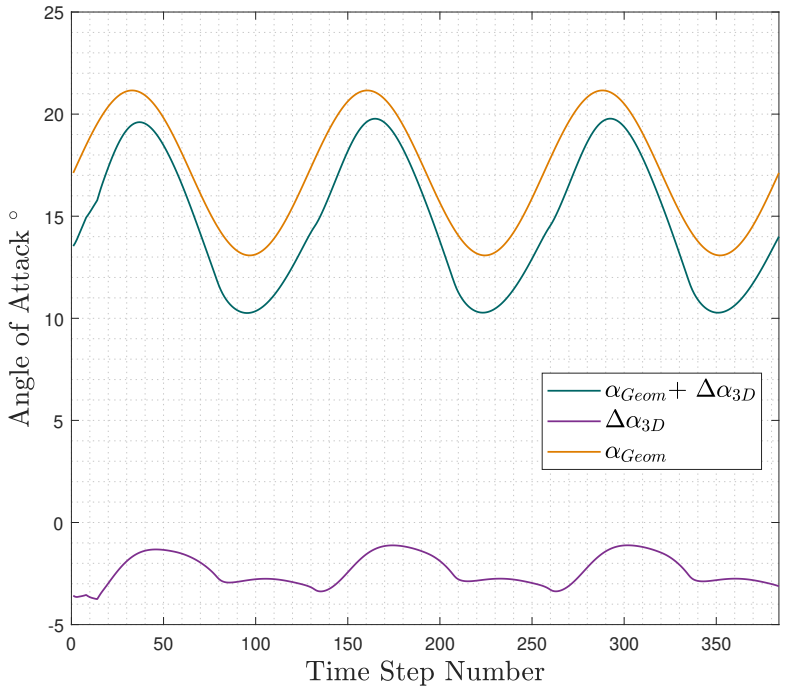

(a) Total induced angle with separation modelled

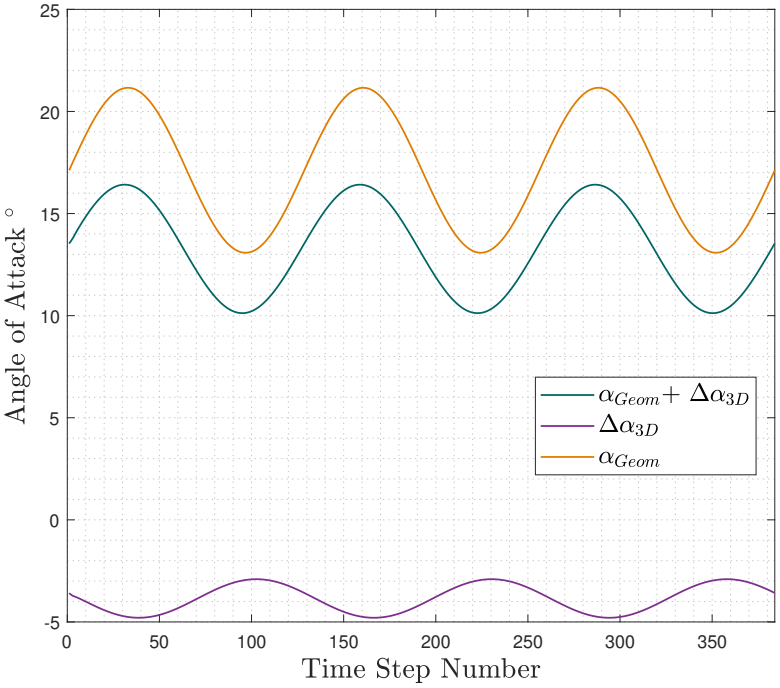

(b) Total induced angle without separation modelled

Figure 5.2: Effective angle of attack due to three-dimensional influence

errors will be introduced into the system by the simplifying assumptions of the model.

5.1.2 Coupling 2D Dynamic Stall Model with a 3D Unsteady Lifting Line Theory

The new model developed in this work couples a 2D dynamic stall model from Chapter 3 with a 3D unsteady lifting line method implemented in Chapter 4. The new nonlinear method is described and then the response of a finite wing is evaluated. Dynamic stall models are typically applied using strip theory, which neglects the influence of other spanwise stations. This can be problematic, since small variations in angle of attack, in the form of downwash induced by trailing vortices can lead to dramatically different nonlinear responses.

The purpose of coupling a 2D dynamic stall model with a 3D linear unsteady lifting line theory is to model the spanwise changes in the lift coefficient, whilst the dynamic stall model can change the bound circulation strength based on the local separation position. In the following work, the dynamic stall model used is the Beddoes-Leishman model. As previously discussed, the model applies lags to the separation position which can be deduced using Kirchhoff flow. This allows a spanwise separation line to be calculated. An example of this is shown in Figure 5.3 for a clean rectangular wing of aspect ratio 12.5, along with the spanwise distribution of C_l. The inboard section of the wing, where the lift coefficient is greater, leads to a separation point closer to the leading edge. As the lift reduces in the vicinity of the wing tip, the model predicts little separation, in this region the line of separation is very close to the trailing edge. A relationship has already been deduced which gives $C_l = C_m(C_l, f'')$. Therefore a basis is given to extend the two-dimensional moment model using the three-dimensional separation position.

Initially the 2D attached subsystem of the B-L model and the 3D linear ULLT solvers calculate the response to a change in the angle of attack to obtain $c_{l_{\text{lin}}}(t, y)$ and $C_{l_{\text{lin}}}(t, y)$. From this an effective angle of attack can be calculated that maps the 3D C_l to an

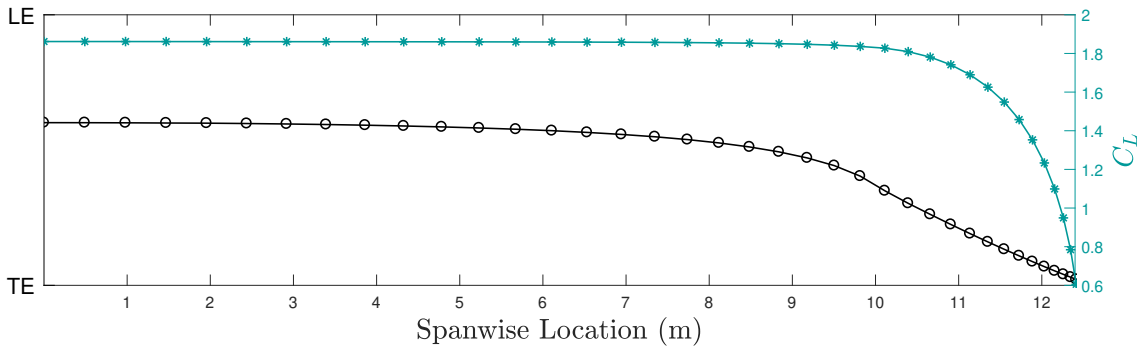

Figure 5.3: Example output of the separation line and sectional lift coefficient from the coupled model

effective 2D angle of attack. It should be noted that the subscript lin identifies the use of a linear aerodynamic solver, this could either be the unsteady lifting line, or two-dimensional indicial aerodynamic model. The angle of attack used may be modified with a corrective angle of attack, which is associated with flow separation, but the model does not directly compute the effects of flow separation or dynamic stall.

$$\alpha_{\text{eff}}^{3D}(t,y) = [c_{l_{\text{lin}}}(t,y) - C_{l_{\text{lin}}}(t,y)]/c_{l\alpha} + \alpha_{\text{Geom}}(t,y) \tag{5.1}$$

where $\alpha_{\text{Geom}}(t,y)$ represents the angle of attack due to the motion of the wing and any geometrical twist for the spanwise station at the current timestep:

$$\alpha_{\text{Geom}}(t,y) = \alpha_{\text{inst}}(t,y) + \alpha_{\text{twist}}(y) \tag{5.2}$$

where $\alpha_{\text{inst}}(t,y)$ is the instantaneous angle of attack at time, t, and spanwise position, y. Also geometrical twist, for example any washout, is included in the term $\alpha_{\text{twist}}(y)$.
For the initial iteration at a new timestep, $\alpha_{\text{eff}}^{3D}(t,y)$ would not take into consideration any viscous corrective angle of attack. The C_l would be calculated assuming the full geometrical angle of attack for attached flow. However, there is some subtlety here in that the aerodynamic states of the ULLT and B-L model (z_1 to z_6 for the ULLT, and the deficiency functions of the B-L model) will be generated from the viscous calculation at

the previous timestep.

Next the dynamic stall model is called, however the true angle of attack is not given, instead the effective angle of attack, $\alpha_{\text{eff}}^{3D}(t,y)$ is inputted. It is here that the subscript nonlin will be used: only quantities that are output from the B-L model will use this subscript. The B-L model achieves a lift coefficient for the modified time history, $C_{l_{\text{nonlin}}}(t,y)$, but this neglects the influence of the change in circulation on all other spanwise stations. The use of the superscript $3D$ is justified because there is the inclusion of the 3D downwash in $\alpha_{\text{eff}}^{3D}(t,y)$. However this does not necessary give a valid solution. From the Biot-Savart law [70], changing the angle of attack and hence the circulation at spanwise stations will modify the influence it has on all other spanwise stations. In order to account for this, a further corrective angle of attack is used:

$$\alpha_{\text{corr}}(t,y) = [C_{l_{\text{nonlin}}}(t,y) - C_{l_{\text{lin}}}(t,y)]/c_{l\alpha} \; + \; \alpha_{\text{corr}}(t-\Delta t,y) \tag{5.3}$$

even if the velocity influence calculated from the Biot-Savart law was neglected, applying $\alpha_{\text{corr}}(t,y)$ would still not lead to the ULLT giving the same result as the B-L model. This is because the sectional lift curve slope, which varies across the span, is not the same as the 2D aerofoil. In order to account for the effects of velocity influence and spanwise changes in sectional lift curve slope, the correction angle $\alpha_{\text{corr}}(t,y)$ can be included in the unsteady lifting line. Generally if there is substantial flow separation, the largest component of $\alpha_{\text{corr}}(t,y)$ is found on the first iteration. However, the value of $\alpha_{\text{corr}}(t,y)$ may still be modified by subsequent iterations to give a valid solution when considering the Biot-Savart law. This process is iterated until:

$$\sum_{y=1}^{\text{n}} \left(C_{l_{\text{nonlin}}}(t,y) \; - \; C_{l_{\text{lin}}}(t,y)\right) < \epsilon \tag{5.4}$$

where ϵ represents some convergence tolerance, and a value $\epsilon = 1e^{-4}$ has been used in this work. When little separation is presents, this will typically converge with a low

number of iterations, motions in the post-stall regime needing more (typically up to ten).

A useful way to understand how α_{corr} evolves throughout the iterative procedure described by Equation (5.3) and (5.4) is to consider a static case. Figure 5.4 shows the final timestep of the procedure applied to the NACA LRN 1015 wing held at a constant angle of attack of 16°. Here the model has reached a steady-state solution. Within each timestep there is a inner iteration which is repeated until Equation (5.4) is satisfied, this inner iteration is the correction number displayed in Figure 5.4. In this case, flow separation causes a reduction in lift, therefore a pitch-down corrective angle (negative in sign) is seen over the majority of the wing. However, due to the fact the C_l tends to zero at the tip, little separation occurs in this region. In the viscous solution, the sign of α_{corr} is positive. This is due to the reduction in circulation where there is substantial separation, which through the Biot-Savart law actually reduces the downwash at the tip, therefore the increasing the effective angle of attack. This can be seen in Figure 5.4 at spanwise positions further out than approximately 10.5 m.

In order to implement the coupled model the process described in the flowchart presented in Figure 5.5 is followed. A more compact form of the procedure is also detailed in Algorithm 1.

5.2 Comparison of New Model to Experimental Data

5.2.1 Experiment Details

In order to evaluate the performance of the new 3D nonlinear lifting line model, firstly experimental data produced by Piziali [12] is used.

For the validation of the model, it is important not only to have high angle of attack three-dimensional data, it is also necessary to have two-dimensional data that is consistent

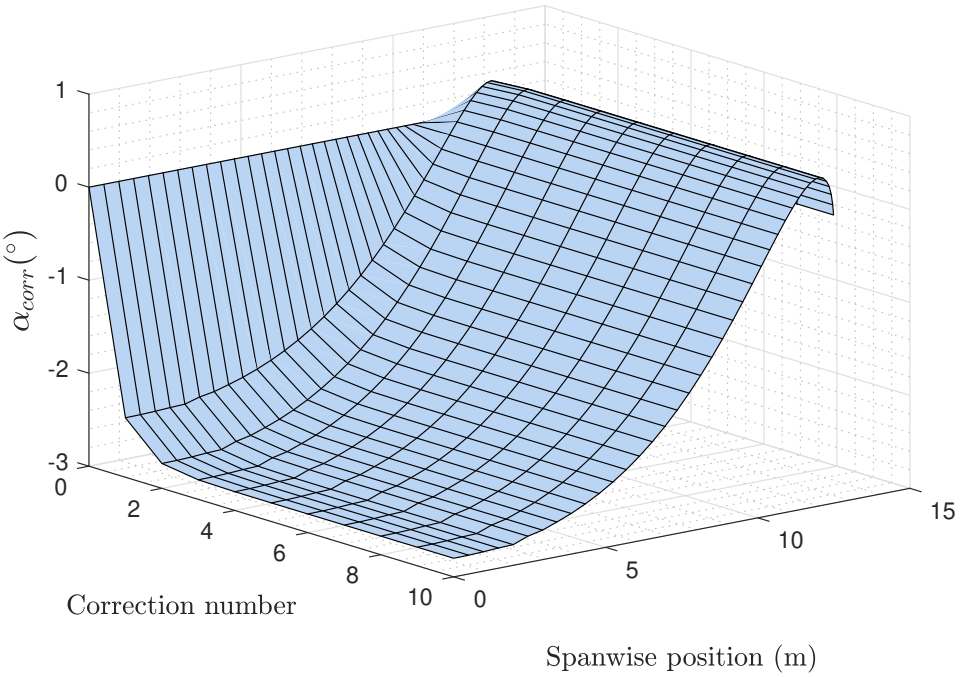

Figure 5.4: Evolution of α_{corr}, across the UAV wing span, for a static case where $\alpha = 16°$

Algorithm 1 Unsteady Coupling Algorithm

Solve the unsteady lifting line method to calculate the initial inviscid C_l distribution $C_{l_{\text{lin}}}(t,y)$
for Every strip y **do**
  Calculate the 2D unsteady lift coefficient, $c_{l_{\text{lin}}}(t,y)$
  Calculate the effective angle of attack
    $\alpha_{\text{eff}}^{3D}(t,y) = [C_{l_{\text{lin}}}(t,y) - C_{l_{\text{lin}}}(t,y)]/c_{l\alpha} + \alpha_{\text{Geom}}(t,y)$
  Using the Beddoes-Leishman model, calculate

$$C_{l_{\text{nonlin}}}(t,y)$$

  Calculate the correction to the angle of attack:
    $\alpha_{\text{corr}}(t,y) = [C_{l_{\text{nonlin}}}(t,y) - C_{l_{\text{lin}}}(t,y)]/c_{l\alpha} + \alpha_{\text{corr}}(t-\Delta t,y)$
  Update the angle at each station by $\alpha_{\text{corr}}(t,y)$
end for
The steps above are repeated until $\sum_{y=1}^{n}\left(C_{l_{\text{nonlin}}}(t,y) - C_{l_{\text{lin}}}(t,y)\right) < \epsilon$

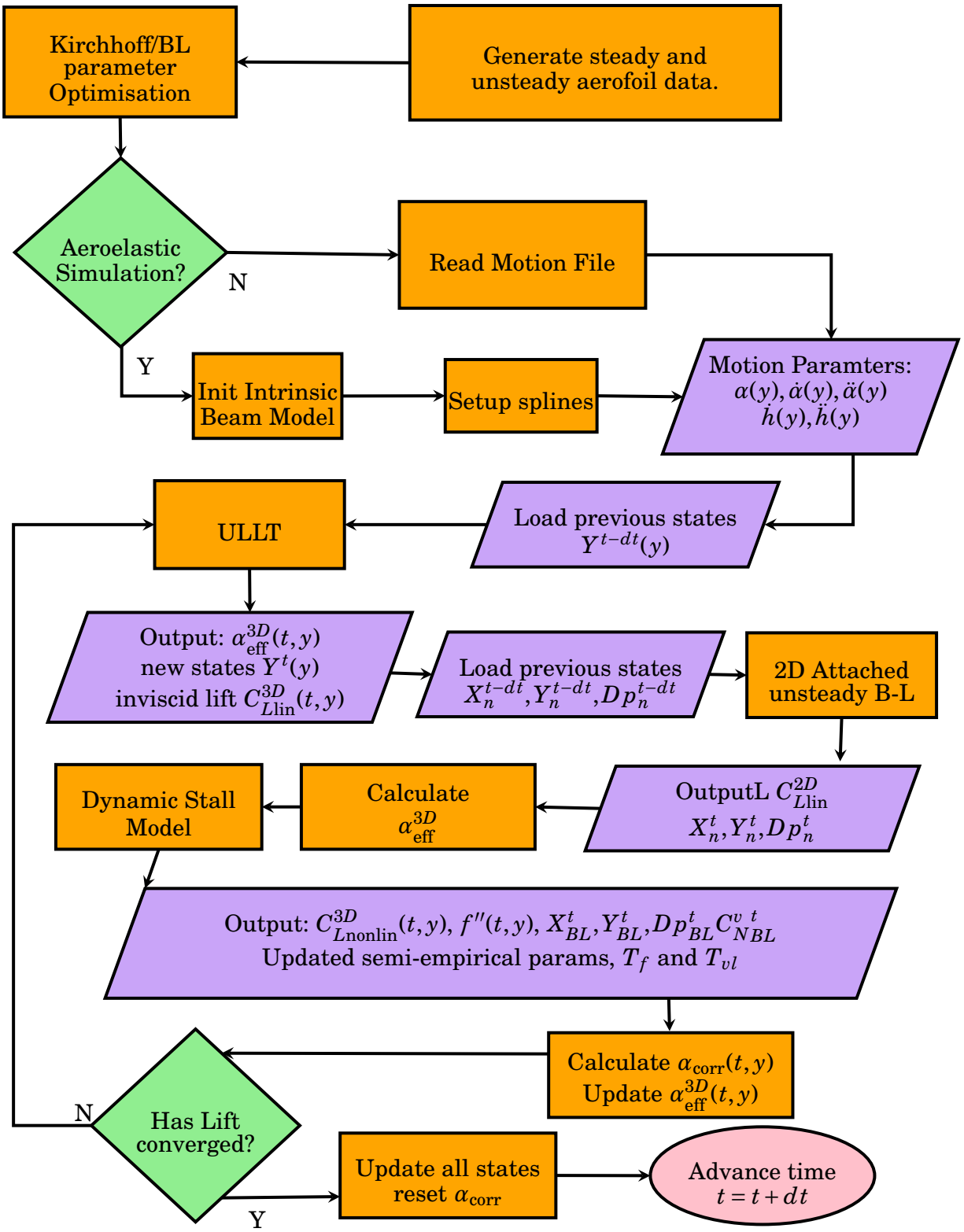

Figure 5.5: Flowchart of the coupled model

with the 3D data to build the model. It has been shown in Section 1.6 that it is difficult to achieve consistent unsteady separated results, even when using similar grid densities in different CFD solvers. Work by Sanchez Martinez *et al.*[122] document the difficulties of matching 2D CFD to experimental data. This is what makes the data collected by Piziali [12] attractive. Three different configurations are investigated. Firstly a two-dimensional configuration which includes an outboard splitter plate. The other two configurations are the three-dimensional cases, one wing model has a round tip whilst the other a square tip.

The wing model is straight, untwisted and has a span of 1.5240 m with a constant chord of 0.3048 m. The wing uses solely the NACA 0015 aerofoil section. The NACA 0015 typically experiences trailing edge stall [123] [44], which means it is thus suited to modelling with the Beddoes-Leishman model.

The static parameters in the Beddoes-Leishman model in section 3.4.1 were calculated using the averaged data from all spanwise measuring stations for all three runs conducted, with the correction placed on the lift coefficients acquired from the differential pressure transducers. These were then fitted using an exponential fit, similar to the original Beddoes-Leishman implementation [65]. This process is documented more thoroughly in Chapter 3, with the same data being used here. It should be noted that when fitting the static moment, the aerodynamic centre is found to be ahead of the quarter chord where it is expected to be for a symmetrical aerofoil and is accounted for in the moment fit.

In order to find the remaining parameters from the dynamic data, which comes in the form of pure pitching oscillations, a genetic algorithm is used as described in Chapter 3 to find the remaining parameters T_p, T_f, T_V, T_{vl} and C_{L_1}.

Once the semi-empirical coefficients are obtained, the 3D nonlinear unsteady lifting line theory can be used to estimate the three-dimensional force and moment distribution on the finite wing. Due to the fact only one aerofoil profile is present, the Beddoes-Leishman

C_{L_α}	α_{0L}	α_{ss}	S_1	S_2
6.2735	$-0.3173°$	$13.48°$	0.1350	0.0311

Table 5.1: Static parameters for the Beddoes-Leishman model, fitted from the experimental static data [12].

model only needs to be fitted once. This also reduces the amount of aerofoil data needed to generate the 3D model. Using the 3D nonlinear unsteady lifting line for wings with varying aerofoil sections has not yet been investigated.

5.2.2 Experimental Lift Results

Initially the new coupled model is run with a quasi-steady input ($k = 0.001$), a pure pitching motion with $\alpha_0 = 10°$ and $\alpha_1 = 10°$. The results for this are displayed in Figures 5.6(a) and 5.6(b). The resulting lift coefficient distribution predicted by the model gives a very good representation of the quasi-steady experimental data. The spanwise critical angle is well captured, along with the C_l in the post-stall region. This clearly shows the three-dimensional separation mechanism is similar to that of the 2D section. Therefore with just 2D data, the 3D static lift can be very well modelled using the new coupled methodology.

Even at low angles of attack when separation is not playing a significant role, a correction is implemented through the lift curve slope and zero-lift angle of attack. The first unsteady results presented are under nominally attached flow. For this reason an inviscid result, i.e. with the separation position forced to the trailing edge is not included in the figures. The lift coefficient time history is shown in Figures 5.7(a) and 5.7(b). This is also supplemented by Figures 5.8 and 5.9, which consist of four 2D plots. The Figures contain the responses at the four spanwise positions where the experimental data was acquired for direct comparison. The largest error observed in the case displayed in Figure 5.7(a) is 5%, this occurs on the strip located at $y/b = 0.475$. This seems to be a systematic error since all other spanwise strips have an error less than 1%, even for

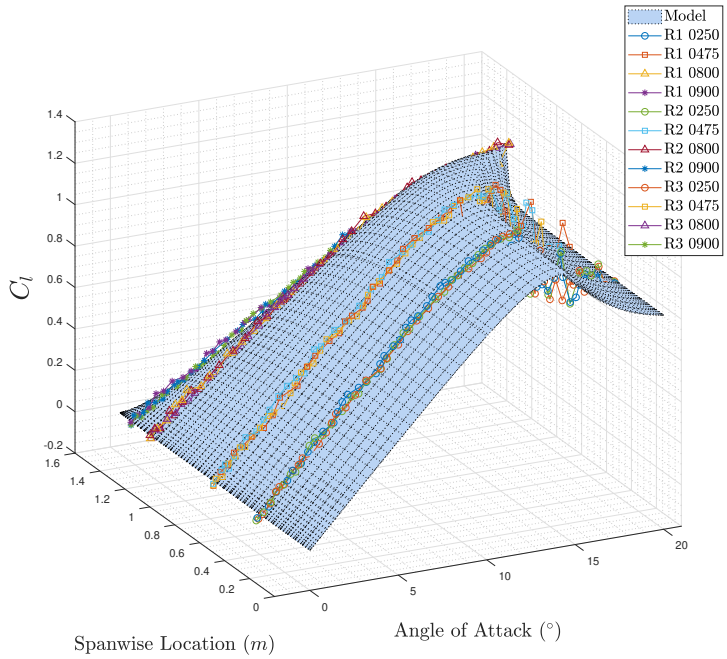

(a)

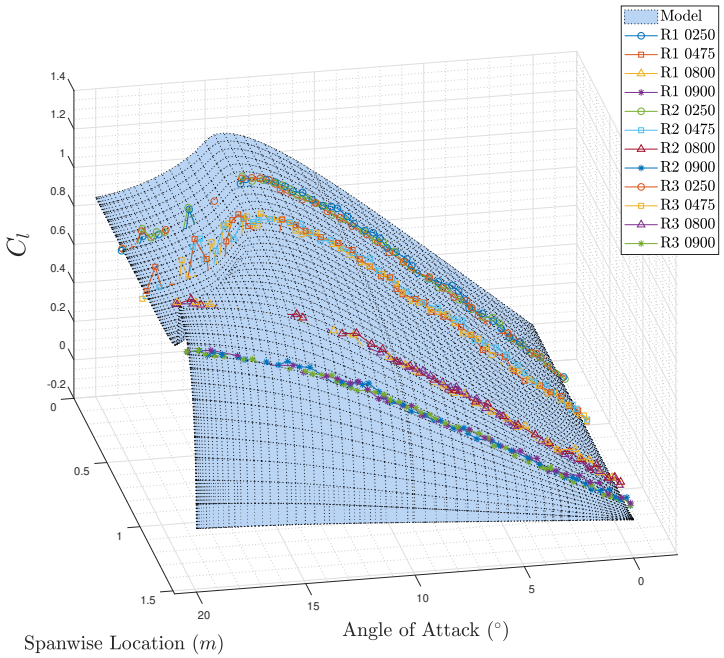

(b)

Figure 5.6: Model v 3D Quasi-steady Experimental Data. R1 - R3 represent the repeat number in the Piziali report [12].

locations near the tip. The amplitude of the pitching motion is then increased to 4° and the reduced frequency increased to a value of $k = 0.095$. Here the lift response is well captured producing an anti-clockwise elliptical loop. Note that uncorrected potential flow methods will always produce an anti-clockwise C_l loop when pitching around the aerodynamic centre, as mentioned in Chapter 2. It is in fact the separation that causes the loop reversal in this case. The reason for this is that when the wing is pitching up, the positive $\dot{\alpha}$ term causes a reduction in lift, and vice versa, however the separated flow conditions override this behaviour.

The mean angle of attack is increased so that $\alpha_0 \approx \alpha_{SS}$. This allows for a considerable amount of separation, $f < 0.7$, however leading edge separation does not occur and therefore the vortex lift module remains inactive. Figure 5.10(a) shows the lift hysteresis loop for the motion $\alpha = 12.96° \pm 2.05°$. Here the uncorrected solution still predicts an elliptical lift hysteresis loop with an anti-clockwise direction. However due to the lag in the movement of the separation position, the lift loop becomes thicker and importantly the direction of the viscous loop becomes clockwise. The reversal of the loop and delay in the separation position is captured by the model, giving a much more realistic result than the purely inviscid model. The comparison of the measured experimental data and the nonlinear unsteady lifting line theory is shown in Figure 5.11. Increasing the oscillation amplitude to 4° causes the wing to experience greater amounts of flow separation, the results are shown in Figures 5.10(b) and 5.12. The elliptical shape is no longer apparent now the flow is dominated by separation.

Two further cases are presented, both with a reduced frequency of 0.095. The sectional lift coefficient response for the wing undergoing a pitching oscillation of $\alpha = 12.98° \pm 4.16° \sin(0.095S)$ is shown in Figure 5.13(a). The NULLT is able to predict a good agreement with the CFD, capturing the upstroke and peak lift well, this is highlighted in Figure 5.14. The downstroke is also captured closely for the outboard strips located at $y/b = 0.800$ and $y/b = 0.900$. However, once again the model predicts premature reat-

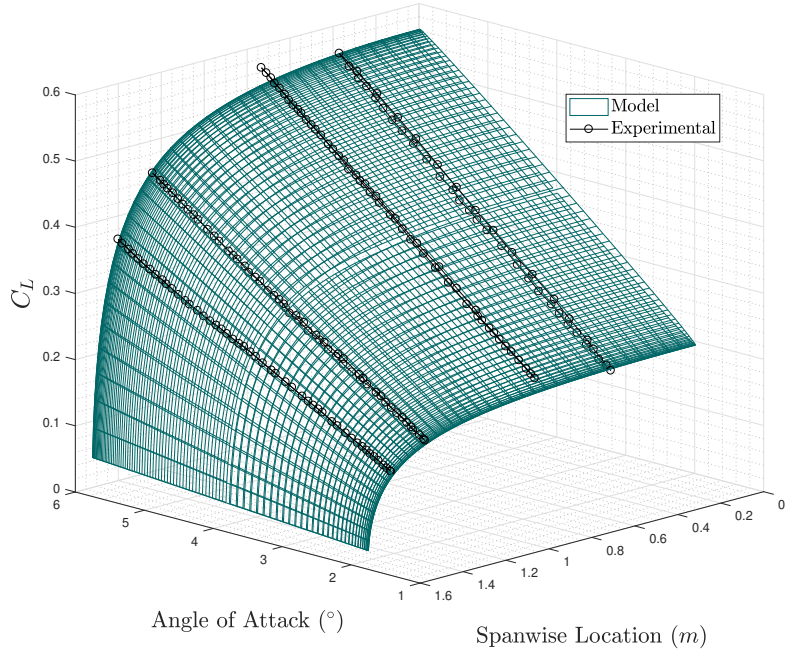

(a) $\alpha = 3.99° + 2.00° \sin(0.038S)$

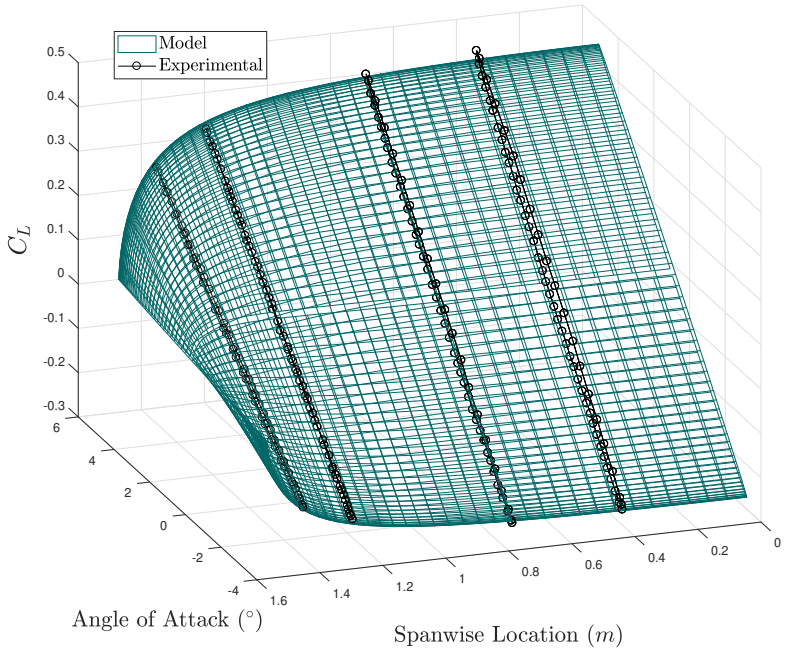

(b) $\alpha = 0.95° + 4.15° \sin(0.095S)$

Figure 5.7: C_l surface for nominally attached flow conditions

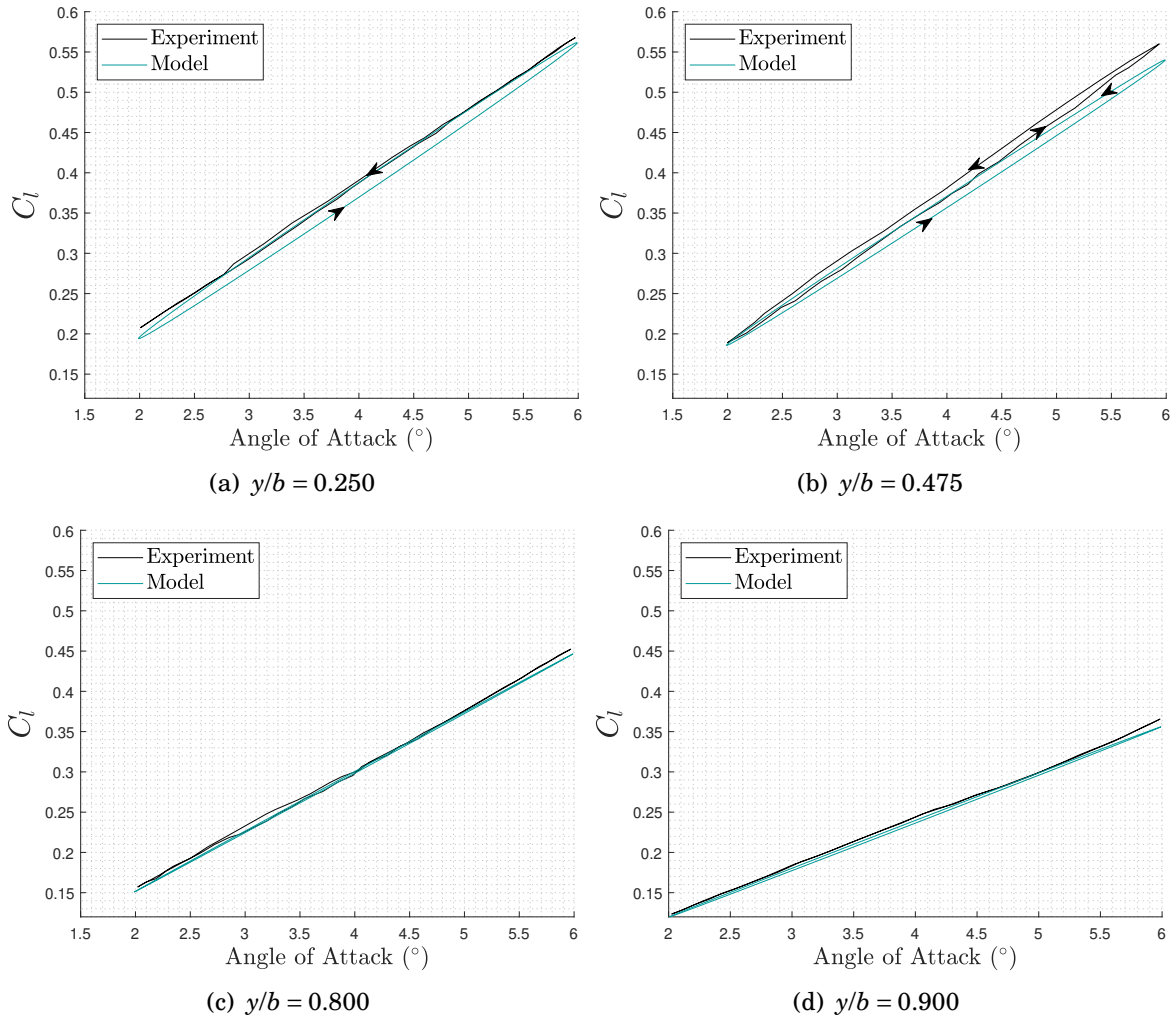

(a) $y/b = 0.250$ (b) $y/b = 0.475$

(c) $y/b = 0.800$ (d) $y/b = 0.900$

Figure 5.8: $\alpha = 3.99° + 2.00° \sin(0.038S)$. Note that the direction arrows for the hysteresis loop is left out of (c) and (d) since little hysteresis is present.

tachment, on the downstroke further inboard which as previously mentioned, may be helped by a more advanced variation of the Beddoes-Leishman model. The next case is for the pitching oscillation $\alpha = 15.03° \pm 2.04° \sin(0.095S)$ and is shown in Figure 5.13(b). Once again model response at the outboard strips ($y/b = 0.800$ and $y/b = 0.900$) offer very good agreement, shown in Figure 5.15, likely due to less severe flow separation. A reasonable prediction is also found at the other spanwise locations, offering a much better approximation than the uncorrected unsteady lifting line, which once again fails to capture the hysteresis loop direction.

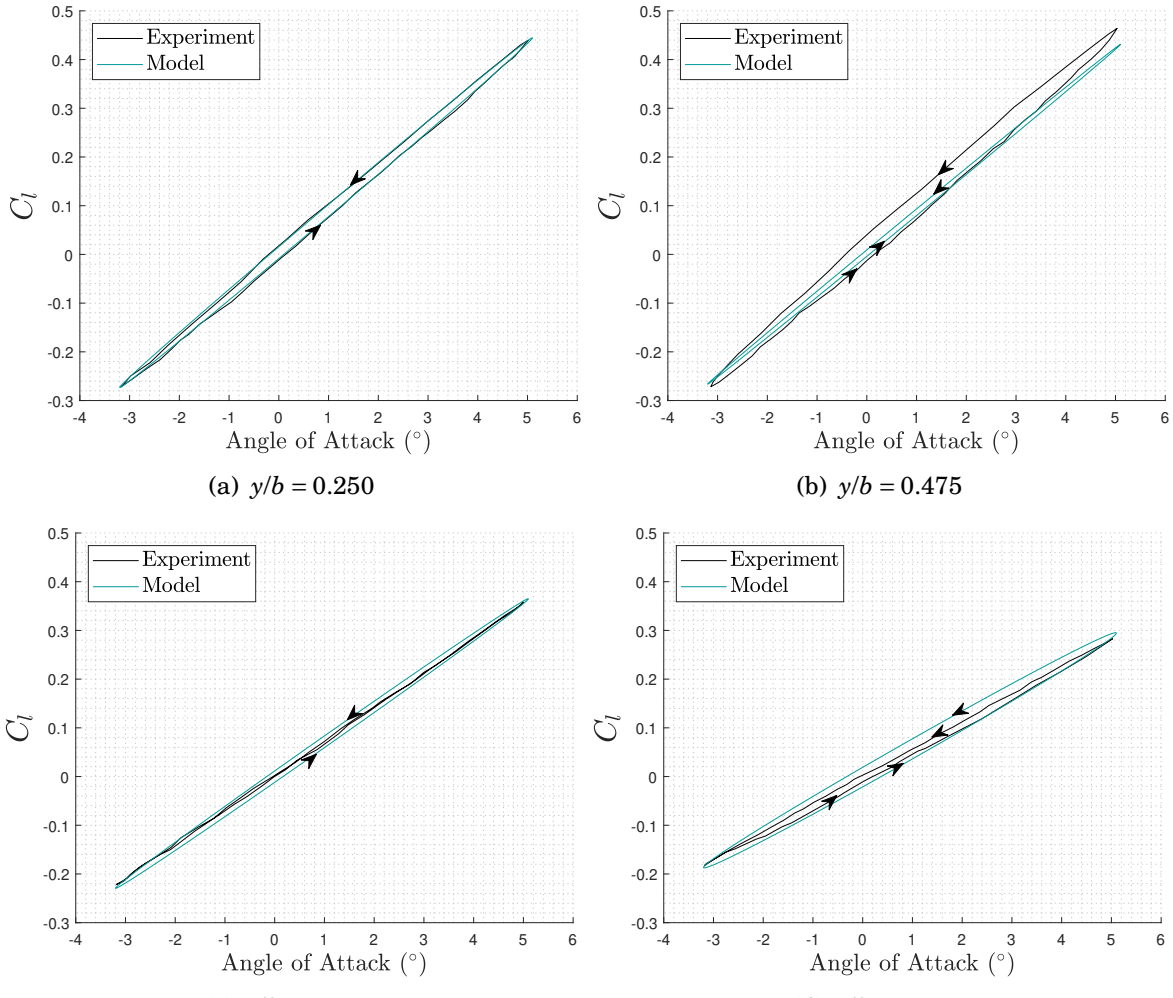

(a) $y/b = 0.250$ (b) $y/b = 0.475$

(c) $y/b = 0.800$ (d) $y/b = 0.900$

Figure 5.9: $\alpha = 0.95° + 4.15° \sin(0.095S)$

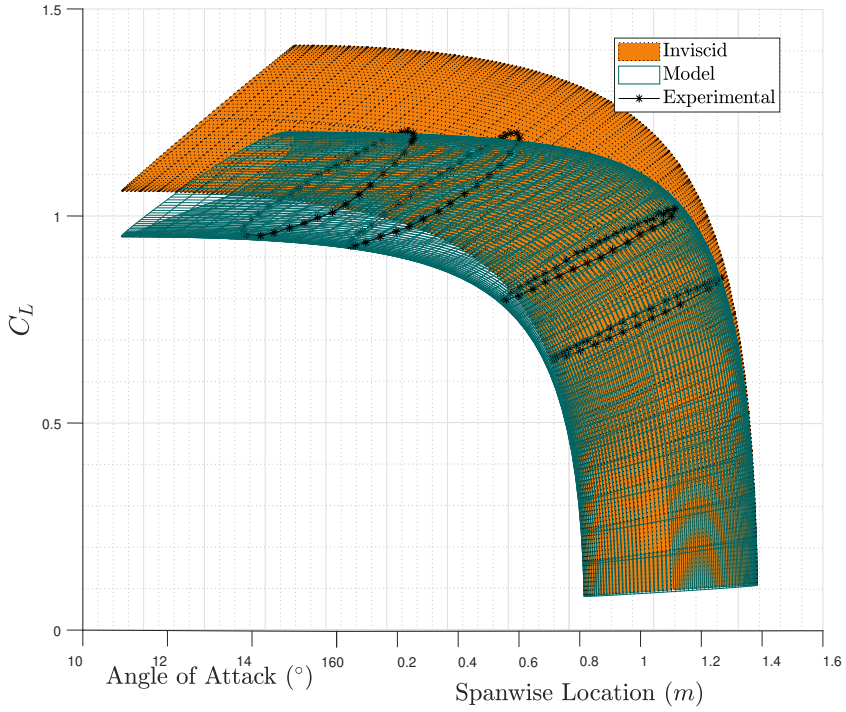

(a) $\alpha = 12.96° \pm 2.05° \sin(0.095S)$

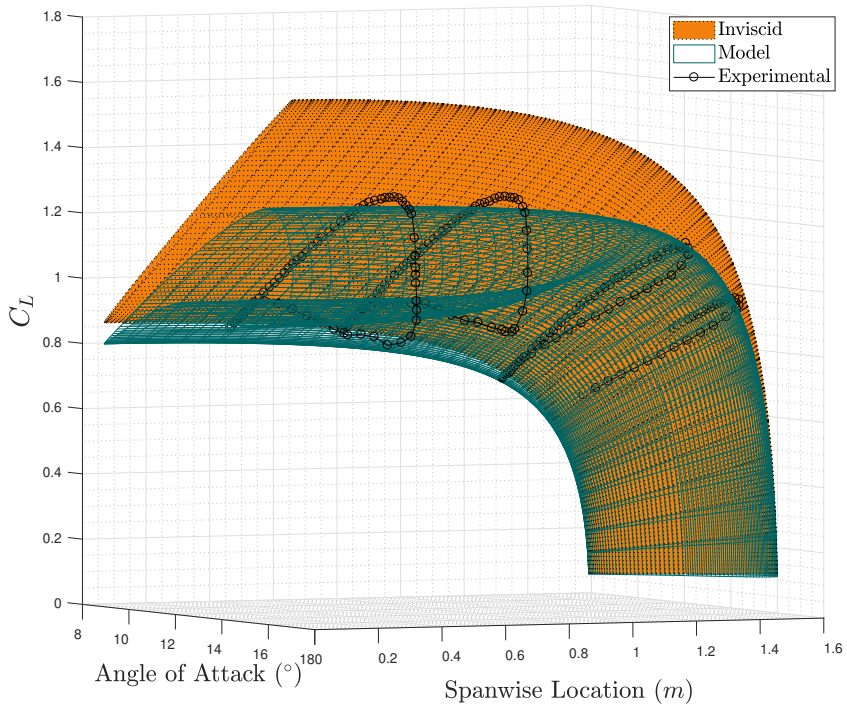

(b) $\alpha = 13.00° \pm 4.06° \sin(0.038S)$

Figure 5.10: Unsteady nonlinear lifting line against experimental data

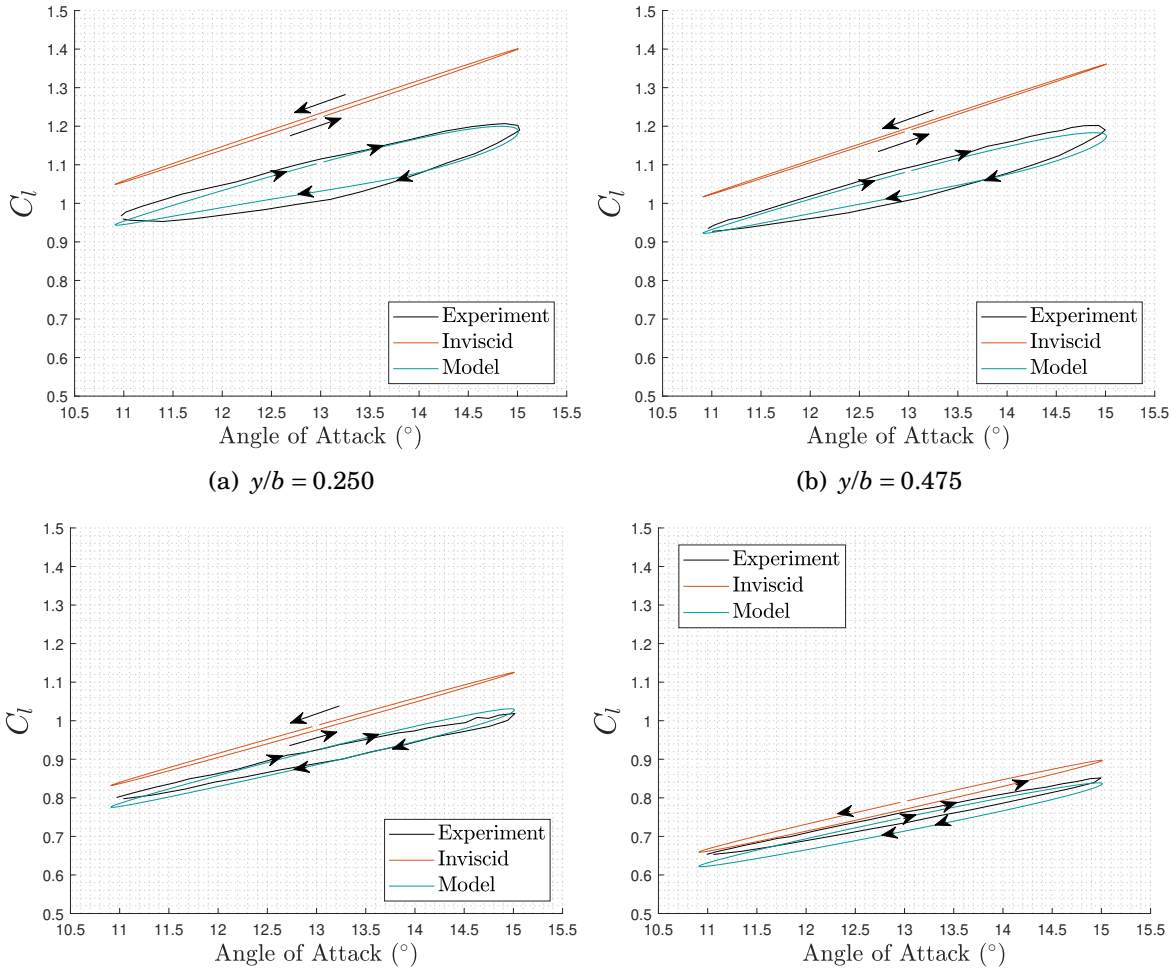

(a) $y/b = 0.250$

(b) $y/b = 0.475$

(c) $y/b = 0.800$

(d) $y/b = 0.900$

Figure 5.11: $\alpha = 12.96° \pm 2.05° \sin(0.095S)$

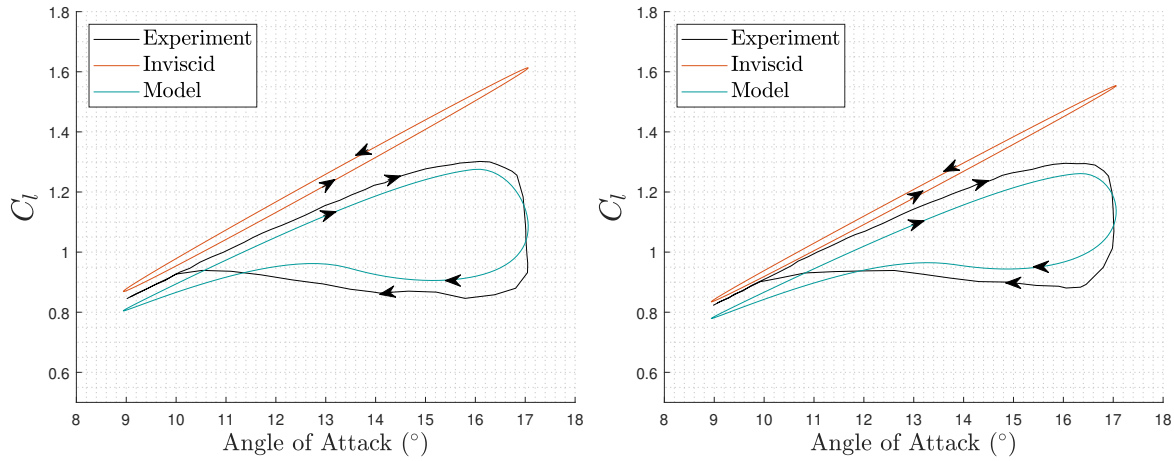

(a) $y/b = 0.250$

(b) $y/b = 0.475$

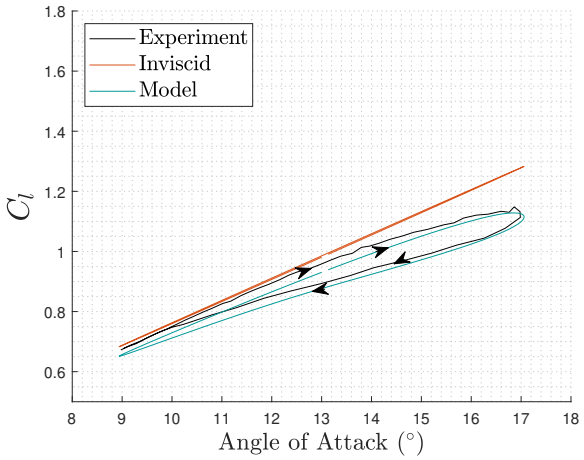

(c) $y/b = 0.800$

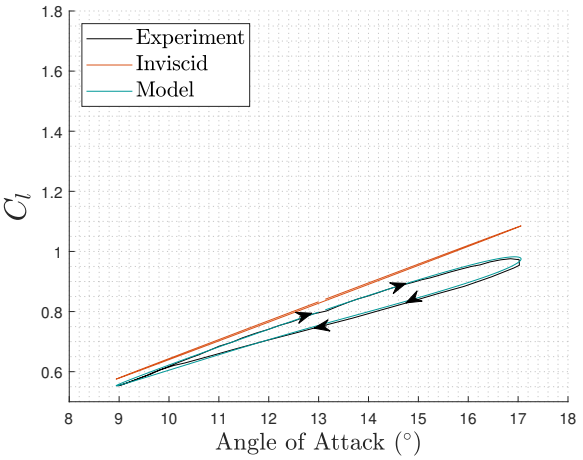

(d) $y/b = 0.900$

Figure 5.12: $\alpha = 13.00° \pm 4.06° \sin(0.038S)$

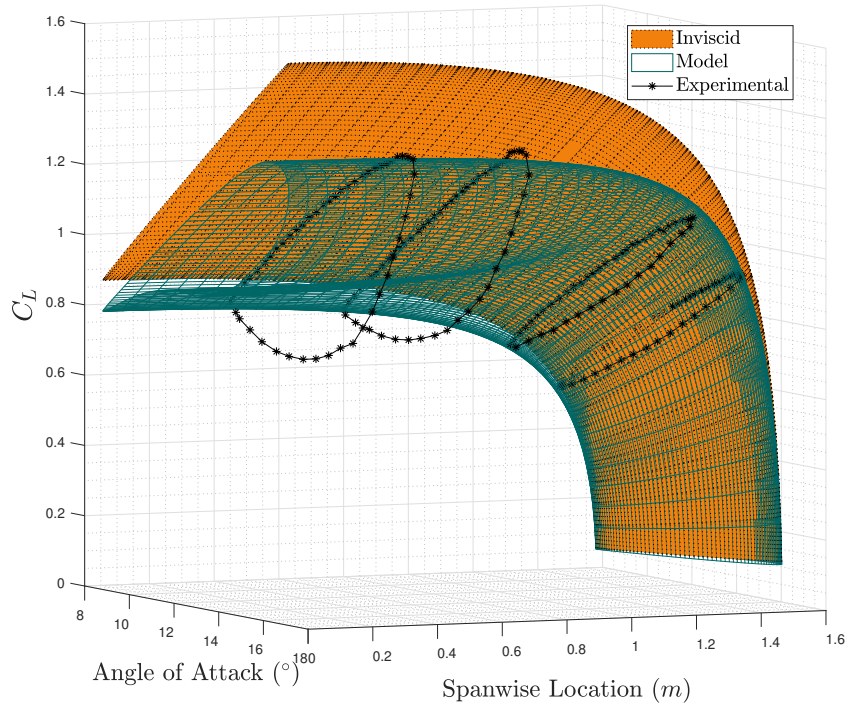

(a) $\alpha = 12.98° \pm 4.16° \sin(0.095S)$

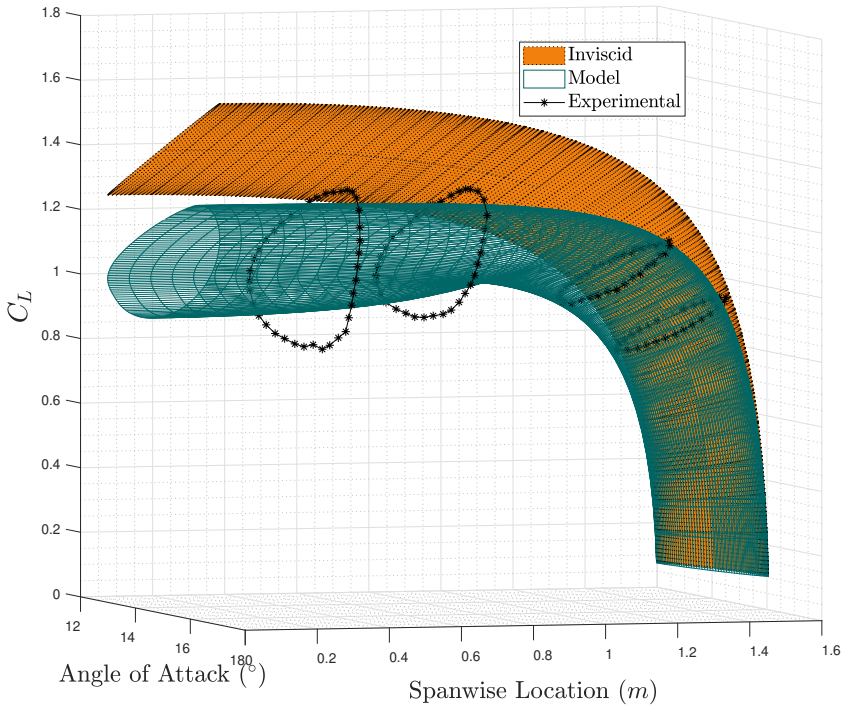

(b) $\alpha = 15.03° \pm 2.04° \sin(0.095S)$

Figure 5.13: Unsteady nonlinear lifting line against experimental data

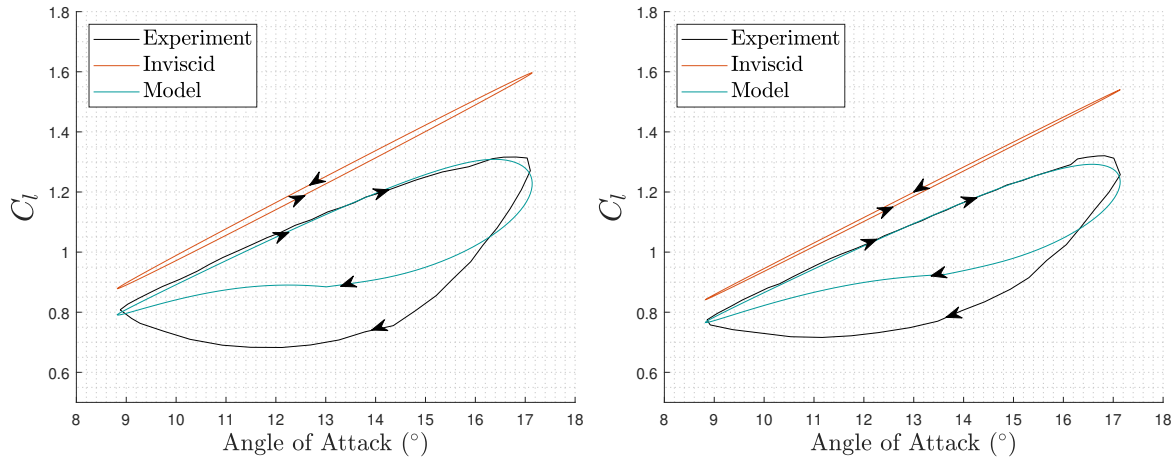

(a) $y/b = 0.250$

(b) $y/b = 0.475$

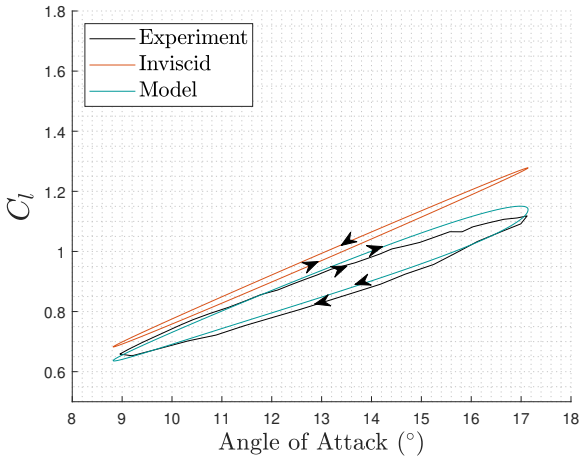

(c) $y/b = 0.800$

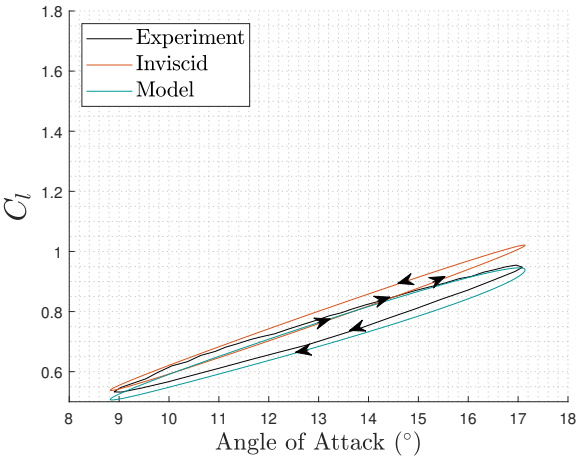

(d) $y/b = 0.900$

Figure 5.14: $\alpha = 12.98° \pm 4.16° \sin(0.095S)$

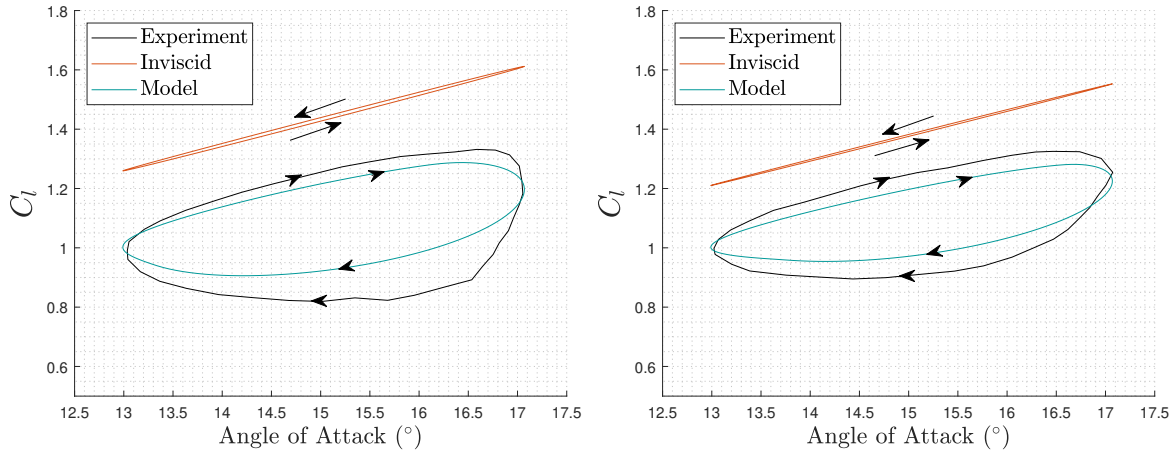

(a) $y/b = 0.250$

(b) $y/b = 0.475$

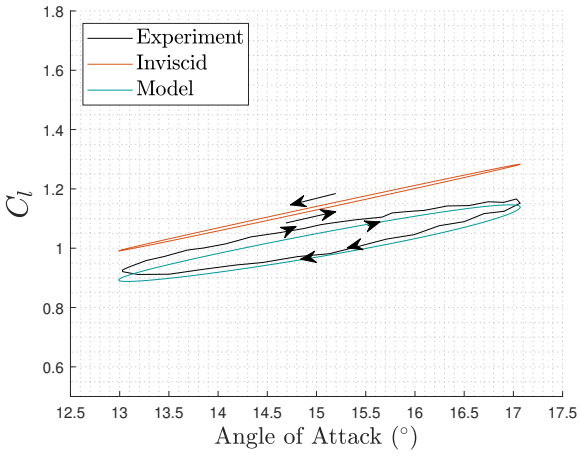

(c) $y/b = 0.800$

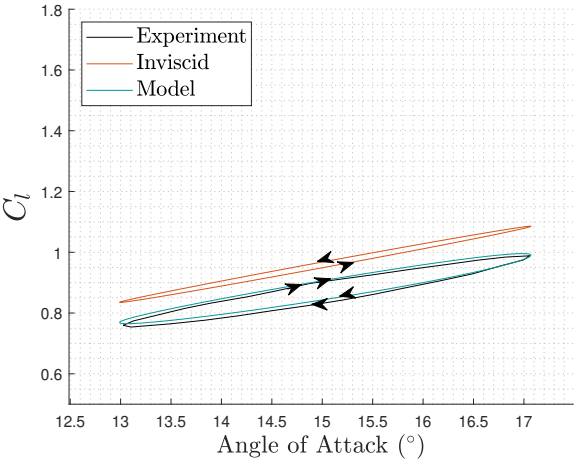

(d) $y/b = 0.900$

Figure 5.15: $\alpha = 15.03° \pm 2.04° \sin(0.095S)$

The mean angle of attack is further increased to $\alpha_0 = 17.12°$ with amplitude $\pm 4.04°$ and the results are presented in Figure 5.16(a) with the 2D comparison to measured experimental data in Figure 5.17. Here the overall geometry of the lift coefficient loops are captured remarkably well, including the variation of the shape along the span which would be missed if using strip theory. The lift coefficient is over-estimated compared to the absolute pressure transducer values at the $y/b = 0.475$. One possible explanation for this behaviour is the aforementioned correction applied to the differential pressure transducers as stated in Section 5.2.1. The data used for the 2D dynamic stall model was fitted using three differential pressure transducers, leaving just one absolute and the correction applied to them is not well defined in the post-stall regime. It is foreseeable that the model will agree more favourably to the absolute pressure transducers compared to the differential results.

Keeping the mean angle of attack $\approx \alpha_0 = 17°$ but reducing the amplitude to $\pm 2°$ appears to create a more difficult condition for the model to handle. From the experimental data, which is displayed in Figures 5.16(b) and 5.18, there appears to be stall cells forming on the wing, highlighted by the reduction in the lift coefficient at $y/b = 0.475$. The model gives a reasonable prediction for the lift coefficient at the $y/b = 0.250$, 0.800 and 0.900 stations. In the region of the midspan, the model forms a localised reduction in the lift coefficient. In order to capture the curvature in the region, the number of strips is increased to 80 and spatial convergence does appear to be found. There are not enough cases or data resolution presented in the region to pass judgement as to whether this is something physical or numerical.

In the three-dimensional data, the shapes of the hysteresis loops are similar to those found in the two-dimensional data, albeit occurring at different geometric angles of attack. This gives a positive indication that the methodology applied to model the finite wing has a sound basis.

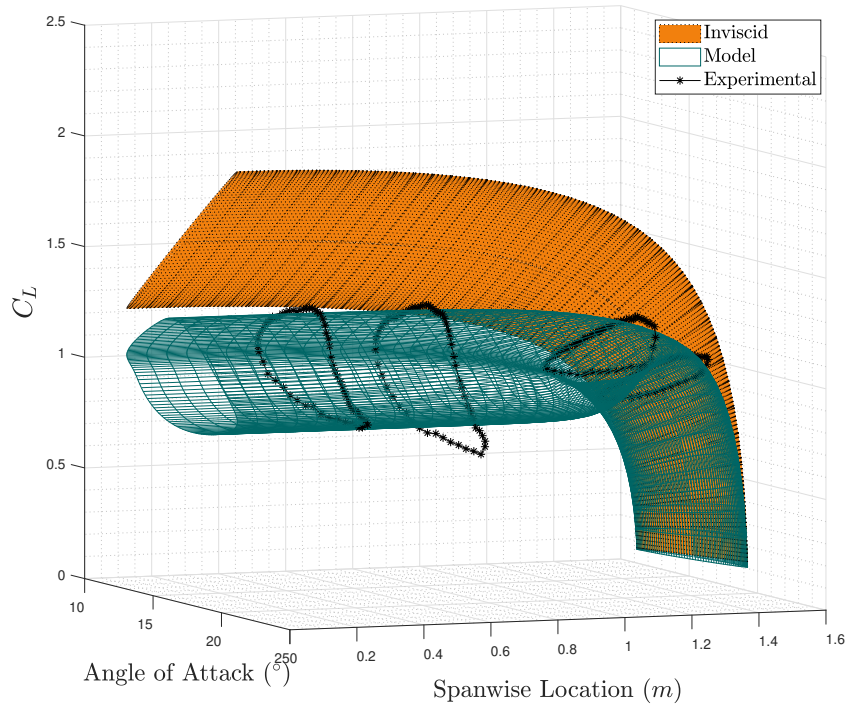

(a) $\alpha = 17.12° \pm 4.04° \sin(0.038S)$

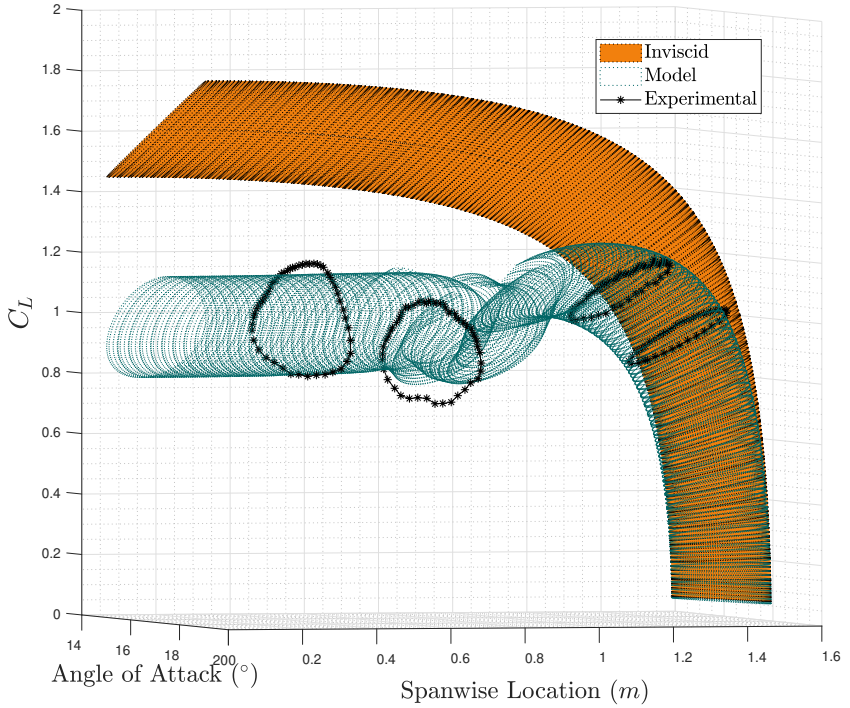

(b) $\alpha = 17.05° \pm 2.03° \sin(0.095S)$

Figure 5.16: Unsteady nonlinear lifting line against experimental data

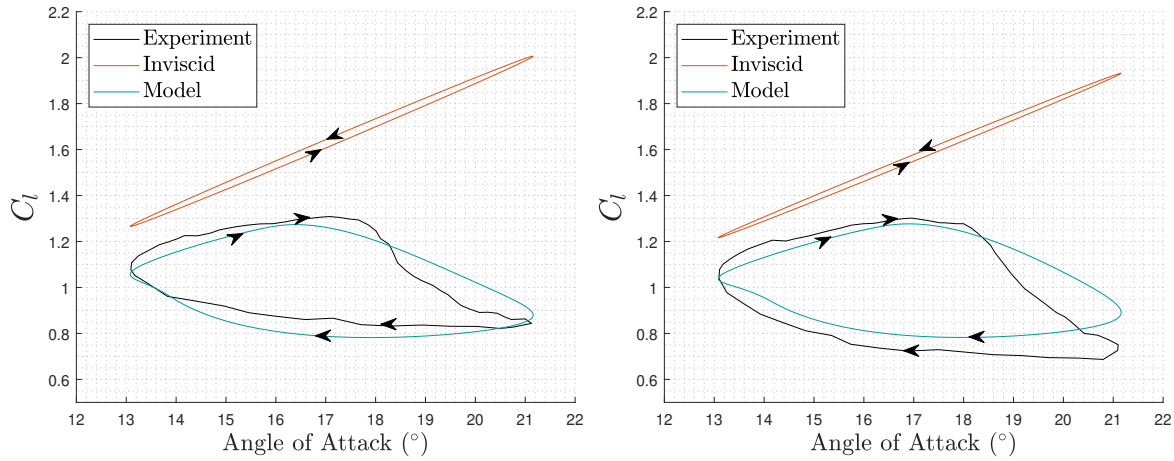

(a) $y/b = 0.250$

(b) $y/b = 0.475$

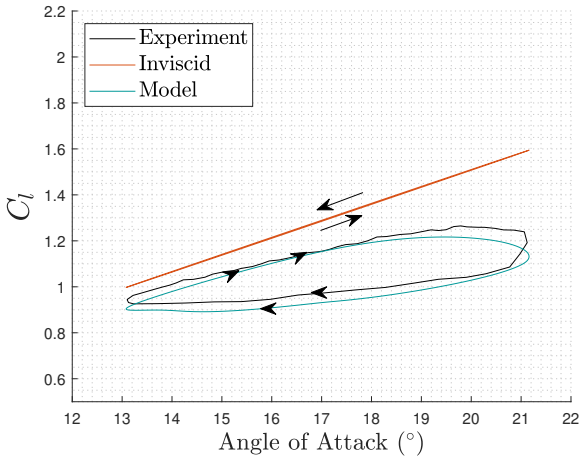

(c) $y/b = 0.800$

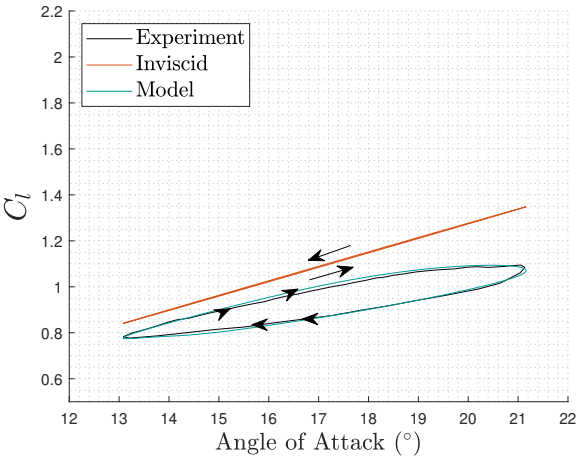

(d) $y/b = 0.900$

Figure 5.17: $\alpha = 17.12° \pm 4.04° \sin(0.038S)$

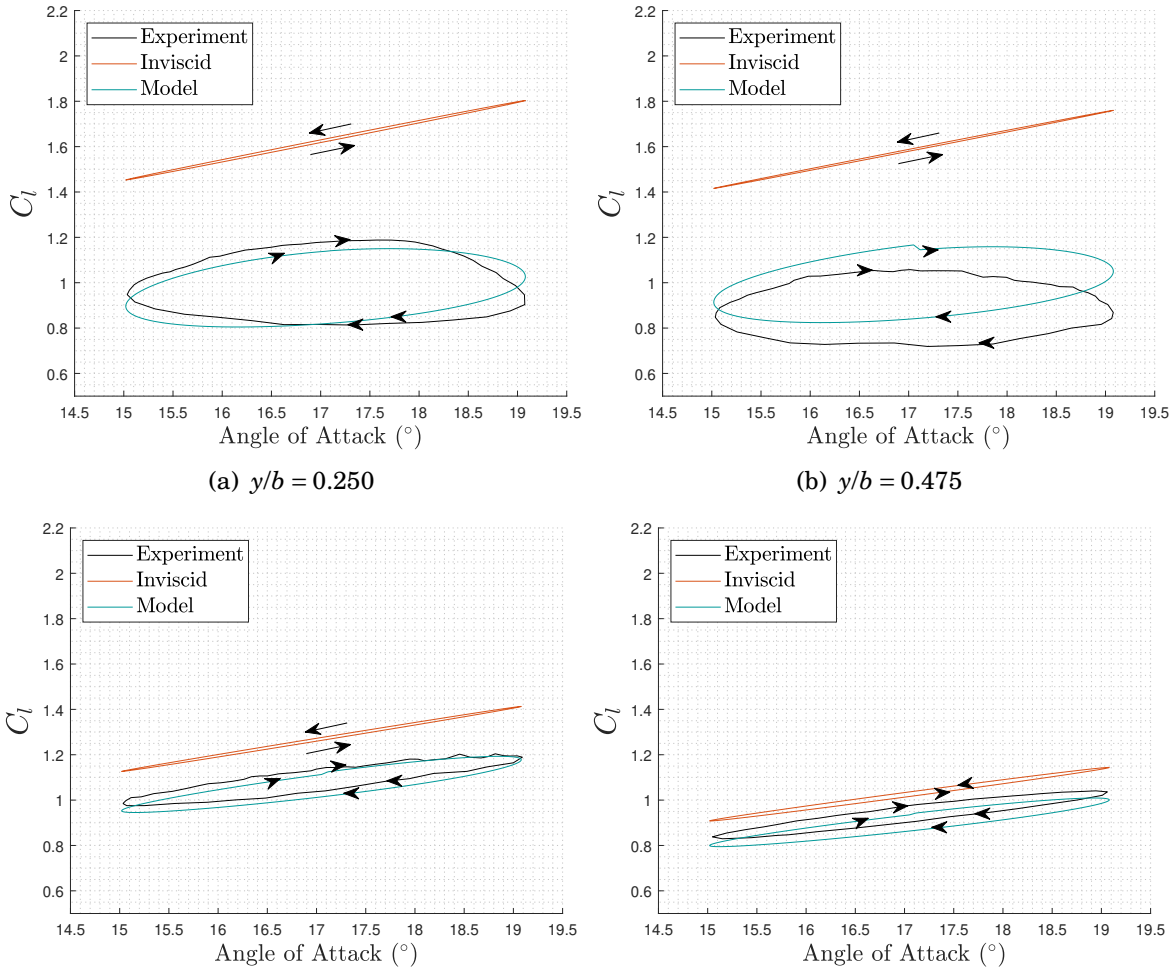

(a) $y/b = 0.250$

(b) $y/b = 0.475$

(c) $y/b = 0.800$

(d) $y/b = 0.900$

Figure 5.18: $\alpha = 17.05° \pm 2.03° \sin(0.095S)$

5.2.3 Experimental Moment Model Results

Here, moment model within the B-L model uses a relationship between the lift coefficient under separated flow, along with the lagged separation position as discussed in Chapter 3. The three-dimensional augmentation to the moment coefficient is introduced through the corrected separation position due to the 3D effects. Whilst this model is simple, it provides a method for the moment to be incorporated into the 3D unsteady lifting line that has some basis around the 3D unsteady separated flow because the spanwise separation position is an output of the new model. Overall the moment model is able to capture the general behavior of the moment. However the behaviour at the tip is not as well matched compared to the C_l, with the experimental results showing a systematic increase in C_m. This is due to the fact the tip produces little lift, the moment model predicts C_m values close to the zero-lift moment, C_{m0}. This can be most clearly shown in the quasi-steady case in Figure 5.19, where the maximum error at the section $y/b = 0.90$ is 35.4% at $\alpha = 19.8°$. This is also where the maximum C_m occurs. The error is largest here due to an inconsistency with the moment curve slope, c_{m_α}. However the delayed onset of moment stall is captured, with an approximately linear response between the moment coefficient and the angle of attack. Figure 5.20 shows four 2D plots for the measured experimental data along with the nonlinear unsteady lifting line outputs at the same spanwise positions for further clarification.

As previously noted, the only absolute pressure transducer is located at the spanwise station $y/b = 0.475$, all other stations with differential pressure transducers are corrected against the absolute data. The model gives a more favourable results where the absolute pressure transducers are used. Here, moment stall is very well replicated, with an error of 4.37% at $\alpha = 13.7°$ where static stall occurs. The response in the post-stall region is also well captured: the experimental data is not smooth and the model cannot match some of the noise that seems inherent in the experimental data, however the general trend for the quasi-steady case is qualitatively good.

The behaviour is similar for the spanwise stations y/b = 0.250 and 0.800. In fact the region close to moment stall at $y/b = 0.800$ is very well captured with error less than 5%. However a moment curve slope error, which is less severe than at $y/b = 0.900$, is present and seems to favour higher angles of attack.

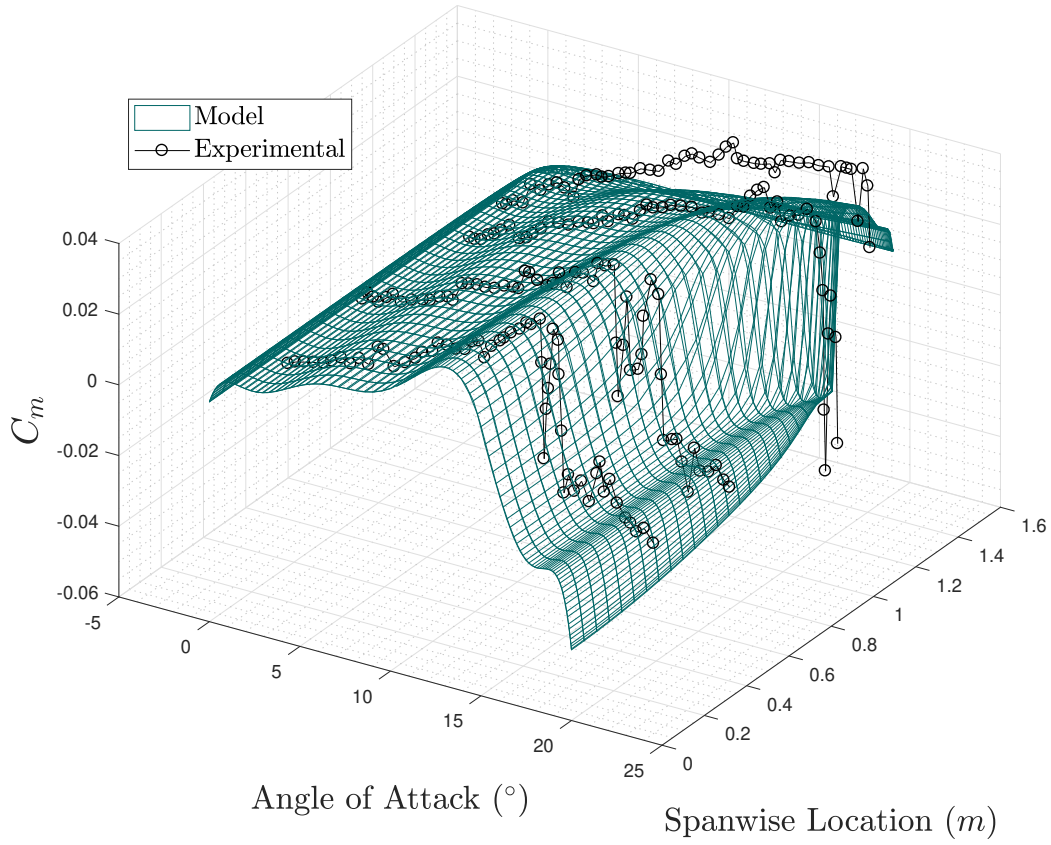

Figure 5.19: Model and experimental data for quasi-steady C_m

When looking at the unsteady moment response the experimental accuracy must be considered. Firstly the experimental moment data has a linear trend in the pre-stall region, however there are many deviations from the original trend that do not seem to be from a consistent and underlying flow phenomenon. To add to this, a correction is applied to the absolute pressure transducers which is obtained from a very limited dataset. Unlike in the quasi-steady data where a large range in angle of attack is displayed, it has to be understood that when only small deviations in angle are shown, discrepancies between the moment are to be expected. It is useful to consider the qualitative shape of

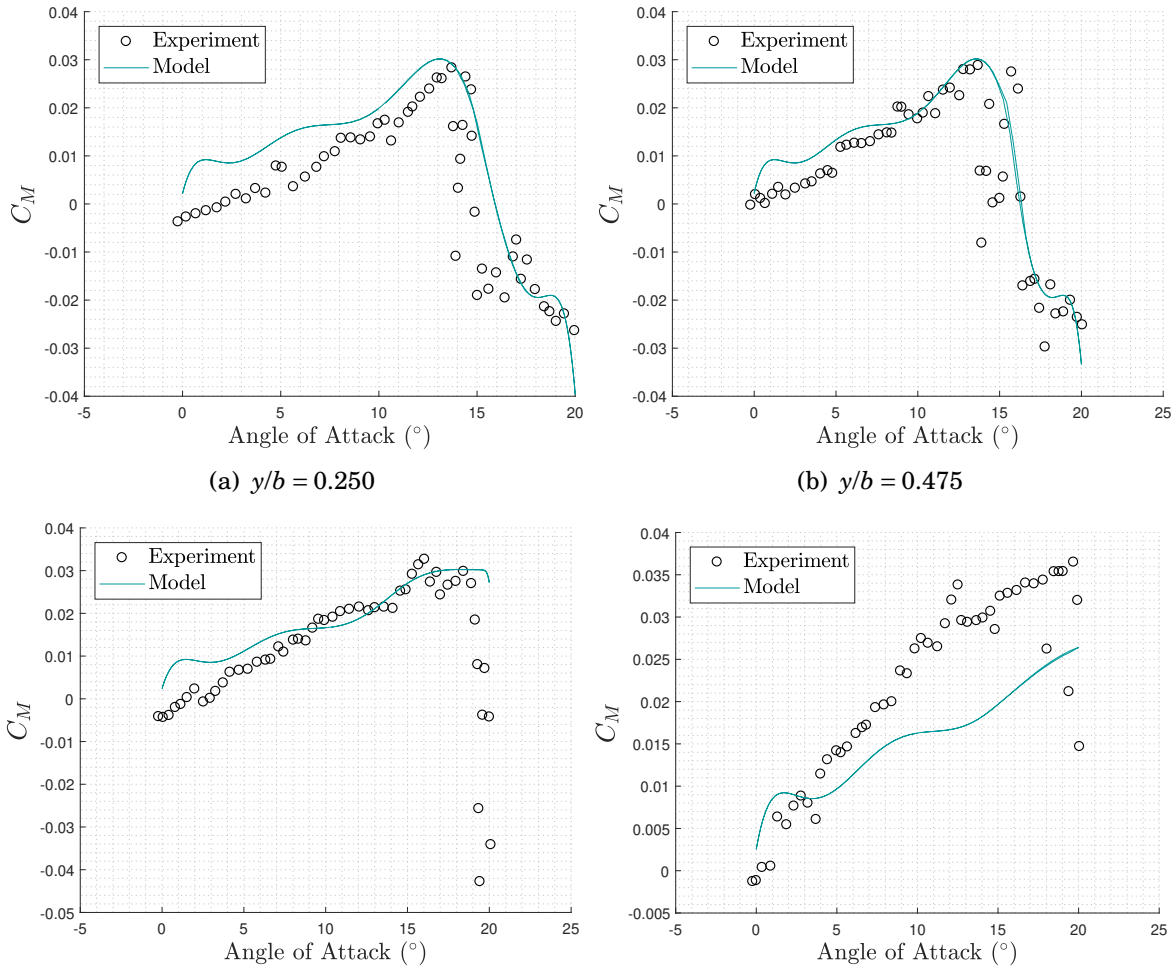

(a) $y/b = 0.250$ (b) $y/b = 0.475$

(c) $y/b = 0.800$ (d) $y/b = 0.900$

Figure 5.20: Model and experimental data for quasi-steady C_m

the moment response, not just the absolute value.

The lowest mean angle of attack case presented is $\alpha_0 = 11°$, with a variation in angle of attack of 2°, see Figures 5.21(a) and 5.22. The moment is well matched when compared to the stations located at $y/b = 0.250$ and 0.475. The maximum error when looking at these aforementioned two strips is 19% and this is using data from the differential pressure transducer during the down-stroke. When considering the rather crude correction used this is very reasonable. The result is substantially better when the wing is pitching up. The error however, as seen in the quasi-steady behaviour, increases near the tip. It ap-

pears that unless the quasi-steady data could be better reproduced, the unsteady results will not be close to the experiment in this region. The results at the tip could perhaps be improved by adding missing impulsive terms in the Beddoes-Leishman formulation. However this pitching oscillation is at a relatively low reduced frequency and the impact of the impulsive terms are likely low.

Increasing the mean angle of attack to 13° and increasing the pitching amplitude to 4°, the experimental data now shows two intersecting loops forming a figure of eight shape, see Figure 5.21(b) for the surface plot and Figure 5.23 for the 2D slices. Away from the tip, this is well captured with the model outputting a similar response. In fact, the model very closely predicts the intersection of the moment loop. The intersection is present at $\alpha = 13.53°$ for the span location $y/b = 0.475$ whilst the model predicts this to happen at $\alpha = 13.13°$. However in the experimental data there is a rapid reduction in moment at the top of the stroke and this is not captured in the model. The aforementioned spike in moment is contained within the final 0.5° and is not present in the quasi-steady data. This is likely due to a dynamic stall vortex which causes a sharp pitch-down moment when it passes aft of the centre of pressure, which is not captured by the model. Including a more advanced version of the B-L model could help capture this behaviour.

With the mean angle of attack held at 13°, the pitching amplitude reduced to 2° and the reduced frequency increased to 0.95, the moment surface still produces the figure of eight response as seen in Figures 5.24(a) and 5.25. On this occasion, the moment intersection is contained to just the strip closest to the root. This is mimicked by the model, with the intersection ceasing before reaching the spanwise location $y/b = 0.475$. Once again the tip is under predicted, the experimental data at $y/b = 0.90$ is centered around the value $C_m \approx 0.035$. Along with this, the model does not perform as well during the downstroke, with the moment being consistently overestimated.

The final case presented is for deep stall where the mean angle of attack is 17.12°. This

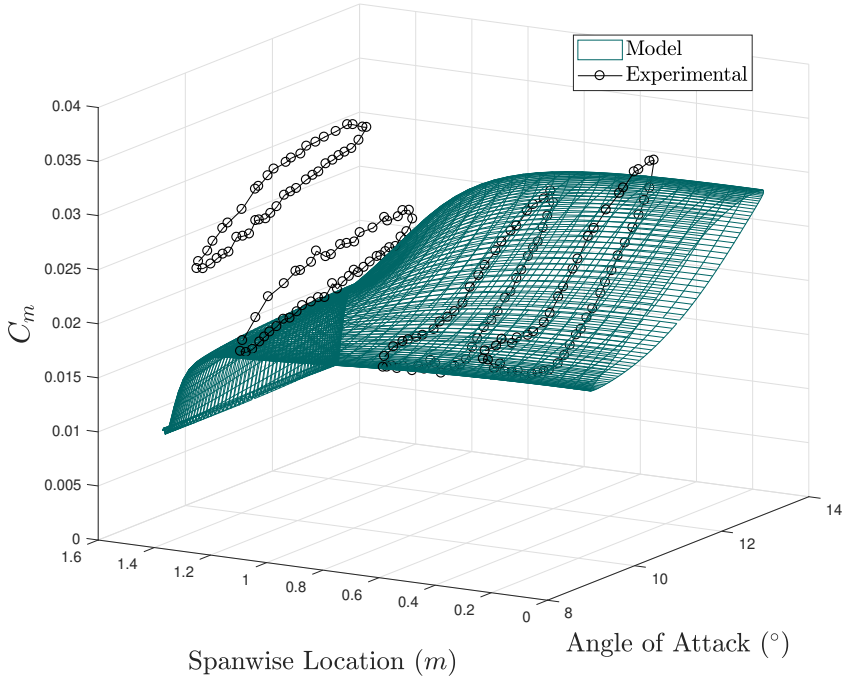

(a) $\alpha = 10.97° \pm 1.99° \sin(0.038S)$

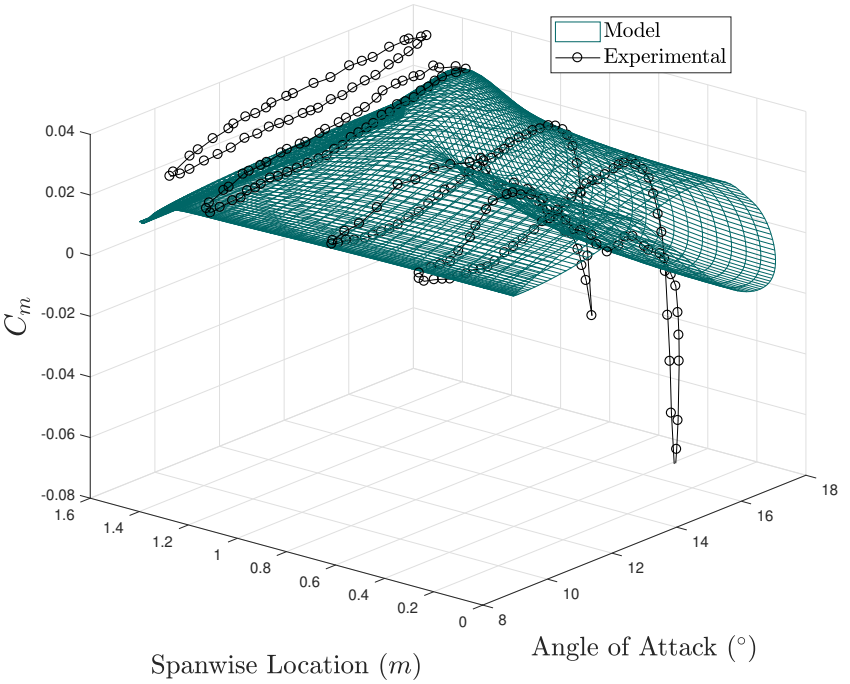

(b) $\alpha = 13.00° \pm 4.06° \sin(0.038S)$

Figure 5.21: Example database with decomposition for directly using 2D URANS

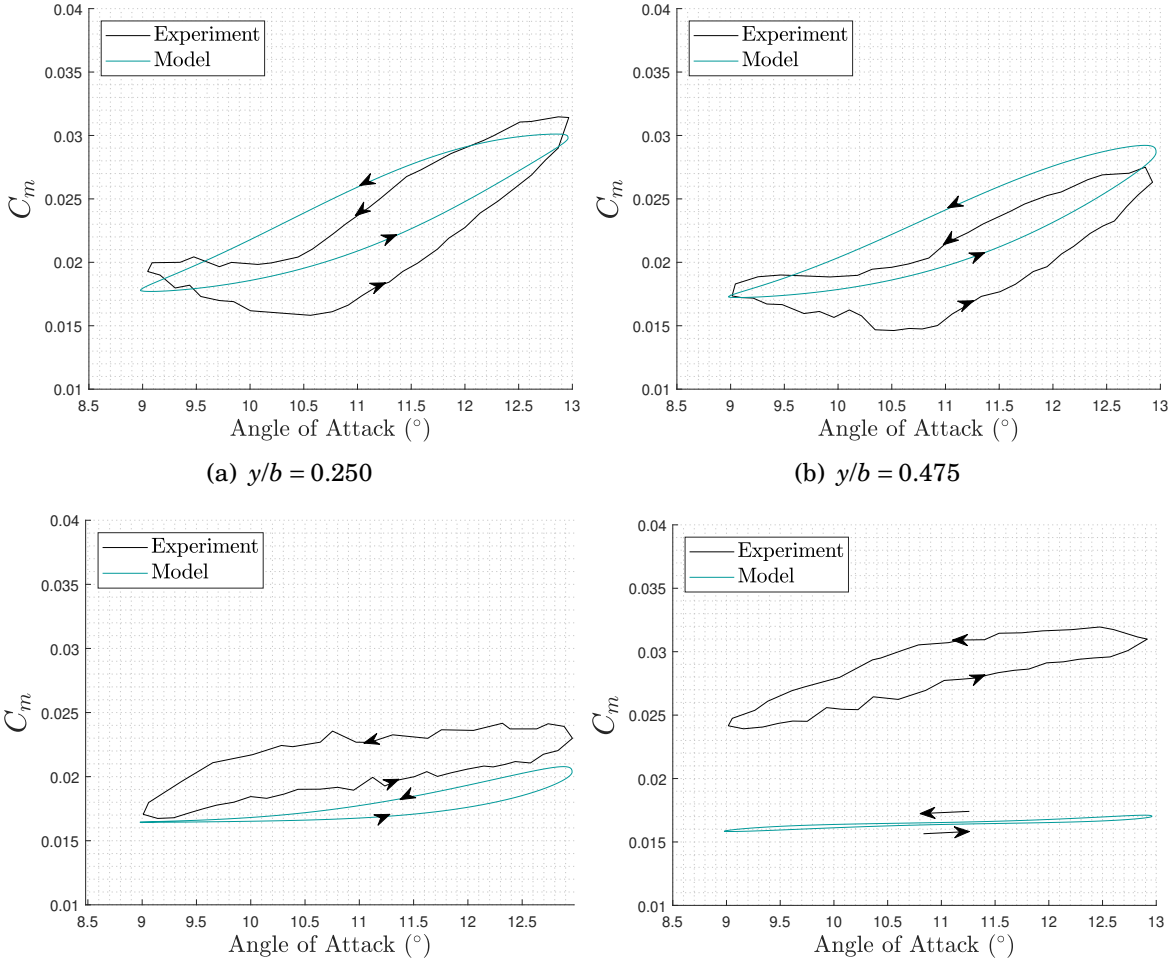

(a) $y/b = 0.250$ (b) $y/b = 0.475$

(c) $y/b = 0.800$ (d) $y/b = 0.900$

Figure 5.22: $\alpha = 10.97° \pm 1.99° \sin(0.038S)$

is shown in Figures 5.24(b) and 5.26. The amplitude of the pitching motion is also the greatest provided in the experimental data with a value of 4°. The range of moment coefficient and general shape of the response is well captured by the model, although the figure of eight in the experimental data at this much higher angle of attack is no longer predicted by the model. Once again, at the tip, the experimental data is underestimated by the model. However, considering the challenges of modelling the unsteady moment response in the deep stall regime, it is deemed acceptable.

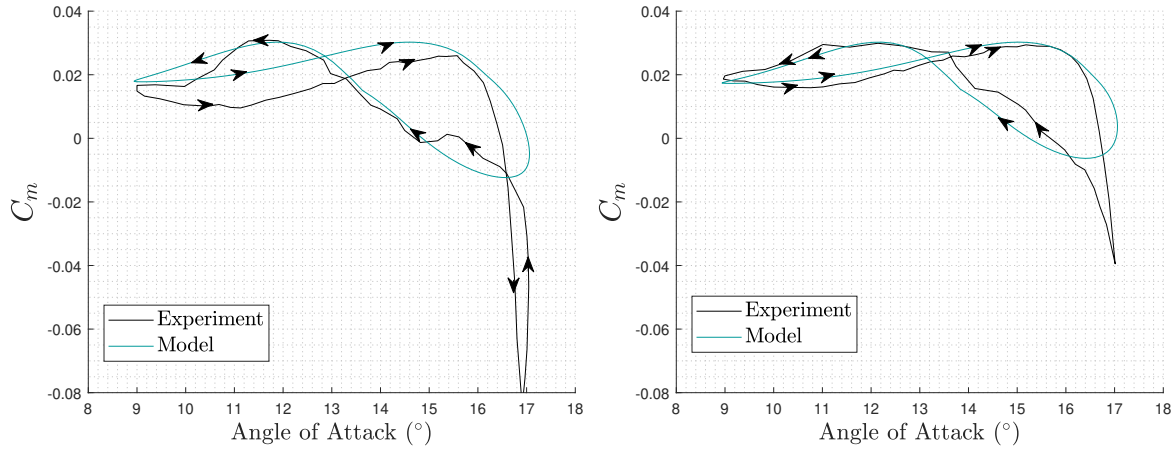

(a) $y/b = 0.250$

(b) $y/b = 0.475$

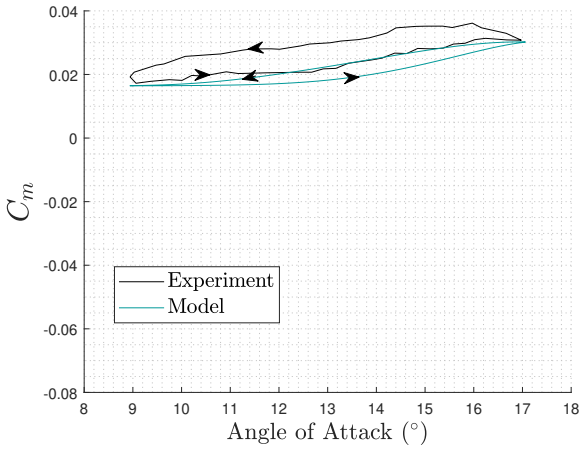

(c) $y/b = 0.800$

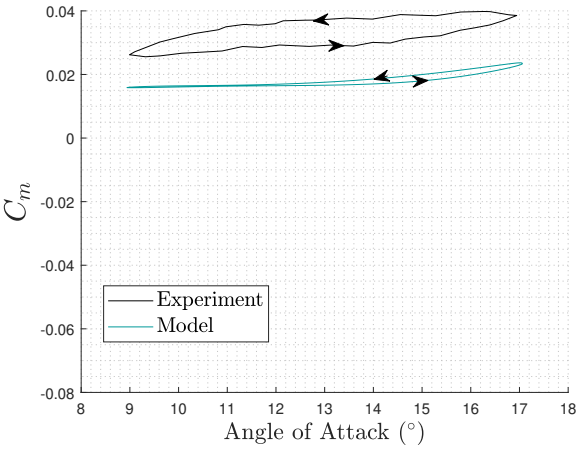

(d) $y/b = 0.900$

Figure 5.23: $\alpha = 13.00° \pm 4.06° \sin(0.038S)$

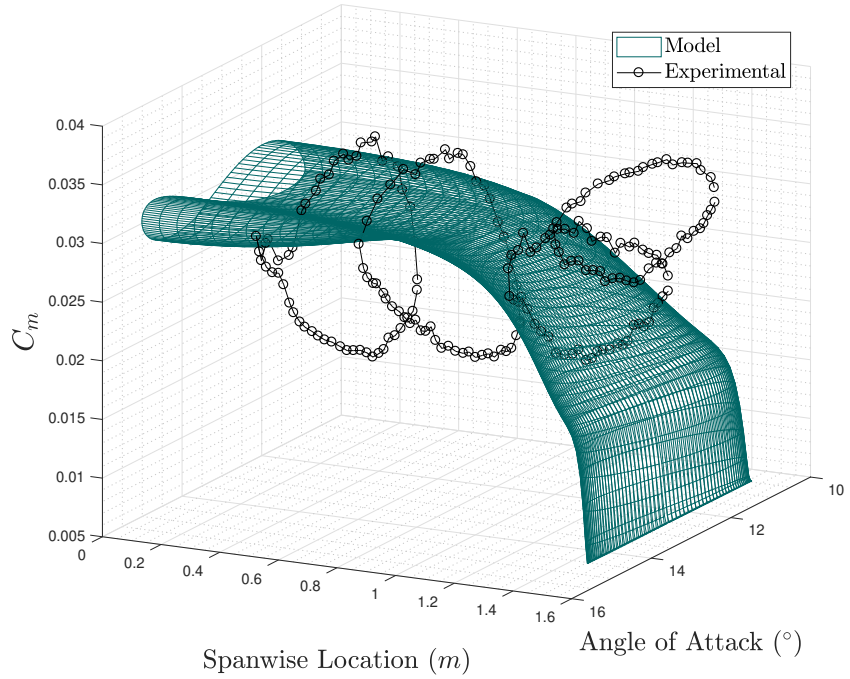

(a) $\alpha = 12.96^\circ \pm 2.05^\circ \sin(0.095S)$

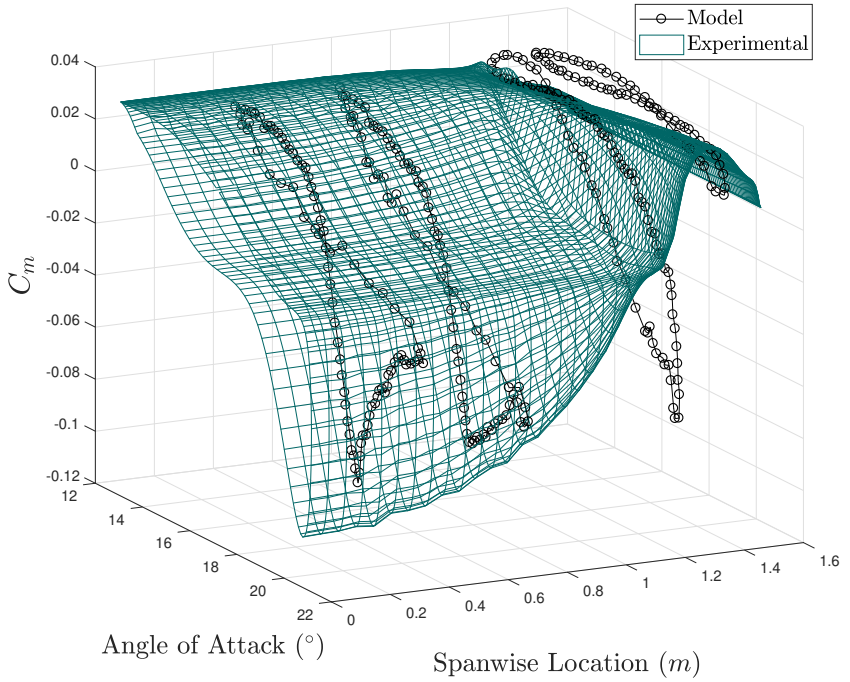

(b) $\alpha = 17.12^\circ \pm 4.04^\circ \sin(0.038S)$

Figure 5.24: Example database with decomposition for directly using 2D URANS

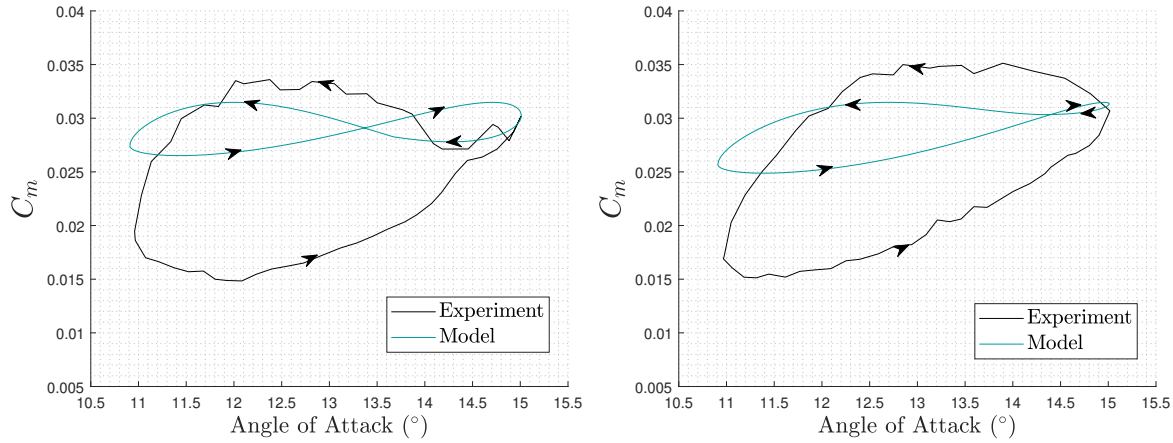

(a) $y/b = 0.250$

(b) $y/b = 0.475$

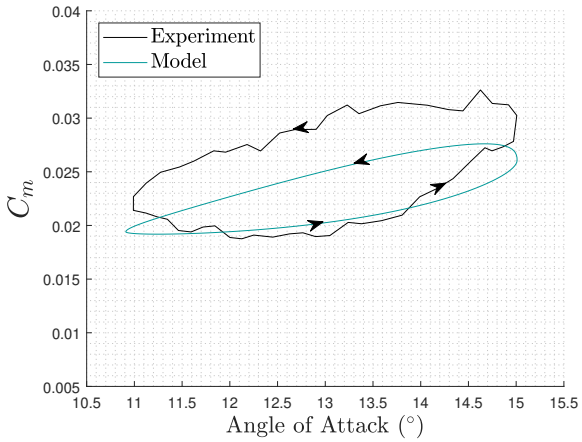

(c) $y/b = 0.800$

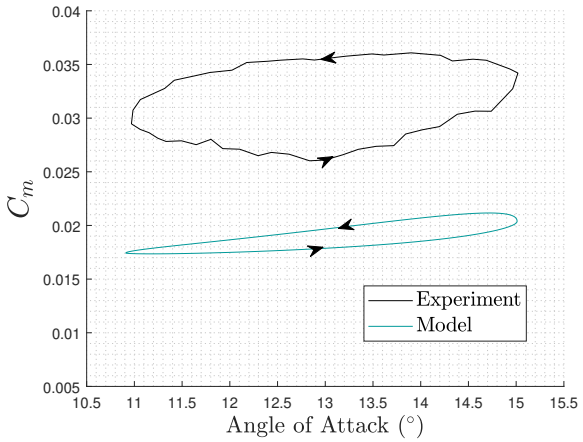

(d) $y/b = 0.900$

Figure 5.25: $\alpha = 12.96° \pm 2.05° \sin(0.095S)$

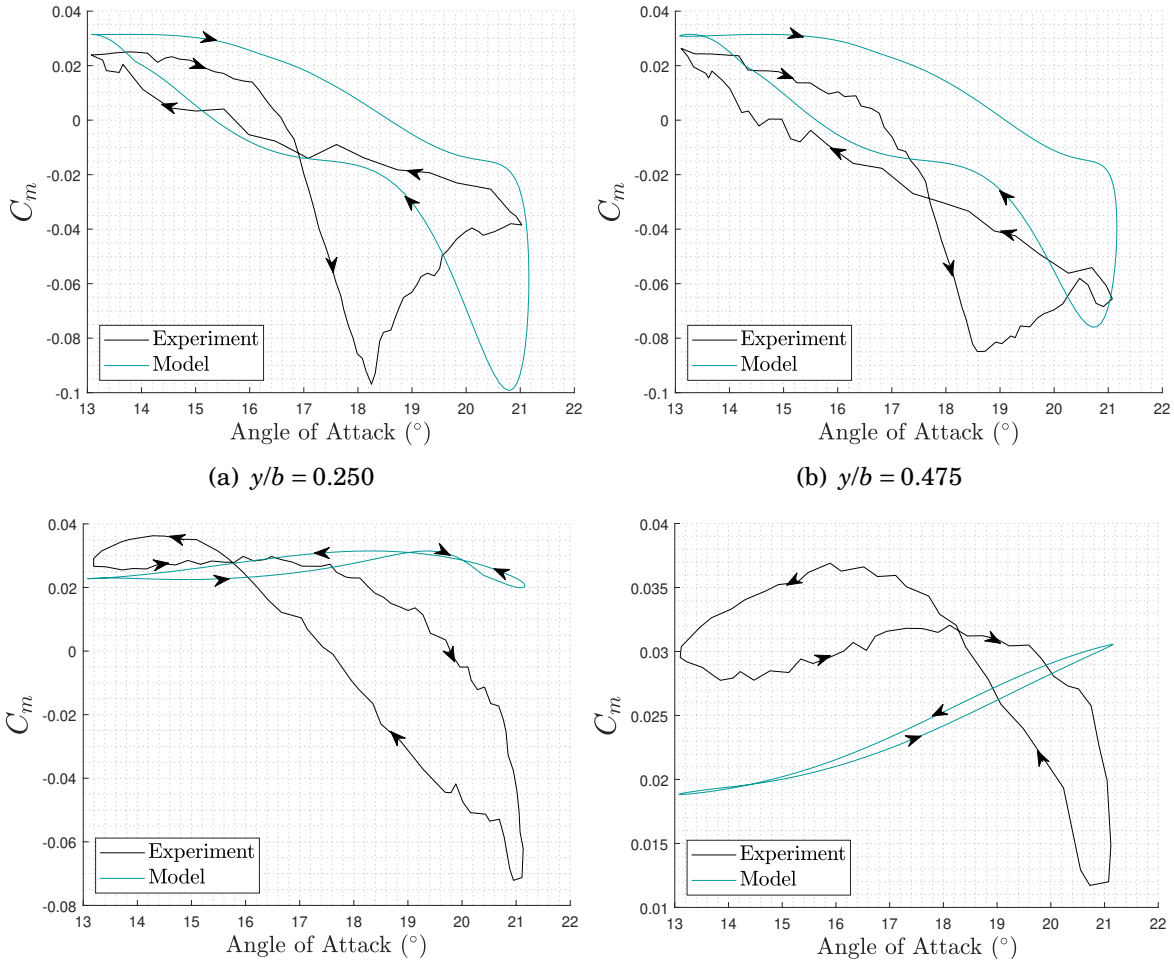

(a) $y/b = 0.250$

(b) $y/b = 0.475$

(c) $y/b = 0.800$

(d) $y/b = 0.900$

Figure 5.26: $\alpha = 17.12° \pm 4.04° \sin(0.038S)$

5.3 Comparison to Computational Fluid Dynamics

The 3D unsteady nonlinear lifting line model can be further compared using higher order computational fluid dynamics. Both two-dimensional and three-dimensional unsteady Reynolds-Averaged Navier-Stokes (URANS) simulations are used in this process. The 2D data is used to build a model, whilst the 3D simulations are only used for validation. As described in Chapter 2, the CFD solver DLR-TAU [59] is used to carry out the simulations with a Spalart-Allmaras negative turbulence model [76].

5.3.1 UAV Aerofoil and Wing Model

The test case geometry is that introduced in Chapter 2. The 3D geometry is a clean wing of aspect ratio 12.5 composed of the NACA LRN 1015 profile throughout, as shown in Figure 2.16. Only one dynamic stall model needs to be built since there is only one aerofoil section considered. The wing has a fixed chord length, this also allows for the dynamic stall model to be built at just one Reynolds number. The NACA LRN 1015 is a 15.2% thick aerofoil which has a trailing edge stall mechanism therefore the Beddoes-Leishman model can be used for the new 3D model.

In order to compare the spanwise CFD output with the model, the CFD surface mesh is divided into strips parallel to the chord, so that the centre of each strip corresponds with a bound vortex section on the 3D unsteady lifting line model. Again, it is to be reiterated that the intention of the model presented here is to be able to compute the spanwise distribution of lift and moment, not just an integrated force.

5.3.2 CFD Lift Coefficient Results

The model overall gives a good prediction of the CFD results, especially when the computational savings are taken into account. For the majority of the cases run, the largest errors are seen at the wing root. This is at least in part due to the highly three dimensional flow that occurs near the root, along with the probable formation of stall cells in

this region which was discussed in Chapter 2.3.5. In fact the root sections often separates severely when the further outboard sections show little separation. This is not aided by the 3° of washout that is incorporated into the wing. Some typical results are presented, which illustrate key conclusions. For example, Figures 5.27(a) and 5.28 show the C_l response for the wing undergoing a pitching motion defined by $\alpha = 11° \pm 2° \sin(0.15S)$. Here the CFD data is displaying some characteristics of the root stalling more severely as seen by the flaring of the lift coefficient surface at the wing root. Increasing the mean amplitude to 12°, as shown in Figures 5.27(b) and 5.29 further causes the root separation to become more pronounced. This behaviour extends throughout all of the high angle of attack data.

The overall behaviour remains similar when the amplitude of the pitching motion is increased to 4° (Figures 5.30(a) and 5.31), however when the mean angle is increased to 16°, the response appears to be more complex, Figures 5.30(b) and 5.32. This is captured in the model with the lift hysteresis being no longer elliptical in shape and a localised decrease in lift coefficient at the inboard section. The inboard section is shown in Figure 5.32(a), this is attributed to the highly three-dimensional flow at the wing root through the formation of a stall cell. This can cause leading edge separation and thus significant loss of lift. The model also shows a spanwise drop in lift at the root and ideally further refinement in spanwise bound circulation nodes should be used to capture this and aid the convergence of the NULLT. It believed that a kink in the model response at $\alpha = 16°$ at the inboard section originates because of this. Increasing the mean angle of attack further to 20°, as shown in Figures 5.33(a) and 5.34, reveals that the flow is dominated by separation. Once again the model is able to capture the overall behaviour well. As with Figure 5.32(a), Figure 5.35(a) suffers from significant loss of lift at the top of the stroke, which is also likely attributed to the formation of a stall cell. Once again the model shows a kink at $\alpha = 18°$, which is the mean angle of attack and therefore alludes to convergence issues.. At this point it is worth noting how unrealistic the result from the uncorrected lifting line response is. At the top of the stroke the lift is overestimated

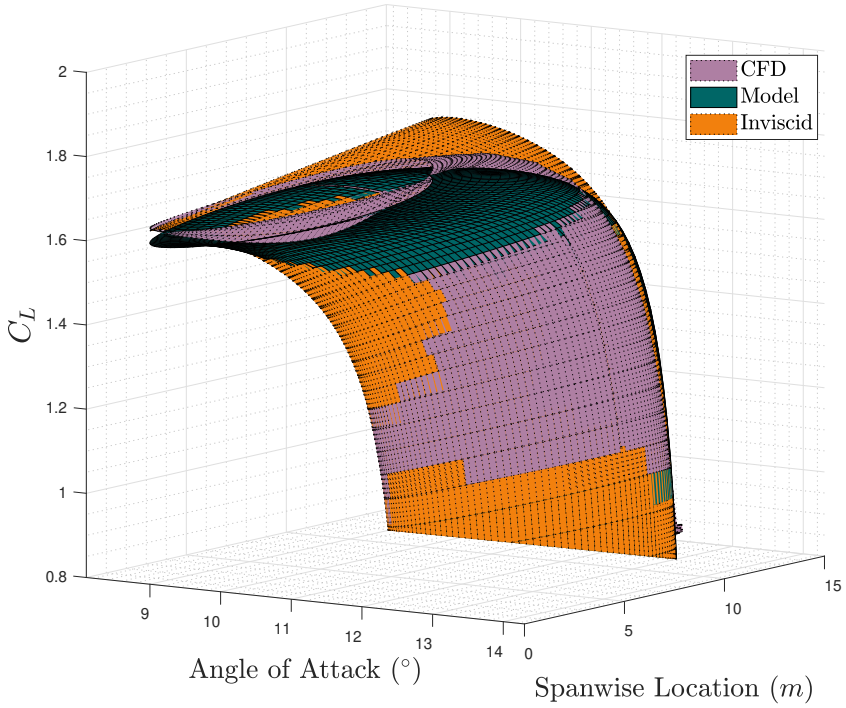

(a) $\alpha = 11° \pm 2° \sin(0.15S)$

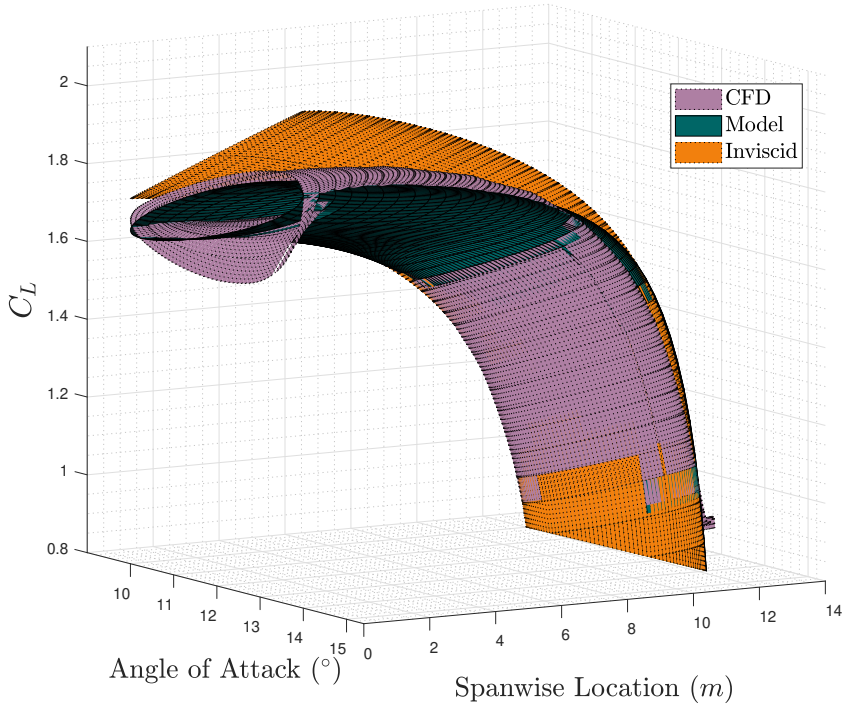

(b) $\alpha = 12° \pm 2° \sin(0.15S)$

Figure 5.27: C_l Model output against 3D URANS

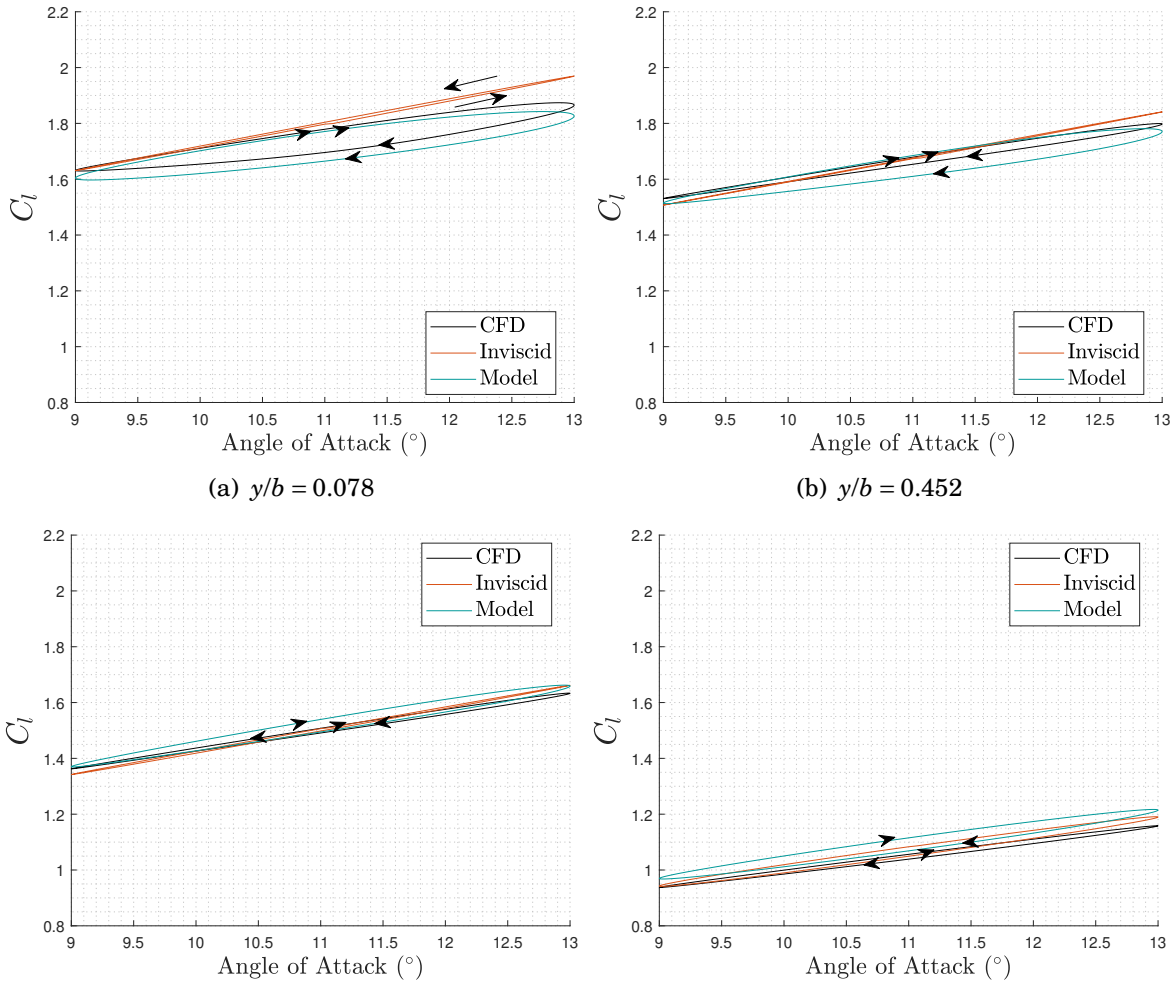

(a) $y/b = 0.078$ (b) $y/b = 0.452$

(c) $y/b = 0.707$ (d) $y/b = 0.924$

Figure 5.28: $\alpha = 11° \pm 2° \sin(0.15S)$

in excess of 100%. Further, like in the comparison to Section 5.2.2, the direction of the lift hysteresis loop is also in the incorrect direction in the uncorrected, inviscid, lifting line. The errors for a larger sample of cases are shown in Figure 5.36, where it can be seen that the corrected model consistently outperforms the standard unsteady lifting line. As with the two-dimensional flow when the reduced frequency is increased, the flow separation is suppressed and the error is reduced.

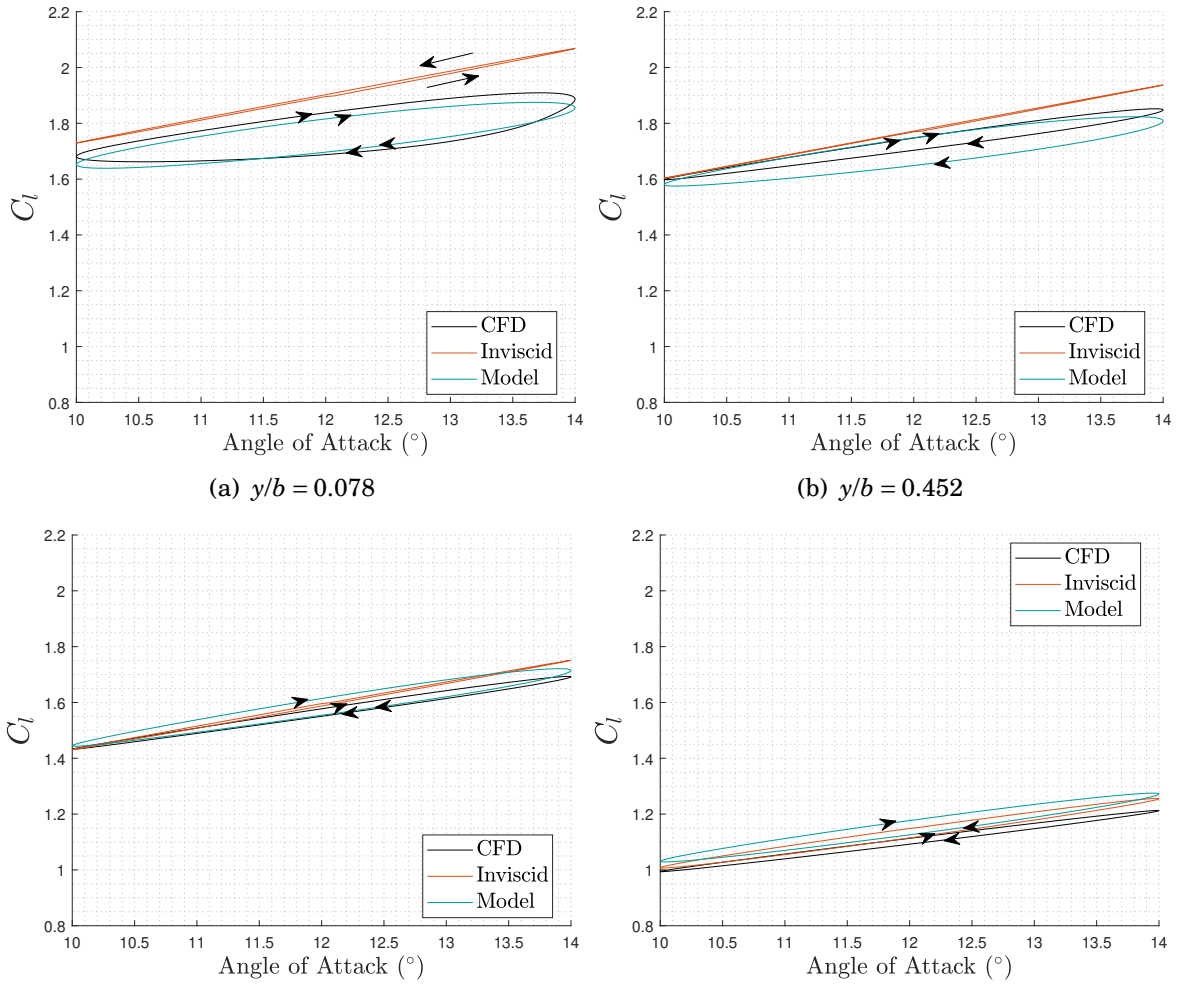

(a) $y/b = 0.078$

(b) $y/b = 0.452$

(c) $y/b = 0.707$

(d) $y/b = 0.924$

Figure 5.29: $\alpha = 12° \pm 2° \sin(0.15S)$

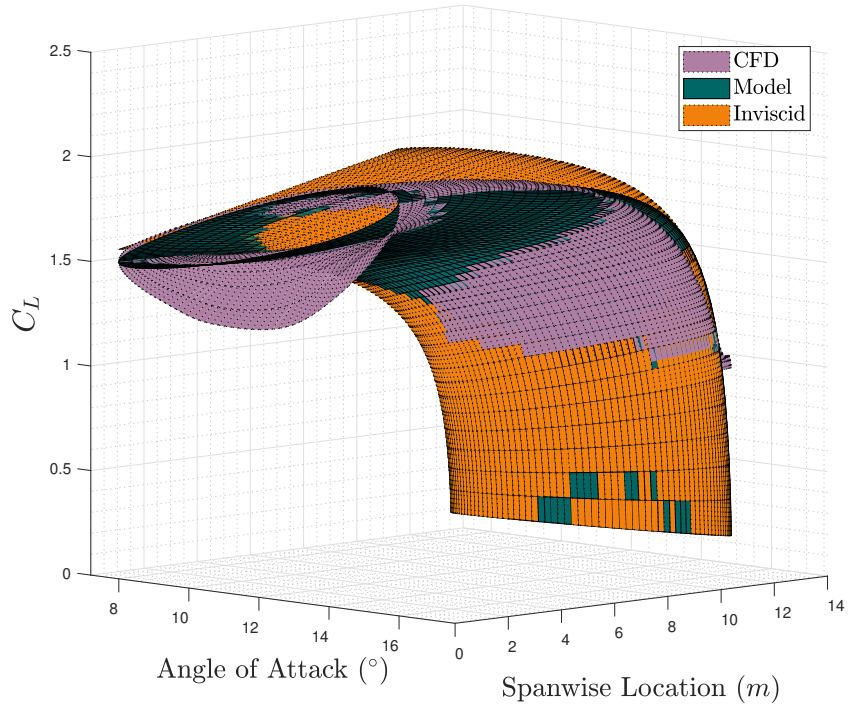

(a) $\alpha = 12° \pm 4° \sin(0.2S)$

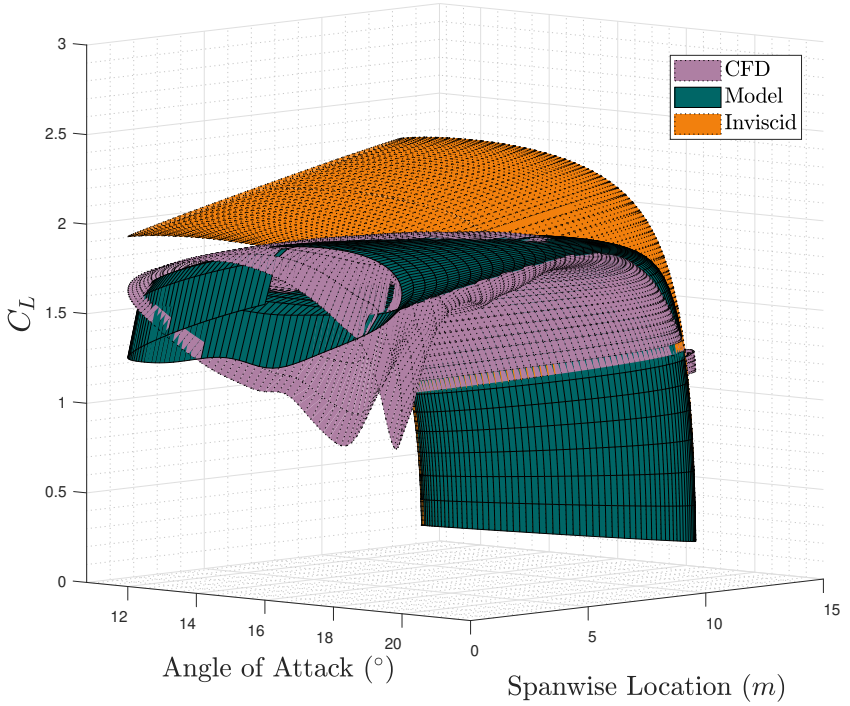

(b) $\alpha = 16° \pm 4° \sin(0.2S)$

Figure 5.30: C_l Model output against 3D URANS

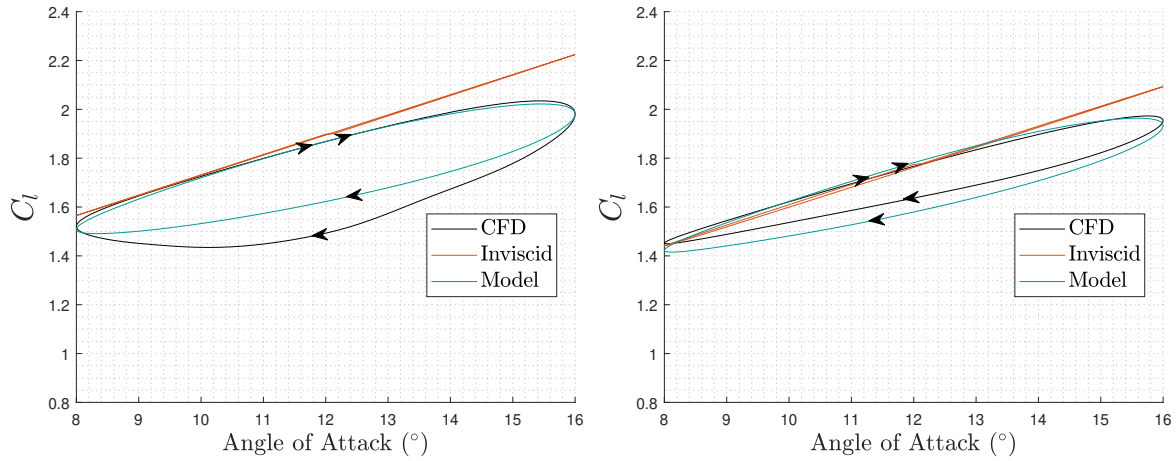

(a) $y/b = 0.078$

(b) $y/b = 0.452$

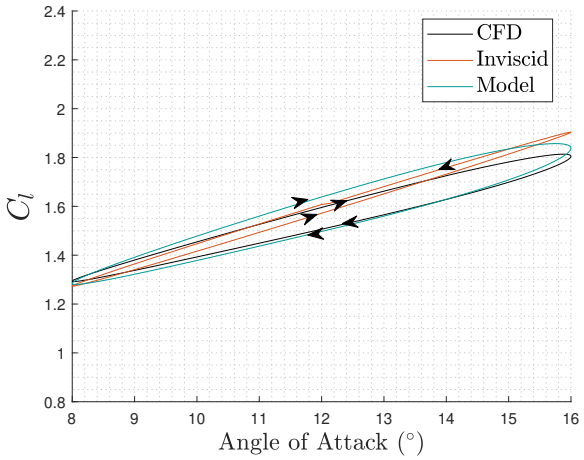

(c) $y/b = 0.707$

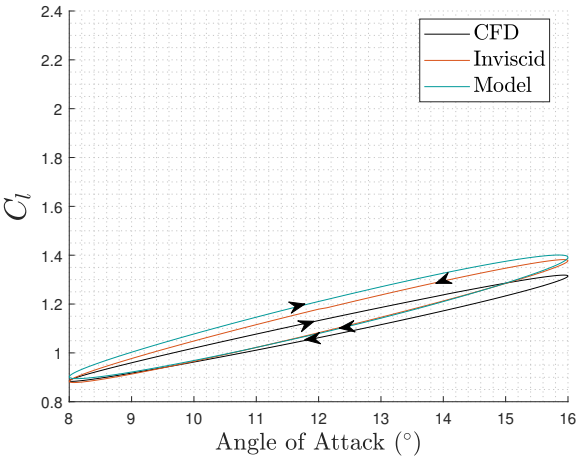

(d) $y/b = 0.924$

Figure 5.31: $\alpha = 12° \pm 4° \sin(0.2S)$

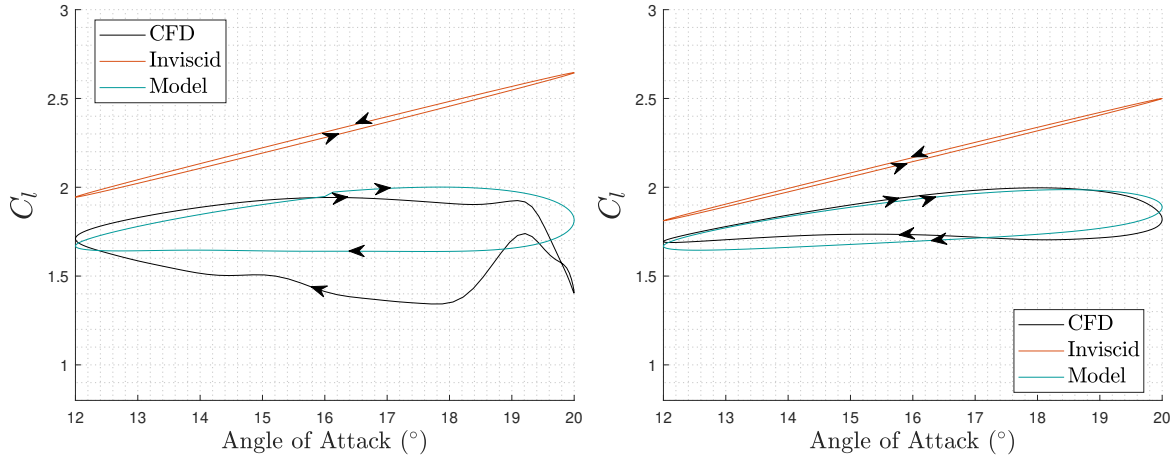

(a) $y/b = 0.078$ (b) $y/b = 0.452$

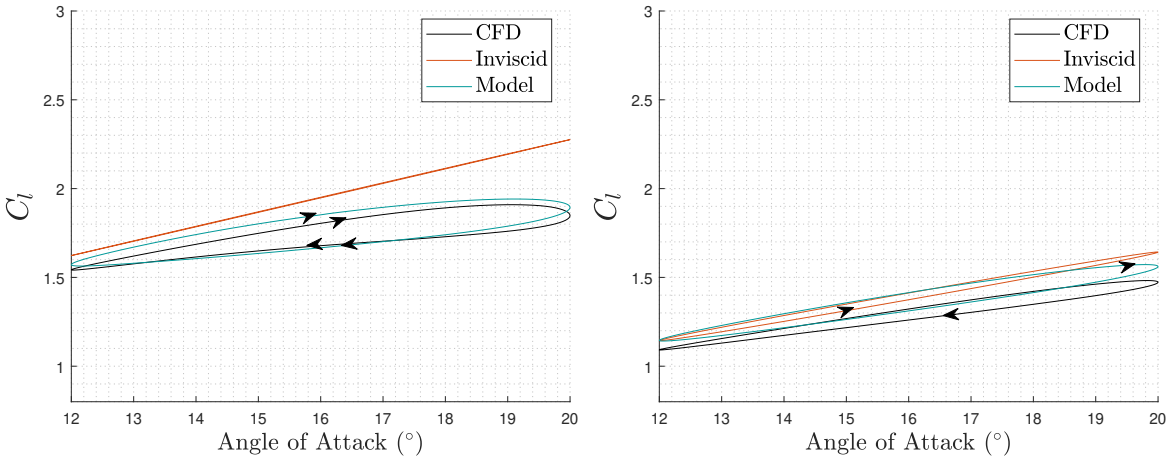

(c) $y/b = 0.707$ (d) $y/b = 0.924$

Figure 5.32: $\alpha = 16° \pm 4° \sin(0.2S)$

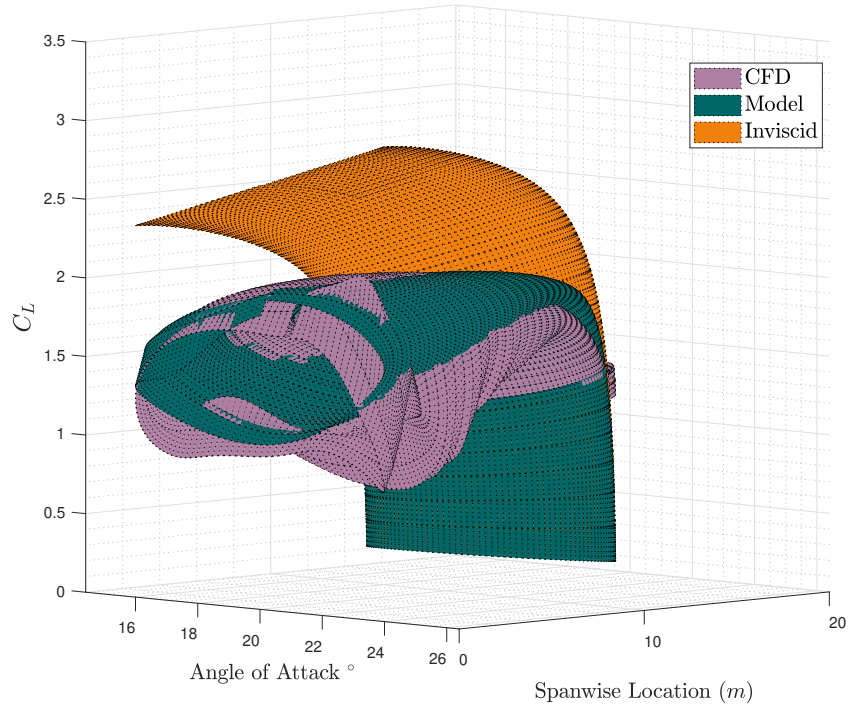

(a) $\alpha = 20° \pm 4° \sin(0.2S)$

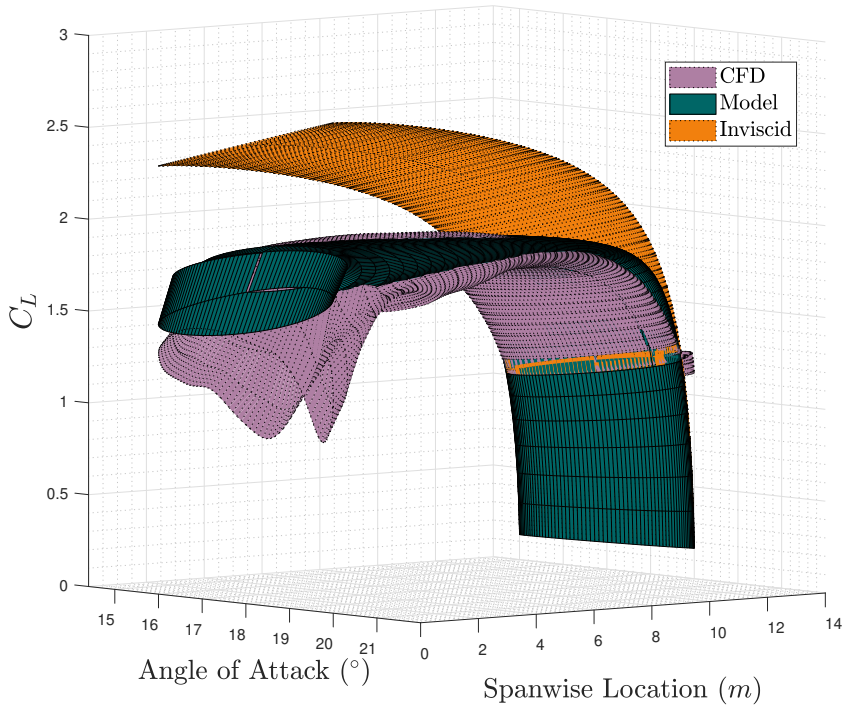

(b) $\alpha = 18° \pm 2° \sin(0.15S)$

Figure 5.33: C_l Model output against 3D URANS

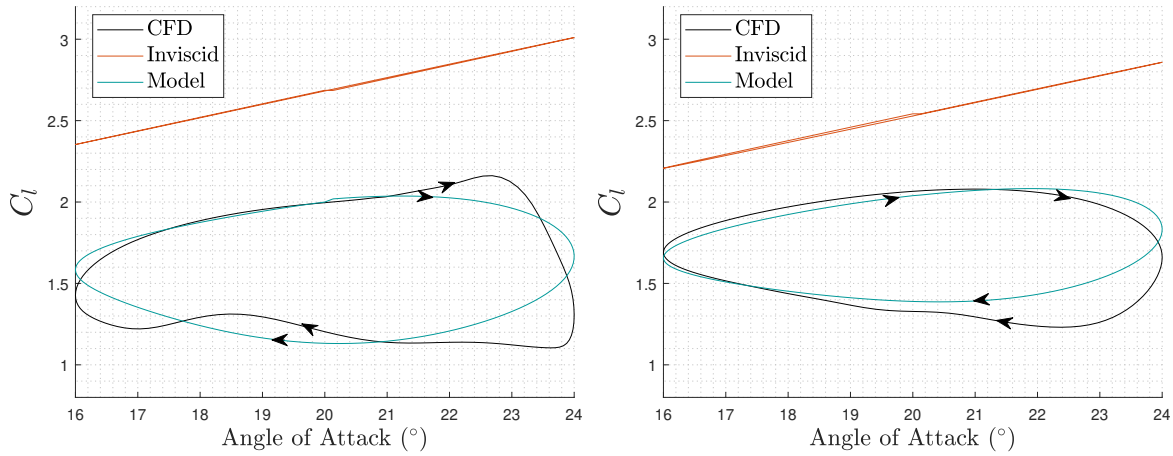

(a) $y/b = 0.078$ (b) $y/b = 0.452$

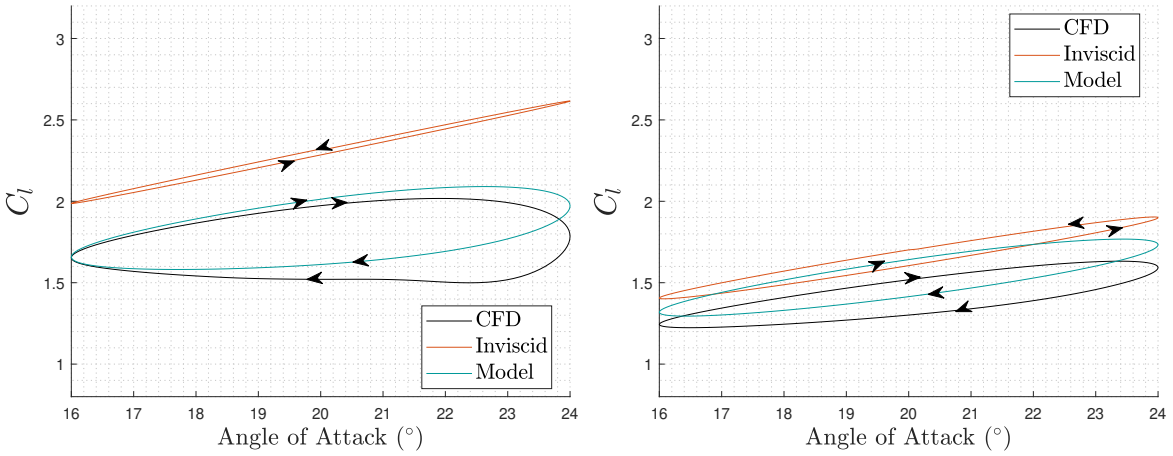

(c) $y/b = 0.707$ (d) $y/b = 0.924$

Figure 5.34: $\alpha = 20° \pm 4° \sin(0.2S)$

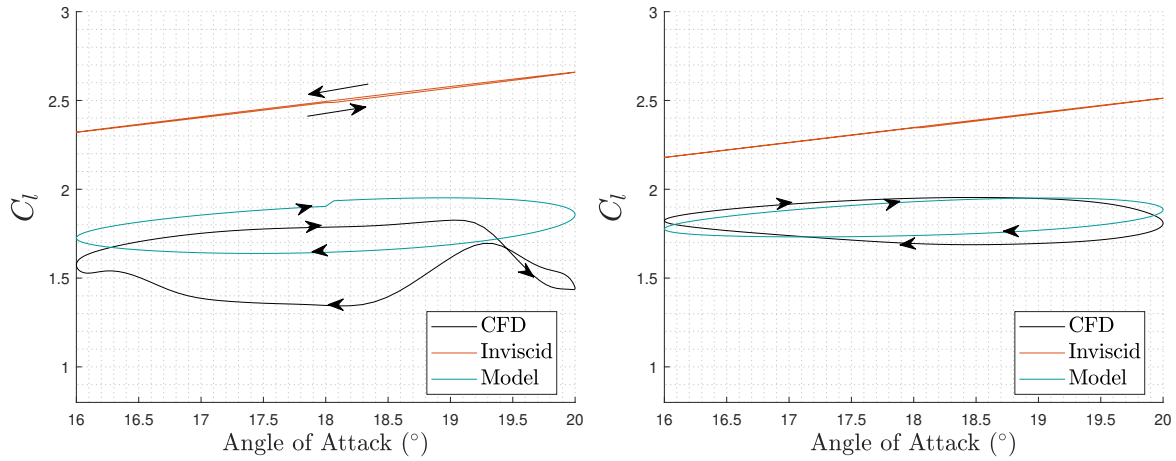

(a) $y/b = 0.078$

(b) $y/b = 0.452$

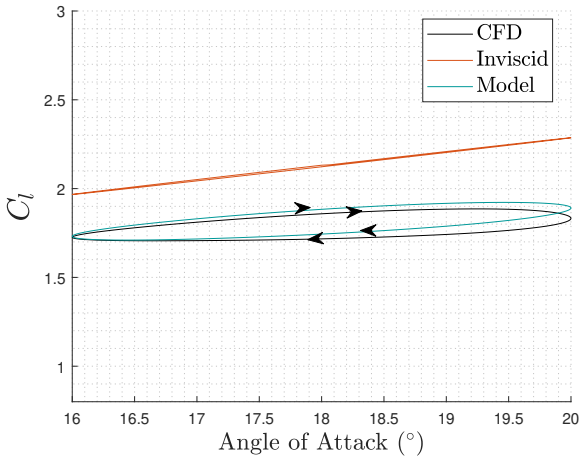

(c) $y/b = 0.707$

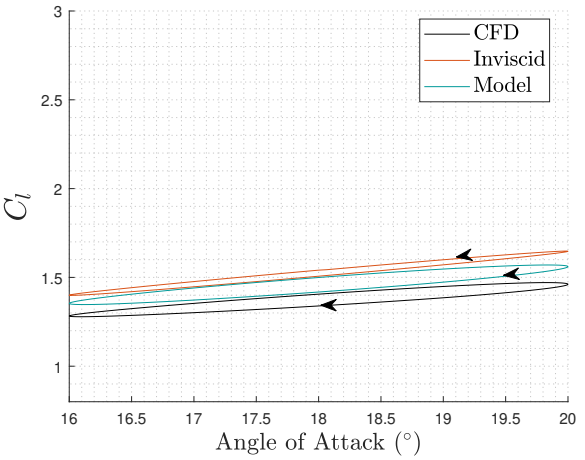

(d) $y/b = 0.924$

Figure 5.35: $\alpha = 18° \pm 2° \sin(0.15S)$

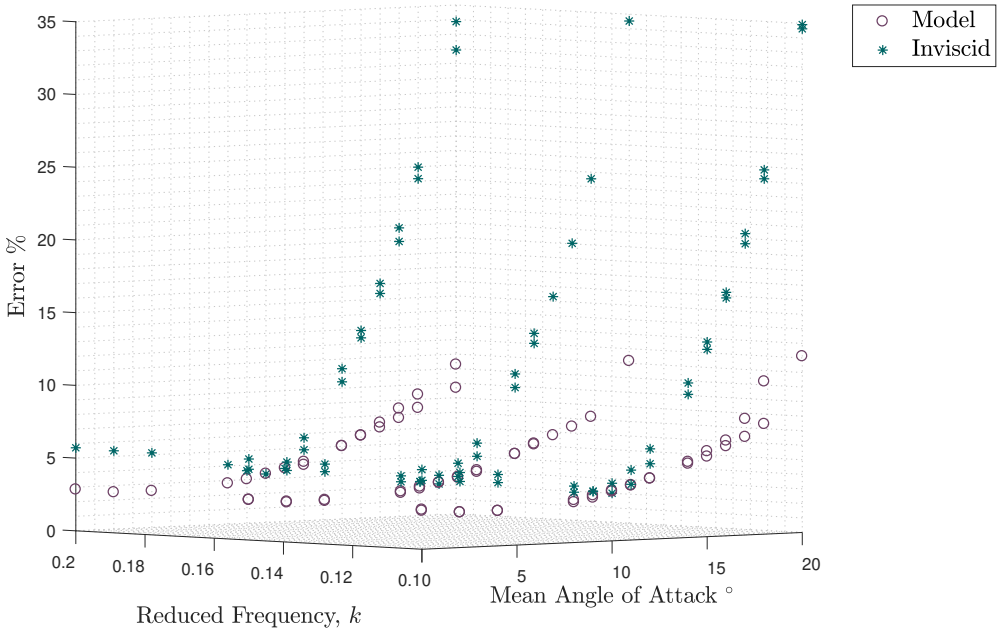

Figure 5.36: Cycle averaged errors for NULLT and ULLT compared to 3D CFD

5.3.3 CFD Moment Results

As with the experimental data discussed previously, the simple moment model is able to produce realistic results for the inboard wing sections however underestimates the moment close to the tip. Figures 5.37(a) and 5.38 show the moment surface for nominally attached flow, demonstrating the lag applied to the angle of attack to account for the unsteady induced angle, performs well away from the tip. Even when the mean angle of attack is increased to 10°, as shown in Figures 5.37(b) and 5.39, the model provides realistic answers for the most inboard 70% of the wing. It is only further outboard that the moment isn't well captured. This suggests refinements to the model are required to capture the behaviour near the tip. It is possible that a rearward shift in the aerodynamic centre close to the tip could be sufficient to achieve better agreement, however more three-dimensional moment data would need to be examined.

As previously discussed, there is a more severe separation that occurs at the wing root. Unsurprisingly this is not well captured by the moment model. Figures 5.40(b) and 5.42 show the moment coefficient surface for the pitching motion defined by $\alpha = 11^\circ \pm 4^\circ \sin(0.15S)$. As with the lift coefficient, the CFD moment coefficient demonstrates a larger range near the root than predicted by the model. This becomes more severe as the mean angle of attack is increased and the flow separation at the root becomes more severe. This is further shown in Figures 5.43(a) and 5.44, along with 5.43(b) and 5.45 . Both of these examples exhibit a large pitch down moment that the model is not capable of predicting. This is unsurprising since this is behaviour that is not featured in the two-dimensional data used to build the moment model.

5.4 Computational Cost

The new unsteady nonlinear lifting line theory presented here gives an efficient tool for the prediction of loads and moments under separated flow conditions. CFD undoubtedly still represents a much more complete model, however it is often infeasible because of the

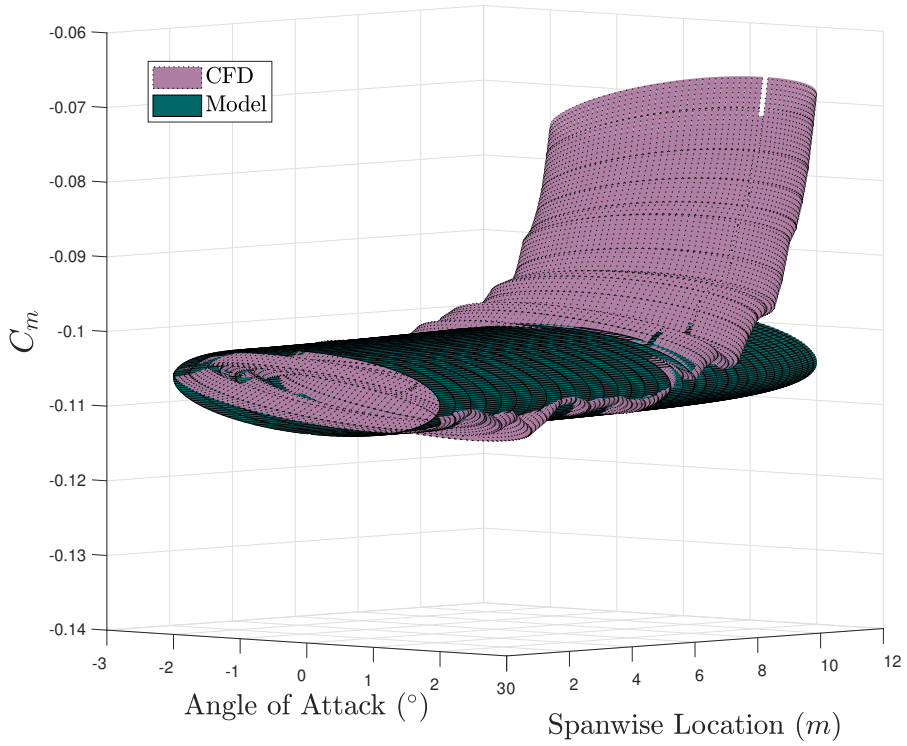

(a) $\alpha = 0° \pm 2° \sin(0.15S)$

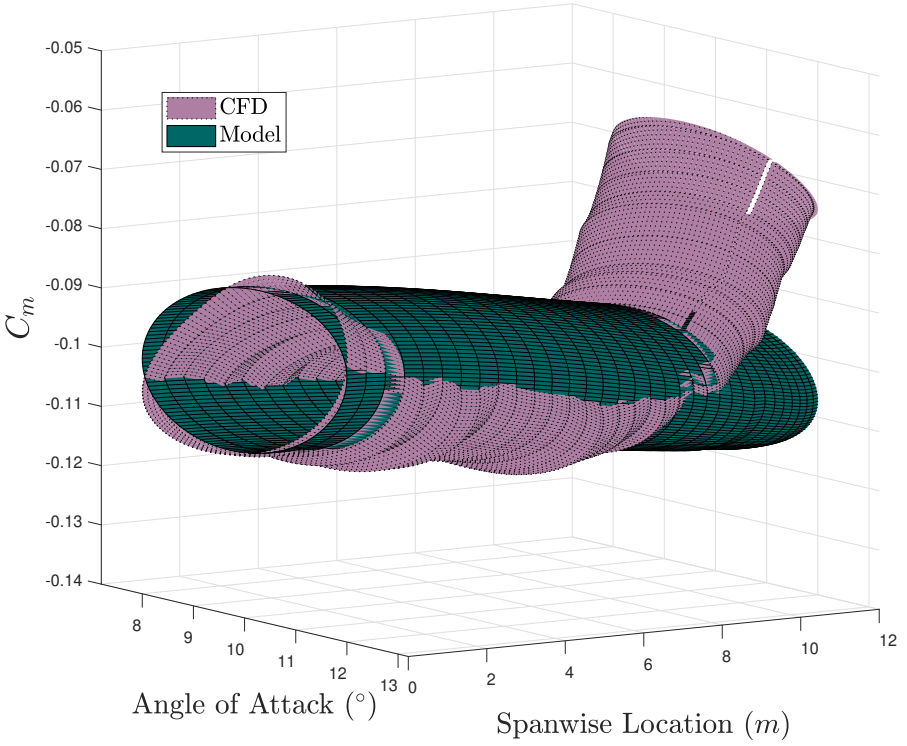

(b) $\alpha = 10° \pm 2° \sin(0.2S)$

Figure 5.37: C_m Model output against 3D URANS

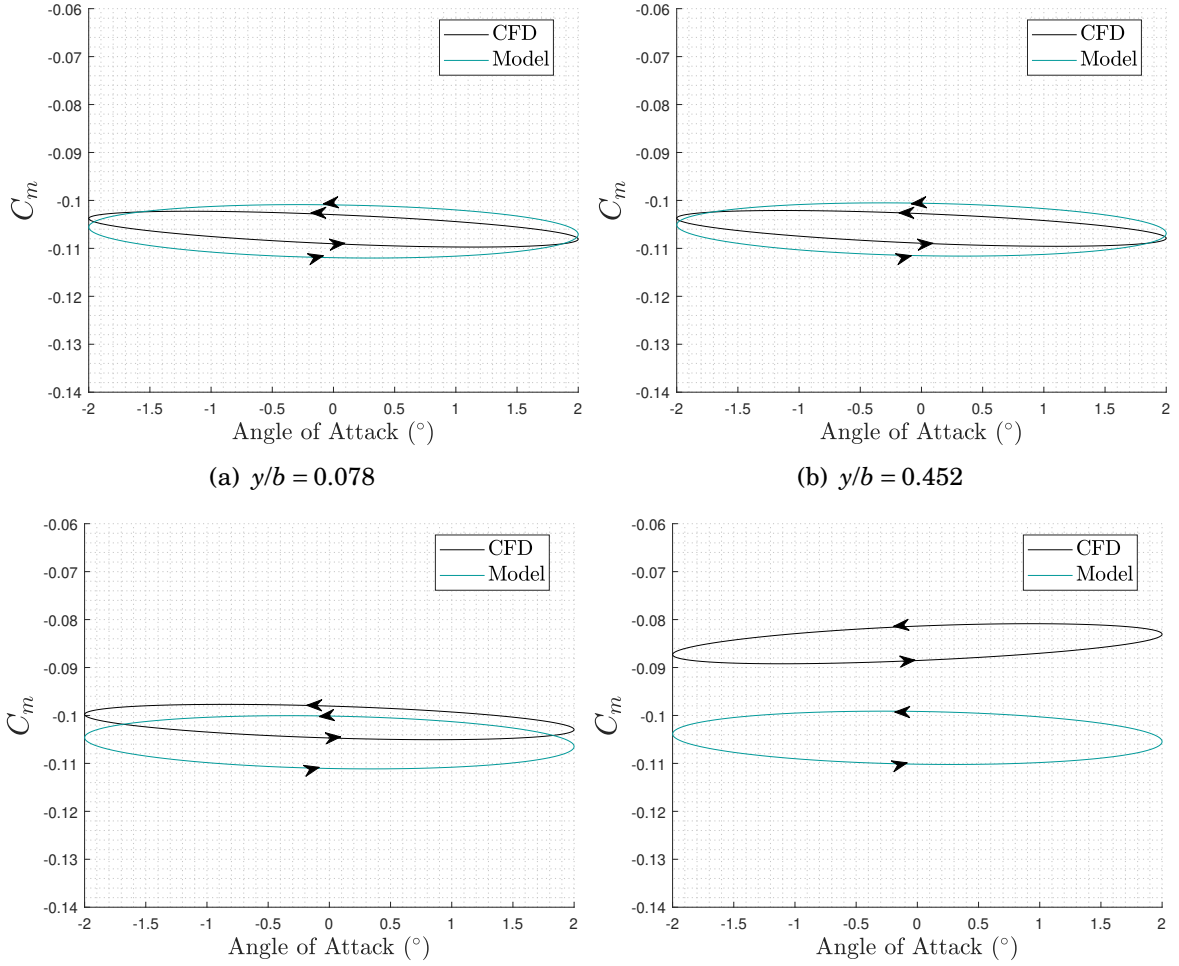

(a) $y/b = 0.078$ (b) $y/b = 0.452$

(c) $y/b = 0.707$ (d) $y/b = 0.924$

Figure 5.38: $\alpha = 0° \pm 2° \sin(0.15S)$

computational expense involved. This is even more prevalent when the number of design evaluations needed to explore a design space are considered. This section compares the relative cost of running a CFD simulation on a half-wing model compared to using the unsteady nonlinear lifting line theory. For the quantification of the CFD runtime, a wing mesh constituted of NACA LRN 1015 sections with a cell count of 3.45×10^6 is compared to the unsteady nonlinear lifting line theory with 40 spanwise stations with a cosine distribution, where stations become closer together with proximity to the tip. Furthermore, due to the computational demand of RANS and URANS, the CFD simulations were executed using high performance computing (HPC) and were run on a

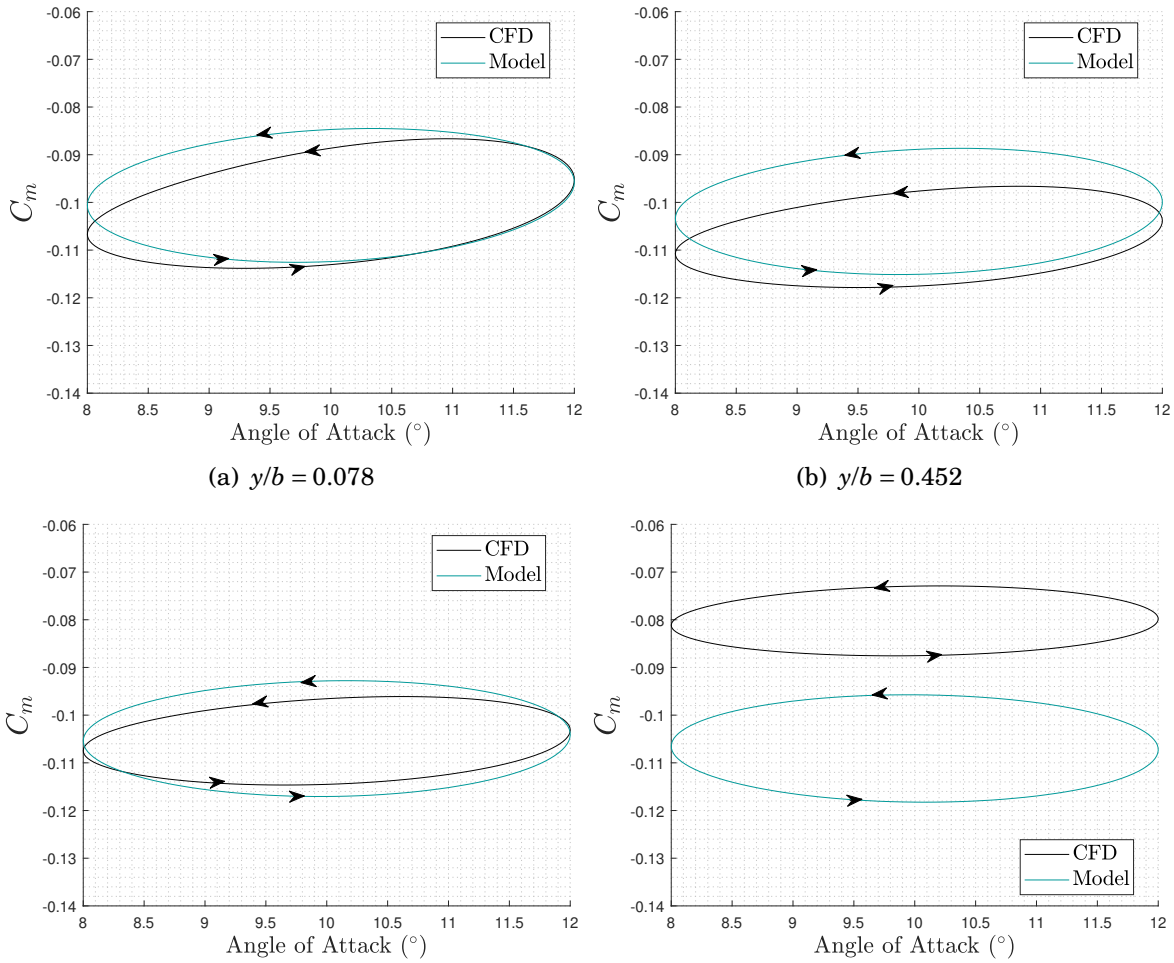

(a) $y/b = 0.078$ (b) $y/b = 0.452$

(c) $y/b = 0.707$ (d) $y/b = 0.924$

Figure 5.39: $\alpha = 10° \pm 2° \sin(0.2S)$

single Lenovo nx360 m5 compute node which has two 14-core 2.40 GHz Intel E5-2680 v4 (Broadwell) CPUs, and 128 GB of RAM. The unsteady nonlinear lifting line theory was executed on a desktop PC with a Intel Core i7-4790 CPU with a clock speed of 3.60 GHz. A typical static CFD simulation, seeded a further unsteady run took approximately 5 hours using HPC. The unsteady nonlinear lifting line can achieve results for a static case in 40 s, which represents a speed-up of 450 times compared to the CFD. The computational benefit is increased when running unsteady pitching oscillations. As with the static cases, the dynamic cases were first run using a steady solver before being run unsteady for at least three full pitching cycles, with 128 timesteps per cycle. This required 36 hours

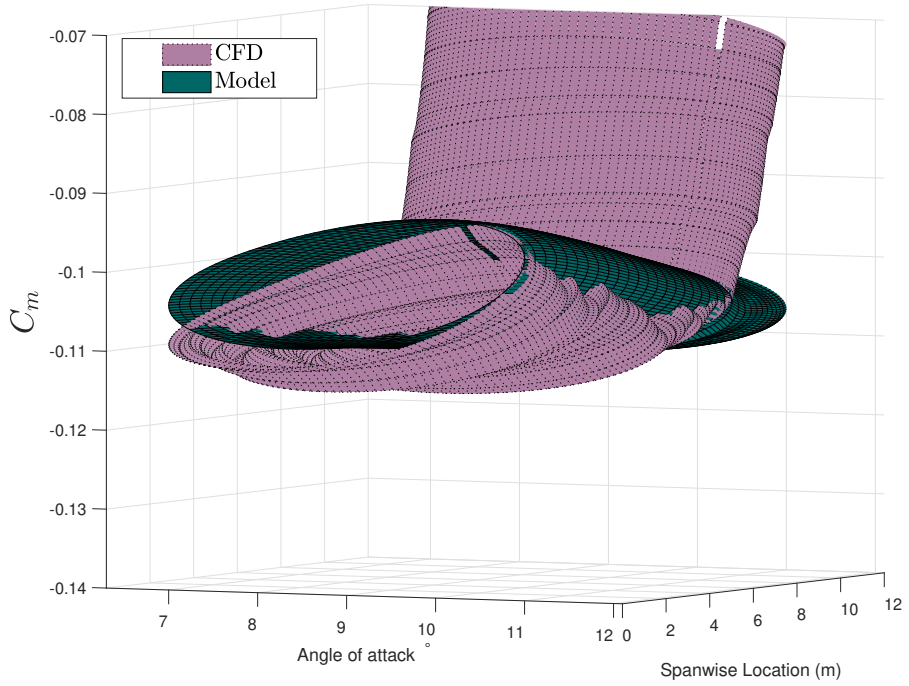

(a) $\alpha = 9° \pm 2° \sin(0.1S)$

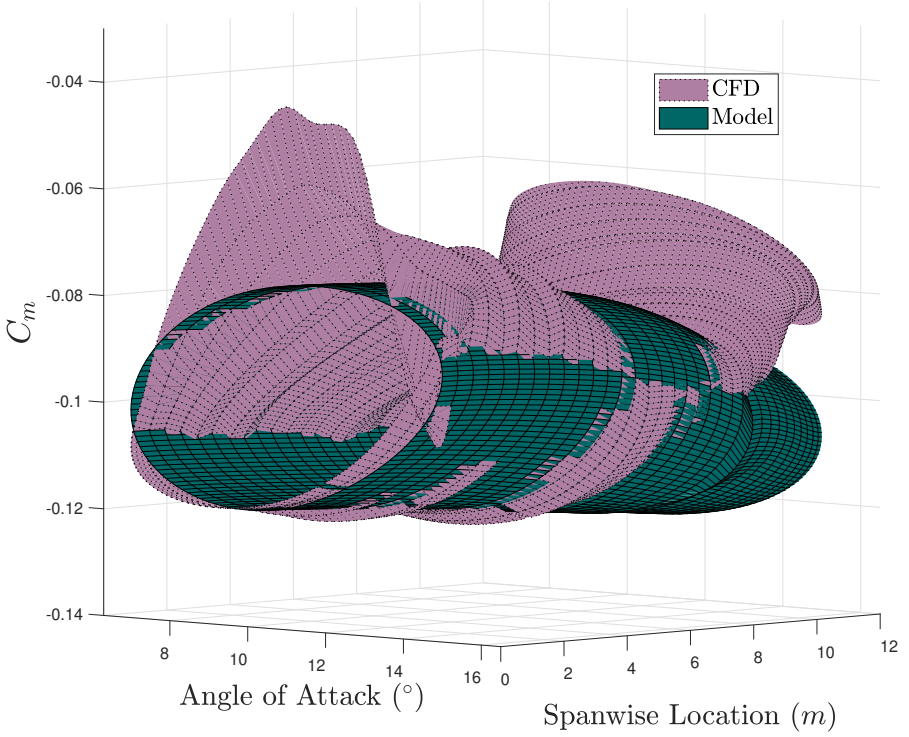

(b) $\alpha = 11° \pm 4° \sin(0.15S)$

Figure 5.40: C_m Model output against 3D URANS

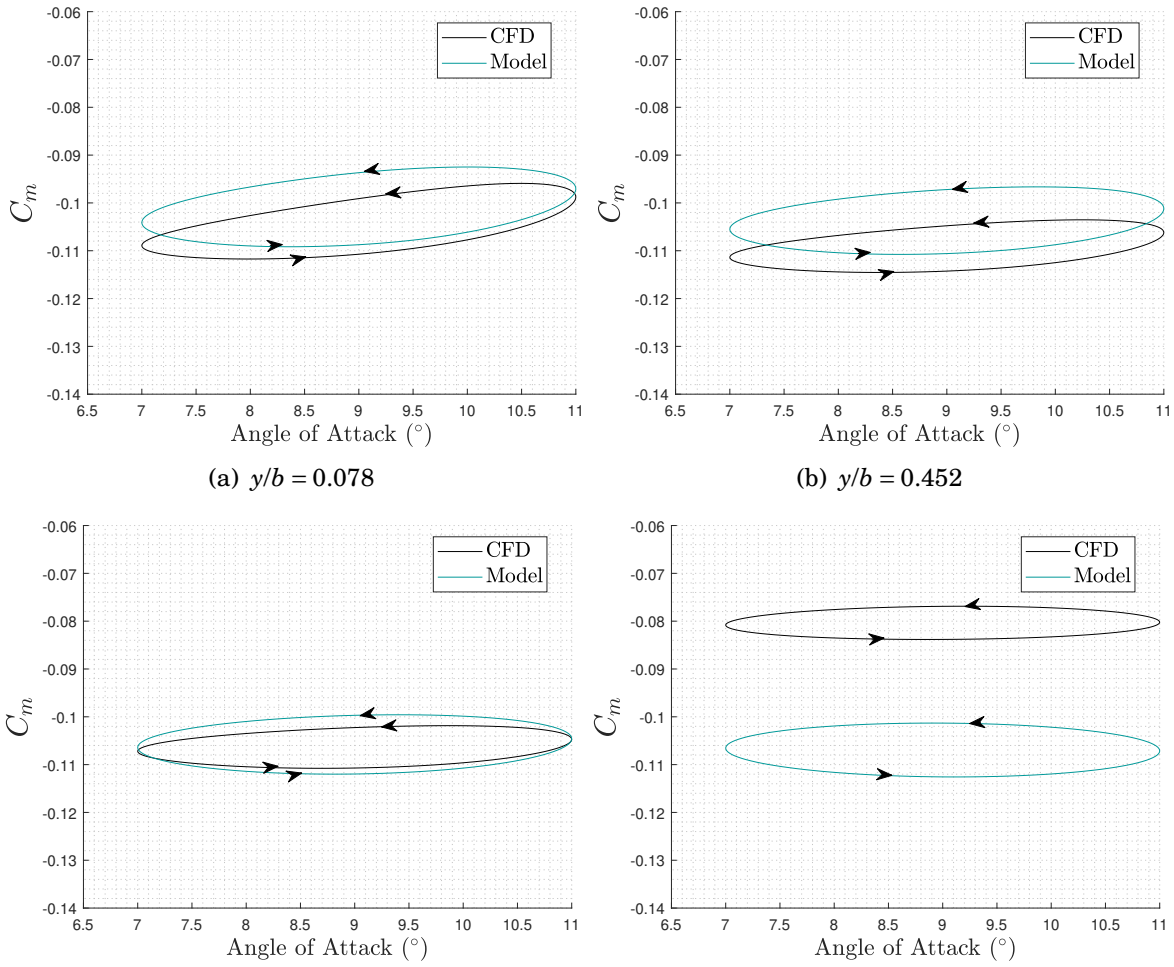

(a) $y/b = 0.078$ (b) $y/b = 0.452$

(c) $y/b = 0.707$ (d) $y/b = 0.924$

Figure 5.41: $\alpha = 9° \pm 2° \sin(0.1S)$

of computation using HPC. The unsteady nonlinear lifting line requires 135 s for the same setup, which represents a speed up of 950 times compared to the CFD, almost three order of magnitude. The data used to build the model should also be factored in: if data is not available for the aerofoil section and conditions required, they will need to be obtained using 2D CFD. The nonlinear lifting line theory relies on high-fidelity steady and unsteady data. Therefore, in order to build the model the time taken to generate this data should be considered. Typically, a static 2D polar can be computed quickly with modern computational resources. The static runs take approximately 10 minutes to converge and therefore a sweep of angles of attack can be obtained without a few hours.

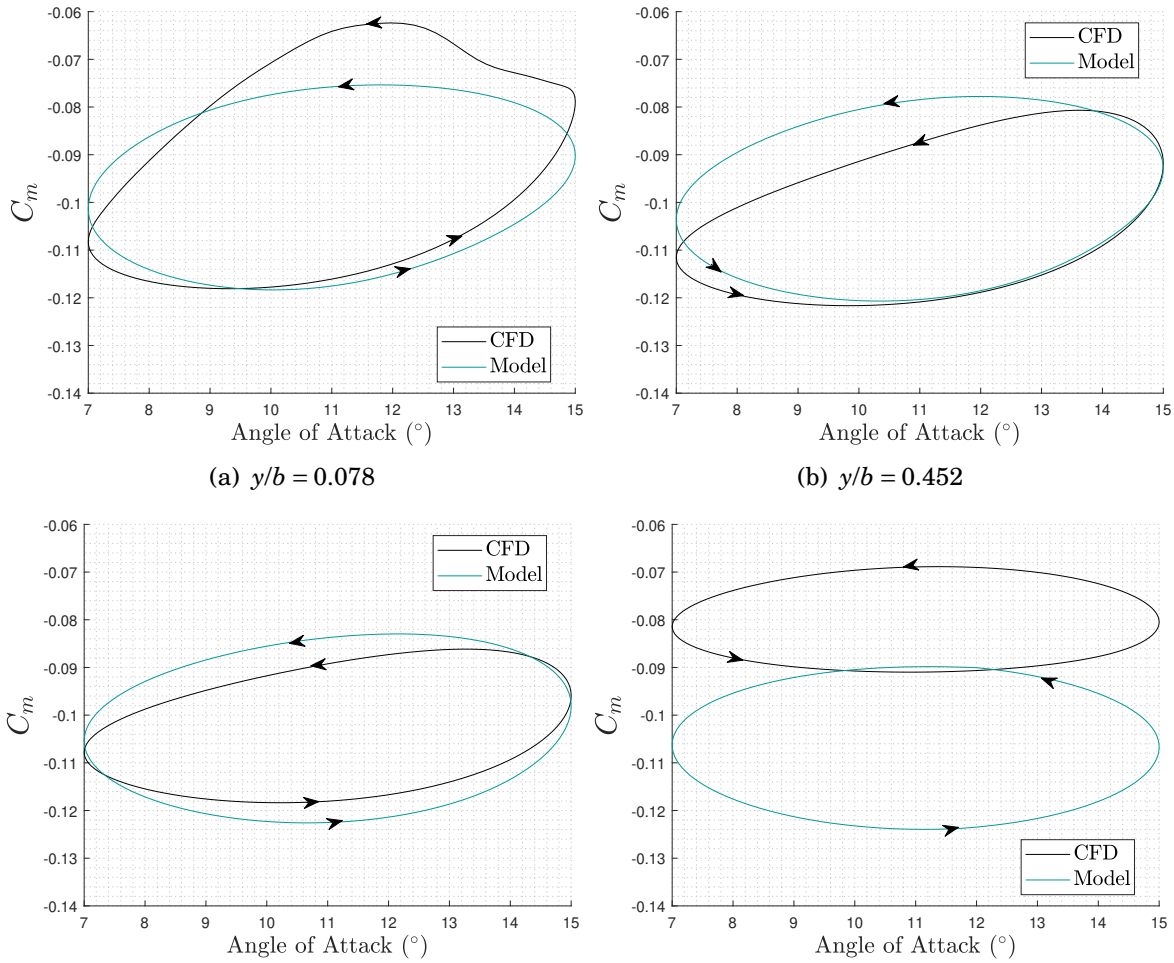

(a) $y/b = 0.078$

(b) $y/b = 0.452$

(c) $y/b = 0.707$

(d) $y/b = 0.924$

Figure 5.42: $\alpha = 11° \pm 4° \sin(0.15S)$

The unsteady data typically will take longer to generate, it was found that approximately an hour on the HPC setup above is needed. Furthermore, although no attempt to quantify the necessary number of cases was carried out, approximately 50 unsteady cases were used to build the B-L model. Therefore, assuming no parallel running of cases, around 50 hours of HPC was necessary. When this is compared to a single 3D simulation taking 36 hours, this may not seem good value even though three-dimensional mesh generation is avoided. The relative computational benefit of the unsteady nonlinear lifting line theory will then be increased dependent on the number of 3D cases desired. If for example ten cases were needed, this would take 360 hours using the aforementioned setup. On the

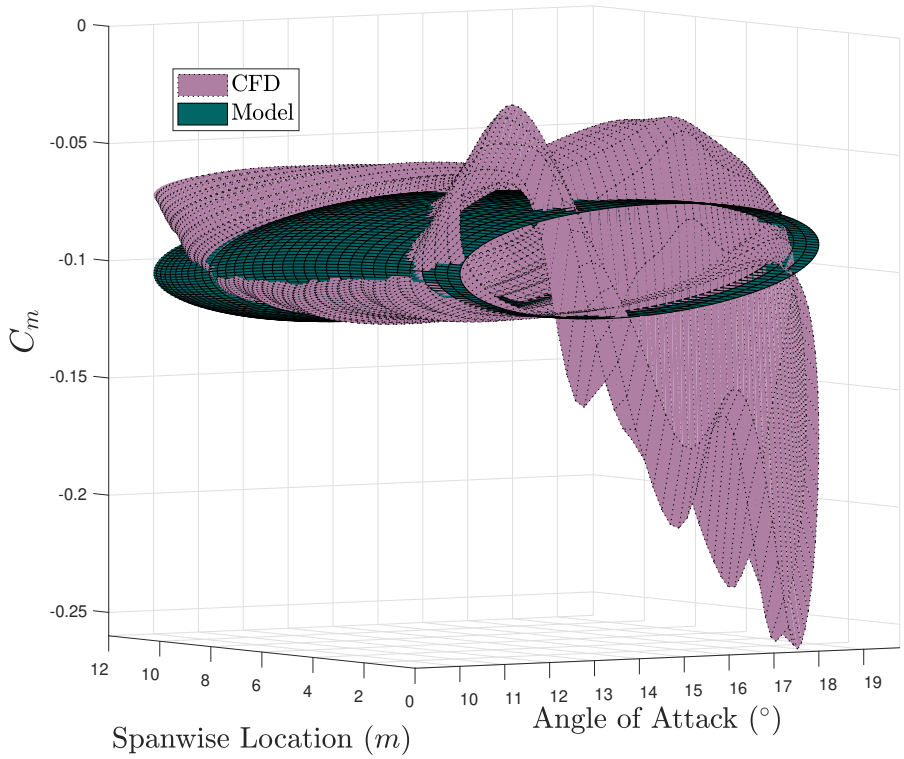

(a) $\alpha = 14° \pm 4° \sin(0.2S)$

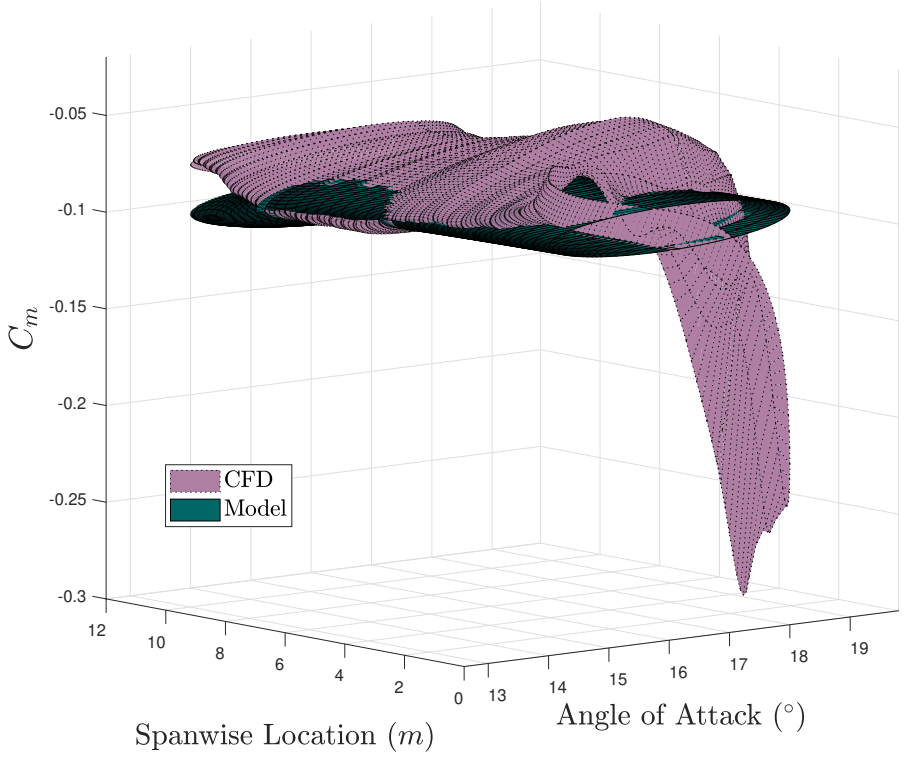

(b) $\alpha = 16° \pm 2° \sin(0.2S)$

Figure 5.43: C_m Model output against 3D URANS

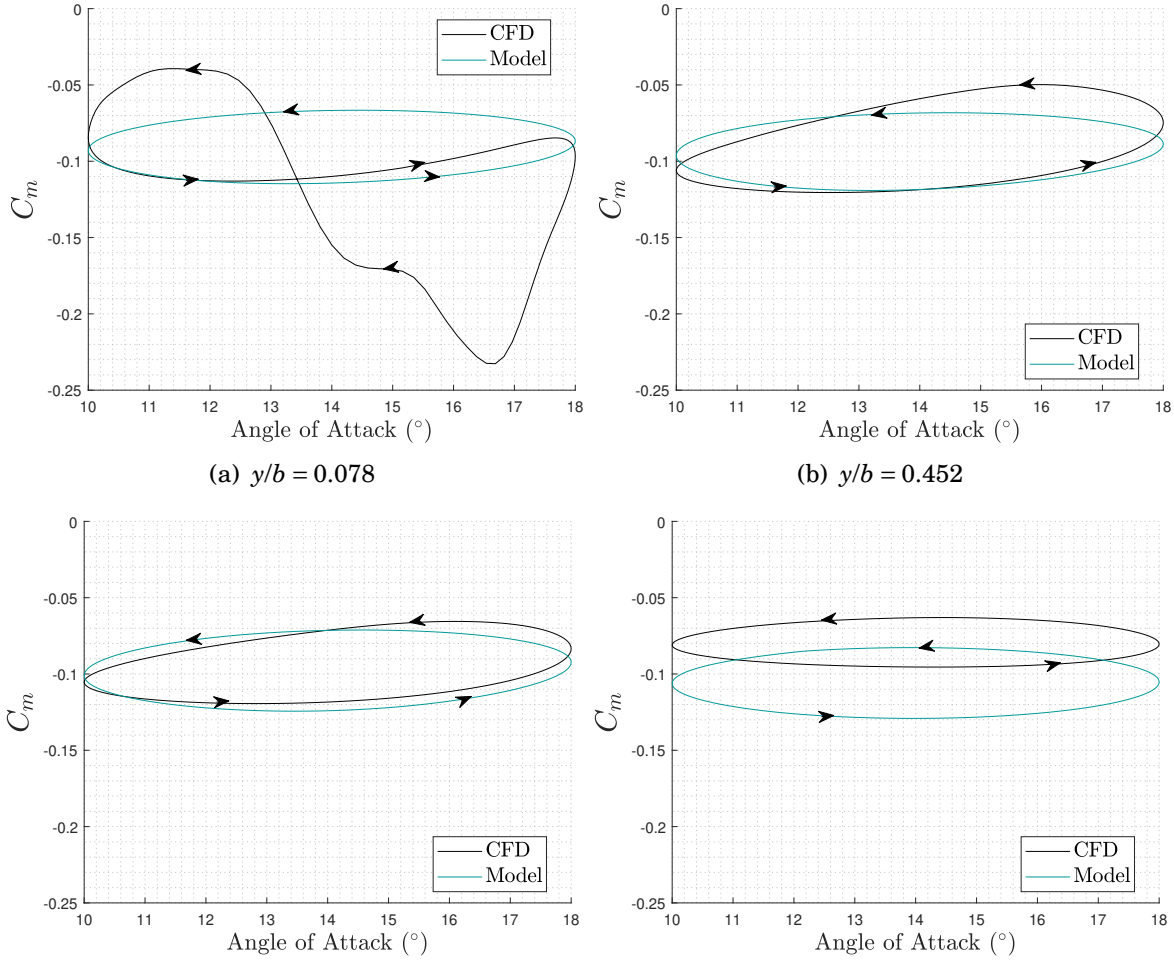

(a) $y/b = 0.078$

(b) $y/b = 0.452$

(c) $y/b = 0.707$

(d) $y/b = 0.924$

Figure 5.44: $\alpha = 14° \pm 4° \sin(0.2S)$

other hand, once the initial cost of setting up the nonlinear unsteady lifting line theory has been completed, each subsequent case is practically free.

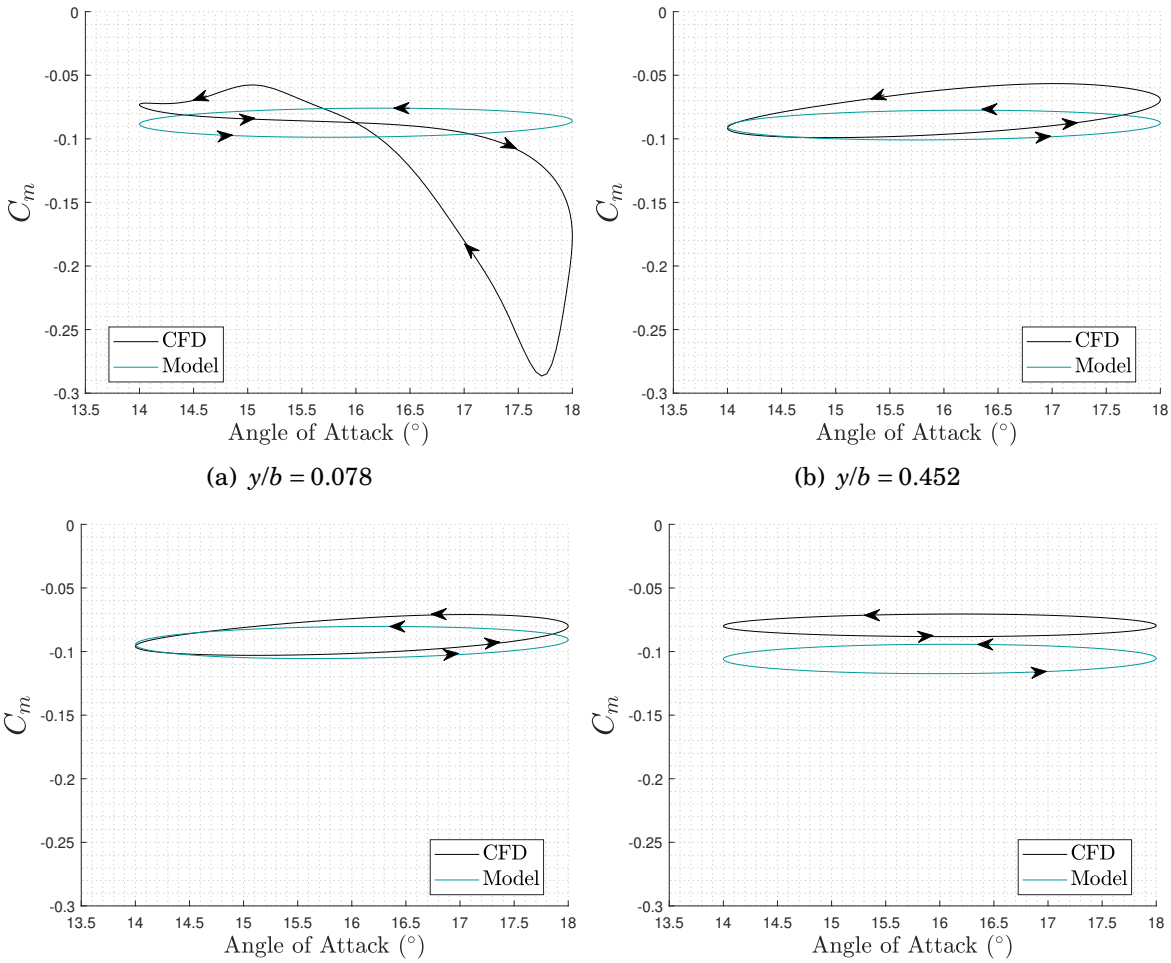

(a) $y/b = 0.078$ (b) $y/b = 0.452$

(c) $y/b = 0.707$ (d) $y/b = 0.924$

Figure 5.45: $\alpha = 16° \pm 2° \sin(0.2S)$

5.5 Aeroelastic Coupling

5.5.1 Structural Model

In order to simulate the aeroelastic response of a finite wing, the new 3D nonlinear unsteady lifting line model is coupled to a nonlinear intrinsic beam formulation which is based on the model presented by Hodges [124]. The intrinsic beam formulation is geometrically exact and allows for the beam to undergo large displacements and arbitrarily large rotations. A more detailed overview of the implemented structural model used in this work is given by Cook *et al.* [9]. The basis of the intrinsic beam model is to describe

a beam using a one dimensional coordinate system, s, which deforms along the length of the beam. Along the beam the local strains, $\gamma(s)$, and curvatures, $\kappa(s)$, are used as degrees of freedom. Note that in order to account for the washout which was present on the wing constructed from NACA LRN 1015 aerofoil sections, pre-curvature, $\kappa_0(s)$, needs to be applied. Further to the strain and curvature, translational velocity, $V_T(s)$, and angular velocity, $V_R(s)$ can vary along along the beam.

This model is implemented by discretising the beam into piecewise-linear finite elements. The intrinsic beam equations in this approach are then solved directly. The intrinsic variables of beam velocities, strains and curvature are directly solved. This then allows for the beam orientation and displacements to be integrated from the velocities. It also should be noted that due to the fact that nonlinearities in material properties are not relevant for this work, the strain to force and curvature to moment relationship is assumed to be linear.

5.5.2 Aero-strucural Coupling

Velocities and displacements are transferred using splines from the structural code to the NULLT. The forces are then evaluated by the NULLT model and are transferred back using splines to the structural elements. The splines used are Piecewise Cubic Hermite Interpolating Polynomial (PCHIP), which is a MATLAB R2018b function. The forces are rotated using quaternions from the global z direction to the normal direction with respect to the local chord, since this is how the loads are calculated in the unsteady lifting line. The loads are splined on to the structural loads, which do not necessarily share the same locations as those in the NULLT. The structural model has nodes running along the 40% chord line as well as the leading and trailing edge. At each spanwise location in the beam model, force vectors are placed at the three chordwise positions to create the correct force and moment. An example of the force vectors at the structural nodes is shown in Figure 5.47. Here the wing is cantilevered by fixing the wing root at $y = z = 0 \quad m$. With the positive z-force shown in the figure, the wing tip bends upwards as well as experiencing

torsional deformation. The forces are then splined onto the deflected structural nodes. A limitation of this approach is the aerodynamic influence matrix is not updated for deformation. This comes as a result of using the Prandtl lifting line theory. This could be resolved by using a numerical unsteady lifting line theory.

Multiple iterations are performed at each time step, until the structural and aerodynamic models reach equilibrium, or a maximum number of inner iterations has been reached. Figure 5.46 displays the C_l and C_l at every inner aero-structural iteration, at the mid-span of the NACA LRN 1015 wing. Initially the aeroelastic model is trimmed and once a steady state has been reached, the wing root is forced to undergo a 1-cosine pitching motion of a given amplitude, α_1 and reduced frequency, k.

$$\alpha(S) = \alpha_0 + \alpha_1(1 - \cos(kS)) \tag{5.5}$$

The example presented in Figure 5.46 is trimmed at a freestream angle of attack, $\alpha = 8°$. The wing is then subject to a 1-cosine pitching motion of amplitude 2° and a reduced frequency, $k = 0.10$.

In order to evaluate the aerodynamic modelling, the displacements from the aeroelastic model are applied to the CFD mesh so that the unsteady motion used in the CFD simulation is forced and identical to that output from the new model. This methodology was chosen because the aim is to validate non-periodic and realistic aeroelastic motions.

5.5.3 Aeroelastic results

The first aeroelastic case presented is for a root motion defined by $\alpha(S) = 10° + 2°(1 - \cos(0.1S))$. Before the root excitation, the wing is trimmed. The wing deformations are shown in Figure 5.48(a). This shows that the wing root is fixed, with the tip displaced to 0.76 m. Once the 1-cosine impulse at the root is applied, the angle of incidence increases as

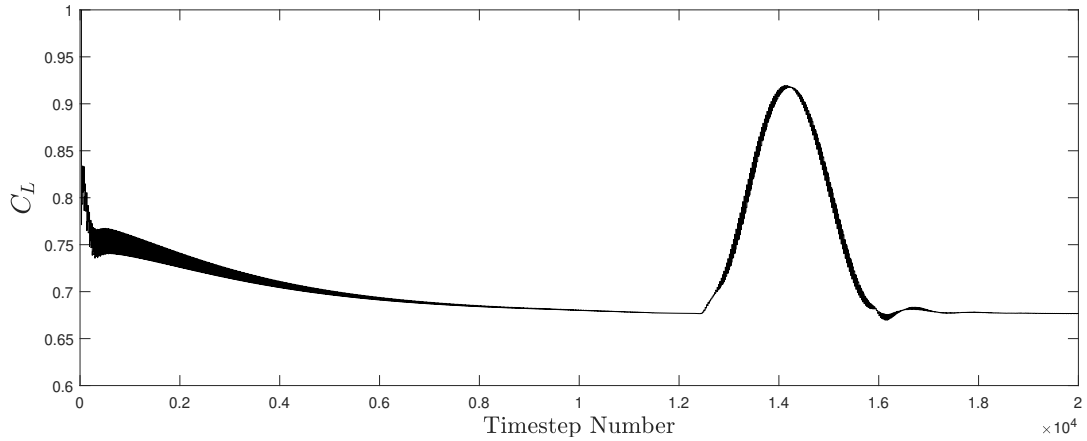

(a) C_l response at all inner iterations

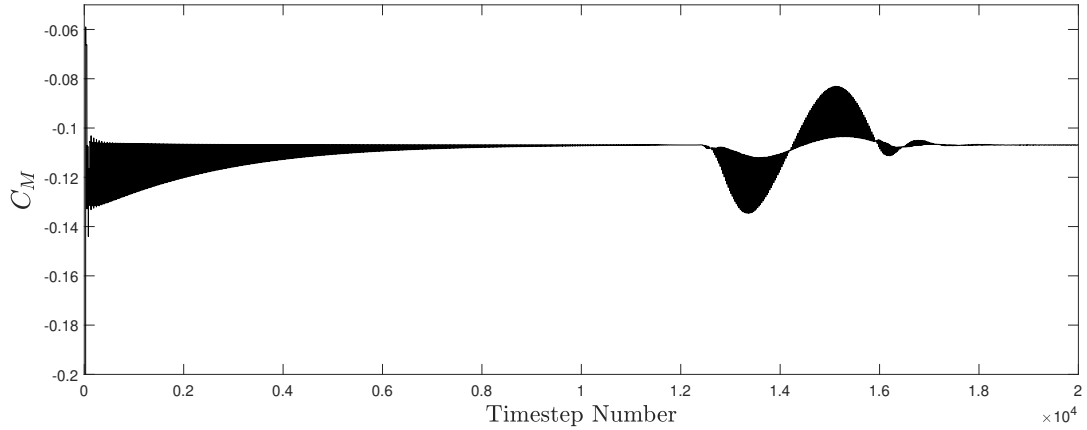

(b) C_m response at all inner iterations

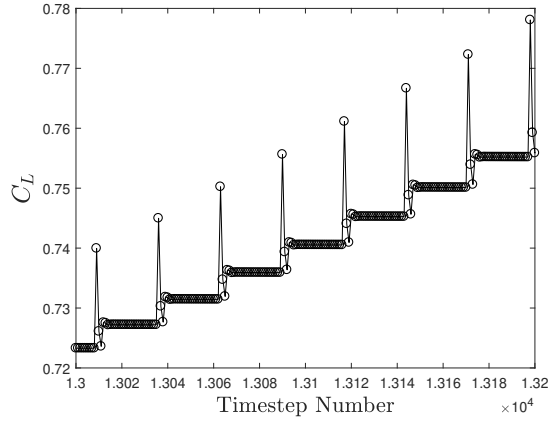

(c) C_l response at all inner iterations - close up

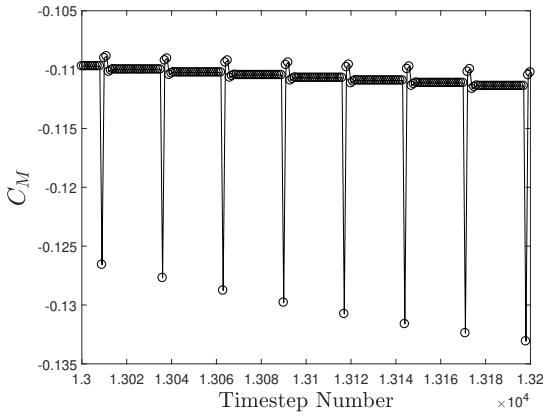

(d) C_m response at all inner iterations - close up

Figure 5.46: C_l and C_m response at each inner aeroelastic iteration

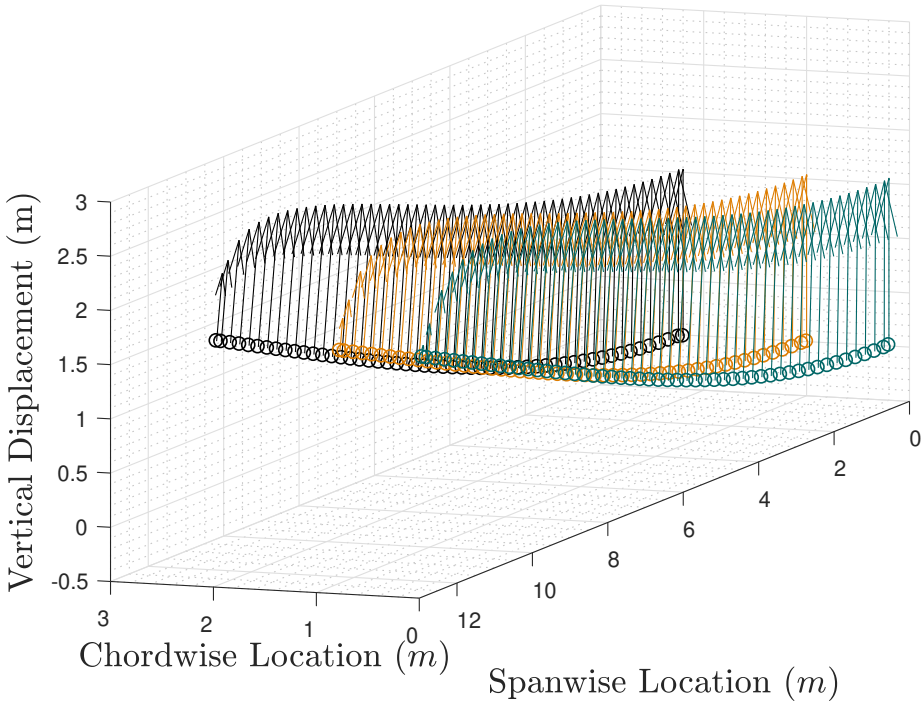

Figure 5.47: Forces splined and applied to the structural nodes, corrected for moment

does the lift force causing the deflections to increase. The lift coefficient history for the motion is shown using a surface in Figure 5.49(a) and cross sections in Figure 5.50. The lift coefficient is very well reproduced by the aeroelastic model. The moment, as with the rigid cases, show a good agreement in the inboard sections however the tip pitch down moment is overestimated, which has consistently been the occurrence in every case investigated, whether it be from experimental or CFD sources. Figures 5.49(b) and 5.51 show the result of this test case and the ability for the model to reproduce non-periodic motions. The pitch down moment also causes the tip to have a reduced angle of attack compared to the fixed root by approximately 6°.

The mean angle of attack is then increased to 12°. At this higher mean angle of attack the wing root begins to stall more severely, similar to the behaviour shown in the high angle of attack rigid CFD; this is displayed in Figure 5.52. Four spanwise results are also given for the lift and moment coefficient in Figures 5.53 and 5.54 respectively. In the aeroelastic cases, the moment also behaves similarly to the rigid pitching CFD with the moment curve slope being larger than predicted outboard. However away from the tip

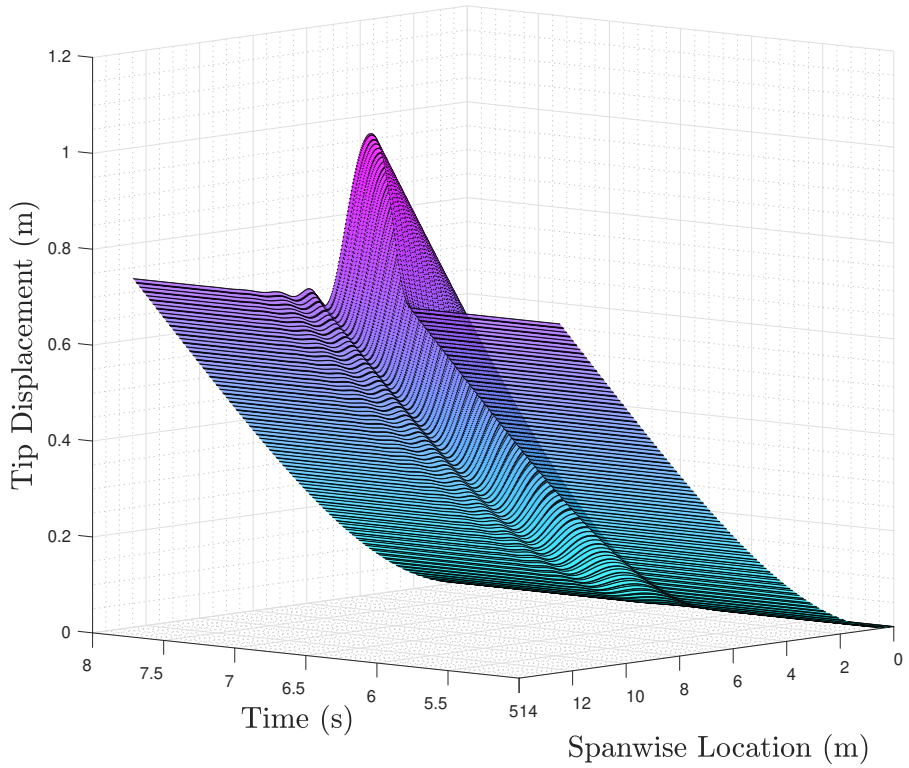

(a) Wing deflection and geometrical angle of attack

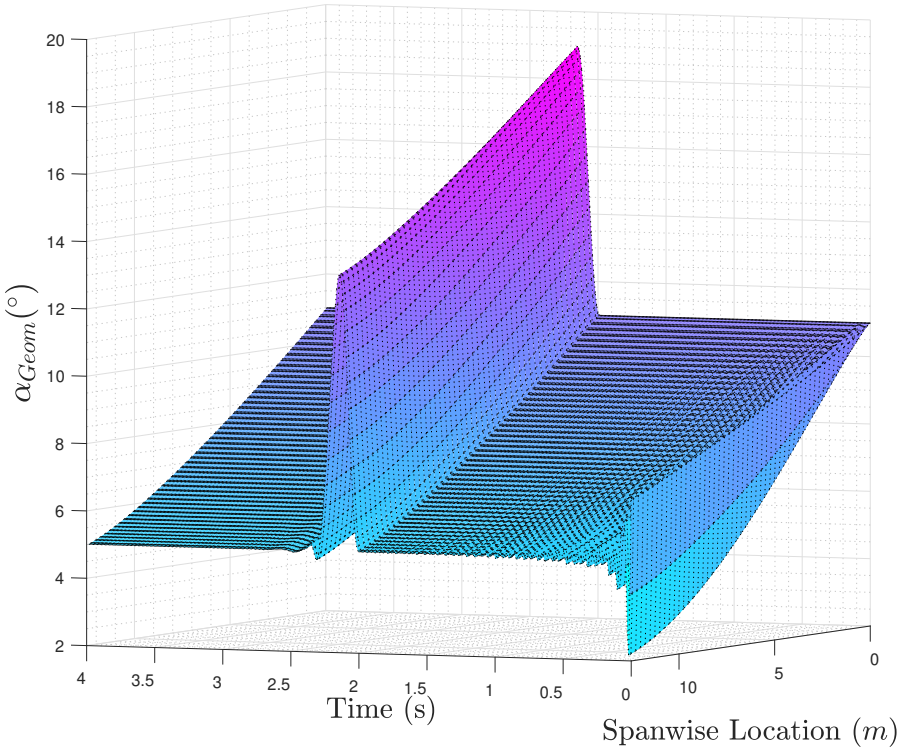

(b) Geometrical Angle of Attack

Figure 5.48: Wing deflection and geometrical angle of attack

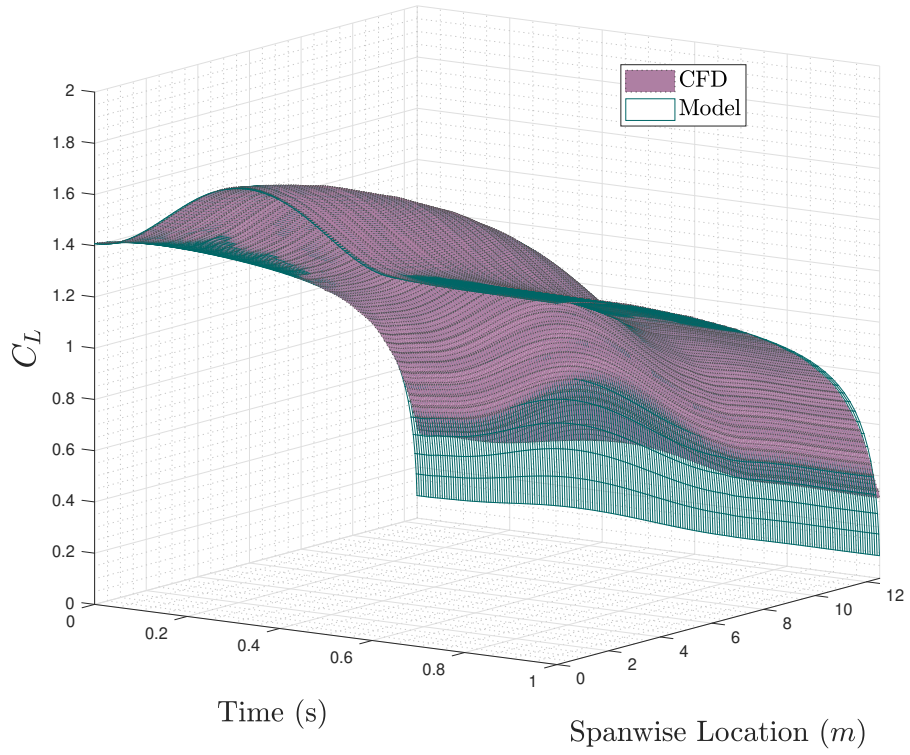

(a) Aeroelastic lift Coefficient surface history

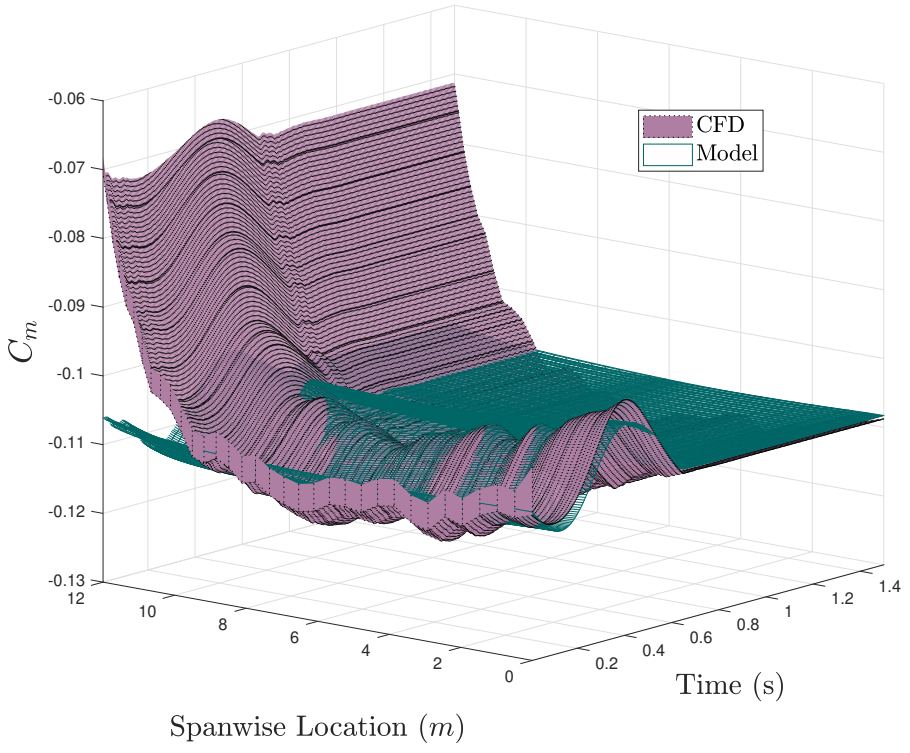

(b) Aeroelastic moment Coefficient surface history

Figure 5.49: Aeroelastic Case 1

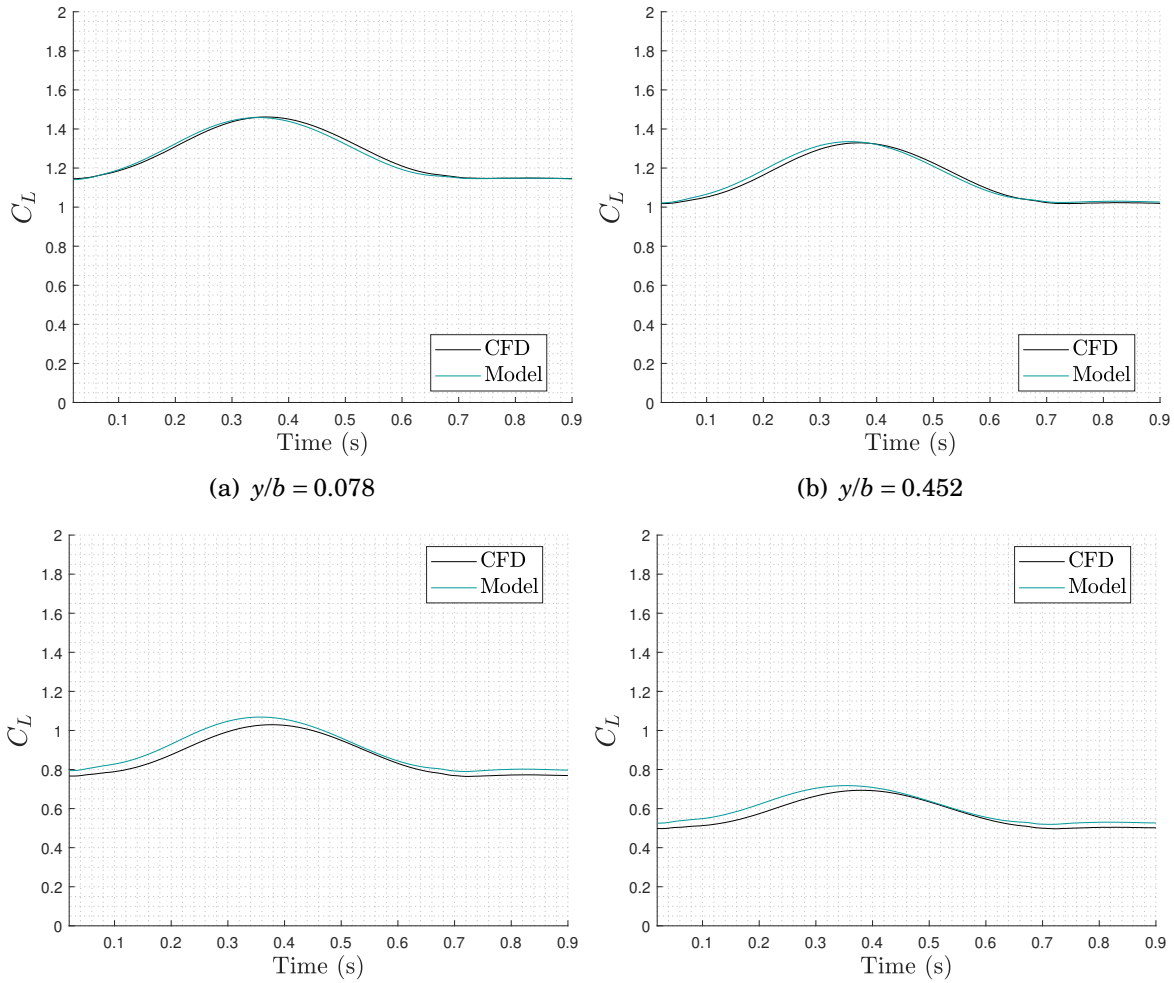

(a) $y/b = 0.078$

(b) $y/b = 0.452$

(c) $y/b = 0.707$

(d) $y/b = 0.924$

Figure 5.50: Aeroelastic lift Coefficient history, case 1

the moment coefficient is reasonably well captured. Overall the model shows promising results for predicting the aeroelastic behaviour of the finite wing at a fraction of the cost of a coupled CFD-CSM simulation.

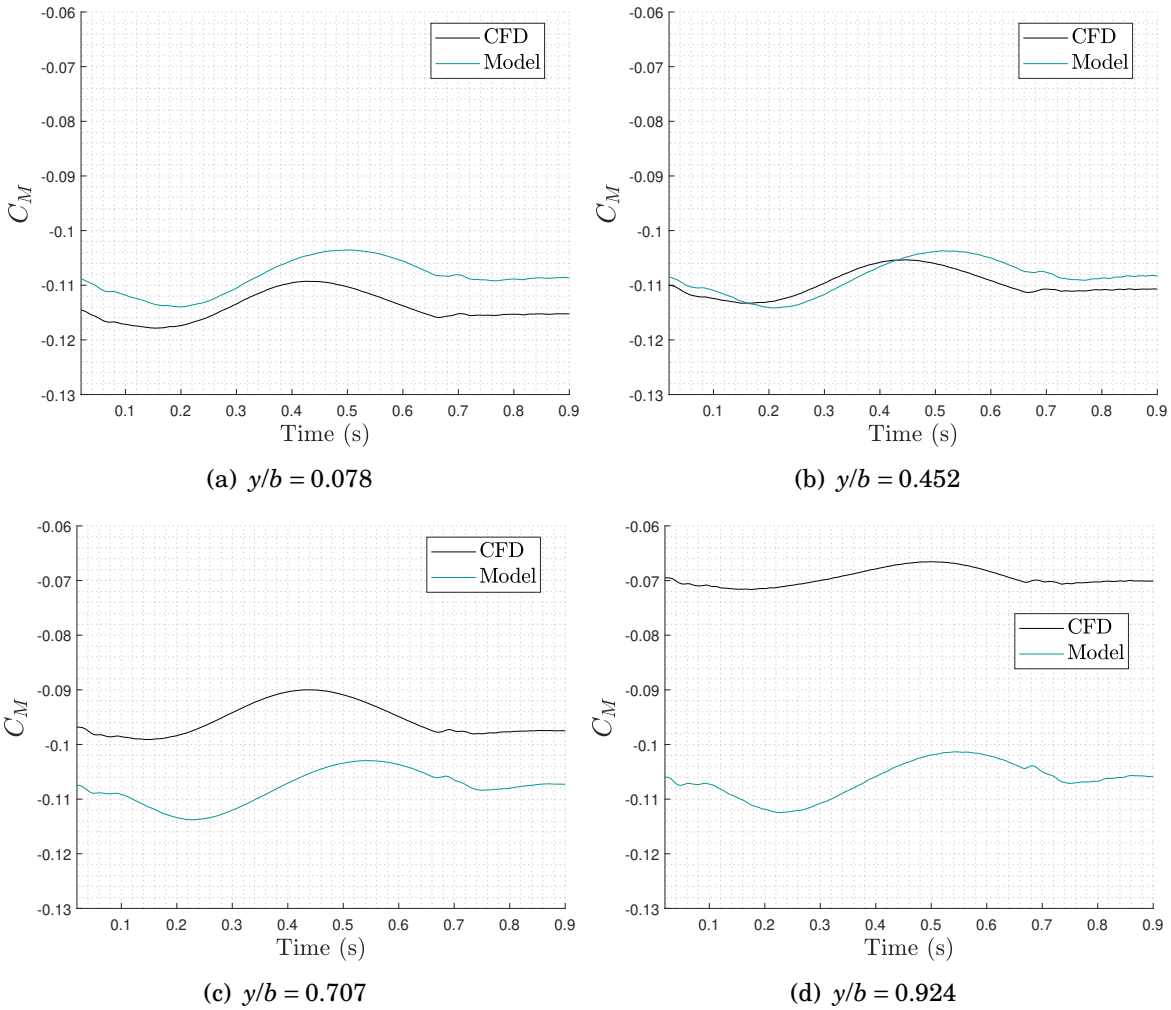

(a) $y/b = 0.078$

(b) $y/b = 0.452$

(c) $y/b = 0.707$

(d) $y/b = 0.924$

Figure 5.51: Aeroelastic moment Coefficient history, case 1

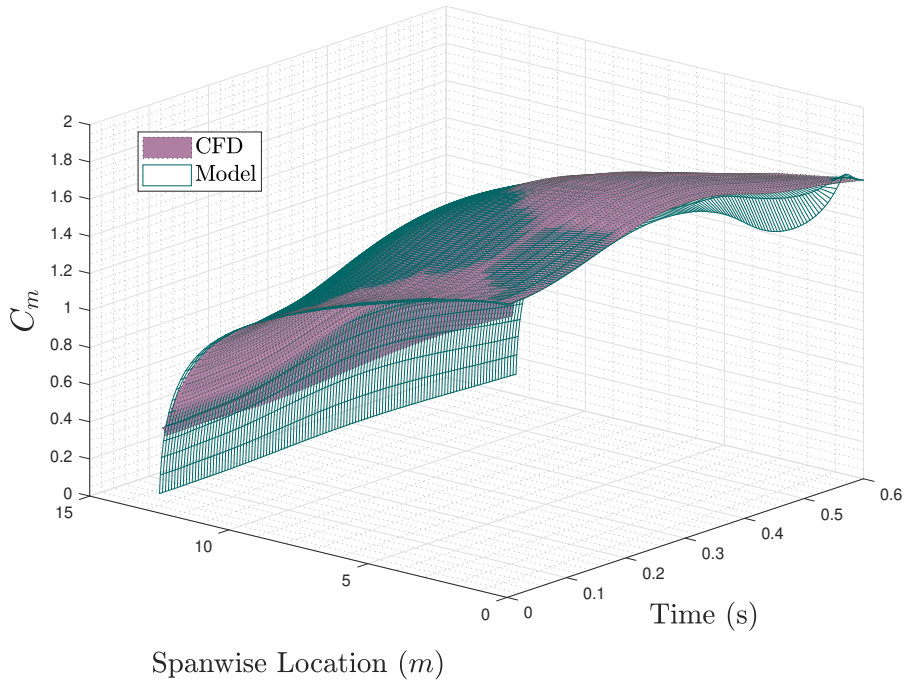

(a) Aeroelastic lift Coefficient surface history

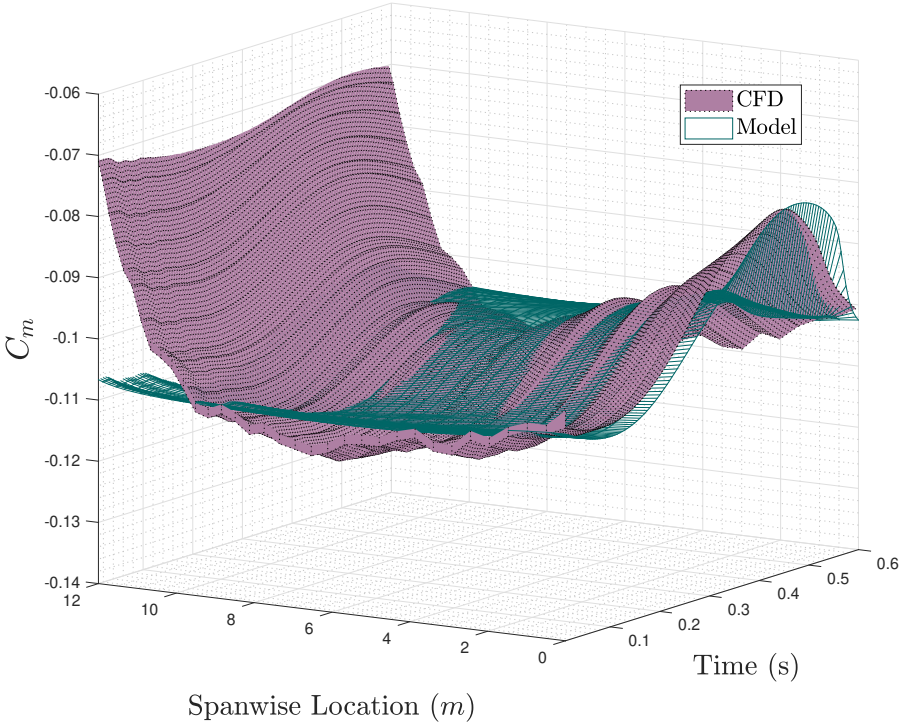

(b) Aeroelastic moment Coefficient surface history

Figure 5.52: Aeroelastic Case 2

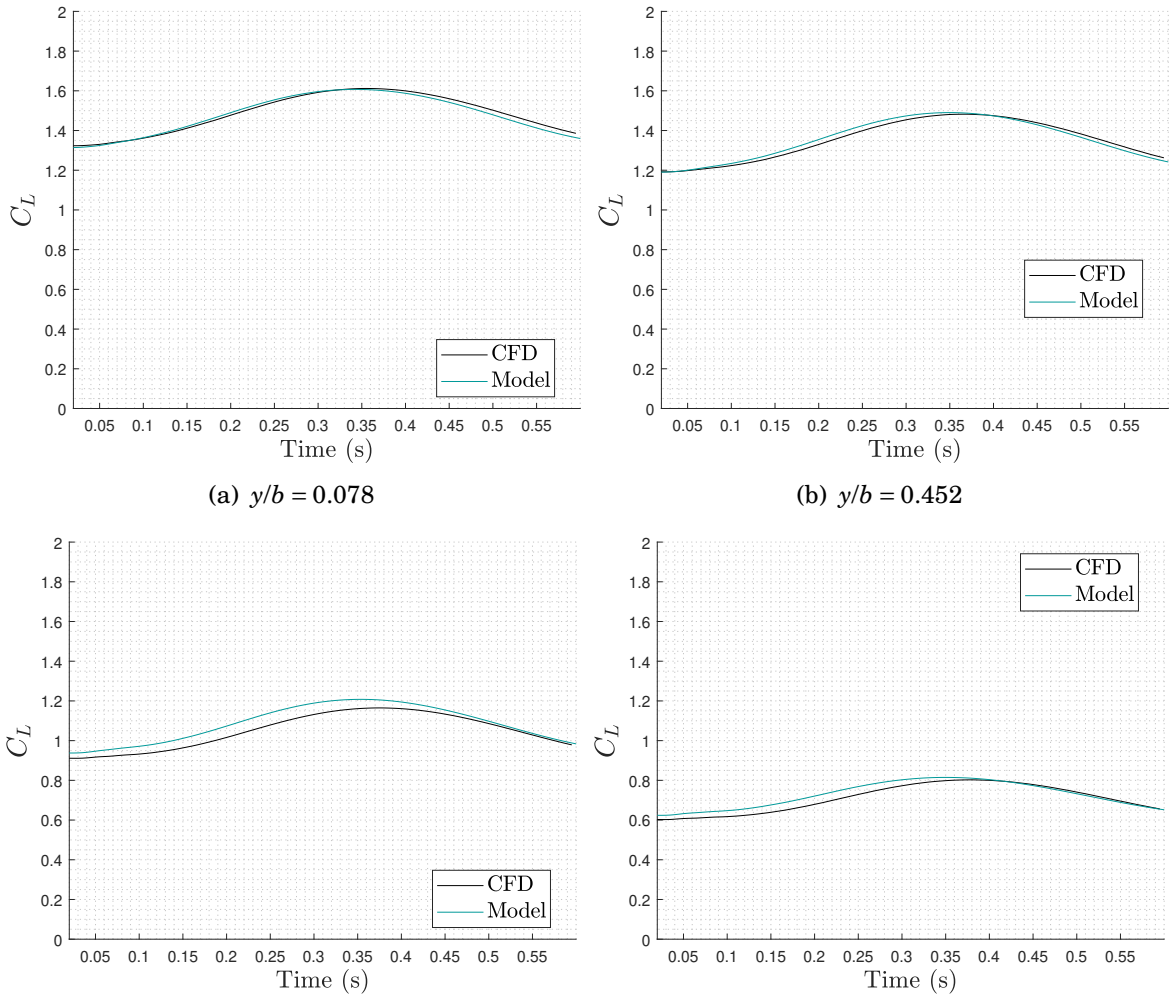

(a) $y/b = 0.078$

(b) $y/b = 0.452$

(c) $y/b = 0.707$

(d) $y/b = 0.924$

Figure 5.53: Aeroelastic lift Coefficient history, case 2

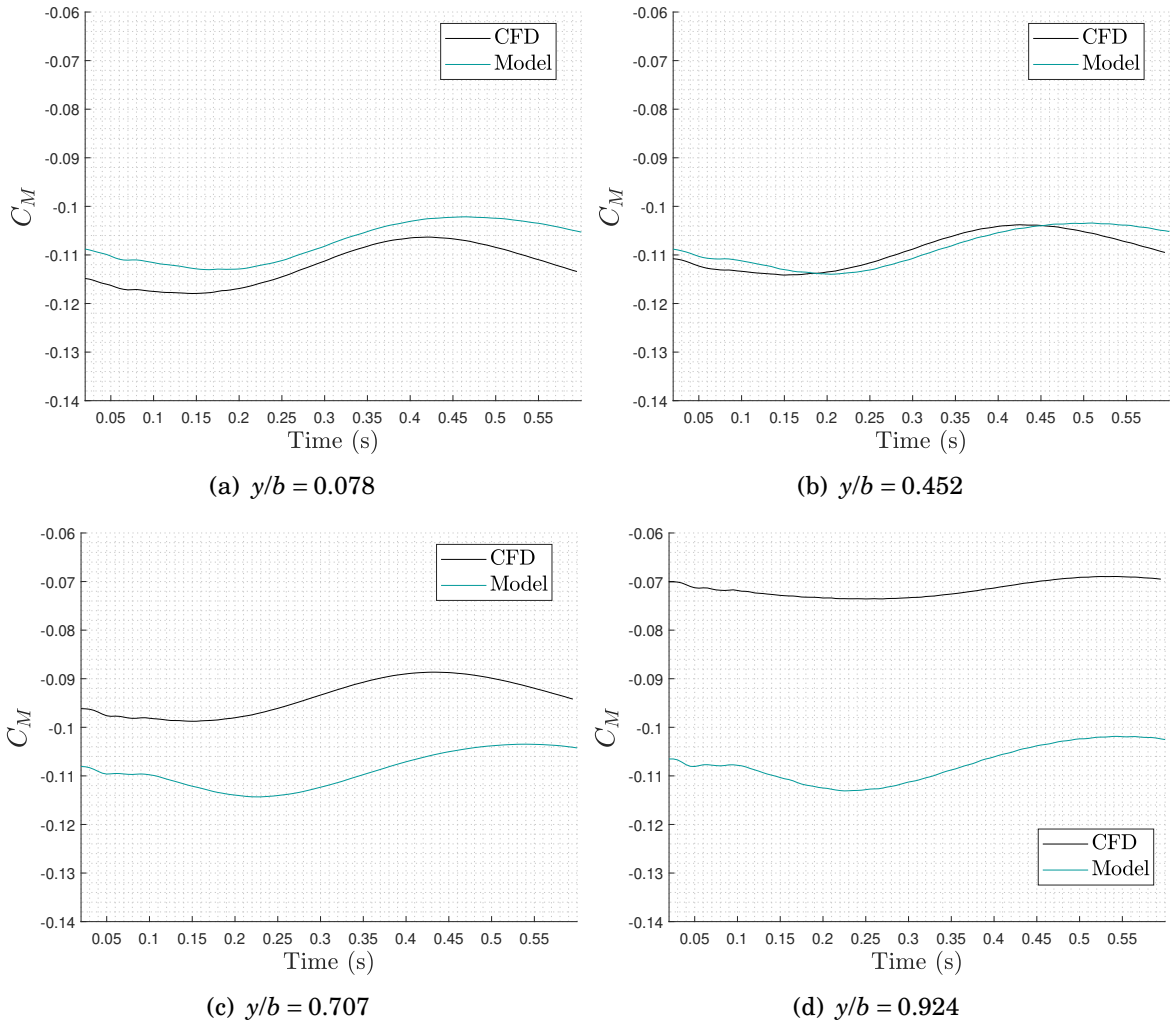

(a) $y/b = 0.078$

(b) $y/b = 0.452$

(c) $y/b = 0.707$

(d) $y/b = 0.924$

Figure 5.54: Aeroelastic moment Coefficient history, case 2

5.6 Comparison to other available models

In this section the coupled model is compared to XFLR5 which has been developed by Drela and Youngren [125]. XFLR5 is not a commercial package and therefore does not guarantee any level of robustness or accuracy. However this being said it is a well documented tool that has been applied to the early design stages of aircraft.

XFLR5 solves the Laplace equation, i.e. it is an inviscid potential flow method, however it introduces a viscous correction that is interpolated from the two-dimensional solver XFoil. XFoil uses a boundary layer solver in order to model the effects of flow separation on sub-critical aerofoils, [125]. Work has been carried out to compare the XFoil prediction to CFD, [126] with reasonable levels of accuracy achieved.

The number of chordwise points to define the aerofoil within XFoil was investigated with research [126] suggesting that 150 is sufficient in order for the polars produced by XFoil to show no discernible difference. Due to the fact XFoil is vastly less computationally expensive than 2D RANS, it was deemed appropriate for the number of points to be left equal to the maximum analyzed, with a total of 500 points defining the geometry.

XFLR5 is only able to simulate the steady response of a finite wing, therefore the comparison has been limited to the coupled unsteady model at very low reduced frequencies. In this case k has been fixed at a value of 0.001, which is considered quasi-steady. The experimental data presented will once again be the quasi-steady data from the three-dimensional experiments carried out by Piziali, [12]. In order for the XFoil correction to be applied within the XLFR5 routine, analysis has been carried out on the NACA 0015 profile in XFoil. A static sweep of c_l was performed on the NACA 0015 at a Reynolds number of 2×10^6, which matches the conditions of the experiment It should be noted that the experimental data from Piziali may not be that close the actual 2D sectional data. The result of this analysis has then been compared to the corresponding two-dimensional data produced by Piziali. Along with the averaged experimental data, the resulting

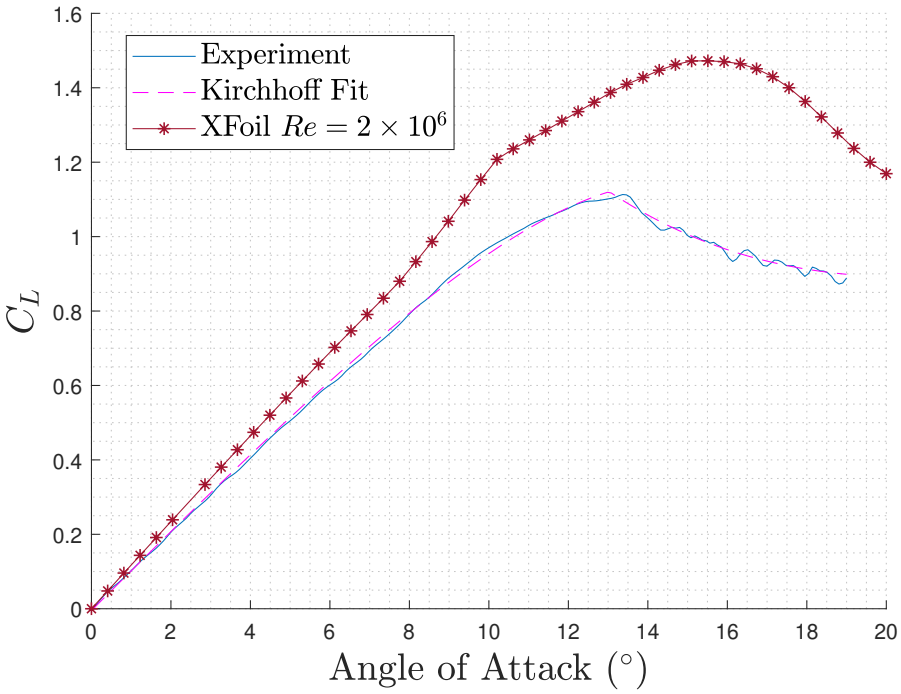

Figure 5.55: NACA 0015 aerofoil static c_l response calculated in XFoil at $Re = 2 \times 10^6$ against experimental data and the corresponding Kirchhoff fit.

Kirchhoff fit is presented in Figure 5.55. This shows that XFoil is unable to capture the lift curve slope, the maximum c_l or the angle at which static stall occurs. The maximum c_l calculated by XFoil is 1.47 and occurs at 15.5°. This is a 35% overestimate of $c_l^{\max}$ which according to the experimental data happens at an angle of attack of 13°. Using the Kirchhoff flow fit on the experimental data obviously gives a much better representation of the 2D static data. However the higher order two-dimensional aerofoil data must be present in order to do so. This being said considered here is the three-dimensional problem and the comparative expense of two-dimensional computational data is currently reasonably inexpensive. Therefore the introduction of higher order 2D data would appear to be of good value.

XFLR5 contains three separate methods capable of 3D analysis, these are a lifting line theory, vortex lattice method and a 3D panel method. Here the XFLR5 LLT and XFLR5 VLM will be considered for comparison. The lifting line theory introduces nonlinear

effects in a similar manner to alpha methods discussed in 5.1.1, where the downwash modifies the z-component of the free-stream velocity which in turn changes the effective angle of attack. The nonlinear sectional data can in turn be interpolated at the effective angle of attack which is inclusive of the downwash. The XFLR5 package also includes a linear VLM which can output some quasi-nonlinear data. From the three-dimensinal linear C_l distribution calculated, the values of, for example, C_m can be interpolated from sectional polars exported from XFoil. However issues arise when the 3D linear lift coefficient exceeds the 2D viscous $c_l^{\max}$, causing the code to fail.

Figures 5.56 to 5.57 show the 3D quasi-steady experimental data from Piziali [12] along with the NULLT model and both the XFLR5 lifting line theory and vortex lattice method. In this case superior results are achieved by the NULLT model, XFLR5 gives reasonable results at low angles of attack in which separation is not prevalent, however at larger angles of attack the results are generally poor. The XFLR5 VLM captured the lift distribution in the vicinity of the tip more favorably than the XFLR5 LLT at low angles of attack but failed to converge once the sectional C_l exceeded the 2D $c_l^{\max}$ from XFoil. The XFLR5 LLT is able to reduce the lift coefficient due to viscous effects although the magnitude of this were too small. This is likely due to the overestimation calculated by XFoil rather than the alpha-method coupling algorithm, yet this cannot be concluded. Furthermore, convergence issues were found within the XFLR5 LLT at angles of attack greater than 17°.

Included in Figure 5.57 is the uncorrected unsteady lifting line model, run in a quasi-steady manner. It is encouraging to see good agreement between the low angle of attack outputs of the XFLR5 LLT and VLM.

Overall these finding show that the introduction of higher-order two-dimensional data can be valuable for the correction of three-dimensional potential flow methods, the new corrected model outperformed the LLT and VLM in XFLR5 and also proved to be more

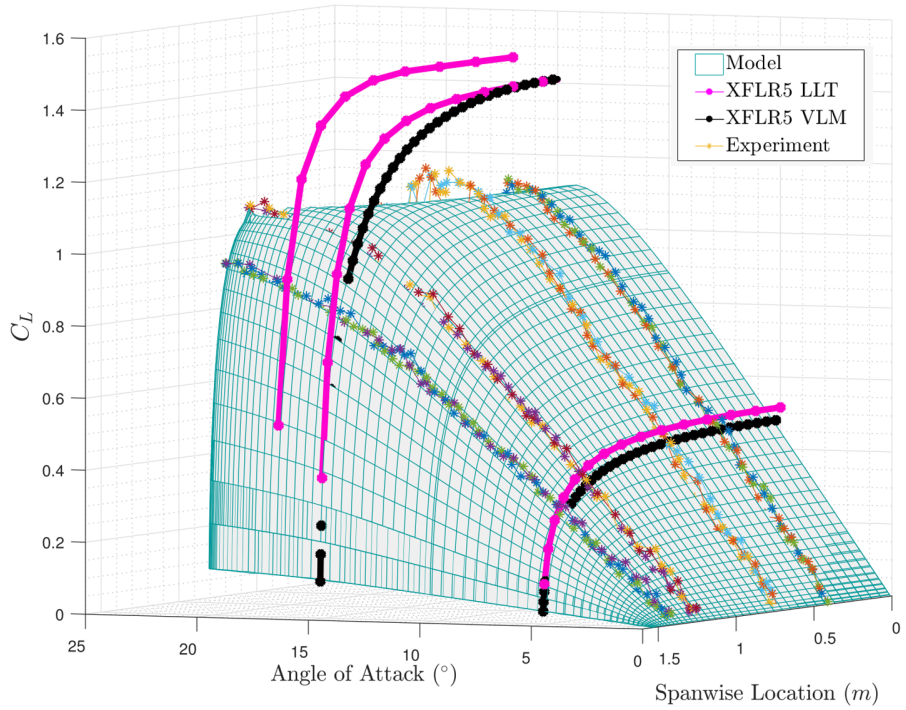

(a)

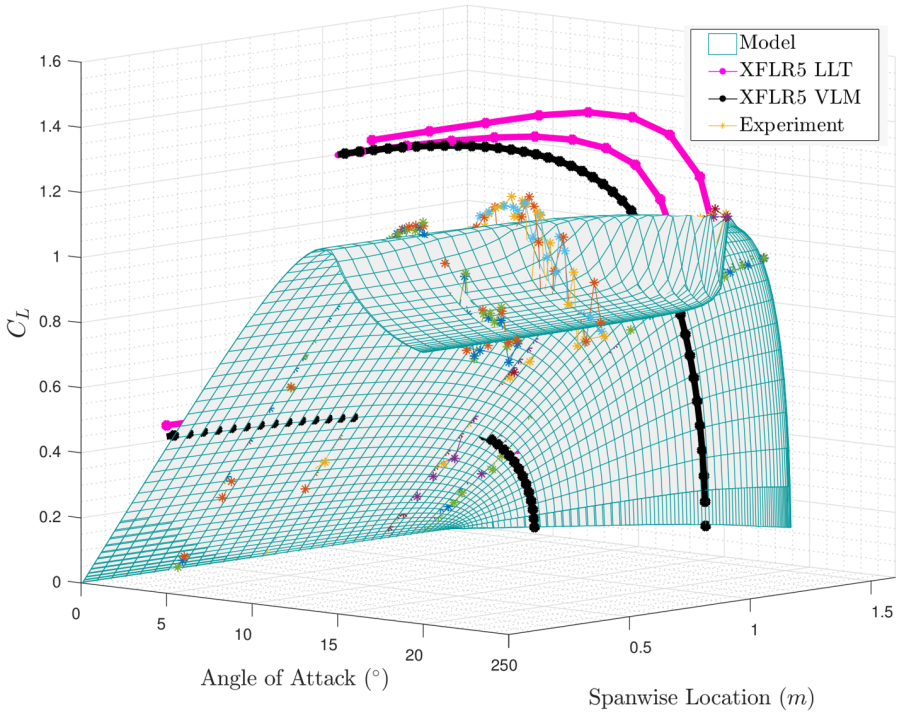

(b)

Figure 5.56: Quasi-steady results: Experimental, Coupled Model, XFLR5 LLT and XFLR VLM.

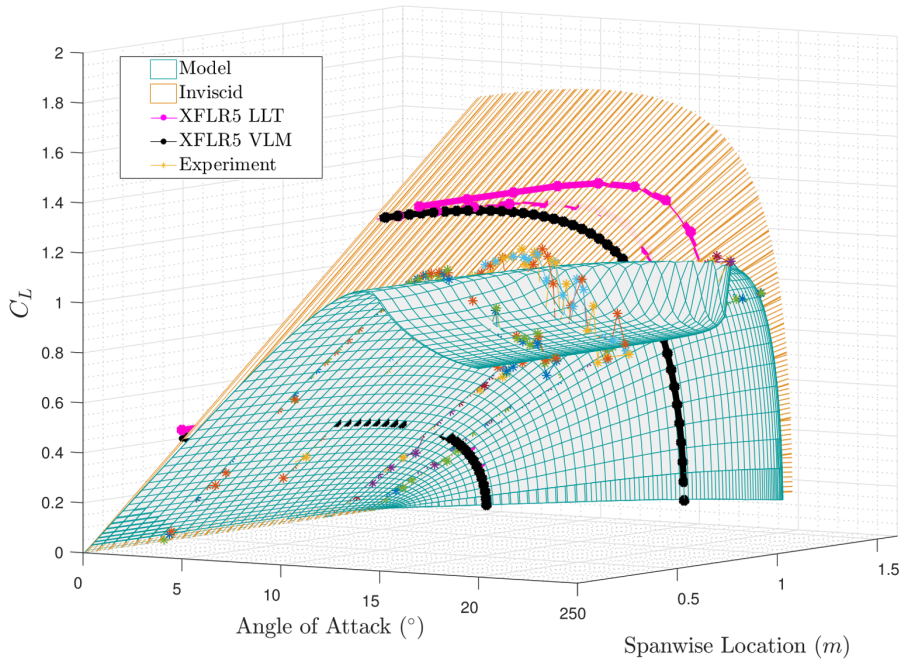

Figure 5.57: With linear ULLT

stable at higher angles of attack. The VLM did not contain any direct viscous correction to the lift coefficient and is intended to be used in more complex configurations which the XFLR5 LLT is incapable of modelling. When it is considered that the corrected model can also account for unsteady inviscid/viscous effects, the new model developed in this research has the potential to be a powerful design tool for the aerospace industry.

CHAPTER 6

CONCLUSIONS AND FURTHER WORK

This chapter concludes the work presented in this thesis and gives some suggestions for further work based on the findings.

6.1 Conclusions

A model has been presented that is intended for the use in the early design phase of aircraft with high aspect ratio wings. Cases have been presented for a clean, straight, wings utilising both experimental and CFD data. In order to reach a point in which the nonlinear unsteady lifting line could be implemented it was necessary to follow a number of steps. First both 2D and 3D CFD were used to investigate unsteady flow separation over an aerofoil and a finite wing constructed of the same profile. After this a number of dynamic stall models were explored in order to model two-dimensional flow separation with a more compact model. The Beddoes-Leishman model [65] was selected for this work and was shown capable of modelling the unsteady response of aerofoils undergoing unsteady separation. This was achieved by building the B-L model with experimental data for a NACA 0015 aerofoil [12] and using CFD for a NACA LRN 1015 section. The final piece was the addition of an unsteady, three dimensional potential flow code which

gives the ability to include the induced velocities over a finite wing. An unsteady lifting line was chosen due to the computational efficiency and because the representation using a single bound vortex at each spanwise location suited coupling to a dynamic stall model.

Overall the nonlinear model has shown very good results for complex flows containing unsteady flow separation. Both the lift and moment coefficient calculations have invariably been improved over traditional unsteady, inviscid methods by the inclusion of a dynamic stall model. The method has been shown to be a useful tool for the prediction of separation and it is foreseeable that the tool could be used to assess the impact of flow separation in both magnitude and whether unfavourable tip stall occurs within a flight envelope.

The largest errors produced by the nonlinear unsteady lifting line in lift coefficient were found at the wing centreline, where separation was underpredicted by the model. The flow behaviour at the centreline generally appeared to be more complex at high angles of attack due to the formation of stall cells. In order to account for this a more advanced model is needed that can simulate three dimensional separation and attachment mechanisms. Generally, the largest errors in the moment model were found close to the wing tip. Although further investigation is needed to properly determine the reason, it is thought to be caused by an offset in aerodynamic centre due to the the induced velocities from the tip.

Considering the massive computational savings the proposed model has compared to methods such as URANS, the findings provide a potential method for exploring more of the design space in the early stages of aircraft design. The nonlinear usteady lifting line theory was extended to aeroelastic cases through the coupling of a nonlinear intrinsic beam model. Whilst a detailed aeroelastic study was not conducted, this method has an opportunity to assess the impact of flow separation on the stability of an aircraft undergoing large deformations by means of a computationally inexpensive method.

6.2 Future Work

The results shown in Chapter 5 demonstrate excellent agreement in lift away from root stall cells. However accurate modelling of the moment distribution is essential for ensuring aeroelastic accuracy. Further research should therefore consider the improvement of both modelling the moment coefficient near to the wing tip as well as the formation of stall cells.

With respect to the moment coefficient, future research could explore the potential of a spanwise shift in the aerodynamic center to alter the moment curve slope because of the underestimation that was witnessed on the outboard sections of the wings in both the CFD and experimental data. Exploration of other Beddoes-Leishman dynamic stall models, with algorithms to modify the dynamic stall parameters should also be considered. This could help aid the prediction of flow reattachment. Furthermore the inclusion of further impulsive terms could improve the moment prediction close to the tip. Alternatively the method could be generalised to use the vortex lattice method rather than lifting line to investigate if a more three-dimensional method solves these issues. A careful view of Figure 5.5 shows that the nonlinear method can be interpreted as an iterative implementation of a series of projections. The solution is first projected from 3D to 2D inviscid, then from 2D inviscid to 2D viscous. Finally the 2D viscous solution is projected back to 3D. Therefore it would seem feasible to project a 3D vortex lattice method to a 2D series of discrete vortices and the rest of the method would remain unchanged. Using such a scheme should also benefit swept wing calculations.

A key improvement that would benefit the nonlinear unsteady lifting line is the ability to model stall cells. Some thought has been given on how to achieve this, however it could not be implemented and assessed in the given time. The basis of the stall cell

extension is to add an additional lifting line, therefore having two bound vortices and two collocation points at each spanwise location along a finite wing. The first bound vortex would no longer sit on the quarter-chord, instead it would be placed at $x = cf/4$, representing quarter of the chordwise distance in the attached region. Likewise a bound vortex would be placed at the one quarter point of the separated region, $cf + c(1-f)/4$. An example of this setup is shown in Figure 6.1.

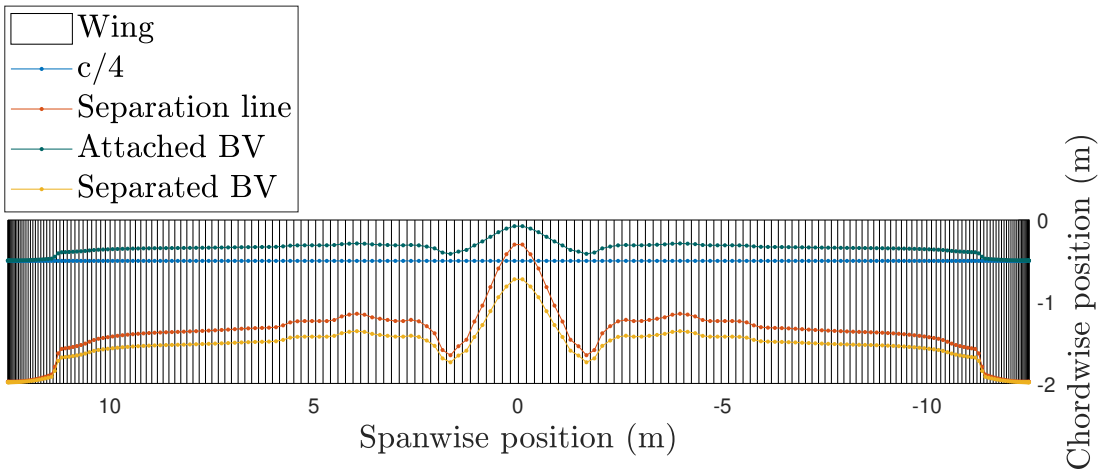

Figure 6.1: Example of the two lifting lines

In the simplest form this can be applied to an aerofoil undergoing static changes in angle of attack. Here two bound vortices are used as described above with the corresponding collocation points placed at the $3/4c$ position of the attached and separated regions. The attached and separated collocation points are therefore:

$$x^a_{col} = \frac{3cf}{4} \quad \text{and} \quad x^f_{col} = cf + \frac{3c(1-f)}{4} \tag{6.1}$$

respectively.

The aerodynamic influence matrix, A can then be formed for the two bound vortices and collocation points through the Biot-Savart law:

$$\mathbf{A} = \begin{bmatrix} 1/(cf\pi) & -4c\pi \\ 4/(3c\pi) & 1/(\pi c(1-f)) \end{bmatrix} \tag{6.2}$$

It is easily shown that this still gives the usual attached flow solution. Returning to Wood's original work [15], it can be seen that the representation of the flow is based on two potential distributions: one which represents the attached flow on the whole aerofoil and one which represents the shed vorticity from separation. This separated vortex sheet is assumed to lie on the aerofoil - changing the velocity influence but not the Kutta-Joukowski theorem. This could be approximated in a number of ways but will now be described in terms of a double lifting line method: one lifting line for the attached flow and one for the separated. The strength of the circulation in the separated region can then be modified by a factor to represent the shed vorticity and so give the original Kirchhoff flow relation.

It is desired for the two lifting lines to gives the same summed lift coefficient as Kirchhoff flow. In order to do this a coefficient, F, is placed on the circulation strength in the separated region. The coefficient is purely a function of the separation magnitude, as follows:

$$F = \frac{G(2f+3)}{3f\left(G\left(\frac{3-2f}{1-f}\right)-K\right)} \tag{6.3}$$

where G is given as

$$G = \frac{3f(1-f)}{3+4f(1-f)} \tag{6.4}$$

and K is the Kirchhoff relation:

$$K = \left(\frac{1+\sqrt{f}}{2}\right)^2 \tag{6.5}$$

Note that $G = 0$ when $f = 1$ and the flow is fully attached. This allows a new influence matrix, A_F to be formed:

$$\mathbf{A_F} = \begin{bmatrix} 1/(cf\pi) & -4Fc\pi \\ 4/(3c\pi) & F/(c\pi(1-f)) \end{bmatrix} \tag{6.6}$$

$$\Gamma = \mathbf{A_F}^{-1}\mathbf{U}_\infty \tag{6.7}$$

The circulation vector for the two bound vortices, Γ, can then be solved for $\mathbf{U}_\infty = [-|\mathbf{u}_\infty|\sin\alpha \quad -|\mathbf{u}_\infty|\sin\alpha]^T$. The total circulation for the aerofoil can be calculated by summing the two circulation values within Γ to achieve Γ_T. From this the C_l can be calculated by:

$$C_l = \frac{2\Gamma_T}{c|\mathbf{u}_\infty|} \tag{6.8}$$

This method acts like the Kirchhoff model, as shown in Figure 6.2, however two bound vortices are implemented. Figure 6.2 also displays the inviscid result along with the separation position. A suggestion for future work is to then apply this to a finite wing where the bound vortex in the separated region will have an influence at all spanwise locations, which may aid capturing complex three-dimensional flow separation. For example, if two adjacent bound vortices in the separated region have different chordwise positions and strengths, they will have an influence on one another which will likely further change their positions and strengths. It is foreseeable that this would need to undergo an iterative process, even under steady conditions, in order to converge on a solution. It should be noted that classical lifting line theory could not be used, since the separation line can change chordwise position along the span, effectively acting like sweep. For this reason a numerical lifting line theory, as described in Chapter 4, would need to be used. However a working implementation was not achieved during this research and therefore the ideas have not been tested.

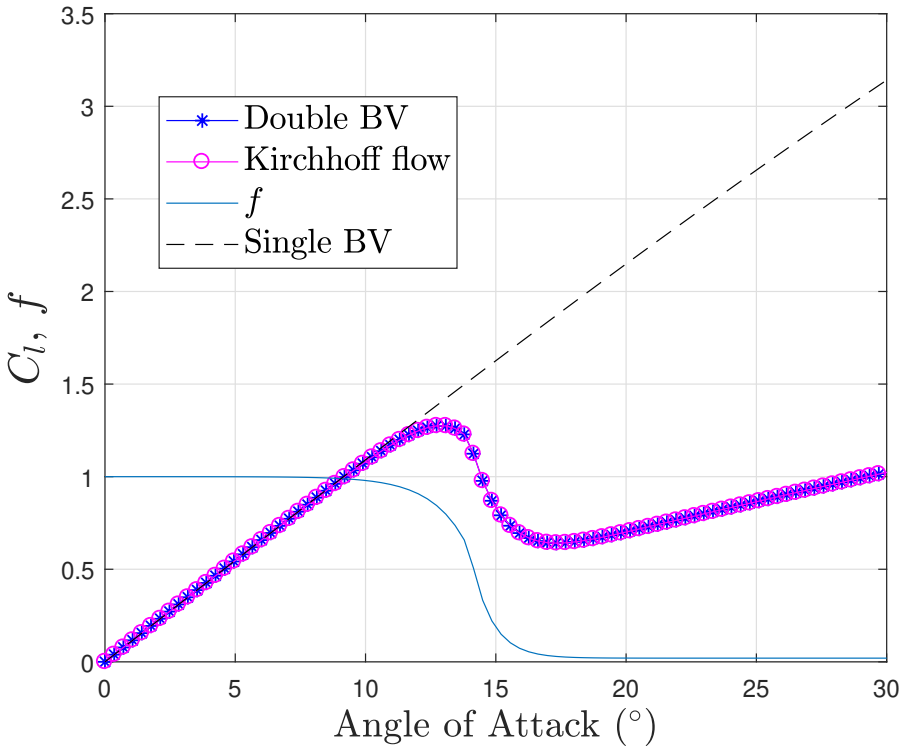

Figure 6.2: Static lift response for two bound vortices against Kirchoff model

It may be possible to combine the vortex lattice, as described for improving moment near the tip, in a similar manner to the double lifting line method. However this may be cumbersome to develop as the VLM mesh would have to constantly shift with the separation position and the relation to Kirchhoff will require more analysis.

Further improvement could be found by automating the process by which the dynamic stall model is built. This would give a more systematic approach to the process. Further to this the nonlinear unsteady lifting line could be evaluated for a wing consisting of varying sections. This would require multiple dynamic stall models to be built to assess the response of the wing.

APPENDIX A

A.1 Two-dimensional URANS used for building the Beddoes-Leishman model

Table A.1 gives the mean angle, amplitude and reduced frequency for the CFD sinusoidal pitching cases used for building the Beddoes-Leishman model for the NACA LRN 1015.

α_0 (rad)	α_1 (rad)	k
0.052	0.070	0.05
0.070	0.070	0.05
0.087	0.035	0.05
0.105	0.070	0.05
0.122	0.105	0.05
0.140	0.105	0.05
0.175	0.035	0.05
0.209	0.105	0.05
0.227	0.070	0.05
0.244	0.070	0.05
0.262	0.070	0.05
0.279	0.070	0.05
0.297	0.070	0.05
0.314	0.070	0.05
0.323	0.070	0.05
0.349	0.070	0.05
0.052	0.035	0.1
0.087	0.035	0.1
0.122	0.035	0.1
0.157	0.035	0.1
0.192	0.035	0.1
0.244	0.035	0.1
0.323	0.035	0.1
0.332	0.035	0.1
0.087	0.070	0.1
0.122	0.070	0.1
0.262	0.070	0.1
0.279	0.070	0.1
0.288	0.070	0.1
0.323	0.070	0.1
0.279	0.035	0.15
0.297	0.035	0.15
0.314	0.035	0.15
0.323	0.035	0.15
0.332	0.035	0.15
0.340	0.035	0.15

Table A.1: CFD data used to build the B-L model for the NACA LRN 1015

APPENDIX B

B.1 Two-dimensional URANS for the NACA LRN 1015

Table B.1 and B.2 give the coefficients needed to reconstruct the raw URANS data which has been used within this work. Lift and moment coefficients from two-dimensional URANS using the NACA LRN 1015 have been fitted with a ninth-order polynomial. In doing so errors are introduced into the C_L and C_M. The maximum percentage error when linearly sampling with 100 points is 3.19%. The mean error for the 100 points is approximately 0.5%.

B.1.1 Using the data

The following polynomial can used to estimate the aerodynamic coefficient, y_p, at the query points, x_p, as follows:

$$y_p = c_9 x_p^9 + c_8 x_p^8 + ... + c_0 \tag{B.1}$$

where , for example, c_9, represents the polynomial coefficient in column titled 9 in Tables B.1 and B.2. The query points, x_p, must be within the limits $0 : kV_\infty/\pi c$. The angle attack at x_p can then be calculated as follows:

$$\alpha_{xp} = \alpha_0 + \alpha_1 \sin kS \tag{B.2}$$

where α_0, α_1 and k are in columns 1, 2 and 3 in tables B.1 and B.2 respectively.

α_0	α_1	k	9	8	7	6	5	4	3	2	1	0
0.052	0.070	0.05	-2.85004	25.67888	-82.3496	128.3994	-112.474	66.37971	-27.9723	2.784978	2.041065	0.878262
0.070	0.070	0.05	-2.28664	24.10719	-83.682	138.1631	-126.485	74.92091	-29.9788	2.889597	1.992681	0.992465
0.087	0.035	0.05	0.34974	0.651221	-6.76639	12.46811	-11.4118	10.47903	-7.48075	0.533169	1.003947	1.126418
0.105	0.070	0.05	-11.7052	85.98225	-254.613	394.16	-349.088	185.8549	-59.0138	6.394375	1.67694	1.215276
0.122	0.105	0.05	-180.81	1149.428	-3060.34	4406.903	-3701.09	1825.242	-502.395	62.92866	-0.43175	1.342138
0.140	0.105	0.05	-270.327	1694.117	-4449.96	6325.1	-5238.6	2534.858	-676.303	81.96226	-1.41653	1.454899
0.157	0.105	0.05	-228.909	1445.938	-3818.81	5433.163	-4467.19	2112.206	-532.523	55.41593	0.188594	1.523949
0.175	0.035	0.05	-12.7471	94.59968	-284.931	451.6316	-407.249	210.5643	-58.6419	6.244805	0.381914	1.60476
0.192	0.105	0.05	140.4592	-726.935	1550.658	-1798	1291.215	-638.445	227.3788	-51.9278	5.173619	1.626227
0.209	0.105	0.05	229.5387	-1250.29	2831.131	-3482.29	2572.249	-1200.23	358.5159	-63.5282	4.501208	1.707871
0.227	0.105	0.05	143.8394	-765.056	1666.988	-1937.97	1333.431	-584.372	171.8569	-30.3894	1.270008	1.796831
0.244	0.105	0.05	-26.3646	193.2102	-598.631	983.3074	-898.492	442.4639	-104.456	10.36978	-1.75617	1.836004
0.262	0.105	0.05	-76.7465	453.2182	-1147.35	1589.047	-1267.32	558.6865	-117.31	9.143255	-1.58834	1.786412
0.279	0.105	0.05	31.78231	-180.049	409.8883	-505.536	404.0627	-243.394	106.4338	-23.5984	0.340472	1.708858
0.297	0.105	0.05	142.1277	-775.15	1754.801	-2156.66	1594.634	-750.537	227.1794	-36.9408	0.562904	1.673762
0.227	0.070	0.05	143.0113	-805.313	1880.144	-2362.15	1740.069	-771.133	202.8226	-28.7364	1.076624	1.758525
0.244	0.070	0.05	-12.0339	71.07298	-196.543	315.6592	-300.762	162.7488	-45.7537	6.682103	-1.216	1.768725
0.262	0.070	0.05	-102.95	588.6559	-1418.59	1858.33	-1417.85	622.5781	-143.974	15.02576	-1.26953	1.722835
0.279	0.070	0.05	-65.0123	400.9197	-1026.01	1397.371	-1075.21	451.684	-87.8466	4.779222	-0.65239	1.684313
0.297	0.070	0.05	34.93872	-150.552	245.9377	-190.73	86.01924	-50.3939	34.72848	-9.60772	-0.30048	1.65418
0.314	0.070	0.05	119.5931	-640.7	1421.75	-1696.98	1191.623	-512.402	135.986	-18.3804	-0.4374	1.618816
0.323	0.070	0.05	108.6928	-583.033	1289.443	-1521.4	1041.285	-427.177	105.3775	-12.0841	-1.04705	1.601567
0.332	0.035	0.05	30.10105	-161.561	355.1311	-411.753	272.6124	-107.554	26.54583	-2.78476	-0.67324	1.525824
0.340	0.087	0.05	62.47065	-324.489	680.2087	-737.796	447.356	-161.383	38.45692	-2.60185	-2.11956	1.562333
0.349	0.070	0.05	8.102191	-44.3236	91.15391	-88.649	46.13351	-23.2952	14.6688	-2.23516	-1.41744	1.490482
0.052	0.035	0.1	272.7506	-517.729	508.9832	-466.757	247.1467	6.431725	-38.0727	1.350528	1.887671	0.90861
0.087	0.035	0.1	596.3002	-1328.07	1273.567	-775.616	275.8458	17.41386	-38.788	1.066914	1.819827	1.131003
0.122	0.035	0.1	1066.021	-2274.53	1797.649	-615.794	-12.0787	132.4135	-55.9936	1.968303	1.675795	1.339188
0.157	0.035	0.1	4286.182	-9756.67	8141.499	-2613.91	-219.385	411.4984	-113.405	5.82542	1.376231	1.527407
0.192	0.035	0.1	19291.93	-48076.9	46798.93	-21672.8	4213.406	106.2522	-141.625	7.810454	0.89437	1.681146
0.244	0.035	0.1	-2880.49	6646.151	-5566.95	1578.035	461.0489	-459.845	137.8308	-17.5574	-0.15576	1.757606
0.262	0.035	0.1	1783.295	-1466.24	-2998	5224.993	-3264.96	994.5484	-140.905	7.8832	-1.00963	1.727883
0.279	0.035	0.1	1208.636	1499.826	-8443.09	10175.75	-5700.13	1624.909	-212.256	9.027922	-0.8736	1.695858
0.288	0.035	0.1	544.138	4203.776	-12813.3	13858	-7440.6	2077.136	-269.716	11.90716	-1.00213	1.68313
0.297	0.035	0.1	-6115.66	23513.43	-36265.8	29276.73	-13335	3375.653	-421.485	20.11091	-1.29559	1.670292
0.314	0.035	0.1	-7593.14	24280.87	-32421.6	23117.8	-9254.28	1933.567	-142.623	-5.59379	-0.72534	1.6288
0.323	0.035	0.1	7493.215	-22362.9	28088.23	-19534.2	8409.415	-2399.3	457.9675	-46.6134	0.179763	1.599966
0.332	0.035	0.1	23247.71	-69803.9	88004.64	-60556	24810.75	-6231.3	949.3519	-75.5666	0.590192	1.570877
0.340	0.035	0.1	28532.85	-86423.1	109689.5	-75625.2	30735.99	-7508.57	1077.006	-77.4018	0.230135	1.54199
0.367	0.035	0.1	-47551.5	134988.4	-159906	102371.8	-38296.9	8408.926	-1025.82	66.77472	-3.78716	1.452287
0.401	0.035	0.1	109619.3	-303833	350526.5	-217492	78225.31	-16383.7	1900.532	-101.36	-0.2336	1.290701
0.244	0.035	0.15	-547067	1085047	-894821	394095.6	-98494.9	13361.17	-730.874	-17.6	0.745447	1.796694
0.262	0.035	0.15	219477.6	-346768	213357.2	-64149.4	10064.45	-1205.25	261.8711	-37.8154	-0.01082	1.778935
0.279	0.035	0.15	282533.3	-427892	233140.3	-45019.7	-4545.6	2919.394	-285.162	-5.41205	-0.72988	1.744616
0.297	0.035	0.15	477470.4	-724351	397158.8	-77927	-7615.36	5234.17	-612.658	10.66646	-1.20851	1.716193
0.314	0.035	0.15	-237259	646390.5	-703299	400212.9	-128573	22943.87	-2000.47	61.0957	-2.33113	1.687731
0.323	0.035	0.15	-1082657	2172862	-1836863	844461.3	-226232	34638.22	-2661.01	72.39684	-2.47978	1.667468
0.332	0.035	0.15	-1904470	3602511	-2841882	1205761	-294473	40476.36	-2700.91	53.64664	-2.1461	1.642877
0.340	0.035	0.15	-2394157	4408428	-3356861	1358868	-311286	38984.67	-2190.17	18.24863	-1.75368	1.615484
0.052	0.070	0.1	1880.768	-3831	2875.141	-979.579	0.509068	247.1085	-119.459	5.719357	3.716379	0.885879
0.087	0.070	0.1	2719.242	-5570.9	3890.001	-735.689	-503.67	449.4324	-148.831	6.861838	3.554517	1.112042
0.122	0.070	0.1	5892.945	-11312.3	5880.734	1818.836	-3200.36	1475.629	-324.708	19.61324	2.946886	1.328734
0.157	0.070	0.1	33547.77	-77522.2	66297.93	-22514.9	-677.909	2602.368	-671.722	50.07296	1.622265	1.531574
0.192	0.070	0.1	-17102.4	69235.66	-112840	96550.11	-46900.9	12918.03	-1855.11	102.615	0.253424	1.702114
0.244	0.070	0.1	-5746	9693.109	-2441.74	-6001.64	6550.913	-3114.26	796.3737	-100.144	2.833565	1.829079
0.262	0.070	0.1	-25691.5	78686.12	-101579	71012.84	-28649.1	6517.909	-739.021	33.22662	-2.77392	1.859847
0.279	0.070	0.1	-44997.4	142153.4	-188550	135250.8	-56245.3	13440.82	-1701.69	99.74571	-4.76414	1.824804
0.288	0.070	0.1	-34980.2	112358.2	-150933	108937.3	-45092.7	10505.1	-1232.93	58.76526	-3.28728	1.78636
0.297	0.070	0.1	-9761.73	35786.12	-52747.9	39925.25	-16234.4	3220.889	-160.901	-24.0667	-0.71962	1.744016
0.314	0.070	0.1	43082.2	-128256	161622.4	-112818	47972.29	-12857.8	2137.006	-190.076	3.673363	1.674453
0.323	0.070	0.1	51629.73	-157587	203264.2	-144496	61919.21	-16426.9	2637.623	-222.114	4.085099	1.652158

Table B.1: Two-dimensional URANS C_L data for the NACA LRN 1015

α_0	α_1	k	9	8	7	6	5	4	3	2	1	0
0.052	0.070	0.05	1.46656	-10.12518	28.88034	-43.88977	38.11404	-18.72504	4.72550	-0.44990	0.00965	-0.11344
0.070	0.070	0.05	1.272375	-9.36628	28.07241	-44.31804	39.544523	-19.6793	4.911462	-0.45004	0.018419	-0.11423
0.087	0.035	0.05	-0.06706	-0.17755	1.999641	-4.884858	5.4890107	-3.06881	0.740442	-0.03599	0.006647	-0.11228
0.105	0.070	0.05	2.066379	-15.0008	44.66702	-70.44898	63.055716	-31.5558	7.980142	-0.82325	0.063096	-0.11465
0.122	0.105	0.05	22.05222	-140.003	372.5633	-536.2271	448.28408	-216.487	56.21458	-6.79428	0.405828	-0.12076
0.140	0.105	0.05	21.41955	-138.115	372.5137	-541.829	455.70417	-219.647	56.03244	-6.46976	0.397873	-0.1189
0.157	0.105	0.05	-1.73016	-2.92504	41.27738	-100.3436	108.74212	-56.7687	12.00353	-0.33769	0.081571	-0.11192
0.175	0.035	0.05	1.304798	-9.95471	30.72987	-49.81264	45.43635	-22.8147	5.60067	-0.5755	0.082057	-0.10187
0.192	0.105	0.05	-73.2171	414.0585	-976.14	1242.545	-925.5495	409.822	-104.829	13.79967	-0.50362	-0.09705
0.209	0.105	0.05	-88.3647	503.3643	-1193.88	1524.014	-1129.952	489.9491	-118.714	13.93269	-0.36693	-0.09364
0.227	0.105	0.05	-84.8482	485.351	-1152.55	1464.789	-1069.498	446.7057	-99.4997	9.555732	-0.0222	-0.09052
0.244	0.105	0.05	-70.0683	403.5262	-960.834	1215.142	-869.6598	344.6927	-67.1826	4.095964	0.264298	-0.08328
0.262	0.105	0.05	-51.473	302.2155	-731.015	932.8763	-664.6051	254.2623	-43.8034	1.275584	0.233744	-0.06967
0.279	0.105	0.05	-32.7907	200.2605	-501.675	658.494	-476.4977	180.223	-28.4263	0.332015	0.039503	-0.05831
0.297	0.105	0.05	-23.4888	144.607	-365.622	482.6368	-346.6203	125.1112	-16.0078	-0.54387	-0.11032	-0.05501
0.227	0.070	0.05	-38.5839	223.592	-538.559	695.7926	-518.7946	223.6279	-52.6778	5.585452	-0.00161	-0.08332
0.244	0.070	0.05	-19.665	118.4494	-294.213	386.9033	-286.8781	117.5348	-23.777	1.43809	0.182801	-0.07358
0.262	0.070	0.05	-12.9691	81.58284	-210.79	286.5499	-217.189	88.97814	-17.1778	0.893863	0.090175	-0.06142
0.279	0.070	0.05	-16.8976	100.6678	-249.133	327.2851	-240.7452	95.11464	-17.09	0.74705	0.023517	-0.05593
0.297	0.070	0.05	-13.3468	79.9789	-198.998	261.2805	-188.8262	69.8396	-9.72673	-0.20615	-0.01315	-0.0546
0.314	0.070	0.05	-5.956	42.02304	-119.71	175.3952	-138.3535	55.03581	-8.63317	0.37776	-0.18741	-0.05459
0.323	0.070	0.05	-3.62174	30.01407	-94.7458	148.8631	-123.5751	51.39831	-8.76435	0.692081	-0.26284	-0.05691
0.332	0.035	0.05	0.24137	2.597458	-16.23	33.24514	-31.74578	14.21177	-2.43927	0.245592	-0.11773	-0.05847
0.340	0.087	0.05	11.17332	-53.386	101.8757	-104.1097	71.132845	-40.6321	16.75348	-2.51234	-0.28446	-0.07063
0.349	0.070	0.05	10.40302	-53.0081	111.5749	-130.1993	99.074272	-54.7668	20.28014	-3.20878	-0.12406	-0.07746
0.052	0.035	0.1	-53.958	87.45502	-6.10944	-74.98914	65.22226	-23.5379	3.311572	0.031261	-0.0048	-0.11356
0.087	0.035	0.1	-140.64	294.4483	-190.986	-5.216522	59.610724	-25.7827	3.397685	0.075752	0.010781	-0.11436
0.122	0.035	0.1	-225.197	475.8822	-314.55	-2.064719	92.951581	-40.5686	5.579949	-0.0579	0.038895	-0.11284
0.157	0.035	0.1	-597.055	1268.529	-864.87	40.9041	215.74047	-100.429	16.12094	-0.79166	0.091794	-0.10848
0.192	0.035	0.1	-3539.59	9222.946	-9641.34	5099.458	-1406.078	188.8387	-12.9325	0.909551	0.107403	-0.09975
0.244	0.035	0.1	-472.571	2218.931	-3820.1	3280.314	-1544.565	405.1856	-56.7669	3.1287	0.184254	-0.07475
0.262	0.035	0.1	-1518.42	4663.271	-6004.04	4137.571	-1610.203	342.4808	-34.9585	0.751883	0.184307	-0.06435
0.279	0.035	0.1	-1822.12	5516.432	-6975.36	4700.925	-1777.831	362.3659	-34.4587	0.903818	0.073803	-0.05743
0.288	0.035	0.1	-2875.04	8519.868	-10545.8	6979.132	-2613.023	536.2495	-53.5904	2.032303	0.002756	-0.05554
0.297	0.035	0.1	-3734.18	11026.26	-13586.4	8949.18	-3338.41	684.0322	-68.41	2.727869	-0.05104	-0.0548
0.314	0.035	0.1	-2539.06	7867.98	-10065	6761.845	-2491.175	468.3409	-33.6556	0.127321	-0.07819	-0.05647
0.323	0.035	0.1	363.5759	-197.29	-722.719	920.9288	-358.5314	9.025607	21.86656	-2.91867	-0.07784	-0.05887
0.332	0.035	0.1	3559.89	-9181.01	9746.863	-5604.389	1978.7436	-470.665	74.13662	-5.14318	-0.11565	-0.06228
0.340	0.035	0.1	5049.135	-13319	14438.21	-8367.953	2861.3682	-610.401	80.01928	-4.07809	-0.23815	-0.06652
0.367	0.035	0.1	-1726.66	4502.825	-4706.41	2382.735	-475.3707	-63.8369	42.26048	-3.87637	-0.22493	-0.08985
0.401	0.035	0.1	-7145.29	24219.21	-34360.6	26488.05	-12028.15	3258.238	-512.616	45.1321	-2.02131	-0.11609
0.244	0.035	0.15	18005.33	-15133.7	-7657.79	14084.71	-6992.331	1720.257	-230.625	14.85123	-0.00719	-0.08108
0.262	0.035	0.15	-111579	227723.5	-195816	91452.52	-24885.26	3940.071	-344.735	13.88294	0.10633	-0.07209
0.279	0.035	0.15	-119612	243898.5	-207889	95145.03	-24912.86	3672.363	-281.228	9.191172	0.063877	-0.06318
0.297	0.035	0.15	-219868	440533.7	-369197	166433.9	-43077.37	6309.027	-483.222	17.00695	-0.22078	-0.05818
0.314	0.035	0.15	-216316	433325.9	-361356	160662.3	-40301.61	5500.377	-354.343	8.272751	-0.17922	-0.05929
0.323	0.035	0.15	-98519.6	199654.8	-166032	71321.55	-16021.33	1525.216	21.26899	-9.30046	0.043676	-0.06228
0.332	0.035	0.15	94359.38	-184872	155713.7	-75058.18	23152.818	-4693.61	578.8792	-33.5789	0.349427	-0.06694
0.340	0.035	0.15	278617.3	-556013	468509.7	-217717.1	61135.067	-10616.7	1089.076	-53.9578	0.544785	-0.07245
0.052	0.070	0.1	113.8063	-699.726	1366.58	-1285.76	658.95698	-185.57	25.57383	-1.06589	0.014622	-0.11725
0.087	0.070	0.1	-252.646	174.4015	581.2313	-980.4763	628.74655	-195.579	27.34814	-1.07794	0.04732	-0.11865
0.122	0.070	0.1	-735.361	1020.707	345.5871	-1434.199	1069.5543	-358.754	54.98265	-3.16051	0.157766	-0.11848
0.157	0.070	0.1	-5707.51	13469.01	-11997.7	4583.577	-330.4578	-264.577	69.50356	-5.29907	0.300357	-0.11591
0.192	0.070	0.1	-4889.32	12727.87	-13149.7	6755.66	-1762.962	225.7164	-23.7049	3.686853	0.058686	-0.1066
0.244	0.070	0.1	-11929.3	37604.47	-49351.2	34790.76	-14170.1	3339.429	-431.789	26.06368	-0.1969	-0.08621
0.262	0.070	0.1	-10121.5	31008.67	-39413.5	26644.92	-10169.04	2129.116	-213.344	5.468618	0.463595	-0.08129
0.279	0.070	0.1	-12418.4	36407.42	-44220.3	28438.07	-10190.11	1926.745	-150.887	-0.75143	0.430751	-0.07026
0.288	0.070	0.1	-12182.6	35233.13	-42113.9	26521.06	-9196.447	1625.474	-100.47	-4.25691	0.38226	-0.06642
0.297	0.070	0.1	-8172.67	23362.93	-27368.7	16547.52	-5212.076	674.4023	28.57657	-12.4878	0.455707	-0.06523
0.314	0.070	0.1	7422.636	-21080.4	25533.54	-17514.06	7612.6017	-2167.73	379.0192	-32.264	0.599125	-0.06668
0.323	0.070	0.1	13619.48	-38414.6	45701.81	-30122.63	12169.525	-3115.78	482.9348	-36.3374	0.471167	-0.06792

Table B.2: Two-dimensional URANS C_m data for the NACA LRN 1015

BIBLIOGRAPHY

[1] S. Kallas, M. Geoghegan-Quinn, M. Darecki, C. Edelstenne, T. Enders, E. Fernandez, and P. Hartman, "Flightpath 2050 Europe's Vision for Aviation," *Report of the high level group on aviation research, European commission, Brussels, Belgium, Report No. EUR 98*, 2011.

[2] Anon., "Towards sustainable aviation." https://www.atag.org/component/attachments/?task=download&id=196:2012-Summit-Declaration_WEB-RES-3, 2008.
Accessed on 05.04.2019.

[3] C. Howcroft, D. Calderon, L. Lambert, M. Castellani, J. E. Cooper, M. H. Lowenberg, and S. Neild, "Aeroelastic Modelling of Highly Flexible Wings," in *15th Dynamics Specialists Conference*, p. 1798, 2016.

[4] M. K. Bradley, C. K. Droney, and T. J. Allen, "Subsonic Ultra Green Aircraft Research. Phase ii-Volume i; Truss braced wing design exploration," *NACA Technical Report: NASA/CR2015-218704*, 2015.

[5] T. Wilson, A. Castrichini, J. Paterson, and R. Arribas Ardura, "Non-linear aeroelastic behaviour of hinged wing tips," Oct 2018.

[6] Anon., "How the albatross is inspiring next generation of aircraft wings." https://www.airbus.com/newsroom/press-releases/en/2019/06/how-the-albatross-is-inspiring-next-generation-of-aircraft-wings.html#media-list-image-image-all_ml_0-2, 2019.
Accessed on 19.05.2019.

[7] N. T. Nguyen, E. Ting, D. Chaparro, M. C. Drew, and S. S.-M. Swei, "Multi-objective flight control for drag minimization and load alleviation of high-aspect ratio flexible wing aircraft," in *58th AIAA/ASCE/AHS/ASC Structures, Structural Dynamics, and Materials Conference*, p. 1589, 2017.

[8] D. L. Rodriguez, M. J. Aftosmis, M. Nemec, and G. R. Anderson, "Optimized off-design performance of flexible wings with continuous trailing-edge flaps," in *56th AIAA/ASCE/AHS/ASC Structures, Structural Dynamics, and Materials Conference*, p. 1409, 2015.

[9] R. Cook, D. Calderon, M. H. Lowenberg, S. Nield, J. E. Cooper, and E. Coetzee, "Worst case gust prediction of highly flexible wings," in *58th AIAA/ASCE/AHS/ASC Structures, Structural Dynamics, and Materials Conference*, p. 1355, 2017.

[10] O. Stodieck, J. E. Cooper, and P. Weaver, "Interpretation of bending/torsion coupling for swept, nonhomogenous wings," *Journal of Aircraft*, vol. 53, no. 4, pp. 892–899, 2016.

[11] P. Bekemeyer, M. Ripepi, R. Heinrich, and S. Görtz, "Nonlinear unsteady reduced-order modeling for gust-load predictions," *AIAA Journal*, vol. 57, no. 5, pp. 1839–1850, 2019.

[12] R. Piziali, "2-D and 3-D Oscillating Wing Aerodynamics for a Range of Angles of Attack Including Stall," *NASA TM-4632*, Sept. 1994.

[13] G. B. McCullough and D. E. Gault, "Example of three representative types of airfoil-section stall at low speed," *National Advisory Committee for Aeronautics - Technical Note 2502*, 1951.

[14] MIT, "Fluids – lecture 3 notes." `https://web.mit.edu/16.unified/www/FALL/fluids/Lectures/f03.pdf`, 2000.
Accessed on 10.04.2020.

[15] L. C. Woods, *The theory of subsonic plane flow*, vol. 3.
Cambridge University Press, 2011.

[16] Anon., *Oxford English Mini Dictionary*.
Oxford University Press, 2013.

[17] J. Oh and D. S. Bernstein, "Semilinear duhem model for rate-independent and rate-dependent hysteresis," *IEEE Transactions on Automatic Control*, vol. 50, no. 5, pp. 631–645, 2005.

[18] Z. Yang, H. Igarashi, M. Martin, and H. Hu, "An experimental investigation on aerodynamic hysteresis of a low-Reynolds number airfoil," in *46th AIAA Aerospace Sciences Meeting and Exhibit*, p. 315, 2008.

[19] T. Rendall, "Guide to AERO2 Labs," *Faculty of Engineering, University of Bristol*, 2018.

[20] W. J. McCroskey, "The phenomenon of dynamic stall," *NASA Technical Memorandum 81264*, 1981.

[21] G. Dimitriadis, *Introduction to nonlinear aeroelasticity*.
John Wiley & Sons, 2017.

[22] S. Brunton and C. Rowley, "Modeling the unsteady aerodynamic forces on small-scale wings," in *47th AIAA Aerospace Sciences Meeting Including the New Horizons Forum and Aerospace Exposition*, p. 1127, 2009.

[23] T. Theodorsen, "General theory of aerodynamic instability and the mechanism of flutter, naca," *NACA, Technical Report no 496*, no. 496, pp. 413–433, 1934.

[24] M. Kargarnovin and A. Mamandi, "Aeroelastic response for pure plunging motion of a typical section due to sharp edged gust, using jones approximation aerodynamics," *World Academy of Science, Engineering and Technology*, vol. 36, no. 1, pp. 154–161, 2007.

[25] L. E. Ericsson and J. P. Reding, "Fluid dynamics of unsteady separated flow. part ii. lifting surfaces," *Progress in Aerospace Sciences*, vol. 2, 1987.

[26] A. Niven and R. M. Galbraith, "Modelling dynamic stall vortex inception at low Mach numbers," *The Aeronautical Journal*, vol. 101, no. 1002, pp. 67–76, 1997.

[27] D. Tang and E. Dowell, "Experimental investigation of three-dimensional dynamic stall model oscillating in pitch," *Journal of aircraft*, vol. 32, no. 5, pp. 1062–1071, 1995.

[28] L. Ericsson, "Moving wall effects in unsteady flow," *Journal of Aircraft*, vol. 25, no. 11, pp. 977–990, 1988.

[29] K. W. McAlister, L. W. Carr, and W. J. McCroskey, "Dynamic Stall Experiments on the NACA 0012 Airfoil," *NASA Technical Paper 1100*, Jan 1978.

[30] K. Mulleners and M. Raffel, "The onset of dynamic stall revisited," *Experiments in Fluids*, vol. 52, no. 3, pp. 779–793, 2012.

[31] A. Spentzos, G. Barakos, B. K, B. Richards, P. Wernert, S. Schreck, and R. M, "Investigation of three-dimensional dynamic stall using computational fluid dynamics," *AIAA Journal, Vol. 43, No. 5, pp. 1023-1033*, 2005.

[32] J. G. Leishman, *Principles of Helicopter Aerodynamics*. Cambridge University Press, 2006.

[33] W. J. McCroskey, K. W. McAlister, L. W. Carr, and S. L. Pucci, "An Experimental Study of Dynamic Stall on Advanced Airfoil Sections Volume 1. Summary of the Experiment," *NASA Technical Memorandum 84245*, Jul 1982.

[34] L. U. Dadone, "Two-dimensional wind tunnel test of an oscillating rotor airfoil," *NASA Contractor Report 2914*, vol. I, Dec 1977.

[35] L. W. Carr, W. J. McCroskey, K. W. McAlister, S. L. Pucci, and O. Lambert, "An experimental study of dynamic stall on advanced airfoil sections volume 3.

hot-wire and hot-film measurements," *NASA Technical Memorandum 84245*, 1982.

[36] L. Carr and M. Chandrasekhara, "An assessment of the impact of compressibility on dynamic stall," in *33rd Aerospace Sciences Meeting and Exhibit*, p. 779, 1995.

[37] L. W. Carr, W. J. McCroskey, K. W. McAlister, S. L. Pucci, and O. Lambert, "Dynamic Stall on Advanced Airfoil Sections," *Journal of American Helicopter Society*, pp. 40–50, jul 1987.

[38] T. Fukushima and L. U. Dadone, "Comparison of dynamic stall phenomena for pitching and vertical translation motions," *NASA Contractor Report CR-2793*, 1977.

[39] D. Rival and C. Tropea, "Characteristics of pitching and plunging airfoils under dynamic-stall conditions," *Journal of Aircraft*, vol. 47, pp. 80–86, Jan 2010.

[40] L. W. Carr, K. W. McAlister, and W. J. McCroskey, "Analysis of the development of dynamic stall based on oscillating airfoil experiments," *NASA Technical Note D-8382*, Jan 1977.

[41] W. Sheng, R. A. Galbraith, and F. N. Coton, "Improved dynamic-stall-onset criterion at low Mach numbers," *Journal of aircraft*, vol. 44, no. 3, pp. 1049–1052, 2007.

[42] L. Seto and R. Galbraith, "The effect of pitch rate on the dynamic stall of a NACA 23012," in *Eleventh European Rotorcraft Forum, London*, 1985.

[43] F. O. Carta, "Experimental investigation of the unsteady aerodynamic characteristics of a NACA 0012 airfoil," *UAC RL Report M-1283-1*, Jul 1960.

[44] D. E. Gault, "A Correlation of Low-Speed, Airfoil-Section Stalling Characteristics with Reynolds Number and Airfoil Geometry," *NASA Technical Note 3963*, 1957.

[45] A. O. S. Hilaire, F. O. Carta, M. R. Fink, and W. D. Jepson, "The Influence of Sweep on the Aerodynamic Loading of an Oscillating NACA 0012 Airfoil," *NASA Contractor Report 3092*, 1979.

[46] J. G. Leishman, "Modeling sweep effects on dynamic stall," *Journal of the American Helicopter Society*, vol. 34, pp. 18–29, jul 1989.

[47] M. B. Horner, G. A. Addington, J. W. Young, and M. W. Luttges, "Controlled Three-dimensionality in Unsteady Separated Flows about a Sinusoidally Oscillating Flat Plate," in *28th Aerospace Sciences Meeting*, p. 689, 1990.

[48] A. Spentzos, G. Barakos, K. Badcock, B. Richards, P. Wernert, S. Schreck, and M. Raffel, "CFD investigation of 2D and 3D dynamic stall," in *Conference, CFD investigation of 2D and 3D dynamic stall, San Francisco, California. AHS*, 2004.

[49] K. Kaufmann, A. Gardner, and M. Costes, "Comparison Between Two-Dimensional and Three-Dimensional Dynamic Stall," in *New Results in Numerical and Experimental Fluid Mechanics X*, pp. 315–325, Springer, 2016.

[50] R. Newsome, "Navier-Stokes simulation of wing-tip and wing-juncture interactions for a pitching wing," in *Fluid Dynamics Conference*, p. 2259, 1994.

[51] S. J. Schreck and H. E. Helin, "Unsteady vortex dynamics and surface pressure topologies on a finite wing," *Journal of Aircraft*, vol. 31, pp. 899–907, jul 1994.

[52] R. M. Wernert P., Geissler W. and K. J., "Experimental and numerical investigations of dynamic stall on a pitching airfoil," *AIAA Journal*, vol. 34, pp. 982–989, May 1996.

[53] G. Volpe, "Performance of compressible flow codes at low Mach numbers," *AIAA Journal*, vol. 31, no. 1, pp. 49–56, 1993.

[54] A. Spentzos, G. N. Barakos, K. J. Badcock, B. E. Richards, F. N. Coton, R. A. M. Galbraith, E. Berton, and D. Favier, "Computational fluid dynamics study

of three-dimensional dynamic stall of various planform shapes," *Journal of Aircraft*, vol. 44, pp. 1118–1128, jul 2007.

[55] S. Moir and F. N. Coton, "An examination of the dynamic stalling of two wing planforms," *University of Glasgow Aero. Rept. 9526*, Jan 1995.

[56] K. Kaufmann, M. Costes, F. Richez, A. D. Gardner, and A. L. Pape, "Numerical investigation of three-dimensional static and dynamic stall on a finite wing," *Journal of the American Helicopter Society*, vol. 60, no. 3, pp. 1–12, 2015.

[57] A. Le Pape, G. Pailhas, F. David, and J.-M. Deluc, "Extensive wind tunnel tests measurements of dynamic stall phenomenon for the OA209 airfoil including 3D effects," in *33rd European Rotorcraft Forum, Kazan*, 2007.

[58] K. Kaufmann, C. B. Merz, and A. D. Gardner, "Dynamic stall simulations on a pitching finite wing," *Journal of Aircraft*, vol. 54, no. 4, pp. 1303–1316, 2017.

[59] D. Schwamborn, T. Gerhold, and R. Kessler, "DLR-TAU Code-an overview," 1999.

[60] J. Slotnick, A. Khodadoust, J. Alonso, D. Darmofal, W. Gropp, E. Lurie, and D. Mavriplis, "CFD vision 2030 study: a path to revolutionary computational aerosciences," *NASA Technical Report NASA/CR-2014-218178*, 2014.

[61] M. J. Patil, D. H. Hodges, and C. E. S. Cesnik, "Nonlinear aeroelasticity and flight dynamics of high-altitude long-endurance aircraft," *Journal of Aircraft*, vol. 38, no. 1, pp. 88–94, 2001.

[62] R. G. Cook, R. Palacios, and P. Goulart, "Robust gust alleviation and stabilization of very flexible aircraft," *AIAA journal*, vol. 51, no. 2, pp. 330–340, 2013.

[63] J. Murua, R. Palacios, and J. M. R. Graham, "Applications of the unsteady vortex-lattice method in aircraft aeroelasticity and flight dynamics," *Progress in Aerospace Sciences*, vol. 55, pp. 46–72, 2012.

[64] M. Kretz, "Active expansion of helicopter flight envelope," in *Proceedings of the Fifteenth European Rotorcraft and Powered Lift Aircraft Forum*, Sep 1989.

[65] J. G. Leishman and T. S. Beddoes, "A semi-empirical model for dynamic stall," *Journal of the American Helicopter Society*, vol. 34, no. 3, pp. 3–17, 1989.

[66] C. T. Tran and D. Petot, "Semi-emprical model for the dynamic stall of airfoils in the view of the application to the calculation of responses of a helicopter blade in forward flight," *Vertica*, vol. 5, pp. 35–53, 1981.

[67] M. Goman and A. Khrabrov, "State-space representation of aerodynamic characteristics of an aircraft at high angles of attack," *Journal of Aircraft*, vol. 31, no. 5, pp. 1109–1115, 1994.

[68] R. E. Gormont, "A mathematical model of unsteady aerodynamics and radial flow for application to helicopter rotors (No. D210-10492-1)," tech. rep., Boeing Vertol Co Philadelphia Pa, 1973.

[69] R. Palacios, J. Murua, and R. Cook, "Structural and aerodynamic models in nonlinear flight dynamics of very flexible aircraft," *AIAA journal*, vol. 48, no. 11, pp. 2648–2659, 2010.

[70] J. Katz and A. Plotkin, *Low-speed aerodynamics*, vol. 13.
Cambridge university press, 2001.

[71] D. C. Wilcox, *Turbulence Modeling for CFD (Third Edition)*.
D C W Industries, 2006.

[72] S. B. Pope, *Turbulent Flows*.
Cambridge University Press, 2000.

[73] T. J. Chung, *Computational Fluid Dynamics*.
Cambridge University Press, 2010.

[74] D. Schwamborn, T. Gerhold, and R. Heinrich, "The DLR TAU-code: recent applications in research and industry," in *European Conference on Computational Fluid Dynamics ECCOMAS CFD*, 2006.

[75] A. Gaitonde, "A dual-time method for the solution of the 2D unsteady Navier-Stokes equations on structured moving meshes," in *13th Applied Aerodynamics Conference*, p. 1877, 1995.

[76] P. R. Spalart and S. R. Allmaras, "A one equation turbulence model for aerodynamic flows.," *AIAA Journal*, vol. 94, 1992.

[77] C. L. Rumsey and S. X. Ying, "Prediction of high lift: review of present CFD capability," *Progress in Aerospace Sciences*, vol. 38, no. 2, pp. 145–180, 2002.

[78] Aerogust, "Aeroelastic gust modelling." `https://www.aerogust.eu/`, 2016.

[79] R. M. Hicks and S. E. Cliff, "An evaluation of three two-dimensional computational fluid dynamics codes including low Reynolds numbers and transonic Mach numbers," *NASA Technical Memorandum 102840*, 1991.

[80] G. De Santis, P. Mortier, M. De Beule, P. Segers, P. Verdonck, and B. Verhegghe, "Patient-specific computational fluid dynamics: structured mesh generation from coronary angiography," *Medical & biological engineering & computing*, vol. 48, no. 4, pp. 371–380, 2010.

[81] Y. Ito and K. Nakahashi, "Improvements in the reliability and quality of unstructured hybrid mesh generation," *International Journal for Numerical Methods in Fluids*, vol. 45, no. 1, pp. 79–108, 2004.

[82] R. Morita, F. Inada, M. Mori, K. Tezuka, and Y. Tsujimoto, "CFD calculation and experiments of unsteady flow on control valve," in *ASME 2004 Heat Transfer/Fluids Engineering Summer Conference*, pp. 51–58, American Society of Mechanical Engineers, 2004.

[83] L. Kedward, C. B. Allen, and T. C. Rendall, "Efficient and exact mesh deformation using multiscale RBF interpolation," *Journal of Computational Physics*, vol. 345, pp. 732–751, 2017.

[84] M. Schuff, P. Kranzinger, M. Keßler, and E. Krämer, "Advanced CFD-CSD coupling: Generalized, high performant, radial basis function based volume mesh deformation algorithm for structured, unstructured and overlapping meshes," in *40th European Rotorcraft Forum (Southhampton)*, 2014.

[85] A. De Boer, M. Van der Schoot, and H. Bijl, "Mesh deformation based on radial basis function interpolation," *Computers & Structures*, vol. 85, no. 11-14, pp. 784–795, 2007.

[86] R. Cook, C. Wales, A. Gaitonde, D. Jones, and J. Cooper, "Uncertainty Quantification in Gust Loading Analysis of a Highly Flexible Wing," *International Forum on Aeroelasticity and Structural Dynamics*, 2017.

[87] J. A. Ekaterinaris, "Numerical investigation of dynamic stall of an oscillating wing," *AIAA Journal*, vol. 33, no. 10, pp. 1803–1808, 1995.

[88] D. Weihs and J. Katz, "Cellular patterns in poststall flow over unswept wings," *AIAA Journal*, vol. 21, no. 12, pp. 1757–1759, 1983.

[89] A. E. Winkelman and J. B. Barlow, "Flowfield model for a rectangular planform wing beyond stall," *AIAA Journal*, vol. 18, no. 8, pp. 1006–1008, 1980.

[90] D. M. Luchtenburg, C. W. Rowley, M. W. Lohry, L. Martinelli, and R. F. Stengel, "Unsteady high-angle-of-attack aerodynamic models of a generic jet transport," *Journal of Aircraft*, vol. 52, no. 3, pp. 890–895, 2015.

[91] D. W. Gross and F. D. Harris, "Prediction of in-flight stalled airloads from oscillating airfoil data," in *Proceedings of the 25th Annual Forum of the American Helicopter Society*, pp. 14–16, 1969.

[92] D. A. Peters, "Toward a unified lift model for use in rotor blade stability analyses," *Journal of the American Helicopter Society*, vol. 30, no. 3, pp. 32–42, 1985.

[93] D. Petot, "Differential equation modeling of dynamic stall," *La Recherche Aérospatiale*, vol. 5, pp. 59–72, 1989.

[94] K. W. McAlister, O. Lambert, and D. Petot, "Application of the ONERA Model of Dynamic Stall," *NASA Technical Paper 2399*, Nov 1984.

[95] W. J. Hewson, D. Jones, A. Gaitonde, and E. Coetzee, "CFD Aerodynamic Models for Separated Flow on High Aspect Ratio Flexible Wings," in *2018 AIAA/ASCE/AHS/ASC Structures, Structural Dynamics, and Materials Conference*, p. 1682, 2018.

[96] J. G. Leishman, "Challenges in Modelling the Unsteady Aerodynamics of Wind Turbines," *Wind Energy: An International Journal for Progress and Applications in Wind Power Conversion Technology*, vol. 5, no. 2-3, pp. 85–132, 2002.

[97] M. H. Hansen, M. Gaunaa, and H. A. Madsen, "A Beddoes-Leishman type dynamic stall model in state-space and indicial formulations," *Technical Report Risø–R–1354(EN), Risø National Laboratory, Denmark*, 2004.

[98] J. G. Leishman, "Validation of approximate indicial aerodynamic functions for two-dimensional subsonic flow," *Journal of Aircraft*, vol. 25, no. 10, pp. 914–922, 1988.

[99] T. Beddoes, "Practical computation of unsteady lift," *Vertica 8*, pp. 55–71, 1982.

[100] H. Lomax, M. A. Heaslet, F. B. Fuller, and L. Sluder, "Two-and three-dimensional unsteady lift problems in high-speed flight," *NACA Report No. 1077*, 1952.

[101] J. G. Leishman and T. S. Beddoes, "A generalized model for unsteady airfoil behaviour and dynamic stall using the indicial method," in *Proceeding of the 42nd Annual Forum of the American Helicopter Society*, p. 243, 1986.

[102] D. Marques, Flavio, A. Pereira, Daniel, and M. Vasconcellos, Rui, "Nonlinear airfoil torsional response induced by separated flows," in *56th AIAA/ASCE/AHS/ASC Structures, Structural Dynamics, and Materials Conference*, p. 1423, 2015.

[103] W. Sheng, R. Galbraith, and F. Coton, "A modified dynamic stall model for low Mach numbers," *Journal of Solar Energy Engineering*, vol. 130, no. 3, 2008.

[104] M. S. Chandrasekhara and L. W. Carr, "Lift-curve characteristics for an airfoil pitching at constant rate," *Journal of Aircraft*, vol. 24, no. 10, pp. 680–687, 1987.

[105] M. S. Chandrasekhara and L. W. Carr, "Flow visualization studies of the Mach number effects on Dynamic Stall of an Oscillating Airfoil," *Journal of Aircraft*, vol. 27, no. 6, pp. 516–522, 1990.

[106] J. Leishman and K. Nguyen, "State-space representation of unsteady airfoil behavior," *AIAA Journal*, vol. 28, no. 5, pp. 836–844, 1990.

[107] S. Ahmed and M. Chandrasekhara, "Reattachment studies of an oscillating airfoil dynamic stall flowfield," *AIAA Journal*, vol. 32, no. 5, pp. 1006–1012, 1994.

[108] J. D. Anderson and S. Corda, "Numerical lifting line theory applied to drooped leading-edge wings below and above stall," *Journal of Aircraft*, vol. 17, no. 12, pp. 898–904, 1980.

[109] A. Kuethe, *Foundations of aerodynamics*.
New York: Wiley, 1987.

[110] W. Phillips and D. Snyder, "Modern adaptation of Prandtl's classic lifting-line theory," *Journal of Aircraft*, vol. 37, no. 4, pp. 662–670, 2000.

[111] H. Multhopp, *Methods for calculating the lift distribution of wings (subsonic lifting-surface theory)*.
Aeronautical Research Council London, 1950.

[112] J. Boutet and G. Dimitriadis, "Unsteady Lifting Line Theory Using the Wagner Function for the Aerodynamic and Aeroelastic Modeling of 3D Wings," *Aerospace*, vol. 5, no. 3, p. 92, 2018.

[113] J. S. Izraelevitz, Q. Zhu, and M. S. Triantafyllou, "State-space adaptation of unsteady lifting line theory: twisting/flapping wings of finite span," *AIAA Journal*, pp. 1279–1294, 2017.

[114] J. Boutet and G. Dimitriadis, "Unsteady lifting line theory using the Wagner function," in *Proceedings of the 55th AIAA Aerospace Sciences Meeting*, pp. AIAA–2017, AIAA, 2017.

[115] C. Wales, C. Valente, R. Cook, A. Gaitonde, D. Jones, and J. E. Cooper, "The future of non-linear modelling of aeroelastic gust interaction," in *2018 Applied Aerodynamics Conference*, p. 3632, 2018.

[116] R. J. Simpson, R. Palacios, and J. Murua, "Induced-drag calculations in the unsteady vortex lattice method," *AIAA journal*, vol. 51, no. 7, pp. 1775–1779, 2013.

[117] L. N. Long and T. E. Fritz, "Object-oriented unsteady vortex lattice method for flapping flight," *Journal of Aircraft*, vol. 41, no. 6, pp. 1275–1290, 2004.

[118] B. K. Stanford and P. S. Beran, "Analytical sensitivity analysis of an unsteady vortex-lattice method for flapping-wing optimization," *Journal of Aircraft*, vol. 47, no. 2, pp. 647–662, 2010.

[119] S. F. Hoerner and H. V. Borst, "Fluid-dynamic lift, practical information on aerodynamic and hydrodynamic lift," tech. rep., BORST (HENRY V) AND ASSOCIATES WAYNE PA, 1975.

[120] C. van Dam, "The aerodynamic design of multi-element high-lift systems for transport airplanes," *Progress in Aerospace Sciences*, vol. 38, no. 2, pp. 101 – 144, 2002.

[121] M. Parenteau, F. Plante, E. Laurendeau, and M. Costes, "Unsteady coupling algorithm for lifting-line methods," *55th AIAA Aerospace Sciences Meeting*, May 2017.

[122] M. Sanchez Martinez, J. Boutet, X. Amanodlese, V. Terrapon, and G. Dimitriadis, "Computation of Leishman-Beddoes model parameters using a combination of experiments and simulations," in *AIAA Scitech 2019 Forum*, p. 1854, 2019.

[123] D. Greenblatt and I. Wygnanski, "Effect of leading-edge curvature on airfoil separation control," *Journal of Aircraft*, vol. 40, no. 3, pp. 473–481, 2003.

[124] D. H. Hodges, "A mixed variational formulation based on exact intrinsic equations for dynamics of moving beams," *International journal of solids and structures*, vol. 26, no. 11, pp. 1253–1273, 1990.

[125] M. Drela, "XFOIL: An analysis and design system for low Reynolds number airfoils," in *Low Reynolds number aerodynamics*, pp. 1–12, Springer, 1989.

[126] J. Morgado, R. Vizinho, M. Silvestre, and J. Páscoa, "XFOIL vs CFD performance predictions for high lift low Reynolds number airfoils," *Aerospace Science and Technology*, vol. 52, pp. 207–214, 2016.